



Universitat Autònoma de Barcelona

ADVERTIMENT. L'accés als continguts d'aquesta tesi queda condicionat a l'acceptació de les condicions d'ús establertes per la següent llicència Creative Commons:  http://cat.creativecommons.org/?page_id=184

ADVERTENCIA. El acceso a los contenidos de esta tesis queda condicionado a la aceptación de las condiciones de uso establecidas por la siguiente licencia Creative Commons:  <http://es.creativecommons.org/blog/licencias/>

WARNING. The access to the contents of this doctoral thesis it is limited to the acceptance of the use conditions set by the following Creative Commons license:  <https://creativecommons.org/licenses/?lang=en>



Universitat Autònoma de Barcelona

MECHANISTIC INSIGHTS INTO METAL-CATALYZED HYDROAMINATION REACTIONS

Almudena Couce Ríos

Ph.D. Thesis

Chemistry

Supervisors:

Gregori Ujaque Pérez

Agustí Lledós Falcó

Departament de Química

Facultat de Ciències

2017



Universitat Autònoma de Barcelona

MECHANISTIC INSIGHTS INTO METAL-CATALYZED HYDROAMINATION REACTIONS

Memoria presentada para optar al Grado de Doctor por

Almudena Couce Ríos

Almudena Couce Ríos

Visto bueno,

Gregori Ujaque Pérez

Agustí Lledós Falcó

Bellaterra, 23 de febrero de 2017

Acknowledgments

Here, I would like to thank all those who have supported me, in one or another way, during the course of this Ph.D. Thesis. This section is divided in two parts: the “non-official” acknowledgements (written in Spanish, my mother language) and official acknowledgements (written in English).

Unofficial Acknowledgments

Este trabajo ha sido posible gracias a mis directores de tesis, Agustí y Gregori. A ellos les tengo que agradecer que me hayan acogido en el grupo *Transmet* y me hayan guiado a lo largo de mis estudios de doctorado. También les quiero dar las gracias por todo el conocimiento científico que me han aportado y por la confianza depositada en mí a lo largo de estos años.

También quiero agradecer a toda la planta de química física de la UAB por la cálida acogida, especialmente a Irene, Eli y Sergi por el soporte informático y a todos mis compañeros de del grupo *Transmet*. De entre los muchos que han pasado por aquí, tengo que hacer una mención especial a Sergi Montserrat y Max con quienes, a pesar de no haber coincidido en el despacho, he compartido agradables momentos a lo largo de diversas cenas; a Rosa por haberme enseñado catalán durante las comidas en mi primer año de tesis, a Víctor y Bea quienes han sido grandes compañeros, a Manu por guiar mis primeros pasos sobre terreno computacional, a Eli quien siempre estaba dispuesta a solucionarme mis problemas informáticos y por supuesto por haberme recomendado el RockSmith y por todas las conversaciones sobre otros muchos juegos y series y a Laia por todas esos cafés de media tarde. También tengo que hacer una mención a aquellos que han pasado por aquí temporalmente como son Jordi, Martí, Karel y Mireia y especialmente a Sara Muñoz durante sus proyecto de fin de grado/máster, a Judith con quien tuve el placer de trabajar en sus prácticas de verano y otros compañeros con los que compartí despacho durante sus estancia de investigación como son Rafik, Ivana, Sara Ruíz, Dave (quien siempre será el Scottisch) y como no a Héctor con el que he tenido la suerte de compartir varias noches frikis.

También tengo que agradecer a todos que aquellos con los que tengo la suerte de compartir actualmente el despacho cada día quienes además de ser compañeros de doctorado considero amigos. A Lur por sus deliciosos postres, a Giuseppe por su agradable vapeo y compañía durante esas visitas express a la primera planta a tomar el café, a Sergi por todas esas horas hablando de “frikadas” y obviamente por enseñarme el gran juego de los Munchkin, a Pablo por todas esas conversaciones de química (ya se agradece otro químico por aquí que cada vez somos menos) y por las barbacoas tan ricas que nos prepara y a Jaime por enseñarme el apasionante mundo de la programación y todas esas bromas con las que tanto me he reído y que solo él tiene el don de que se le ocurran en el momento oportuno.

Por último, pero no menos importante, quiero agradecer a Pietro por todo el conocimiento que me ha aportado y todas las dudas que me resolvió en esas últimas horas del día cuando solo quedábamos los dos por la facultad.

To my colleagues abroad, particularly to Kelvin Jackson, Rob Simion, Willian Cortopassi, Ruchuta Ardkhean and Ignacio Funes for the great coffee times making easier my stay in Oxford and also to Qian Peng for all the knowledge and scientific discussions and of course to Robert Paton for the confidence granted to me.

También me gustaría agradecer a todos esos profesores que me han marcado empezando ya por el señor Barros en Bachiller como otros muchos a lo largo de mi licenciatura y máster en la Universidade da Coruña. También me gustaría agradecer a mis “niñas” de la Universidade da Coruña como son Lucía, Mari, María, Iria por esas múltiples cenas de verano/navidad a lo largo de estos años y a Laura Fra quien siempre está ahí cuando se la necesita.

Por ultimo me gustaría agradecer a todas las personas que quiero y que son o considero familia. Concretamente a toda la familia de Jesús, a mis grandes amigos Borja y Luis y sobre todo a mis padres, mis abuelos y mi hermano sin los cuales no habría podido llegar hasta donde he llegado ni ser quien soy. También tengo que agradecer a Jesús por toda el asesoramiento sobre qué imagen queda mejor, las muchas veces que me has escuchado ensayar para las diversas charlas en congresos, por toda la paciencia que has tenido aguantando mis nervios y todo eso siempre con una sonrisa, pero sobre todo por hacer que todos los días sean maravillosos. A todos vosotros, gracias de todo corazón.

Official Acknowledgments

I would like to thanks the Spanish *Ministerio de Economía y Competitividad* (project CTQ-2011-23336) for (i) the predoctoral FPI fellowship that made me possible the present PhD thesis and (ii) the travel scholarship that allowed me to stay for three months in the research group of Prof. Robert Paton (University of Oxford). CESCA and BSC are also acknowledged for providing computational resources.

*Dedicado a mis padres,
mi hermano, mis abuelos y Jesús.*

List of Abbreviations

Abbreviations used along the dissertation are collected as follows.

Abbreviation	Meaning
ACP	Alkylidenecyclopropane
CAAC	Cyclic(alkyl)(amino)carbene
COD	Cyclooctadiene
DFT	Density Functional Theory
EDA	Energy Decomposition Analysis
HF	Hartree-Fock
M06	Zhao and Truhlar's Minnesota 06 density functional
MCB	Methylenecyclobutene
NHC	N-heterocyclic carbene
PES	Potential Energy Surface
PCM	Polarizable Continuum Model
RDS	Rate Determining Step
SCF	Self-consistent Field
SDD	Stuttgart-Dresden effective core potential
SMD	Solvent model density
TOF	Turnover frequency
TON	Turnover number

Atom Caption



Preface

The topic of this thesis is the DFT study of the mechanism of intermolecular hydroaminations catalyzed by rhodium and gold catalyst.

The nitrogen-containing compounds are very valuable and have a lot of uses ranging from pharmaceutical to chemical. The hydroamination reaction is the most economical pathway to synthesize substituted amines. Metal catalyst developed for direct hydroamination includes lanthanides, as well as early and late transition metals. The most versatile catalysts for the intermolecular hydroamination are based on late transition metals. There are a lot of studies published in recent years about this reaction, but despite the effort some questions remain open.

The main challenges of hydroamination reactions are the use of simple amines and unactivated substrates, the intermolecular version, the control of regioselectivity (especially the *anti*-Markovnikov version) and the asymmetrical version. In this thesis we mainly focused on the study of the control of regioselectivity in the intermolecular version of this reaction and an asymmetric process.

The first and second chapters are an introduction to the subject and a theoretical explanation of all the topics used in this thesis. In the third chapter are collected the points this work pretends to achieve, in the fourth chapter we studied an *anti*-Markovnikov hydroamination of alkenes catalyzed by a rhodium catalyst. The fifth chapter deals with the enantioselective hydroamination of allenes catalyzed by a rhodium catalyst. The sixth chapter is devoted to the hydroamination reaction of alkynes, alkenes and allenes with hydrazine catalyzed by a cationic gold catalyst and in the seventh chapter we studied an Au-catalyzed *anti*-Markovnikov hydroamination. The last chapter of this thesis includes a brief conclusion and summary of the outcome of the work carried out.

I hope you enjoy the dissertation as much as I did. Thanks for reading and have fun!

Almudena Couce Ríos

Contents

1 Introduction	1
1.1 Basic Concepts	3
1.1.1 Organometallic Chemistry	3
1.1.2 Reaction mechanism.....	7
1.1.3 Homogeneous Catalysis	9
1.2 Hydroamination reaction.....	11
1.2.1 Reaction mechanism.....	13
1.2.2 Rhodium-catalyzed hydroamination reactions	18
1.2.3 Gold-catalyzed hydroamination reactions	21
2 Computational methods	25
2.1 Quantum Mechanics.....	27
2.1.1. Historical Background of Quantum Mechanics	27
2.1.2 The Schrödinger Equation.....	28
2.1.3 Born-Oppenheimer approximation	30
2.1.4 Approaches for the resolution of Schrödinger equation.....	31
2.1.5 Potential Energy Surface.....	32
2.2 Density Functional Theory	33
2.2.1 Exchange-Correlation Energy.....	35
2.3 Scope of Application	40
2.3.1 Exchange-Correlation functionals used	40
2.3.2 Basis Sets.....	40
2.3.3 Solvation Model.....	42
2.3.4 Gibbs energy in solution	45
3 Objectives	47
4 Rhodium-catalyzed <i>anti</i>-Markovnikov hydroamination of alkenes.....	51
4.1 Introduction	53
4.2 Computational methods and models	53
4.3 Results and Discussion	54
4.3.1 Analysis of the reaction mechanism.....	54

4.3.2 Analysis of the selectivity (amine vs enamine).....	65
4.3.3 Analysis of the regioselectivity	67
4.4 Conclusions	77
5 Enantioselective hydroamination of allenes	79
5.1 Introduction	81
5.2 Computational methods and models	81
5.3 Results and Discussion	83
5.3.1 Coordination of allene to the [Rh(Josiphos)] ⁺ catalyst	83
5.3.2 Mechanistic analysis of the feasible pathways.....	86
5.3.3 Isotopic labeling experiments.....	90
5.3.4 Study of the regioselectivity in the nucleophilic addition.	94
5.3.5 Study of enantioselectivity of this reaction	97
5.3.6 Effect of temperature	108
5.3.6 Theoretical enantiomeric excess	108
5.4 Conclusions	109
6 Gold-catalyzed hydroamination reaction using hydrazine as N-nucleophile	111
6.1 Introduction	113
6.2 Computational methods and models	114
6.3 Results and Discussion	115
6.3.1 Generation of the active species	115
6.3.2 Hydroamination of alkynes.....	117
6.3.3 Hydroamination of alkenes.....	124
6.3.4 Hydroamination of allenes.....	126
6.4 Conclusions	131
7 Gold-catalyzed <i>anti</i>-Markovnikov hydroamination of alkenes	133
7.1 Introduction	135
7.2 Computational methods and models	135
7.3 Results and Discussion	136
7.3.1 Analysis of the reaction mechanism.....	136
7.3.2 Effect of modifying the alkene.....	141
7.3.3 Effect of modifying the ligand.....	144
7.3 Conclusions	149

8 General Conclusions	151
Bibliography	155
Annex A: Publish Papers related to the Ph.D. Thesis.....	177

Chemistry, unlike other sciences, sprang originally from delusions and superstitions, and was at its commencement exactly on a par with magic and astrology.

Thomas Thomson

~ Chapter 1 ~

INTRODUCTION

This chapter introduces some basic concepts on organometallic chemistry, transition metal complexes, catalysis and reaction mechanisms. Regarding the reaction studied, hydroamination, the proposed mechanisms as well as the most important theoretical and experimental studies about the reaction are described.

1.1 Basic Concepts

The first chapter of this thesis introduces some basic concepts related with the topic of this thesis which is the computational study of the hydroamination reaction catalyzed by organometallic complexes. In the first part of this chapter some general ideas on organometallic chemistry and transition metal complexes, what is a catalyst and how it works and what is a reaction mechanism are described. The second part of this chapter is devoted to present the hydroamination reaction and the most important theoretical and experimental studies about this reaction.

1.1.1 Organometallic Chemistry

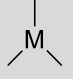
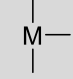
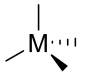
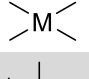
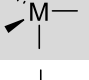

Coordination compounds (also named as coordination complexes) are a class of substances with chemical structures in which a central metal atom (neutral or positively charged) is surrounded by nonmetal atoms or groups of atoms, called ligands (neutral or negatively charged). Organometallic complexes are a particular type of coordination complexes. Organometallic compounds are defined in Elschenbroich and Salzer's book as "*materials which possess direct, more or less polar bonds $M^{\delta+}-C^{\delta-}$ between metal and carbon atoms*".¹ The most common metals used in organometallic complexes are transition metals^{2,3} because of the presence of electrons in their valence d-subshells and their ability to easily change their oxidation state along the reaction.

The nature of the metal, the spin state and the steric and electronic effects of the ligands define the geometry around the metal center, as well as its behavior during the reaction process. Some basic concepts about the structure of transition metal complexes are given in this section.

The most extended guide to explain the structure of transition metal complexes is the 18-electrons-rule.⁴ This rule is based on the fact that the metal atom should fulfill 9 orbitals (one s orbital, three p orbitals and five d orbitals) which overall count to 18 electrons. This means that a metal complex which has 18 electrons is going to have a noble gas configuration and is going to be stable. But several exceptions are found in the literature, in special the 16-electron transition metal complexes.⁴

The simplest approach to explain the geometry of the coordination complexes is based on the coordination number which is the number of occupied sites on the metal center atom and the number of non-bonded electron pairs of the metal. In **Table 1.1** are collected the most important geometries.

Table 1.1: The most common geometries presented in coordination complexes.

Coordination number	Geometry	
2	Linear	—M—
3	Trigonal-planar	
	T-shaped	
4	Tetrahedral	
	Square-planar	
5	Trigonal bipyramidal	
6	Octahedral	

The geometry of the coordination complex affects to the energy of the d-type orbitals of the metal center. This effect was first studied by a crystal field model, developed by Hans Bethe and John Hasbrouck van Vleck.⁵ This model assumes that the ligands are simple point charges and shows how the ligands disturb the energy of the d-orbitals of the metal by means of classical potential energy equations that take into account the attractive and repulsive interactions between charged particles (the ligands and the electrons of the orbitals). All these d-orbitals have the same energy in an isolated metal atom. Different geometries of the coordination complexes are going to perturb the d orbitals in a different way resulting in different crystal field splittings. The energy difference generated between orbitals is named as crystal field splitting and represented by a Δ symbol. This energy gap depends on the oxidation state of the metal as well as the nature of the ligands. Ligands which generate a small crystal field splitting are called weak field ligands and the ones that generate a large crystal field splitting are called strong field ligands. In **Figure 1.1** is represented the crystal field splitting for an octahedral and a square-planar geometry of the ligands.

For an octahedral geometry, ligands approach the metal ion along x, y and z axes, therefore the orbitals which lie along these axes ($d_{x^2-y^2}$ and d_{z^2} , collectively named as E_g) are going to suffer higher repulsions and be more energetics that the d_{xy} , d_{yz} and d_{xz} orbitals (collectively named as T_{2g}). This means that in an octahedral geometry, the energy level of E_g orbitals are higher than in the free metal atom ($0.6\Delta_o$ where Δ_o is the energy of the orbitals in an isolated metal atom) while T_{2g} orbitals are lower ($0.4\Delta_o$). For a square-planar geometry the strongest repulsions take place at the xy plane. Therefore for the two orbitals in this plane ($d_{x^2-y^2}$ and d_{xy}) are destabilized. Overall, an splitting with four different energies

levels appears (**Figure 1.1**). The splitting energy (from highest orbital to lowest energy orbital) is $1.74\Delta_o$. The square-planar geometry is common in metals containing eight electrons in their d-orbitals such as rhodium(I) complexes while rhodium(III) complexes with six electrons in their d-orbitals prefer an octahedral geometry.

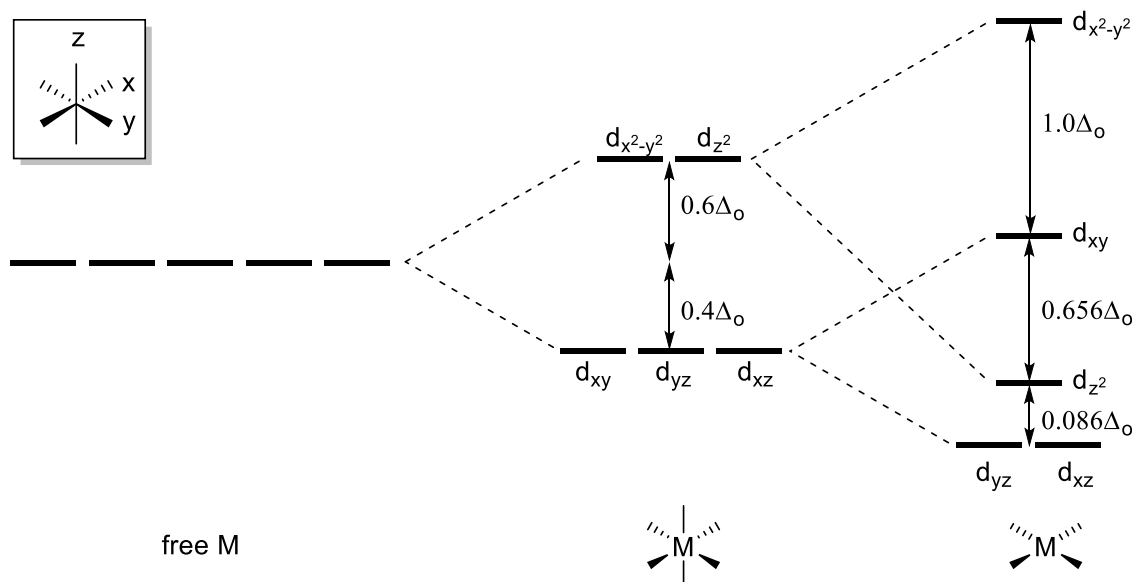


Figure 1.1: Crystal field splitting in octahedral and square-planar geometries.

More recently, the molecular orbital (MO) theory was used to explain the electronic structure of these complexes.⁶ The shape and energy of the molecular orbitals of a complex depend on the number of ligands and their geometrical arrangement around the metal. The interaction between the ligand orbitals (ℓ orbitals) and the nine atomic orbitals of the metal (five d orbitals, one s orbital and three p orbitals) giving rise to ℓ bonding molecular orbital and ℓ anti-bonding molecular orbitals. When the number of ligand orbitals is different to the number of atomic orbitals on the metal, the remaining orbitals ($9 - \ell$ or $\ell - 9$ depending of the number of ligands) stay as nonbonding orbitals. The separation between the energy levels of the nonbonding and anti-bonding orbitals is related with the strength of the interaction between the ligand orbitals and the atomic orbitals of the metal. The bigger is the gap energy (thereby more destabilized are the antibonding orbitals) the stronger is the interaction.

The most used method to construct the molecular orbital diagram of a complex is the “fragment method”. The stages to construct the MO diagrams are: (i) find the point-group symmetry, (ii) determine the symmetry properties of the orbitals on the central metal atom, (iii) consider the ligand orbitals as linear combinations of these orbitals which are adapter to the symmetry of the complex and (iv) allow the metal to interact with the ligand orbitals. Only orbitals of the same symmetry can interact, since their overlap is non-zero.

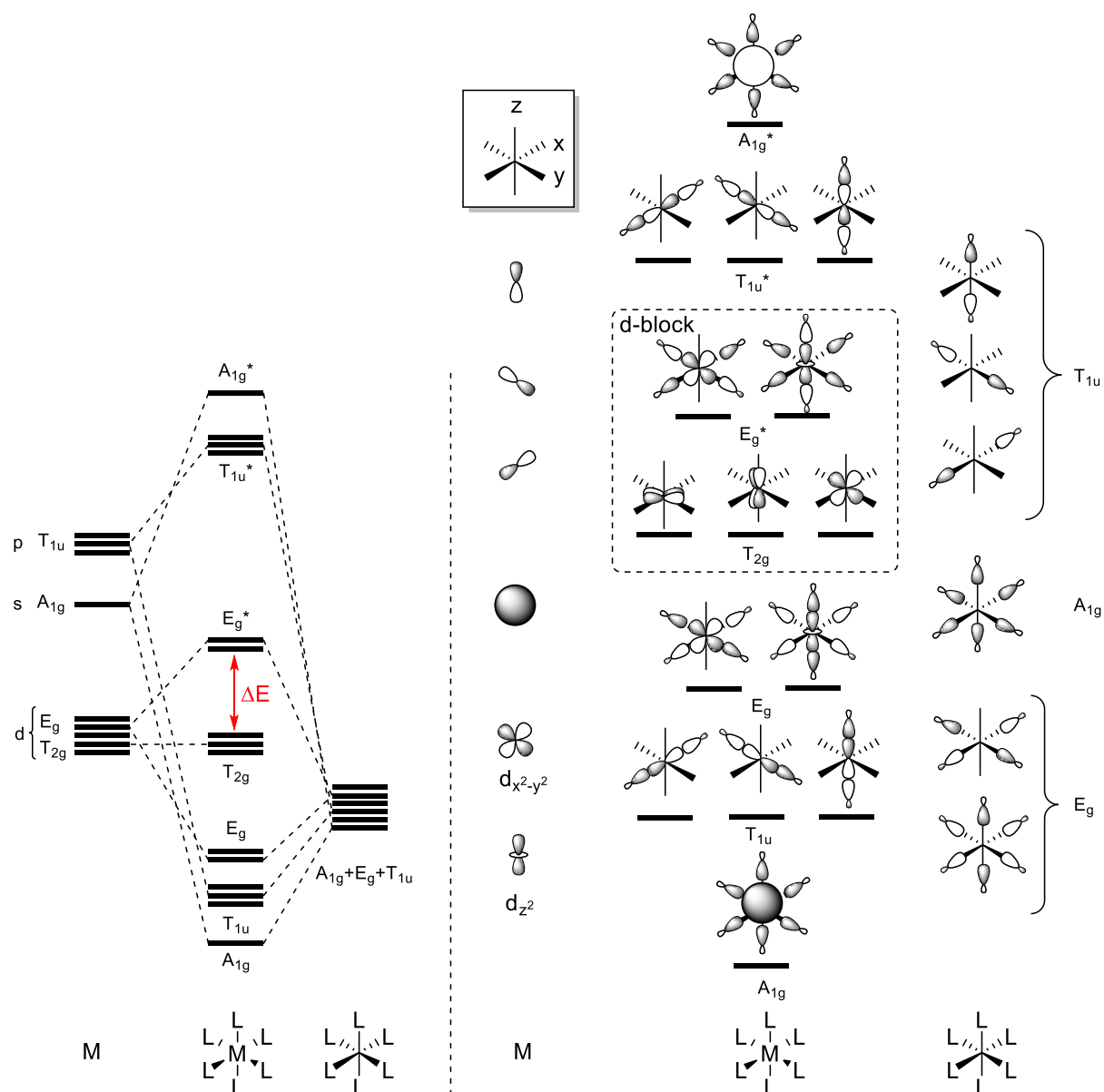


Figure 1.2: MO diagram for an octahedral complex and representation the orbitals involved.

For an octahedral geometry, the point-group symmetry is O_h . The symmetry of the metal orbitals is obtained directly from the table of the octahedral point group. The s orbital has the same symmetry properties as the function $x^2 + y^2 + z^2$, therefore it has A_{1g} symmetry. The p_x , p_y and p_z orbitals transform as x , y and z , respectively and therefore the symmetry is T_{1u} . The d atomic orbitals have two different symmetries: E_g symmetry for $d_{x^2-y^2}$ and d_{z^2} orbitals and T_{2g} symmetry for d_{xy} , d_{yz} and d_{zx} orbitals. The symmetry-adapted σ orbitals for an octahedral complex is $A_{u1}+T_{1u}+E_g$. The last stage to build the MO diagram is to allow the interaction of these symmetry-adapted ligand orbitals with the metal orbitals (fragment method). The interaction of $A_{u1}+T_{1u}+E_g$ ligand orbitals with those with the same symmetry in the metal give rise to A_{u1} , T_{1u} and E_g bonding and the same anti-bonding orbitals whereas T_{2g} orbitals of the metal remain as non-bonding orbitals. The MO diagram for an octahedral complex is represented in **Figure 1.2**.

The representations of the symmetry-adapted σ orbitals for an octahedral complex and orbitals with the same symmetry on the metal center as well as the formed MO orbitals are also depicted in **Figure 1.2**.

Figure 1.2 shows that for an octahedral complex there are six valence atomic orbitals on the metal which contribute to the formation of the six metal-ligand bonds (the s, the three p and two d orbitals). For octahedral complexes, the term “d block” is commonly used. This term is referred to the five molecular orbitals that are mainly concentrated on the d orbitals of the metal: the three nonbonding T_{2g} MOs and the two anti-bonding E_g MOs. The three non-bonding orbitals are purely the d_{xy} , d_{yz} and d_{xz} orbitals from the metals. The E_g^* orbitals are often represented as $d_{x^2-y^2}$ and d_{z^2} orbitals with antibonding contributions on the ligands.

One of the most relevant applications of coordination complexes is homogeneous catalysis for the production of organic compounds. The coordination complexes are able to catalyze a variety of reactions, in particular the hydroamination reaction which is the focus of this dissertation. The next sections are devoted to describe basic concepts in homogeneous catalysis as well as the concept of reaction mechanism which is intimately ligated to that of catalysis.

1.1.2 Reaction mechanism

A reaction mechanism is defined as a step-by-step description of what occurs at the molecular level in a chemical reaction. Usually a reaction takes place through several steps. Each step of the reaction mechanism is known as elementary process so a reaction mechanism consists of multiple elementary processes. A reaction cannot proceed faster than the rate of the slowest elementary step. Therefore, the slowest step in a mechanism establishes the rate of the overall reaction. This step is named the rate determining step of the reaction (RDS).⁷⁻¹²

During a chemical reaction, the reactants go through bond forming and bond breaking steps forming different intermediate species connected by different transition states until forming the products of the reaction. A transition state is defined as a maximum of potential energy along the reaction coordinate and an intermediate is defined as a local minimum of potential energy. The representation of the Gibbs energy of all these species along a given reaction coordinate is named as energy profile diagram or reaction Gibbs energy diagram which is represented in **Figure 1.3**.

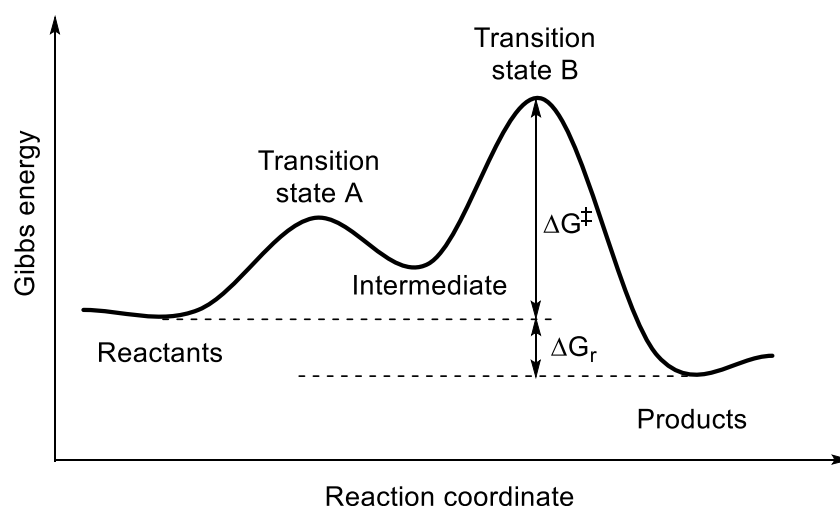


Figure 1.3: Energy profile diagram of a model reaction mechanism.

The thermodynamics of the reaction concerns the difference between Gibbs energy of reactants and products (ΔG_r) and governs the spontaneity of the process. On the other hand, the kinetics is determined by the activation energy of the reaction (E_a) which is an empirical parameter introduced by Arrhenius. The Arrhenius equation derives from empirical observations and ignores any mechanistic considerations, such as whether one or more reactive intermediates are involved in the conversion of a reactant to a product.

The Transition State Theory (TST) defines a new concept: the Gibbs energy barrier which is the Gibbs energy difference between the activated transition state complex and reactants; a fully knowledge of the operative mechanism is required. The experimentally-obtained reaction rate constant (k) can be connected with the Gibbs energy barrier (ΔG^\ddagger) by the Eyring equation:

$$k = \frac{k_B T}{h} e^{-\Delta G^\ddagger / RT} \quad [1.1]$$

where k_B is the Boltzmann constant, h the Planck constant, R the universal gas constant and T the absolute temperature.

Kozuch introduced the concept of energetic span (δE), which is defined as "*the energy difference between the summit and trough of the catalytic cycle*". The energetic span is determined by the transition state and the intermediate that maximize the energetic span which are named as TOF-determining transition state (TDTS) and the TOF-determining intermediate (TDI). Turnover frequency (TOF) concept is explained into the next section.

According to Kozuch, this energetic span can be calculated as the energy difference between these two states whenever the TDTS appears after the TDI, but when the opposite happens, the driving force (ΔG_r) has to be also added to this difference obtaining the following equation:^{13–15}

$$\delta E = \begin{cases} T_{TDTS} - T_{TDI} & (a) \\ T_{TDTS} - T_{TDI} + \Delta G_r & (b) \end{cases} \quad [1.2]$$

Equation (a) has to be used if TDTS appears after TDI and equation (b) if TDTS appears before TDI. The experimentally-obtained reaction rate constant (k) can be connected with the energy span by adapting the Eyring transition state theory.¹⁶ This equation has to be adapted by substituting the Gibbs energy barrier (ΔG^\ddagger) by the energy span (δE).

A mechanism study consists in finding the most feasible pathway to connect reactants with products through the analysis of the thermodynamic as well as the kinetic aspects of the reaction.¹⁷ In our case mechanistic studies are done by means of computational calculations.

1.1.3 Homogeneous Catalysis

A catalyst was defined in 1894 by Ostwald as a chemical substance that accelerates the reaction without being consumed.¹⁸ In the presence and in the absence of the catalyst the reaction has the same initial and final points, but it occurs through different mechanisms, involving different intermediates and transition states. The reaction is faster in presence of the catalyst. This means that a catalyst decreases the activation energy of the reaction allowing it to be carried out under milder conditions and therefore more efficiently.^{19,20} A model energy profile of a reaction in presence and absence of catalyst is represented in **Figure 1.4**.

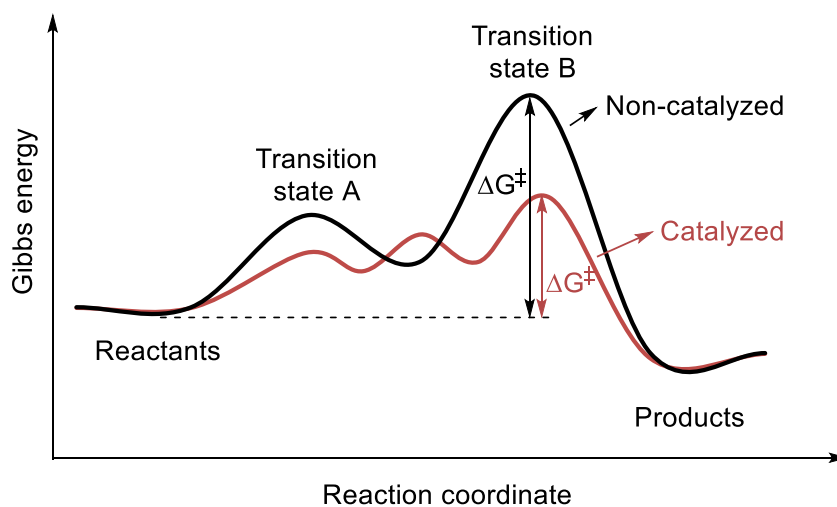


Figure 1.4: Energy profile diagram of a model reaction mechanism in presence (black line) and absence of catalyst (red line).

Catalysts can be classified into homogeneous or heterogeneous depending on whether they exist in the same phase as the substrate or not.^{21–23} Biological catalysts are usually placed in a different group thereby having three different categories to classify the catalysts. In homogeneous catalysis the catalyst is in the same phase as the reactants, most often a liquid phase. Some examples of homogeneous catalysts are simple acids and bases, organic molecules and organometallic complexes, which are the ones studied in this dissertation.

Most often the reaction starts with the coordination of some of the reagents to the organometallic complex. At the end, the reaction product is decoordinated from the catalyst, which in this way is regenerated. A catalytic cycle of a model chemical reaction is represented in **Figure 1.5**. In some cases, at the final point of the reaction, the catalyst is in a different oxidation state or includes different ligands than at the beginning of the reaction, so one or more additional steps are necessary to recover the catalyst and close the catalytic cycle.

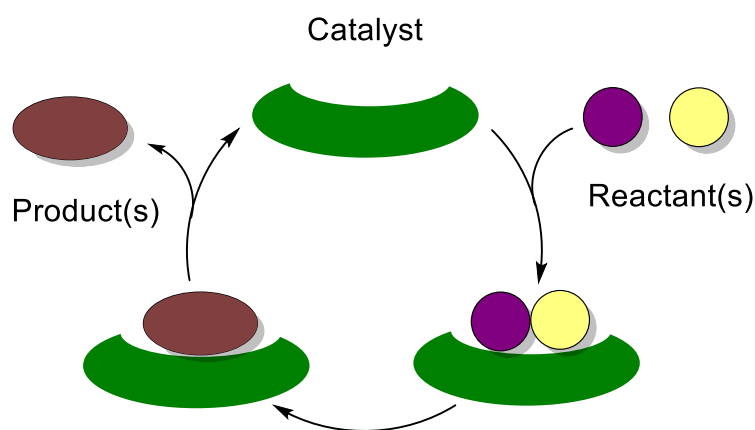


Figure 1.5: Catalytic cycle of a model chemical reaction.

Usually a catalytic cycle is complicated because it involves several elementary steps. In addition, competing side reactions can also occur yielding unwanted products and decreasing the efficiency of the chemical process. For this reason, it is very important to have some magnitudes to measure the efficiency of the catalyst allowing to compare different catalysts. Two magnitudes are usually used to quantify the activity of the catalyst: the turnover number (TON) and the turnover frequency (TOF).²⁰ The turnover number is defined as the total number of moles of substrate that a mole of catalyst can convert into product molecules. This magnitude gives an idea of the robustness of the catalyst by measuring the number of times the catalyst performs the catalytic cycle before becoming inactivated. The turnover frequency is used to refer the turnover per unit time and quantifies the activity of the catalyst. Both magnitudes can be estimated from the energetic span of the reaction^{24–26} which requires a fully knowledge of the operating mechanism.

1.2 Hydroamination reaction

As mentioned above, the topic of this thesis is the computational study of the hydroamination reaction catalyzed by organometallic complexes, so the second part of this chapter is devoted to present the hydroamination reaction and to summarize the most important theoretical and experimental studies about this reaction.

The hydroamination reaction is the addition of a nitrogen-hydrogen bond of an amine to an unsaturated carbon-carbon bond to yield a nitrogen-containing compound. The nitrogen-containing compounds are present in our daily life because they form a part of dyes, drugs, solvents, fertilizers, etc. They also are very important bulk and fine chemical and building blocks in organic synthesis.²⁷⁻²⁹ For this reason, it is very important to develop efficient methods for their synthesis.

The most atom-economic way to synthesize the nitrogen-containing compounds starting from readily available and inexpensive materials is the hydroamination reaction. **Table 1.2** summarizes several methods applied for the synthesis of amines and the efficiency of each method for aliphatic as well as for aromatic amines. The efficiency is calculated as the percentage of the amount of the N-containing product respect of the amount of total product obtained in the reaction. The most used method at the laboratory scale is the nucleophilic substitution of organic halides by amines, azides or cyanides. In accordance with the results presented in **Table 1.2**, the nucleophilic substitution occurs with efficiency between 26 and 54% while the hydroamination reaction has a theoretical 100% efficiency.³⁰

The scope of the hydroamination reaction can be divided into the types of the substrate containing the carbon-carbon bond such as alkenes, alkynes, allenes and dienes. Among these species the hydroamination of alkenes is the most challenging hydroamination. The direct addition of an amine to a carbon-carbon unsaturated bond can yield two different isomers depending on what carbon the addition takes place: the Markovnikov isomer when the addition takes place over the most substituted carbon or the *anti*-Markovnikov if the addition takes place over the less substituted carbon. According to the Markovnikov rule, the Markovnikov product is usually favored in the presence of Brønsted or Lewis acids due to the higher stability of the intermediate carbocation. Consequently, the synthesis of *anti*-Markovnikov amines are rare, being the *anti*-Markovnikov hydroamination of alkenes included in the top ten of challenges of homogeneous catalysis.³¹

Table 1.2: Comparison of various routes to amines. Table adapted from reference 30.

Reaction	Atom-efficiency	
	R ₁ =H	R ₁ =Ph
Nucleophilic substitution followed by reduction		
$\text{R}_1\text{CH}_2\text{Br} + \text{NaCN} \longrightarrow \text{R}_1\text{CH}_2\text{CN} + \text{NaBr} \xrightarrow[\text{catalyst}]{\text{H}_2} \text{R}_1\text{CH}_2\text{NH}_2$	30	54
$\text{R}_1\text{CH}_2\text{CH}_2\text{Br} + \text{NaN}_3 \longrightarrow \text{R}_1\text{CH}_2\text{CH}_2\text{N}_3 + \text{NaBr} \xrightarrow[\text{catalyst}]{\text{H}_2} \text{R}_1\text{CH}_2\text{CH}_2\text{NH}_2 + \text{N}_2$	26	48
Amination of organic halides or alcohols		
$\text{R}_1\text{CH}_2\text{CH}_2\text{Br} \xrightarrow[\text{catalyst}]{\text{NHR}_2} \text{R}_1\text{CH}_2\text{CH}_2\text{NR}_2 + \text{HBr}$	36	60
$\text{R}_1\text{CH}_2\text{CH}_2\text{OH} \xrightarrow[\text{catalyst}]{\text{NHR}_2} \text{R}_1\text{CH}_2\text{CH}_2\text{NR}_2 + \text{H}_2\text{O}$	71	57
Reductive amination of carbonyl compounds		
$\text{R}_1\text{CH}_2\text{CHO} \xrightarrow[\text{H}_2, \text{catalyst}]{\text{NHR}_2} \text{R}_1\text{CH}_2\text{CH}_2\text{NR}_2 + \text{H}_2\text{O}$	71	87
Reduction of nitro compounds		
$\text{R}_1\text{CH}_2\text{CH}_2\text{NO}_2 \xrightarrow[\text{catalyst}]{\text{H}_2} \text{R}_1\text{CH}_2\text{CH}_2\text{NH}_2 + 2 \text{H}_2\text{O}$	56	77
Hydrocyanation of olefins followed by reduction		
$\text{R}_1\text{CH}=\text{CH}_2 \xrightarrow[\text{catalyst}]{\text{HCN}} \text{R}_1\text{CH}_2\text{CH}_2\text{CN} \xrightarrow[\text{catalyst}]{\text{H}_2} \text{R}_1\text{CH}_2\text{CH}_2\text{CH}_2\text{NH}_2$	100	100
Hydroamination of olefins		
$\text{R}_1\text{CH}=\text{CH}_2 \xrightarrow[\text{catalyst}]{\text{NHR}_2} \text{R}_1\text{CH}_2\text{CH}_2\text{NR}_2$	100	100
Hydroaminomethylation of olefins		
$\text{R}_1\text{CH}=\text{CH}_2 \xrightarrow[\text{CO}/\text{H}_2, \text{catalyst}]{\text{NHR}_2} \text{R}_1\text{CH}_2\text{CH}_2\text{CH}_2\text{NR}_2 + \text{H}_2\text{O}$	77	88

The direct addition of amines to unsaturated carbon-carbon bond is thermodynamically accessible but has very high activation energy associated which makes the use of catalysts necessary.^{32–38} Several studies were carried out to develop an efficient catalyst for this reaction and some Brønsted acids^{39,40} and bases^{30,41} and alkali and alkaline metals^{42–46} have been found to be active catalysts for this reaction. Alternative catalysts based on late transition metals are also active for the hydroamination reaction. Particularly, rhodium, iridium and gold catalysts have been developed in the last years.^{36,47–49}

Despite of efforts devoted to this reaction, there are some challenges yet to be solved. The first one is the use of unactivated olefins, like ethylene, because the activation energy is very high.⁵⁰⁻⁵² The second one is the use of small nucleophile molecules, like hydrazine or ammonia because they form very stable compounds with the catalyst that prevent the reaction from happening.⁵³⁻⁵⁷ Other challenges are the intermolecular version of the reaction, which is entropically disfavored and the control of the regioselectivity, especially the *anti*-Markovnikov addition. The last one is the development of enantioselective version of the reaction.

This dissertation is focused to study selected hydroamination reactions catalyzed by rhodium and gold catalysts in order to understand the operating mechanism in each reaction and to explain relevant aspects like the selectivity (hydroamination vs oxidative amination) as well as the regioselectivity and the enantioselectivity observed experimentally. Several different mechanisms have been proposed for the hydroamination reactions. This section describes the different mechanistic alternatives and the most important contributions in rhodium and gold-catalyzed hydroaminations reported in the literature.

1.2.1 Reaction mechanism

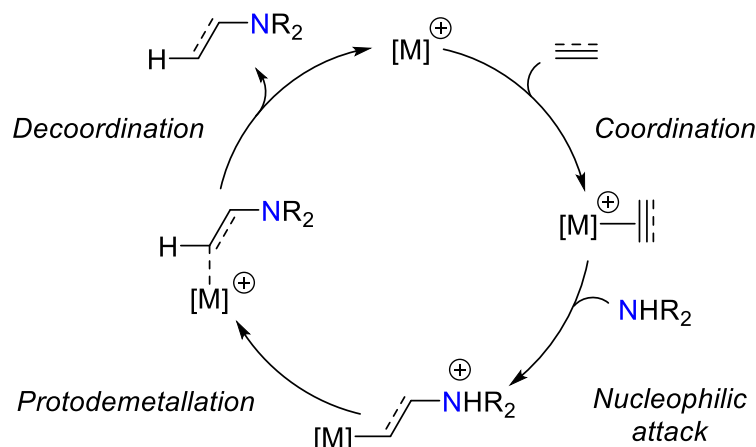
The hydroamination reaction can occur through different mechanisms and the selectivity of the reaction as well as the efficiency depends on the pathway followed. The catalyst, the substrate and the amine employed determine the operative mechanism. This section summarizes all the proposed mechanisms for the hydroamination reaction.

1.2.1.1 Electrophile activation mechanism

In this mechanism the reaction starts with the activation of the unsaturated substrate and it is followed by a nucleophilic attack of the amine. Two different plausible mechanisms could occur along this pathway.

a) Hydroamination by nucleophilic attack of amine on coordinated alkene/alkyne

This pathway is the most common one. A Lewis-acidic catalyst activates the carbon-carbon bond withdrawing electron density, which renders it susceptible to the nucleophilic attack by the lone electron pair of the amine nitrogen atom. This pathway ends with a protodemetalation by a direct protonolysis or with a proton transfer assisted by a second amine. The regioselectivity observed in the hydroamination reaction is defined in the nucleophilic attack step. The most important steps of this pathway are represented in **Scheme 1.1**.



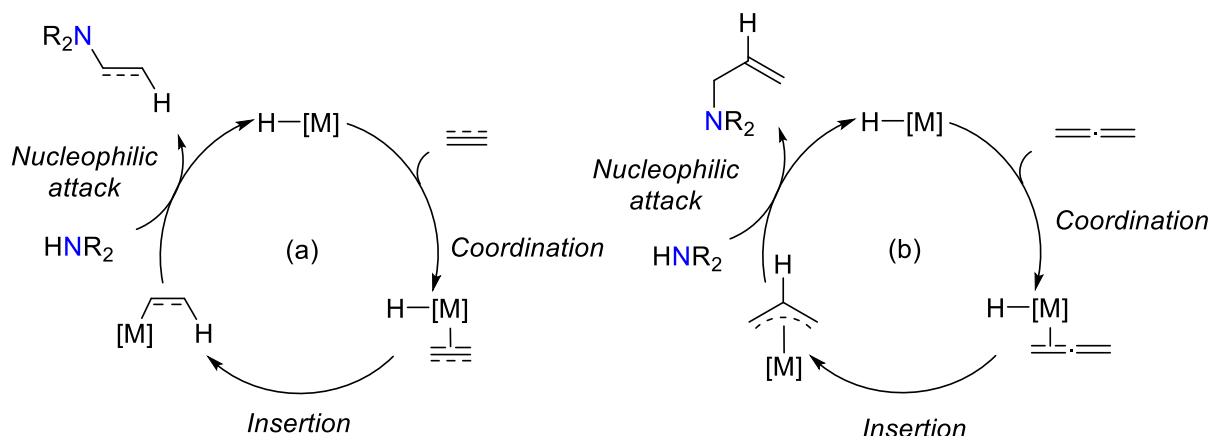
Scheme 1.1: Catalytic cycle for hydroamination by nucleophilic attack of amine on coordinated unsaturated substrate.

This mechanism was proposed for the hydroamination reaction by Trogler et al. for the addition of aniline to the activated dialkyl substrate⁵⁸ based on previous suggestion by Venanzi et al. for the cyclization of aminoalkenes.⁵⁹ The catalyst used was a platinum complex in the first case and a palladium catalyst in the second case. This mechanism was proposed also by Muller et al. for the palladium-catalyzed cyclization of 6-aminohept-1-yne⁶⁰ and supported by kinetic studies.⁶¹ Several groups have reported experiments supporting this mechanism for rhodium and iridium,^{62,63} palladium,^{64,65} platinum,^{66–68} and gold⁶⁹ catalysts. This mechanism has been also proposed for the hydroamination of dienes catalyzed by palladium in absence of acid.⁷⁰

The reaction pathway appears feasible for electron-deficient alkenes and alkynes in combination with electron-rich N-nucleophiles. This pathway was studied at HF level by Åkermark et al. for a Nickel catalyst⁷¹ and later by Seen et al. using DFT calculations for d⁸-transition metal complexes from groups 9 and 10.⁷² Our group established by means of DFT calculations that this mechanism also operates for the hydroamination reaction of alkenes and alkynes catalyzed by gold complexes.^{73,74} Theoretical studies have shown that the slippage of the coordinated substrate is very important for the nucleophilic addition as well as the shape of the LUMO orbital.^{75,76}

b) Insertion of substrate into the Metal-Hydride bond

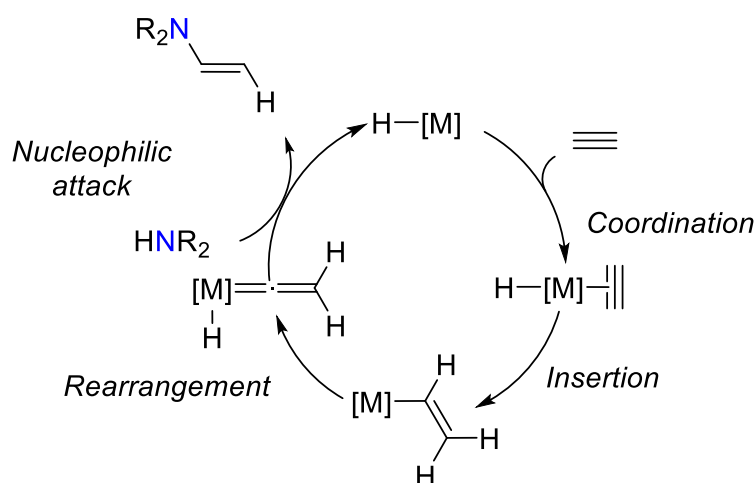
This pathway requires a metal-hydride bond, so the first step of this pathway (when a catalyst is not a hydride) can be a direct protonation of the metal center or an oxidative addition of an acid. This step is followed by the insertion of the substrate into the metal-hydride bond to yield a species which is susceptible to be attacked by the N-nucleophile. In case of the substrate being an alkyne, this step leads to vinyl-metal species; when the substrate is an allene, this step leads to an allylic complex and in case the substrate is an alkene, this step yields an alkyl species. The catalytic cycle for this pathway is represented in **Scheme 1.2**.



Scheme 1.2: Catalytic cycle for hydroamination starting with the insertion of (a) alkene and allenes (b) allenes into a metal-hydride bond.

This pathway has been described for hydroamination of allenes catalyzed by palladium,⁷⁷⁻⁷⁹ alkenes and alkynes catalyzed by copper-hydride complexes^{80,81} and also dienes catalyzed by nickel.⁸² This pathway seems to be operating also in the hydroamination reaction of alkenes⁸³ and dienes⁷⁰ catalyzed by a palladium complex in presence of acid, as well as catalyzed by a palladium complex immobilized over a film of ionic liquid.⁸⁴ The allyl complex formed can be isolated and was identified as the major species,^{82,85} this fact indicates that the nucleophilic addition is the rate determining step when the hydroamination reaction takes place through an insertion of the substrate into a metal-hydride bond.

A similar mechanism has been proposed for the hydroamination reaction of alkynes catalyzed by ruthenium complexes.⁸⁶⁻⁸⁸ This mechanism starts with the formation of a hydride catalyst and it is followed by the insertion of the alkyne into the metal-hydrogen bond. This step produces a vinyl-metal species which can rearrange into the corresponding vinylidene complex. From this intermediate the nucleophilic addition of amine takes place forming the product of the reaction. This mechanism is represented in **Scheme 1.3**.



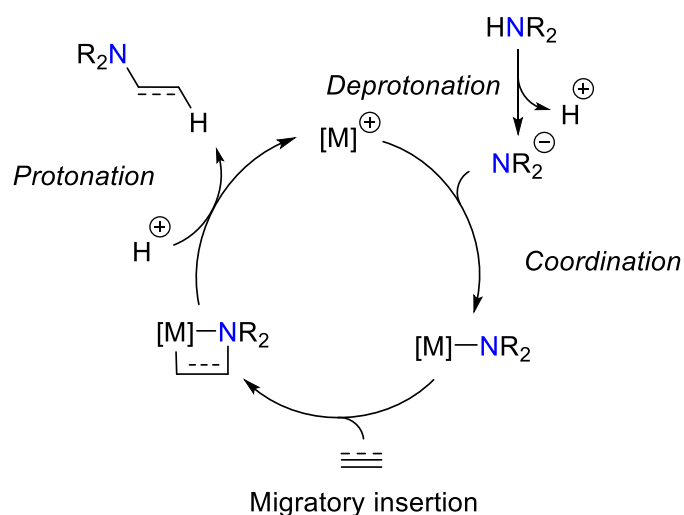
Scheme 1.3: Catalytic cycle for insertion of an alkyne into metal-ruthenium bond pathway.

1.2.1.2 Amine activation mechanism

This mechanism starts with the activation of the amine and it is followed by the insertion of the substrate into the metal-nitrogen bond. Two pathways are possible depending on how the activation of the amine takes place: one is the deprotonation of the amine followed by the coordination of the amine to the metal center and the other is the activation of the amine by an oxidative addition step.

a) Deprotonation of amine

In this pathway the first step of the mechanism is the deprotonation of the amine. This proton can be removed by a ligand of the precatalyst, by another amine or by an external base, for example, the solvent. This step is followed by the coordination of the deprotonated amine and the substrate to the metal center and by a migratory insertion of the substrate into the metal-nitrogen bond. The last step is the protonation of the alkylamine complex to yield the reaction product. This mechanism is represented in **Scheme 1.4**.



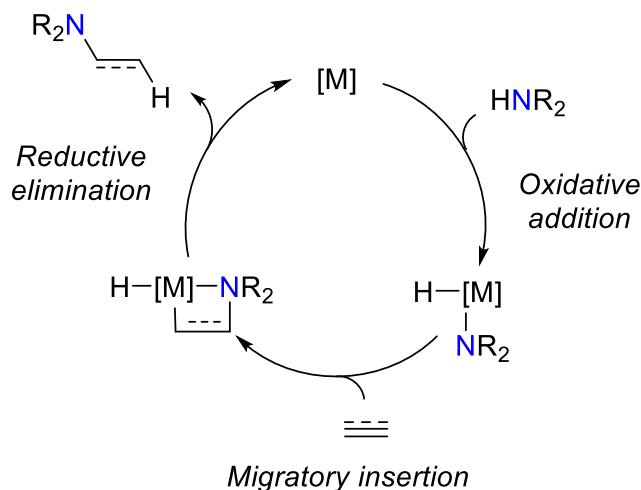
Scheme 1.4: Catalytic cycle for amine activation mechanism starting with deprotonation of amine.

This mechanism was proposed for the hydroamination reaction of alkenes with acrylonitrile catalyzed by platinum complexes.⁸⁹ This pathway was also studied by DFT calculations for the hydroamination of alkenes catalyzed by a rhodium (I) complex.⁹⁰

A similar mechanism was studied by DFT calculations by Uhe et al. for a hydride-rhodium (III) catalyst.⁹¹ In this study the amine is deprotonated by protonating a second amine or a ligand of the precatalyst. Then, the deprotonated amine is coordinated to the metal center and the formation of the carbon-nitrogen bond takes place by a migratory insertion step. The reaction finishes with the reductive elimination of the reaction product.

b) Oxidative addition of amine

In this pathway the reaction starts with the oxidative addition of the amine. During the oxidative addition step the oxidation number of the metal is increased in two units as well as the coordination number. Thus, a coordinatively unsaturated transition metal is required. Subsequently, the migratory insertion of the amine into the metal-hydrogen bond occurs and a reductive elimination of the product regenerates the active low-valent metal catalyst. A representation of this pathway is shown in **Scheme 1.5**.



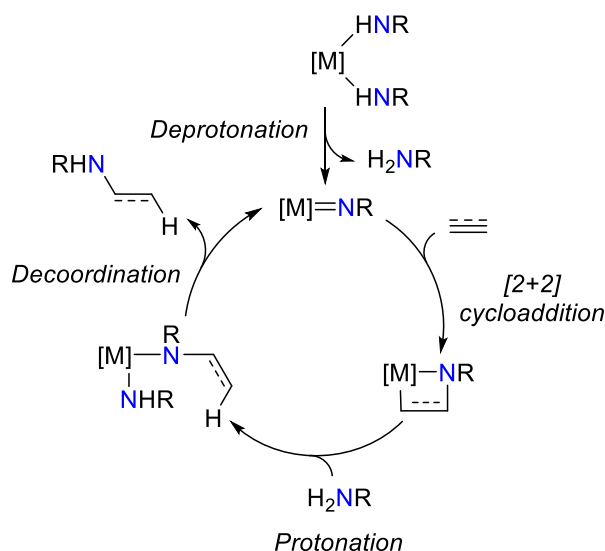
Scheme 1.5: Catalytic cycle for hydroamination through oxidative addition of amine.

This pathway was proposed for the first time by Casalnuovo et al. for the hydroamination reaction of norbornene with aniline catalyzed by an iridium complex.⁹² This pathway was also proposed for the redox couples Ru^0/Ru^{II} ,⁹³ Ir^I/Ir^{III} ,⁹⁴ Pd^0/Pd^{II} ,⁹⁵ Pt^0/Pt^{II} ^{96,97} and Cu^I/Cu^{III} .⁹⁸

Theoretical studies carried out by Tsipsis et al. show that the reductive elimination and oxidative addition steps are the limiting steps in the hydroamination catalyzed by platinum complexes.⁹⁹ The migratory insertion was also studied by means of DFT calculations by Hartwig et al. for the hydroamination catalyzed by rhodium complexes.¹⁰⁰ They found that a reorganization of the substrate as well as the amine is necessary before the migratory insertion. They also affirm that the regioselectivity observed during the migratory insertion step depends on the electronic properties of the substituents of the substrate.

1.2.1.3 [2+2] cycloaddition mechanism

This pathway starts with the deprotonation of the amine by a second amine molecule, and then takes place the formation of a metal-imido complex which undergoes a [2+2] cycloaddition reaction with the alkene, alkyne or allene substrate to yield an azametallacyclobutene. This azametallacyclobutene is protonated by the protonated amine formed in the first step closing the catalytic cycle, and thus restoring the catalyst. The main steps of this mechanism are summarized in **Scheme 1.6**.



Scheme 1.6: Catalytic cycle for hydroamination through a [2+2] mechanism.

This mechanism has been shown to occur in several hydroamination reactions catalyzed by neutral group 4 metal complexes.¹⁰¹ The study of the hydroamination reaction catalyzed by zirconocene complexes show that the reaction follows this [2+2] cycloaddition mechanism and the regioselectivity observed can be related with the nature of the turnover-limiting step (the protonolysis of the azametallacyclobutene or the [2+2] cycloaddition step).¹⁰² The hydroamination reaction of alkenes, alkynes and allenes following this pathway was studied by means of DFT calculations using a titanium-imido catalyst.¹⁰³

1.2.2 Rhodium-catalyzed hydroamination reactions

This section is devoted to summarize the development of hydroamination reactions catalyzed by rhodium-based catalysts as well as the most important studies of its mechanism. There are few mechanistic studies of hydroamination reactions catalyzed by rhodium complexes. Rh complexes show excellent activity in the catalysis of intermolecular *anti*-Markovnikov hydroamination of alkynes and alkenes. Regarding to the operating mechanism for the hydroamination reaction catalyzed by rhodium complexes, two plausible mechanisms has been proposed.¹⁰⁴ The first is an electrophile activation mechanism whose main steps are the coordination of the electrophile substrate to the metal center and the nucleophilic attack of the amine (see **Section 1.2.1.1** for more details). The second proposed mechanism is an amine activation mechanism whose initial step is the oxidative addition of the amine and is followed by a migratory insertion step (see **Section 1.2.1.2** for more details).

1.2.2.1. Hydroamination of alkenes catalyzed by rhodium-complexes

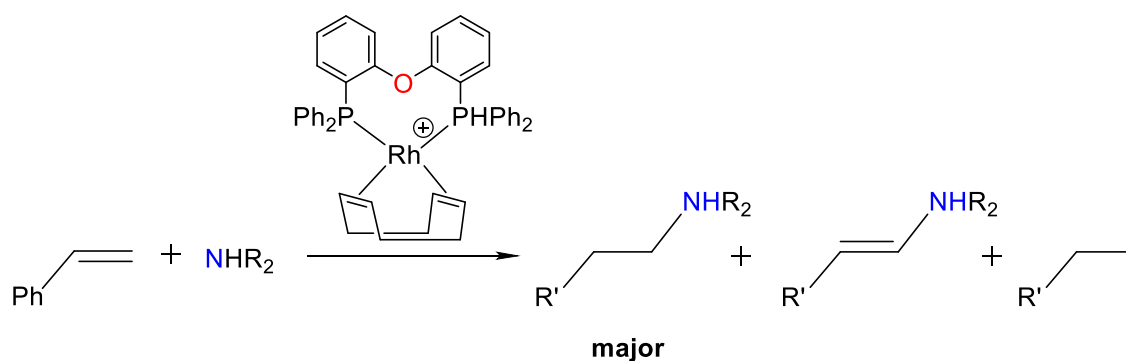
The first example of hydroamination catalyzed by a rhodium-catalyst was in 1971 when Coulson et al. were able to add a secondary alkylamine to ethylene catalyzed by $RhCl_3 \cdot 3H_2O$; high temperatures and pressure are required.⁵⁰ They found that very small changes on

electronic properties of amine produce significant changes on the reaction yield being piperidine, pyrrolidine and dimethylamine the ones that produce the better results. Later, Taube and coworkers identified the $\text{trans-RhCl}(\text{C}_2\text{H}_4)(\text{piperidine})_2$ as a intermediate compound in the reaction between piperidine and ethylene.^{105,106}

In 1979, Diamond and co-workers extended the scope of the reaction to the hydroamination of ethylene with anilines.¹⁰⁷ Building on early studies,¹⁰⁸ Brunet et al. studied the reaction of norbornene with anilines in presence of $[\text{Rh}(\text{PEt}_3)_2\text{Cl}]_2$.¹⁰⁹ It was observed that using less electron rich phosphines (PPh_3), more sterically demanding phosphines (PCy_3) or complexes reminiscent of Wilkinson's catalysts ($(\text{PEt}_3)\text{RhCl}$) provided inferior conversions to products. Brunet and co-workers extended this study to the hydroamination of styrene and 1-hexene using the same catalyst. They found that a mixture of the Markovnikov and the anti-Markovnikov isomer is obtained in 30:65 ratio.¹¹⁰

In 1999, Beller et al. reported the first example of *anti*-Markovnikov hydroamination of alkenes catalyzed by a transition metal catalyst. In this study they used a mixture of $[\text{Rh}(\text{cod})_2]\text{BF}_4$ and PPh_3 .^{104,111} Even in all cases the oxidative amination product is the major one (enamine product), they found that higher yields of the hydroamination product are obtained using morpholine as amine.^{112,113} Later, in 2003, Hartwig et al. were able to obtain the *anti*-Markovnikov hydroamination product as the major one for the hydroamination reaction of vinylarenes with various secondary aliphatic amines catalyzed by a cationic rhodium catalyst with a DPEphos ligand [(Oxydi-2,1-phenylene)bis(diphenylphosphine)]. This reaction is represented in **Scheme 1.7** and studied in **Chapter 4**. Other ligands like Xantphos and DBFphos (4,5-Bis(diphenylphosphino)-9,9-dimethylxanthene and 4,6-Bis(diphenylphosphino)dibenzofuran, respectively) give little or no hydroamination products.¹¹⁴

This reaction was extended to the hydroamination of alkynes in 2007. Fukumoto et al. developed the first Rh(I) catalyst that is able to carry out the *anti*-Markovnikov hydroamination reaction of terminal alkynes with both primary and secondary aliphatic amines.¹¹⁵ Also in 2007, Brunet and co-workers studied the effect of iodide ions in the hydroamination of ethylene.¹¹⁶



Scheme 1.7: First *anti*-Markovnikov hydroamination of styrene catalyzed by a Rh(I) catalyst.

Concerning the intramolecular version of this reaction, Hartwig also reported the intramolecular hydroamination of nonactivated alkenes with primary amines.¹¹⁷ They found that the nucleophile addition of the amine toward the coordinated olefin is the rate-determining step of this reaction.¹¹⁸ In 2010, Buchwald reported the asymmetric intramolecular hydroamination of alkenes catalyzed by a rhodium complex with an dialkylbiaryl phosphine as ligand.¹¹⁹

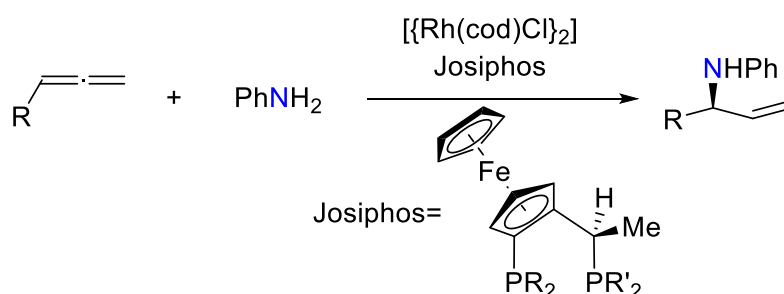
In regard to the study of the mechanism of this reaction, there are a few examples of computational studies of hydroamination reactions catalyzed by rhodium complexes. The first example was published in 2000 when Senn et al. carried out the DFT study of ethylene with group 9 and 10 transition metals catalysts through an alkene activation mechanism.⁷²

Later Hartwig et al. studied the migratory insertion step of ethylene into a rhodium-nitrogen bond.¹⁰⁰ Polo et al. studied by means of DFT calculations the reaction of styrene with a secondary amine using a rhodium catalyst with a hemilabile phosphine ligand.⁹⁰ They affirm that the operating mechanism is an amine activation mechanism starting with the deprotonation of the amine.

The hydroamination reaction was also studied by DFT calculations using a Rh(III) catalyst in 2010 by Uhe et al.⁹¹ The last example of DFT studies of this reaction catalyzed by rhodium complexes was carried out very recently by Balcells and Hartwig. They computationally studied the intramolecular hydroamination of aminoalkenes catalyzed by a Rh(I) catalyst with a phosphine ligand.¹²⁰

1.2.2.2. Hydroamination of allenes catalyzed by rhodium-complexes

There are very few cases of hydroamination of allenes catalyzed by rhodium complexes; the first example was reported by Breit et al. in 2012. In this study they first reported the hydroamination of allenes with anilines catalyzed by a $[\text{Rh}(\text{cod})\text{Cl}]_2/\text{DPEphos}$ system.



Scheme 1.8: First enantioselective hydroamination of allenes catalyzed by a Rhodium catalyst with a Josiphos ligand.

Thus, inspired by the iridium system with a Josiphos ligand described by Togni,¹²¹ they explored the performance of a rhodium catalyst with a Josiphos ligand. They found out that it is able to catalyze the enantioselective hydroamination of aniline to allenes.¹²² This

reaction is represented in **Scheme 1.8** and studied in **Chapter 5**. Later they also reported the enantioselective addition of pyridines to allenes.¹²³

1.2.3 Gold-catalyzed hydroamination reactions

Gold complexes have been intensely investigated as catalyst for the inter- and intramolecular hydroamination reaction of alkynes and allenes, showing very high turnover numbers (TON).^{47,49}

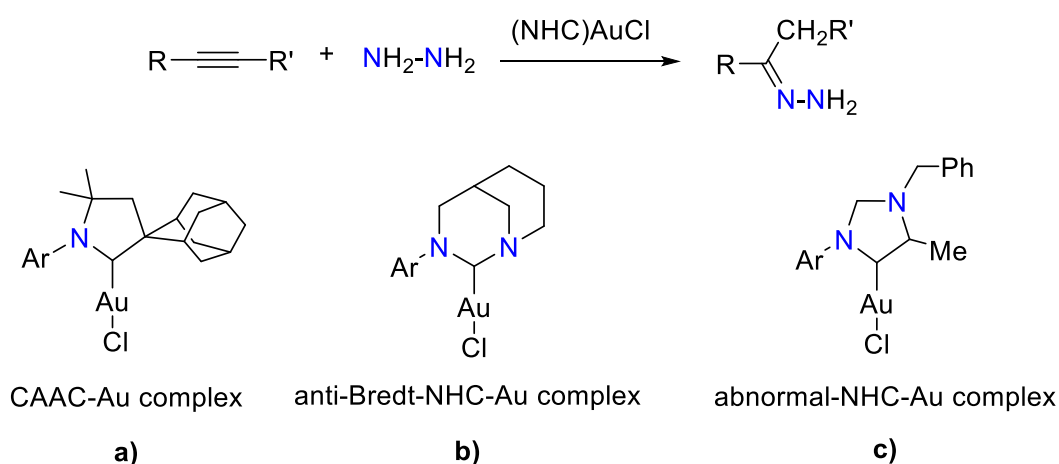
The operating mechanism of hydroamination reactions catalyzed by gold complexes was also object of intense study.^{124–127} The general mechanism can be described as an initial coordination of the amine followed by an exchange of the amine by an electrophile substrate molecule. The reaction continues with the nucleophilic attack of the amine and finally a protodeauration step takes place to close the catalytic cycle (see **Section 1.2.1.1** for more details about this mechanism). Several computational studies support this mechanism for the hydroamination reaction of alkenes,^{73,128} alkynes^{74,129} and allenes.^{130,131}

Despite of the efforts devoted to the study of the mechanism of hydroamination reactions catalyzed by gold complexes, some aspects, such as the associative or dissociative nature of the exchange of the amine with the electrophile substrate or the inner- or outer-sphere mechanism for the nucleophilic attack of the amine have not been substantiated yet.

In this section are summarized the most important gold-catalysts used in the hydroamination reaction, classified depending on the substrate: alkene, alkyne or allene.

1.2.3.1. Hydroamination of alkynes catalyzed by Gold-complexes

In 2003, Tanaka et al. reported TON number of up to 9000 for an acid-promoted gold(I)-catalyzed intermolecular hydroamination of alkynes.¹³² Bertrand and co-workers developed the only example of late transition metal-catalyst which is able to carry out the hydroamination reaction of alkynes using ammonia as N-nucleophile under the influence of a cationic gold complex with a cyclic(alkyl)(amino)carbene (CAAC) ligand.¹³³ The ammonia is a challenging reagent in hydroamination reactions due to its moderate nucleophilicity and its strongly coordinating properties. This reaction was computationally studied by our group.⁷⁴ Later, the same catalyst was employed to catalyze the hydroamination reaction of alkynes using secondary amines^{134–136} as well as hydrazine¹³⁷ in good yield and moderate regioselectivity. This reaction is depicted in **Scheme 1.9** and studied in **Chapter 6**.



Scheme 1.9: Hydroamination of alkynes with hydrazine catalyzed by a Gold(I) catalyst with a) [CAAC] ligand b) anti-Bredt ligand and c) abnormal NHC ligand.

Shi et al. reported in 2009 a very stable triazole-gold complex that is able to catalyze the intermolecular hydroamination reaction of unprotected amines to terminal and internal alkynes.¹³⁸ Later, Hesp and Stradiotto reported a P-N ligand to support the gold complex that is able to catalyze the stereo- and regioselective hydroamination of internal alkynes to give E-enamines.¹³⁹

In 2013, Bertrand group reported a new NHC ligand in which one of the two nitrogen atoms of the classical NHC ligand is placed in a strained bridgehead position. This ligand is named as anti-Bredt NHC ligand. Using a gold(I) complex with this anti-Bredt NHC ligand, Bertrand was able to catalyze the hydroamination reaction of alkynes with hydrazine at room temperature.¹⁴⁰ Very recently, in 2014, Hashmi's group reported the hydroamination of alkynes catalyzed by a gold(I) catalyst with abnormal NHC ligands.¹⁴¹ All these reactions are represented in **Scheme 1.9** and studied in **Chapter 6**.

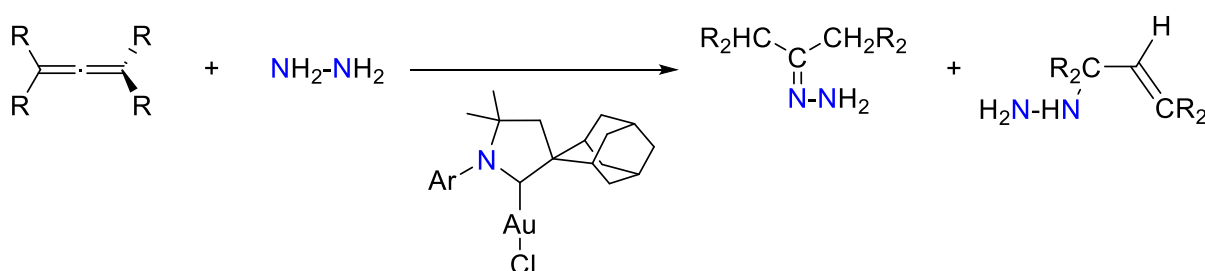
Regarding the intramolecular versions of this reaction, in 2006, Shin and co-workers developed an Au(I)-catalyst which showed very good results in the catalysis of intramolecular hydroamination of alkynes with a significant effect of the counterion used.¹⁴² Hashmi and coworkers studied a similar hydroamination reaction catalyzed by AuCl₃.¹⁴³ Other authors like Ritter and Mitchells also reported intramolecular hydroamination reactions using gold(I) complexes as catalysts.^{144,145}

Jørgenson et al. described the use of a gold catalyst for the asymmetric hydroamination reaction on an alkyne with a very high selectivity.¹⁴⁶ Other authors like Dyker and Takemoto developed different gold catalysts that catalyze intramolecular hydroamination reactions.^{147,148} Asensio's group studied the hydroamination of ureas under the catalysis of a NHC-gold(I) complex.¹⁴⁹

1.2.3.2. Hydroamination of allenes catalyzed by gold-complexes

The addition of amines to allenes has received limited attention, although this transformation produces valuable products such as allylic amines and enamines. In 2006, Nishina and Yamamoto reported for the first time the intermolecular hydroamination of allenes with anilines using AuBr_3 as catalyst.¹⁵⁰ Later, in 2007, they extended this reaction to the hydroamination reaction of allenes with aliphatic amines catalyzed by a gold-phosphine complex.^{151,152}

In 2008, Widenhoefer reported the hydroamination of allenes with a series of different amines catalyzed by AuCl/AgOTf .¹⁵³ The same year, Bertrand and coworkers were able to catalyze the intermolecular hydroamination of allenes with ammonia using a gold(I) catalyst. The reaction of a tetrasubstituted allene with ammonia is carried out under the influence of a cationic gold complex with a CAAC ligand.¹³³ In the subsequent year, the same group extended this reaction to a variety of primary and secondary amines¹⁵⁴ as well as hydrazine.¹³⁷ This reaction is represented in **Scheme 1.10** and studied in **Chapter 6**.



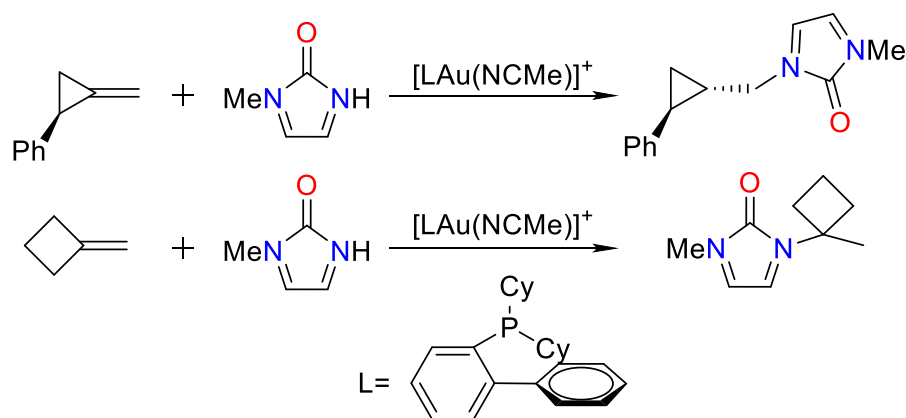
Scheme 1.10: Hydroamination of allenes with hydrazine catalyzed by a gold(I) catalyst with a [CAAC] ligand.

Later, Toste et al. reported the hydroamination of allenes using hydrazide as amine and $\text{Ph}_3\text{PAuNTf}_2$ as catalyst. During mechanistic investigations, they found that the rate-determining step of this reaction involves an activated allene complex. The reaction was found to be first order with respect to the gold catalyst and the allene and zero order with respect to the amine.¹³⁰ This fact supports the mechanism based on the initial coordination of the allene followed by nucleophilic addition of the amine.

With regard to the intramolecular hydroamination of allenes catalyzed by gold complexes, Espinet et al. found that the nitrogen acyclic carbene (NAC) gold(I) complex is an active catalyst.¹⁵⁵ In 2007, Toste et al. developed an enantioselective hydroamination of allenes using a chiral gold complex. This study shows that the effect of the counterion is essential to obtain high enantioselectivities.^{156,157} Further studies from this group showed that sterically differentiating protecting groups on the amines were necessary to improve the enantioselectivities.¹⁵⁸

1.2.3.3. Hydroamination of alkenes catalyzed by gold-complexes

Quite-few gold-catalyzed hydroamination of alkenes have been described. The first report was the intra- and intermolecular addition reported in 2006 by He and coworkers using a Ph_3PAuOTf catalyst.⁶⁹ The same year, Widenhoefer reported the combination of a gold(I) catalyst and AgOTf as active catalyst for this reaction.^{159,160} More recently, in 2009, Widenhoefer and coworkers published an efficient protocol for the intermolecular hydroamination of ethylene and unactivated alkenes with cyclic ureas using a gold(I) catalyst.¹⁶¹ Very recently, Widenhoefer et al. reported the first gold-catalyzed *anti*-Markovnikov hydroamination of alkenes using an urea-based amine.¹⁶² In this study they used a gold(I) complex with a phosphine ligand to catalyze the reaction of alkylidenecyclopropanes (ACP) as alkenes and an urea-based as N-nucleophile. However, the reaction of methylenecyclobutene (MCB) with the same urea-based N-nucleophile yields the Markovnikov isomer. These reactions are summarized in **Scheme 1.11** and studied in **Chapter 7**. In that chapter is also studied the effect of changing the alkene as well as changing the ligand of the gold-catalyst.



Scheme 1.11: Hydroamination of alkylidenecyclopropanes (ACP) and methylenecyclobutene (MCB) with ureas catalyzed by a gold(I) complex.

In contrast with the cases described in previous subsections (hydroamination of alkynes and allenes catalyzed by gold complexes), there are no examples of hydroamination reaction of alkenes catalyzed by gold(I) complexes with NHC ligands. For this reason, and for comparative purposes, this reaction is studied and compared with the hydroamination reaction of alkynes and allenes in **Chapter 6**.

*The most beautiful thing we
can experience is the mysterious.
It is the source of all true art and science.*

Albert Einstein

~ Chapter 2 ~

COMPUTATIONAL METHODS

This chapter introduces the fundamentals of computational chemistry focusing on the density functional theory (DFT), which is the methodology used in this dissertation. Other methodological aspects as the basis set and the solvation models are also discussed.

2.1 Quantum Mechanics

In the beginning of the 20th century, physicists found that classic mechanics failed to describe the behavior of small particles such as electrons, atoms and molecules and founded that the behavior of these particles is governed by a set of principles named as quantum mechanics. Quantum mechanics is the youngest branch of physics and was born to solve the impossibility of reproducing some observations by means of classical mechanics, such as the stability of the atoms and the thermal radiation provided from the microscopic vibration of particles. In the next subsection are briefly commented the most important studies in the history of quantum mechanics.

2.1.1. Historical Background of Quantum Mechanics

In 1801 Thomas Young proved the wave nature of light by observing diffraction and interference phenomena when light passed through two small adjacent holes. In 1860, Maxwell developed four equations, named as Maxwell's equations, which unified the electricity and magnetism laws. According with Maxwell's law, an accelerated charge would radiate energy in the form of electromagnetic waves consisting of oscillating electric and magnetic fields. Maxwell's study also concluded that light is an electromagnetic wave. In 1888, Hertz detected radio waves produced by accelerated electric charges in a spark. All the electromagnetic waves have a speed of $c = 2.998 \cdot 10^8$ m/s in vacuum. The frequency (ν) and wavelength (λ) of an electromagnetic wave are related by $\lambda\nu = c$.

In the end of 1800, the intensity of light at various frequencies emitted by a heated blackbody was measured at a fixed temperature. Statistical mechanics as well as electromagnetic-wave model of light failed to predict the intensity-versus-frequency curve for the emitted blackbody radiation. In 1900, Max Planck developed the theory of energy quantization which reproduces the blackbody-radiation curves. Planck affirmed that the atoms of the blackbody could emit light energy only in amounts given by $h\nu$, where ν is the frequency and h is a proportionality constant, called Placks's constant which value is $6.6 \cdot 10^{-34}$ J·s. This study marked the beginning of quantum mechanics.

The energy quantization was used for the second time to explain the photoelectric effect. In the photoelectric effect, light shining on a metal caused emission of electrons and was observed that the kinetic energy of an emitted electron is independent of the light's intensity but increases as the light's frequency increases. In 1905, Einstein showed that this observation could be explained by assuming that light is composed of particle-like entities called photons which energy is given by $h\nu$. This study demonstrated that light can shows a particle-like behavior in addition to the wave-like behavior displayed in diffraction experiments.

Regarding the structure of matter, in 1909, Rutherford, Geiger, and Marsden passed a beam of alpha particles through a thin metal foil and observed the deflections of the particles by allowing them to fall on a fluorescent screen, concluding that such large deflection could occur only if the positive charge were concentrated in a tiny, heavy nuclei.

In 1913, Bohr applied the concept of energy quantization to the hydrogen atom. He assumed that the electron is constrained to move only on one of a number of allowed circles called orbits. In 1923, Louis de Broglie assumed that the motion of electrons might have also a wave aspect. Following this hypothesis, an electron of mass m and speed v would have a wavelength given by:

$$\lambda = \frac{h}{mv} = \frac{h}{p} \quad [2.1]$$

where p is the linear momentum. De Broglie also arrived to the same equation following the same reasoning with photons. In 1927, Davisson and Germer confirmed the wave-like behavior of electrons showing diffraction effects. Stern observed these effects in helium atoms and hydrogen molecules, verifying that wave effects are present in the motion of all microscopic particles, resulting in a general law: the wave-particle duality of matter and light. Both photons and electron have a particle-like as well as a wave-like behavior but they are not the same kind of entities.

In 1927, Heisenberg discovered that the wave-particle duality of microscopic particles imposes a limit on our ability to measure simultaneously the position and momentum of such particles. This limitation is the uncertainty principle and affirms that the more precisely is determined the position, the less accurate is our determination of momentum.¹⁶³ This principle can be expressed as:

$$\Delta x \cdot \Delta p_x \geq \hbar/2 \quad [2.2]$$

where Δx and Δp_x are the uncertainty of the position and the momentum of the particle. For this reason, the quantum mechanics only provides a range of probability of where a particle might be given and its momentum. This range of probability is described by the wave function or state function (Ψ). The concept of wave function and the equation governing its change with time was discovered in 1926 by Erwin Schrödinger. This equation is explained in next subsection.

2.1.2 The Schrödinger Equation

To describe a state in quantum mechanics, it is postulated the existence of a function of the coordinates of the particle named wave function or state function (Ψ). Since the state will change with the time, the wave function is going to be also a function of time.

To find the future state of a quantum-mechanical system from knowledge of its present state, it is necessary an equation which describes how the wave function changes with time. For a one-particle and one-dimensional system this equation is postulated to be

$$-\frac{\hbar}{i} \frac{\partial \Psi(x, t)}{\partial t} = -\frac{\hbar^2}{2m} \frac{\partial^2 \Psi(x, t)}{\partial x^2} + V(x, t)\Psi(x, t) \quad [2.3]$$

where $i = \sqrt{-1}$, m is the mass of the particle, $V(x, t)$ is the function of the potential energy of the system and \hbar is defined as

$$\hbar = \frac{h}{2\pi} \quad [2.4]$$

This equation is known as time-dependent Schrödinger equation (or the Schrödinger wave equation). This equation contains the first derivative of the wave function with respect to time and allows us to calculate the future state at any time if the wave function at time t_0 is known. It is important to remarks that the quantum mechanics is basically statistical in nature; this means that knowing the state, cannot be predicted the result of a position measurement with certainty; can be only predicted the probabilities of various possible results. This probability is described by function postulated by Max Born:

$$d\rho(x, t) = |\Psi(x, t)|^2 dx \quad [2.5]$$

This function gives the probability at time t of finding the particle in a region between x and $(x + dx)$ and is known as probability density.

A very used approach is to restrict to a special case where the potential energy is not a function of time but depends only on the coordinate x . This consideration transforms the time-dependent Schrödinger equation into the next equation:

$$-\frac{\hbar^2}{2m} \frac{\partial^2 \psi(x)}{\partial x^2} + V(x)\psi(x) = E\psi(x) \quad [2.6]$$

Most methods for studying chemical reaction are based on this equation¹⁶⁴ which is named time-independent Schrödinger equation for a single particle of mass m moving in one dimension. This equation can be expressed as:

$$\hat{H}\psi(x) = E\psi(x) \quad [2.7]$$

where \hat{H} is the Hamiltonian operator (a “mathematical object” that maps one state vector into another) and $\Psi(x)$ are the eigenstates of the Hamiltonian, whose eigenvalues E correspond to the total energies of those states. The time-independent Schrödinger equation used a factor of the wave function that depends only on the coordinate x (ψ), and this factor can be related with the time-dependent wave function (Ψ) by using the next equation:

$$\Psi(x, t) = e^{-\frac{iEt}{\hbar}} \psi(x) \quad [2.8]$$

Note that the Schrödinger equation contains two unknowns: the allowed energies E and the allowed wave functions ψ . To solve for two unknowns it is necessary to impose additional conditions (called boundary conditions) on ψ .

At this point, in order to simplify the resolution of the Schrödinger equation for molecular systems, the Born-Oppenheimer approximation is applied. This approximation is explained in the next subsection.

2.1.3 Born-Oppenheimer approximation

If it is assumed that the nuclei and electrons to be point masses and neglect spin-orbit, the molecular Hamiltonian is:

$$\hat{H} = -\frac{\hbar^2}{2} \sum_{\alpha} \frac{1}{m_{\alpha}} \nabla_{\alpha}^2 - \frac{\hbar^2}{2} \sum_i \frac{1}{m_i} \nabla_i^2 + \sum_{\alpha} \sum_{\beta > \alpha} \frac{Z_{\alpha} Z_{\beta} e'^2}{r_{\alpha\beta}} - \sum_{\alpha} \sum_i \frac{Z_{\alpha} e'^2}{r_{i\alpha}} + \sum_j \sum_{i > j} \frac{e'^2}{r_{ij}} \quad [2.9]$$

where α and β refer to nuclei and i and j refer to electrons. This equation can be simplified as:

$$\hat{H} = \hat{T}_N + \hat{T}_E + (V_{NN} + V_{NE} + V_{EE}) \quad [2.10]$$

where \hat{T}_N and \hat{T}_E are the operators for the kinetic energy of the nuclei and electrons respectively, V_{NE} is the potential energy of the attraction between the electrons and the nuclei and V_{EE} and V_{NN} are the potential energies of the repulsions between electrons and two different nuclei respectively.

The Born-Oppenheimer approximation is based on the fact that nuclei are much heavier than electrons, so the electrons move much faster than the nuclei, and the nuclei can be considered fixed while the electrons carry out their motions.¹⁶⁵ This approximation permits omitting the term of the kinetic energy of the nuclei and leads to the following equation for the molecular Hamiltonian:

$$\hat{H} = \hat{T}_E + (V_{NN} + V_{NE} + V_{EE}) = \hat{H}_{el} + V_{NN} \quad [2.11]$$

This equation can also be expressed as the sum of the purely electronic Hamiltonian (\hat{H}_{el}) and the potential energy of the repulsion between two nuclei (V_{NN}) which can be considered to be constant for a particular nuclear configuration. In equation [2.11] the purely electronic Hamiltonian (\hat{H}_{el}) includes the operators for the kinetic energy of the electrons (\hat{T}_E) and the potential energy of the attraction between the electrons and the nuclei of the repulsions between electrons (V_{NE} and V_{EE} , respectively).

The Born-Oppenheimer approximation separates nuclear and electron variables and to express the wave function as a product of the electronic wave function and the nuclear wave function:

$$\psi(q_i, q_\alpha) = \psi_{el}(q_i; q_\alpha) \psi_N(q_\alpha) \quad [2.12]$$

When this Hamiltonian is applied over the electronic wave function, the equation [2.13] is obtained where q_i and q_α denoted the electronic and nuclear coordinates respectively and n symbolizes the electronic quantum numbers:

$$(\hat{H}_{el} + V_{NN}) \psi_{el}(q_i, q_\alpha) = U_n(q_\alpha) \psi_{el}(q_i, q_\alpha) \quad [2.13]$$

This equation can be only solved exactly for very simple cases, like H_2^+ due to the many-body problem but more complex systems can be dealt with by approximate methods which are discussed in **Section 2.1.4**. From this term, the total energy can be calculated over the nuclear wave function by including the operator for the kinetic energy of the nuclei. The equation for calculating the total energy can be written as:

$$(\hat{T}_N + U_n(q_\alpha)) \psi_N(q_\alpha) = E \psi_N(q_\alpha) \quad [2.14]$$

The term $U_n(q_\alpha)$ is the electronic energy including internuclear repulsions and is also named as adiabatic potential. This dependence of U_n on the nuclear coordinates means that for each nuclear position, different electronic wave functions and corresponding energies are going to be obtained. This adiabatic potential calculated for a large number of nuclear geometries is known as potential energy surface (PES), a concept which is explained in more detail in the **Section 2.1.5**.

2.1.4 Approaches for the calculation of electronic energies

The main approximations to solve the Schrödinger equation and calculate molecular properties are semiempirical methods and ab-initio methods.^{166,167}

Semiempirical molecular quantum-mechanical methods use a simpler Hamiltonian than the molecular Hamiltonian and include parameters whose values are adjusted to fit experimental data or the results of ab-initio calculations.

Ab-initio calculation uses the correct Hamiltonian and does not use experimental data other than the values of the fundamental physical constants. These methods are also known as wave function methods, since they imply the computation of the wave function for a given set of nuclear coordinates. The most important ab-initio method is the Hartree-Fock (HF) method, also called self-consistent field (SCF) method. The essence of this approximation is to avoid the complicated many-electron problem by considering each single electron on an average of electron-electron repulsion potential, so the exact N-body wave function can be approximated by a single Slater determinant and by using the variational method a set of

equations can be obtained. A solution of these equations yields the HF wave function and the energy of the system.

Other important ab-initio calculations are the so-called post Hartree-Fock methods such as the Configuration interaction methods (CI-SD, CI-SDTQ and CIS), the many-body perturbation theory (MBPT) in special the Møller-Plesset (MP) perturbation theory proposed in 1934 by Møller and Plesset (MP2, MP3 and MP4 calculations) and the coupled-cluster (CC) methods introduced by Coester and Kümmel (the CC singles and doubles, CCSD and CC singles, doubles and triples, CCSDT).¹⁶⁸

Other methods to calculate the electronic energy are those based on density-functional methods.¹⁶⁹ In this thesis, all calculations were performed using density-functional methods, thus, these methods will be described in the following section (**Section 2.2**).

There is another approach to calculate molecular properties, the molecular-mechanics method, but this method is not a quantum-mechanical based method, so electronic energies are not calculated. This method describes the molecule as a collection of atoms connected by bonds and expresses the molecular energy in terms of force constants for bond bending and stretching and other parameters.

2.1.5 Potential Energy Surface

As mentioned in **Section 2.1.3**, the potential energy surface (PES) is the adiabatic potential U_n calculated for a set of fixed nuclear coordinates, so the potential energy surface represents the energy of a chemical system as a function of its nuclear coordinates.

In our case, this potential energy surface is obtained through DFT calculations, which are extensively discussed in **Section 2.2**.

Unfortunately, the construction of the complete PES is only feasible for small systems, since a nonlinear molecule with N nuclei is defined by $3N - 6$ independent nuclear coordinates and the electronic energy (U_n) is a function of these coordinates. For this reason, only a few points of the PES are taken into account. A calculation of the adiabatic potential at one particular arrangement of the nuclei is called a single-point calculation, since it gives one point on the molecular PES. An example of a 3D-representation of an arbitrary PES is depicted in **Figure 2.1**.

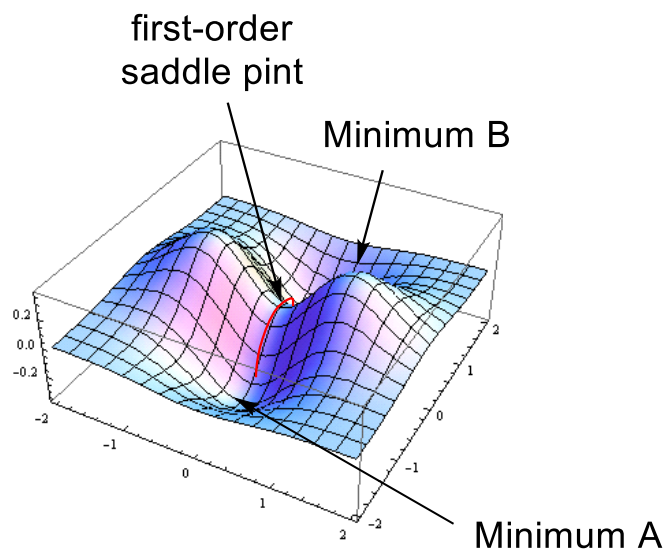


Figure 2.1: 3D-representation of a model potential energy surface.

The most important single-point calculations are the ones those performed at the stationary or critical points (where the energy is stationary with respect to the nuclear coordinates). These points have a gradient of U_n equal to zero, being the gradient defined as the vector constituted by the set of $3N - 6$ first partial derivatives of U with respect to each of its variables. These points may be a minimum, a maximum or a saddle-point.

A first-order saddle point is defined as a point which is an energy maximum for one variable and an energy minimum for the remaining variables. A local minimum is defined as a point that is lower in energy than all PES points in its immediate vicinity and a global minimum is defined as the lowest-energy point on the PES.

2.2 Density Functional Theory

The density-functional methods calculate the molecular electron probability density (ρ) and calculates the molecular electronic energy from ρ .¹⁶⁹

The electron probability density is a function of only three variables $\rho(x, y, z)$ which represents the probability of finding any of the N electrons in a volume element $dx dy dz$. Since the indistinguishability of the electrons, the probability of finding any electron in the volume element is N times the probability for one particular electron. Thus the electron probability density can be expressed as:

$$\rho(x, y, z) = N \int \cdots \int |\psi(x_1, y_1, z_1, x_2, \dots, z_n, m_{s1}, \dots, m_{sn})|^2 dx_2 \dots dz_n \quad [2.15]$$

$$\rho(\vec{r}) = N \int \cdots \int |\psi(\vec{r}_1, \vec{r}_2, \dots, \vec{r}_n, m_{s1}, \dots, m_{sn})|^2 d\vec{r}_2 \dots d\vec{r}_n \quad [2.16]$$

where m_{s_i} is the spin for each electron. The atomic units of the electron density are electrons/bohr³.

The density Functional Theory as is known nowadays^{170,171} was born in 1964 with the Hohenberg-Kohn theorem published by Pierre Hohenberg and Walter Kohn.¹⁷² The authors proved by *reductio ab absurdum* that there cannot be two different external potentials that result in the same ground-state electron density.

The Hohenberg-Kohn theorem proved that for molecules with a nondegenerated ground state, the ground-state electron probability density $\rho_o(\vec{r})$ determines the external potential $v(\vec{r})$ and the number of electrons. Hence, the ground-state wave function and energy (and, for that matter, all excited-state wave functions) are determined uniquely by the ground-state electron probability density.

As is mentioned in **Section 2.1.3**, the purely electron Hamiltonian is the sum of kinetic electronic term, electron-nuclear attraction and electron-electron repulsions ($\hat{H}_{el} = \hat{T}_E + V_{NE} + V_{EE}$). By applying the Hohenberg-Kohn variational theorem, the energy can be expressed as:

$$E_o = E_v[\rho_o] = \bar{T}[\rho_o] + (\bar{V}_{NE}[\rho_o] + \bar{V}_{EE}[\rho_o]) \quad [2.17]$$

The only term dependent on the external potential is the electron-nuclei attraction (\bar{V}_{NE}), so the other two independent terms ($\bar{T}[\rho_o]$ and $\bar{V}_{EE}[\rho_o]$) can be englobed in a new term named as the Hohenberg-Kohn functional ($F_{HK}[\rho_o]$). The energy can be now expressed as:

$$E_v[\rho_o] = F_{HK}[\rho_o] + \bar{V}_{NE}[\rho_o] = F_{HK}[\rho_o] + \int \rho_o(\vec{r}) v(\vec{r}) d\vec{r} \quad [2.18]$$

The electron-electron repulsions can be split into the classical Coulomb part $J[\rho_o]$ and the non-classical contributions $\bar{E}_{ncl}[\rho_o]$ named as exchange energy, so the Hohenberg-Kohn functional can be written as:

$$F_{HK}[\rho_o] = \bar{T}[\rho_o] + J[\rho_o] + \bar{E}_{ncl}[\rho_o] \quad [2.19]$$

Kohn and Sham proposed in 1965 a practical method for calculating the ground-state electron density ρ_o .¹⁷³ They consider a fictitious reference system of n noninteracting electrons where the external potential-energy function is such as to make the ground-state electronic density of the reference system $\rho_s(\vec{r})$ equal to the ground-state electron density of the molecule we are interested in $\rho_o(\vec{r})$. Their basic idea is to calculate the exact value of the kinetic energy term for this noninteracting reference system (denoted by the s subscript) which is not equal to the kinetic energy of the real system, creating a new term: the kinetic correlation energy which is the difference between the kinetic energy of the real and the reference systems ($\bar{T}_c[\rho_o] = \bar{T}[\rho_o] - \bar{T}_s[\rho_o]$).

Taking in consideration the Kohn and Sham approach, the Hohenberg-Kong equation can be rewritten as:

$$F_{HK}[\rho_o] = \bar{T}_s[\rho_o] + \bar{T}_c[\rho_o] + J[\rho_o] + \bar{E}_{ncl}[\rho_o] \quad [2.20]$$

2.2.1 Exchange-Correlation Energy

In equation [2.20], the kinetic energy of the reference system ($\bar{T}_s[\rho_o]$) as well as the classical Coulomb part of the electron-electron repulsions ($J[\rho_o]$) can be easily calculated but the other two terms, the kinetic correlation energy and exchange energy (the non-classical contributions in the electron-electron repulsions) are unknown and are collected into the so-called exchange-correlation energy ($E_{XC}[\rho_o] = \bar{T}_c[\rho_o] + \bar{E}_{ncl}[\rho_o]$), so the Hohenberg-Kohn functional is written as:

$$F_{HK}[\rho] = \bar{T}_s[\rho] + J[\rho] + E_{XC}[\rho] \quad [2.21]$$

For convenience, the zero subscript on ρ_o is omitted in this equation and all over this section. The key to accurate DFT calculations of molecular properties is to get a good approximation for the exchange-correlation energy function.

A common approach for the design of the exchange-correlation functionals is to split the exchange-correlation functional into the exchange part and the correlation part, calculate both separately and combine them into the exchange-correlation functional ($E_{XC}[\rho] = E_X[\rho] + E_C[\rho]$). There are several different approximations to calculate the exchange-correlation energy, which differ on the accuracy level and the computational cost. These approximations were compared with the biblical Jacob's ladder by Perdew (**Figure 2.2**).

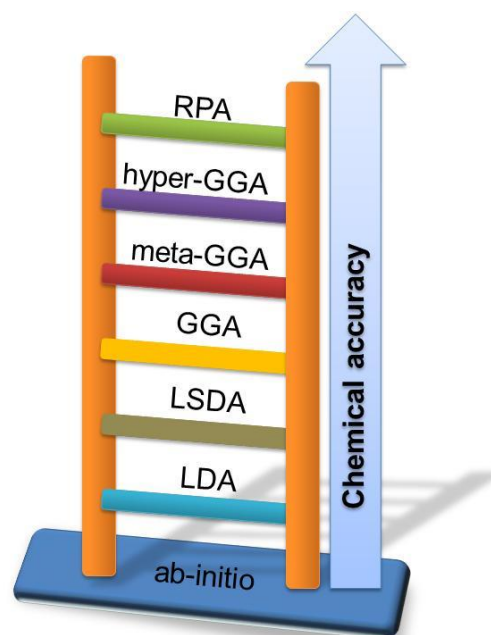


Figure 2.2: Jacob's ladder of DFT approximations.

The first approach is named local density approximation (LDA) and it assumes that the density can be locally treated as a homogeneous electron gas named Jellium, which is a hypothetical electrically neutral, infinite-volume system consisting of an infinite number of interacting electrons moving through a space with positive charge continuously and uniformly distributed.

This approximation allows expressing the exchange-correlation energy as the sum of exchange and correlations parts. The exchange part is given by the Thomas-Fermi-Dirac method:^{174–176}

$$E_X^{LDA}[\rho] = -\frac{3}{4} \left(\frac{3}{\pi}\right)^{1/3} \int [\rho(\vec{r})]^{4/3} d\vec{r} \quad [2.22]$$

The correlation has been calculated and expressed as a very complicated function of the electron density.¹⁷⁷

This method only works in closed-shell systems due that it assumes the total density is the sum of α and β spin densities. For open-shell systems as well as for molecular geometries near dissociations, the local-spin-density approximation (LSDA) provides better results. This approximation allows electrons with opposite spins paired to have different spatial Kohn-Sham orbitals, whereas in the LDA such electrons have the same spatial KS orbital. The exchange-energy functional in the LSDA is:

$$E_X^{LSDA}[\rho] = -\frac{3}{4} \left(\frac{3}{\pi}\right)^{1/3} \int \left[(\rho^\alpha(\vec{r}))^{4/3} + (\rho^\beta(\vec{r}))^{4/3} \right] d\vec{r} \quad [2.23]$$

The LDA and LSDA methods are appropriate for systems where the electron density varies slowly with position, because do not consider the variation of electron density with the position (the integral is over all space $d\vec{r}$). The next generation of functionals considers the variation of electron density with position including the gradient of the electron densities in the integrand, the so-called generalized-gradient approximation (GGA). The general expression for the exchange-correlation functional including the generalized-gradient approximation is:

$$E_{XC}^{GGA}[\rho^\alpha, \rho^\beta] = \int f(\rho^\alpha(\vec{r}), \rho^\beta(\vec{r}), \nabla\rho^\alpha(\vec{r}), \nabla\rho^\beta(\vec{r})) d\vec{r} \quad [2.24]$$

This functional can also be expressed as the sum of the exchange-energy functional and the correlation-energy functional.

$$E_{XC}^{GGA} = E_X^{GGA} + E_C^{GGA} \quad [2.25]$$

The most commonly used gradient-corrected exchange functionals (E_X^{GGA}) are:

- Perdew and Wang's 1986 functional (PW86, PWx86 or P)¹⁷⁸
- Becke's functional (B86)¹⁷⁹

- Becke's 1988 functional (B88, Bx88, Becke88 or B)¹⁸⁰
- Perdew and Wang's 1991 functional (PWx91)^{181–185}
- Handy's modification of Becke's functional (OPTX (O))^{186,187}
- Modified Perdew-Wang functional (mPW)¹⁸⁸

The two first functionals (PW86 and B86) do not contain empirical parameters; the other functionals are based on fitting empirical parameters usually considering experimental data for a set of atoms or model molecules.

The most commonly used gradient-corrected correlation functionals (E_C^{GGA}) are:

- The Lee-Yang-Parr's (LYP) functional¹⁸⁹
- The Perdew's 1986 correlation functional (P86 or Pc86)¹⁷⁸
- The Perdew-Wang's 1991 parameter-free correlation functional (PW91 or PWc91)^{181–185}
- The Becke's correlation functional (Bc95 or B96)¹⁹⁰

Any exchange functional can be combined with any correlation functional forming an exchange-correlation functional. For example, the BLYP functional is the combination of the Becke's 1988 exchange functional (B88 or B) and the Lee-Yang-Parr's (LYP) correlation functional. Another very common gradient-corrected exchange and correlation functional is the Perdew-Burke-Ernzerhof (PBE) functional.^{191,192}

The meta-generalized-gradient approximation (meta-GGA) functionals were proposed in order to improve the GGA functionals. This type of functionals improves the kinetic energy density term of the exchange-correlation energy. Some examples of this kind of functionals are the B98,¹⁹³ TPSS,¹⁹⁴ VSXC¹⁹⁵ and KCIS functionals.^{196–199}

Other very used functionals are the hybrid functionals (also known as hyper-GGA functionals), which uses a Hartree-Fock definition for the exchange energy but replacing the Hartree-Fock orbitals by Kohn-Sham orbitals (KS). To relate the fictitious Kohn-Sham reference system (with no interacting electrons and therefore no interelectronic repulsions) with a real molecule, the adiabatic connection should be introduced:

$$E_x[\rho] = \int_0^1 E_{ncl}^\lambda[\rho] d\lambda \quad [2.26]$$

where λ is the coupling strength factor with values between 0 and 1. This equation allows calculating the exchange-correlation energy as a function of the non-classical contribution of the electron-electron interaction in function of the λ value. A value equal to 0 for λ corresponds with a non-interacting system where the non-classical contribution is only the exchange energy; a value equal to 1 corresponds with a fully interacting system. As this relation is unknown, it has to be calculated using approximations. The simplest

approximation is to consider a linear correlation between both parameters. Using this approximation, the called half-and-half functional (HH) is obtained.²⁰⁰ In this functional the exchange-correlation energy is calculated as an arithmetic media of the non-classical interactions for a non-interacting system ($\lambda=0$) and the non-classical interactions for a fully interacting system ($\lambda=1$).

$$E_{XC}^{HH} = \frac{1}{2}E_X^{\lambda=0} + \frac{1}{2}E_X^{\lambda=1} \quad [2.27]$$

The most famous combination of this functional is the BHandHLYP functional, where the exchange-correlation energy is calculated as:

$$E_{XC}^{BHandHLYP} = \frac{1}{2}E_X^{exact} + \frac{1}{2}E_X^{LSDA} + \frac{1}{2}\Delta E_X^{B88} + E_C^{LYP} \quad [2.28]$$

where the exchange energy is calculated as a combination of the exact exchange energy (E_X^{exact} which sometimes is denoted as E_X^{HF}) calculated using a Hartree-Fock definition, the exchange energy calculated using the local-density approximation (E_X^{LSDA}) and the exchange energy using the gradient-corrected exchange functionals proposed by Becke in 1988.¹⁸⁰ The correlation energy is calculated using Lee-Yang-Parr's gradient-corrected correlation functional.¹⁸⁹

The most famous hybrid functional is the B3LYP functional²⁰¹ developed by Becke²⁰² where the 3 indicates a three parameter functional. The expression for the exchange-correlation energy is given by:

$$E_{XC}^{B3LYP} = aE_X^{exact} + (1 - a - b)E_X^{LSDA} + b\Delta E_X^{B88} + cE_C^{LYP} + (1 - c)E_C^{VWN} \quad [2.29]$$

In this expression, the amount of exact exchange is given by the value of the a parameter which value is 0.20 (20% of exact exchange).

It is well known that most of density functionals used fails to describe the non-covalent interactions (e.g. Van der Waals interactions). The most common way to improve the description of the non-covalent interactions is to include a dispersion correction. Analogue to the "Jacob's ladder" of DFT approximations, a "stairway to heaven" of dispersion correction schemes was proposed.²⁰³

The most used dispersion correction approximation is the semiclassical correction (DFT-D) which is based on an atom pairwise additive treatment of the dispersion energy. This correction consists in the addition of a dispersion energy term to the Kohn-Sham energy. The general expression for the dispersion energy is given by:²⁰⁴

$$E_{disp} = - \sum_{AB} \sum_{n=6,8,10,\dots} S_n \frac{C_n^{AB}}{R_{AB}^n} f_{damp}(R_{AB}) \quad [2.30]$$

where the sum is over all atom pairs in the system, C_n^{AB} denotes the averaged n^{th} -order dispersion coefficient (orders $n = 6, 8, 10, \dots$) for atom pair AB being R_{AB}^n their internuclear distance, and f_{damp} is the damping function, which determines the range of the dispersion correction. Global scaling factors s_n (which are density functional dependent) are typically used to adjust the correction to the repulsive behavior of the chosen density functional.

The most used DFT-D method is the version developed by Grimme in 2010 called DFT-D3²⁰⁵ (also named as Grimme's dispersion correction) which is an update of DFT-D1.²⁰⁶ The DFT-D3 dispersion correction contains accurate dispersion coefficients and cutoff radii for all elements up to $Z = 94$ and can be used for the computation of the dispersion energy in molecules and solids.

Other very common functionals are the Truhlar's functionals named as MXX. This family of functionals was designed in order to provide a good description of the non-covalent interactions by including implicit parameterization. The first of these series of functionals are the M05 functionals^{207–209} (M05 and M05-2X with 28% and 56% of exact exchange respectively). The second of these series is the M06 family which includes the M06 functional²¹⁰ (with 27% of exact exchange), the M06-2X functional²¹⁰ (with 54% of exact exchange), the M06-L functional²¹¹ (without of exact exchange) and the M06-HF functional^{212,213} (with 100% of exact exchange). The last of these functional series are the M08-HX functional, the M08-SO functionals²¹⁴ (with 52.23 % and 56,79% exact exchange, respectively) and the M11 functional.²¹⁵ Very recently Truhlar's group has reported the MN15 functional, that has broader accuracy than the previously available.²¹⁶ These families of functionals have been put into question very recently.²¹⁷

Other very used functional is the PBE0 functional (also denoted as PBE1PBE1 in the literature).²¹⁸ This functional is an improvement of the PBE functional by adding an exact exchange term where the mixing coefficient for the exact exchange is argued to be 0.25 from perturbation arguments.²¹⁹

Another very extensively used functional is the wB97XD functional²²⁰. Such functional includes empirical dispersion, uses a version of Grimme's D2 dispersion model. The w97 and w97X variations are also available²²¹ which also include long range corrections. New density functionals continue to appear in order to improve the description of the weak interaction as well as the excited states. Perdew et al. have developed a non-empirical strongly constrained and appropriately normed (SCAN) meta-GGA functional offering very promising features.²²²

Other important quantum chemistry methods are the so-called composite methods which use ab-initio calculations plus empirical corrections to the aim for high accuracy by combining results of several calculations at different levels. These methods are the Gaussian-3 (G3) method²²³ and his predecessors G1 and G2 and also varieties of CBS (complete basis set) calculations:^{224–231} the CBS-Q,^{230,231} CBS-APNO²²⁹ and CBS-4.^{229,231}

Finally, fully non-local functionals are obtained using the exact exchange and evaluating a part of the correlation energy exactly. An example is the random phase approximation (RPA) functionals,²³² but unfortunately this functional has a very high computational cost making them not widely used.

2.3 Scope of Application

This section is devoted to explain how the computational methodology above commented has been applied to the current dissertation.

2.3.1 Exchange-Correlation functionals used

The selection of the functional used depends on the chemical system under study, the level of accuracy required and the computational cost associated. All the calculations in this Ph.D. thesis have been performed using the Density Functional Theory (DFT) in combination with hybrid (or hyper-GGA) functionals because they provide a very good compromise between accuracy and computational cost.

The M06 hybrid functional was the most employed one.²¹⁰ This functional was tested against databases involving transition metal reaction energies and metal ligand bond energies by Zhao and Truhlar²¹⁰ showing very good results. It was also used in the study of other hydroamination reactions^{120,130,233,234} presenting very good results. In the other hand, PBE0 functional were used for some calculations using the ADF software, where M06 functional is not implemented.

2.3.2 Basis Sets

The choice of an appropriate basis set is crucial for a good description of the atomic orbitals. A basis set is a set of functions which are combined in linear combinations to create molecular orbitals. This section is devoted to describe the most used basis set and the ones selected to carry out the calculations presented in this dissertation.

Molecular systems are usually modeled by orbital-like functions which are functions that are centered on each atomic nuclei and whose shape is similar to the orbital functions obtained for one-electron atoms. There are two types of basis functions, the Slater Type Orbitals (STO) and Gaussian Type Orbitals (GTO). The basis sets used in this dissertation are built up as a linear combination of *Gaussian Type Functions* (GTFs) which can be written in term of polar coordinates as:

$$\phi_{\zeta,n,l,m}(r, \theta, \varphi) = NY_{l,m}(\theta, \varphi)r^{2n-2-l}e^{-\zeta r^2} \quad [2.31]$$

But is most commonly encountered written in terms of Cartesian coordinates as:

$$\phi_{\zeta,l_x,l_y,l_z}(x, y, z) = Nx^{l_x}y^{l_y}z^{l_z}e^{-\zeta r^2} \quad [2.32]$$

where N is a normalization constant, $l_x + l_y + l_z$ the sum that determines the type of orbital (for example $l_x + l_y + l_z = 1$ is a p orbital; if the sum is equal to 0 is a s type orbital and a d type for a value of 2), ζ the pre-exponent and r the distance between the nuclei and the electron. There are subtle differences between the two set of coordinates, for example a d-type GTO written in terms of spherical functions has five components ($Y_{2,2}, Y_{2,1}, Y_{2,0}, Y_{2,-1}, Y_{2,-2}$) but there are six components in the Cartesian coordinates ($x^2, y^2, z^2, xy, yz, xz$). Similarly, for an f-type GTO written in spherical functions there are 7 components which are transformed into ten Cartesian f-functions.

The use of a complete basis set in calculations is not affordable and a finite number of functions must be considered. The smallest basis set is called minimal basis set which is the minimum number of basis functions required to represent all of the electrons on each atom. For example, for hydrogen and helium the minimum basis set is one s function (1s) and for atoms in the second period of the periodic system (Li-Ne) the minimum basis set is a basis set of 5 functions: two s functions (1s and 2s) and 3 p functions.

The most common improvement of the basis sets is a doubling of all basis functions, producing a Double Zeta (DZ) type basis denoted by the Greek letter ζ . A DZ basis thus employs for hydrogen and helium two s-functions (1s and 1s') and for the first row elements four s functions (1s, 1s', 2s and 2s') and two sets of p-functions. A variation of the DZ type basis only doubles the number of valence orbitals producing a split valence basis. Nowadays a doubling of the core orbitals is rarely considered. Other very used functions are the triple Zeta (TZ) functions which contain three times as many functions as the minimum basis set, and some of the core orbitals may again be saved by only splitting the valence basis, producing a triple split valence basis set.

In most cases, higher angular momentum functions are required and are obtained by adding polarization functions which are auxiliary functions with one additional orbital. The p-orbital introduces a polarization of the s-orbital and an f-orbital polarizes d-orbitals. In other words, when polarization functions are added to an atom with valence p-orbitals, a set of d-type functions is added and when polarization functions are added to valence d-orbitals, a set of f-orbitals is added. In cases where polarization is also added to light atoms (hydrogen or helium) with valence s-orbitals, a set of p-functions is added to the hydrogen or helium minimum basis set. This polarization functions make the orbitals more flexible and suitable for the description of chemical bonds. Furthermore, diffuse functions can be also incorporated, allowing larger electron delocalization over space, which can be critical for anions.

A very common notation for the basis sets is the Pople's notation which is implemented in the software used in this dissertation (Gaussian 09). In this notation, the basis set are described following a k-nlmG format, where the number in front of the dash (k) indicates how many GTOs are used for representing the core orbitals and the numbers after the dash

(nlm) indicates how many functions the valence orbitals are split into: two values (nl) indicate split valence and three values (nlm) indicate triple split valence. The polarization functions are placed after G (for Gaussian). The polarization functions are denoted by an asterisk (two asterisks indicate that polarization functions are added also to light atoms such as hydrogen and helium). Another notation is also used to indicate polarization functions which consists in add (d) or (d,p) after the G letter. In this notation, the diffuse functions are denoted by a plus sign and two plus signs indicate that diffuse functions are also added to light atoms (hydrogen and helium).

For systems involving transition metals from the second and the third row of the periodic table which have a large number of core electrons and present relativistic effects, a common approach is to replace the electron density from the inner most electrons with a potential core, and treat only the valence electrons explicitly by using pseudopotentials or Effective Core Potentials (ECP). The two most used ECPs are the Los Alamos National Laboratory (LANL)²³⁵ and the Stuttgart-Dresden (SDD) pseudopotentials.^{236,237}

In this dissertation a SDD pseudopotential was used for the inner most electrons of gold (60 electrons) and rhodium (28 electrons) atoms and the SDD double-zeta basis set was employed to describe the external electrons of such atoms. A 6-31G(d,p) (also named as 6-31G**) basis set was used to describe the valence electrons for the rest of atoms. The 6-31G(d,p) basis set is a split valence double-zeta polarized set that adds to the 6-31G set six d-type polarization functions on atoms from Li to Ca and ten f-type functions to atoms from Sc to Zn and also adds a set of p-type functions to hydrogen and helium. Some single-point calculations were performed using the 6-311++G(d,p) triple split valence polarized basis set including diffuse functions in order to improve the accuracy of the calculations.

2.3.3 Solvation Model

The molecular properties explained in previous sections are calculated for gas-phase molecules; however, most of the reactions are carried out in solution. In this section are explained the most important approaches to include the solvent in calculations employed in this thesis.²³⁸

A rigorous way to deal with solvent effects would be to carry out several quantum-mechanical calculations on a system consisting of a solute molecule surrounded by many solvent molecules (explicit solvent) for various orientations of the solvent molecules. The average properties can be obtained by taking an average over the different calculations with the different orientations of the solvent. Sampling the configurational space for the solvent molecules would give an enormous number of configurations to be used as starting points. These calculations (using QM-based methods) are very impractical due to the large number of calculations having to be done over a very complex system (a solute surrounded by several solvent molecules) and these calculations are very computational demanding. A representation of a system including explicit solvent is depicted in **Figure 2.3**.

The most common way to obtain a full description of the solvent is by using molecular dynamics (MD) simulations over the system including explicit solvent.^{239,240} A MD simulation invokes classical Newton's equations and studies the time evolution of atoms under periodic boundary conditions (PBC). In a molecular dynamic simulation, the atoms can be represented by using force fields (classical MD) or by using quantum mechanics (ab-initio or DFT-based MD). The problem is that classical MD does not describe correctly bond-breaking or bond-forming situations. These reactions can be studied using first principle MD,^{239–242} but are computationally demanding.

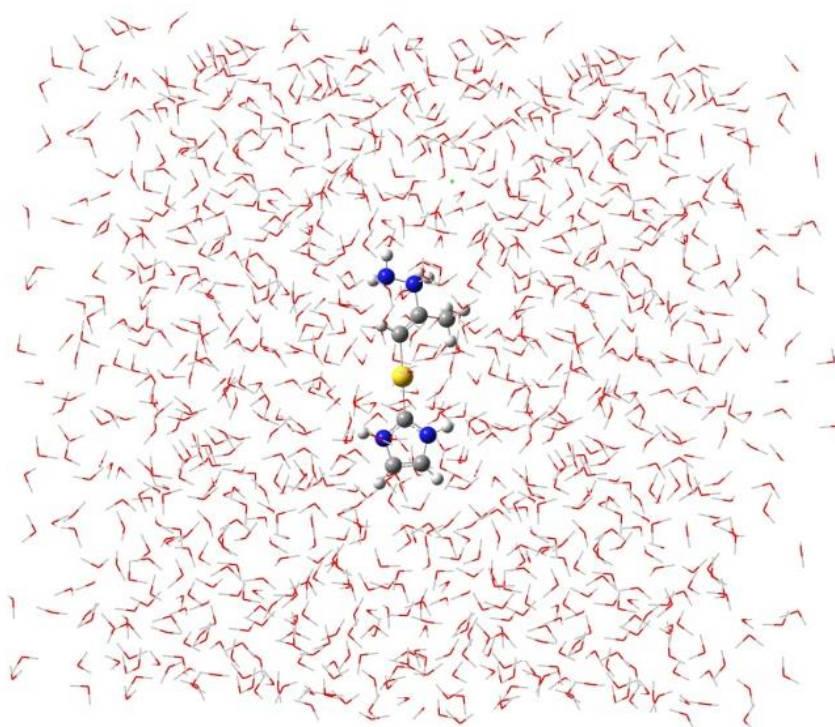


Figure 2.3: Representation of a system including explicit solvent.

The most common way to include solvent effects when studying homogeneous catalytic reactions is by using a continuum solvent model (implicit solvent),^{243,244} where the molecular structure of the solvent is ignored and the solvent is modeled as a continuous dielectric of infinite extent (characterized by its dielectric constant, ϵ_r , also called relative permittivity) that surrounds a cavity containing the solute molecule. A representation of a system including implicit solvent is depicted in **Figure 2.4**.

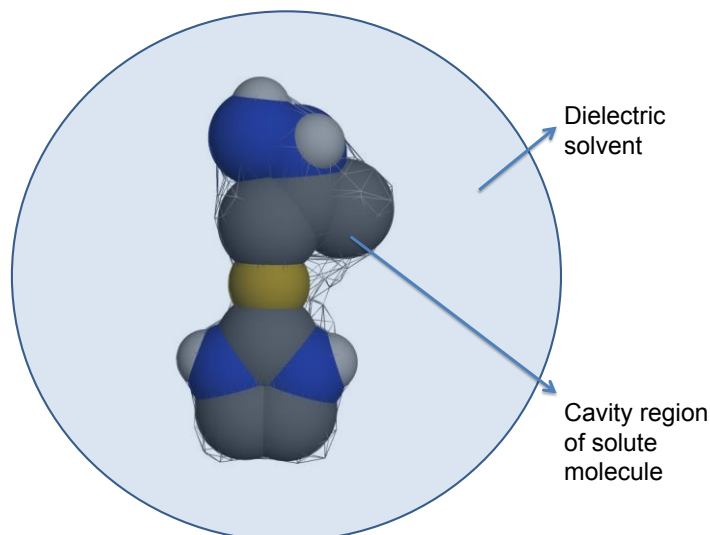


Figure 2.4: Representation of an implicit solvent model where the system is formed by a solute into a molecular-shaped cavity in a continuum dielectric solvent.

In a QM treatment of the solvent, the interaction between the solvent and the solute is modeled by adding a potential term to the molecular electronic Hamiltonian, so mathematically, this approach can be thought of in the following way:

$$\hat{H}_{total}(r_m) = \hat{H}_{solute}(r_m) + \hat{V}_{solute+solvent}(r_m) \quad [2.33]$$

The most used method is the self-consistent reaction field (SCRF) method in which the wave function as well as the electronic probability density of the solute is allowed to change in order to achieve self-consistency between the charge distribution of the solute molecule and the solvent's reaction field.

The self-consistent reaction field model calculates the Gibbs energy of the solvation as the sum of four different terms:

$$G_{solvation} = G_{electrostatic} + G_{cavitation} + G_{dispersion} + G_{drepulsion} \quad [2.34]$$

The first term ($G_{electrostatic}$) is the electrostatic energy which is a stabilizing term that accounts for the electrostatic interactions between the solute and the solvent. The second term ($G_{cavitation}$) is the energy necessary to create the cavity for the solute into the solvent and the third and fourth ($G_{dispersion} + G_{drepulsion}$) terms are associated with the dispersive and repulsive interactions between the solvent and the solute. In particular, the SCRF models that have been used in this thesis are the polarizable-continuum model (PCM)²⁴⁵ and the solvent model density (SMD).²⁴⁶ Polarizable-continuum model (PCM) and solvent model density (SMD) models differs in how the shape of the cavity is defined and in that the latter also includes a non-electrostatic term.

The polarizable-continuum model (developed by Miertus, Scrocco and Tomasi) is based on the Poisson-Boltzmann equation which is an expansion of the original Poisson's equation. The polarizable-continuum model considers that each atomic nuclei in the solute molecule is surrounded by a sphere of radius 1.2 times de van der Waals radius of that atom and the cavity region is taken as the volume occupied by these overlapping atomic spheres.

A very used variant of the PCM method is the conductor polarizable-continuum model (CPCM) in which the continuum is conductor-like, and the charges on the cavity surface are calculated using a condition suitable for a solvent, that is an electric conductor rather than a dielectric.

Another very used solvent method is the solvent model density (SMD).²⁴⁶ In the solvent model density electrostatic energy is calculated by solving the Poisson-Boltzmann equation analogously to PCM, but it does by using a set of specifically parametrized radii which construct the cavity. These radii have been optimized for H, C, N, O, F, Si, P, S, Cl and Br and for any other atom the van der Waals radii with a scaling factor of 1.52 for group 17 elements heavier than Br (I and At) and 1.18 for all other atoms is used.

The last approach consists of considering some explicit solvent molecules in the first coordination sphere and the rest with a continuum representation. This hybrid approach is called as discrete-continuum model²⁴⁷⁻²⁴⁹ and is very commonly applied in reaction involving solvent molecules as reactants.

2.3.4 Gibbs energy in solution

This section discusses how thermodynamic properties can be calculated from the potential energy obtained in our calculations. The equations used are equivalent to those given in a standard text on thermodynamics.²⁵⁰

The internal energy (U) can be calculated from the potential energy by adding the zero-point energy ZPE (which is the vibrational energy at 0 K and is calculated using only the non-imaginary frequencies) and thermic corrections to the internal energy (vibrational, rotational, translational and electronic energies). Statistical mechanics gives the translational contribution to the internal energy of an ideal gas as $\frac{3}{2}RT$, the rotational contribution as RT for a lineal molecule and $\frac{3}{2}RT$ for a non-linear molecule, the vibrational contribution is given by the equation [2.35] and the electronic contribution can be considered as zero since there are no temperature dependent terms in the partition function.

$$U_v = R \sum_K \theta_{v,K} \left(\frac{1}{2} + \frac{1}{e^{\theta_{v,K}/T} - 1} \right)^2 \quad [2.35]$$

From the internal energy, the enthalpy can be calculated by using the next equation:

$$H(T) = U + RT \quad [2.36]$$

From this equation the Gibbs energy can be obtained by applying the next equation:

$$G(T) = H(T) + TS(T) \quad [2.37]$$

Statistical mechanics gives the molar entropy (S) of an ideal gas as the sum of the translational, rotational, vibrational and electronic contributions (S_t , S_r , S_v and S_e , respectively). The translational contribution depends only on the molar mass of the gas, the rotational contribution depends on the symmetry number and the principal moments of inertia, the vibrational contribution depends on the vibrational frequencies and the electronic contribution depends on the degeneracy of the ground and excited electronic states, but in our calculations only the ground state is considered (it is assumed that the first and higher excited states are inaccessible at any temperature).

All the calculations presented in this dissertation were carried out including implicit solvent in the optimization process of the structures, so all the energies obtained are potential energies in solution. The potential energies obtained include Gibbs energies of solvation of solute. The remaining contributions to Gibbs energy have been obtained by means of frequency calculations, using standard statistical thermodynamics formulas. In this way Gibbs energies in solution have been obtained.

In cases where a single point calculation with a bigger basis set (6-311++G(d,p)) was performed, the Gibbs energy in solution was calculated following the next equation:

$$G_{6-311++G(d,p)} = E_{6-311++G(d,p)} + (G_{6-31G(d,p)} - E_{6-31G(d,p)}) \quad [2.38]$$

where $G_{6-31G(d,p)}$ and $E_{6-31G(d,p)}$ are the energies in solution obtained during the optimization calculation with the smallest basis set and $E_{6-311++G(d,p)}$ is the energy in solution obtained in the single point calculation with the biggest basis set.

*Impossible, you say?
Nonsense. Just wait till you
see my calculations.*

Cecil B. Heimerdinger

~ Chapter 3 ~

OBJECTIVES

This thesis is focused into the mechanistic study of the hydroamination reaction catalyzed by organometallic complexes by means of DFT calculations. This chapter is devoted to describe the goals of the present dissertation.

The main topic of this thesis is the mechanistic study of intermolecular hydroamination reactions by means of DFT calculations. As mentioned in the introduction, there are some challenges of the hydroamination reaction yet to be studied, such as the use of unactivated olefins and small N-nucleophile reagents (like hydrazine or ammonia), the control of the regioselectivity, especially the *anti*-Markovnikov addition and the control of the enantioselectivity.

The goal of this dissertation is to address some of the challenges above mentioned by means of analyzing specific reactions for each of the challenges. In this line different reactions involving different substrates and different catalysts have been investigated depending on the topic:

- **Regioselectivity:** to investigate the intermolecular *anti*-Markovnikov hydroamination reaction of styrene catalyzed by a cationic rhodium(I) complex. The system developed by Hartwig et al. has been used for theoretical calculations.¹¹⁴ (**Chapter 4**).

To study the *anti*-Markovnikov hydroamination reaction of alkenes catalyzed by gold(I) complexes. Calculations are based on the only example present in literature of *anti*-Markovnikov hydroamination of alkenes catalyzed by gold complexes which has been reported by Widenhoefer et al.^{161,162} (**Chapter 7**).

- **Enantioselectivity:** to analyze an enantioselective hydroamination reaction of allenes catalyzed by a cationic rhodium (I) complex. The reaction reported by Breit and coworkers has been computed.¹²² (**Chapter 5**).
- **Use of small N-nucleophiles:** to investigate the hydroamination reaction of alkynes, alkenes and allenes catalyzed by a cationic gold(I) complex using hydrazine as N-nucleophile. Three different catalysts experimentally developed by Bertrand and Hasmi's groups were employed.^{137,140,141} (**Chapter 6**).

*Science is not about making
predictions or performing experiments.
Science is about explaining.*

Bill Gaede

~Chapter 4~

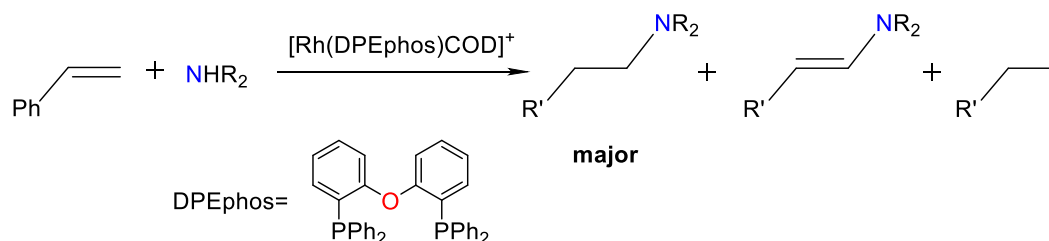
RHODIUM-CATALYZED ANTI-MARKOVNIKOV HYDROAMINATION OF ALKENES

This chapter is devoted to the anti-Markovnikov hydroamination of alkenes catalyzed by rhodium complexes. The oxidative amination reaction (competing side reaction) is also analyzed. These results has been published in Chem. Eur. J., **2016**, 22 (27), 9311–9320: The Origin of Anti-Markovnikov Regioselectivity in Alkene Hydroamination Reactions Catalyzed by [Rh(DPEphos)]⁺ (reference 252).

4.1 Introduction

Rhodium complexes have been extensively studied as catalyst for the hydroamination reaction because they show excellent catalytic activity in the intermolecular *anti*-Markovnikov hydroamination of alkynes and alkenes. A general introduction to the most important hydroamination reactions catalyzed by rhodium complexes has been presented in **Section 1.2.2**.

An important feature of rhodium catalysts is their ability to efficiently promote selective *anti*-Markovnikov hydroamination of vinylarenes. The first example of *anti*-Markovnikov hydroamination of alkenes was reported in 1999 by Beller et al. In this study a mixture of $[\text{Rh}(\text{cod})_2]\text{BF}_4$ and PPh_3 was used to catalyze the hydroamination of styrene. However the oxidative amination product (enamine) was the major product obtained.^{104,111} Later, in 2003, Hartwig et al. improved this reaction by using a cationic rhodium catalyst with a DPEphos ligand. This catalyst yields the *anti*-Markovnikov hydroamination product as the major one for the hydroamination reaction of vinylarenes with a variety of secondary aliphatic amines. The reaction is depicted in **Scheme 4.1**.



Scheme 4.1: *anti*-Markovnikov hydroamination of alkenes developed by Hartwig et al.

Regarding to the operative mechanism for the hydroamination reaction catalyzed by rhodium complexes, two plausible mechanisms have been proposed.¹⁰⁴ The first one is an electrophile activation mechanism (see **Section 1.2.1.1** for more details) while the second proposed mechanism is an amine activation mechanism (see **Section 1.2.1.2** for more details).

This chapter is devoted to computationally study the mechanism for the hydroamination reaction as well as for the formation of the enamine product. The formation of the Markovnikov isomer and the origin of the *anti*-Markovnikov regioselectivity are also analyzed.

4.2 Computational methods and models

All calculations were carried out using Gaussian 09 program. Calculations were performed at DFT level by means of the M06 functional with and ultrafine grid option. The basis sets used were the 6-31G(d,p) for all the atoms, except for Rh where the SDD (with an additional f orbital) along with the associated pseudopotential was employed. The structures were fully

optimized in solution using CPCM model with standard parameters and toluene as solvent ($\epsilon=2.3741$). The nature of stationary points (minima and TS) was confirmed by frequency calculations. Connections between the transition states and the minima were checked by following the IRC and subsequent geometry optimization till the minima. Energy values given in the text correspond to Gibbs energies at 298K calculated including solvent effects.

The energy decomposition analysis was performed using ADF program by means of the hybrid PBE0 functional. Those calculations were carried out in gas phase using ZORA/TZP basis set for all atoms. Preparation energies of EDA were computed with Gaussian 09 software in gas phase using PBE1PBE functional. The basis sets used were 6-31G(d,p) for all the atoms, except for Rh where the SDD (with an additional f orbital) along with the associated pseudopotential was employed. Natural population analysis was performed using NBO6 package.

The chemical system selected for calculations was analogous to that used in the experiment, with no simplifications (**Scheme 4.1**). The catalyst used was $[\text{Rh}(\text{DPEphos})(\text{COD})]^+$. The initial conformation of DPEphos ligand was obtained from the solid-state structure of a cationic complex of rhodium using a DPEphos ligand characterized by Weller et al.²⁵³ Styrene was selected as alkene for the study of the reaction mechanism; for the study of the regioselectivity other substrates were also utilized. The amine employed in all calculations was the simplest dialkylamine used in experiments: NHMe_2 . The structures are named according the following procedure: **4x.y** where x correspond to the point in the energy profile and y correspond to the initial intermediate (for example, **4.3a** correspond to the third point for the reaction starting with intermediate **4.1a**).

4.3 Results and Discussion

This section is divided into three subsections. The first one is devoted to study the operative mechanisms for the hydroamination reaction of alkene and for the competing side reaction (the oxidative amination reaction). The second one is devoted to study the selectivity (amine vs enamine) obtained, and in the third one is to analyze the origin of the *anti*-Markovnikov regioselectivity observed in this reaction.

4.3.1 Analysis of the reaction mechanism

In this section is investigated the operative mechanism in the hydroamination reaction of styrene. Both alkene and amine activation mechanisms were considered. In the first one the reaction starts with the coordination of the alkene to the metal center and it is followed by a nucleophilic addition of the amine into the coordinated alkene. The first step of the second mechanism is the oxidative addition of the amine to the metal center.

The catalyst used is $[\text{Rh}(\text{DPEphos})(\text{COD})]^+$. The first step in both mechanisms must be the exchange of COD by reactants in the coordination sphere of the catalyst. Several

intermediates could be formed depending on which ligands are coordinated to the metal center: the amine (**4.1a**), the alkene (**4.1b**), or both simultaneously (**4.1c**). The optimized structures for these intermediates are depicted in **Figure 4.1**. Their relative energies are 0.0, 1.3 and 1.0 kcal/mol, respectively.

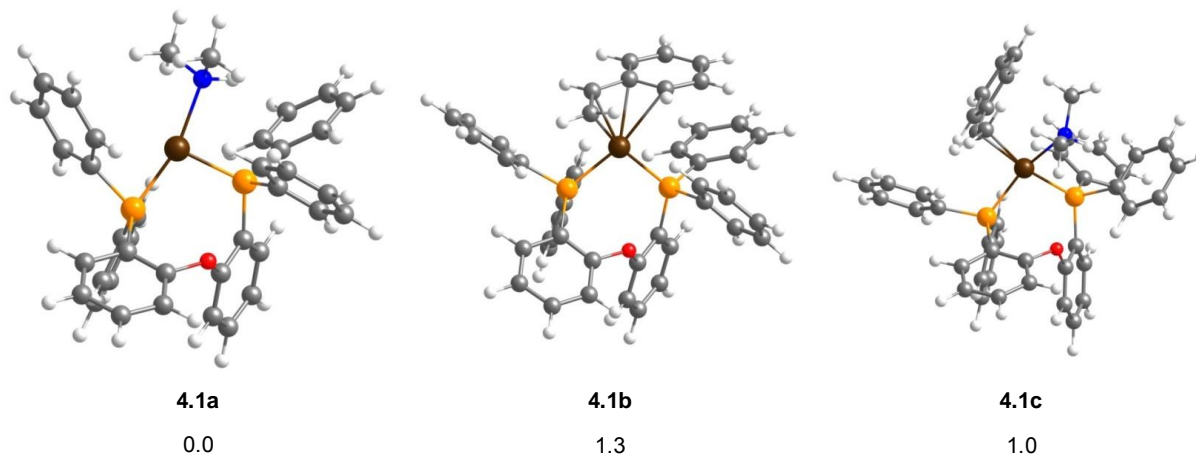


Figure 4.1: Optimized structures for the initial intermediates of the reaction. Relative Gibbs energy values are given under each structure in kcal/mol.

Complex **4.1a** has a square-planar geometry with an empty site; coordination of amine to [Rh(DPEphos)]⁺ fragment has a $\Delta G_{\text{binding}}$ of 28.0 kcal/mol. The distance between rhodium and nitrogen in this intermediate is $d(\text{Rh-N}) = 2.188 \text{ \AA}$. A complex with a coordinating solvent molecule (toluene) at the empty site was not found as a stable structure in the potential energy surface. Another conformation where the DPEphos ligand fulfills the empty site by coordinating the oxygen atom from the DPEphos ligand was checked. This structure (**4.1aO**) is a minimum but it lies 7.1 kcal/mol higher in energy.

Intermediate **4.1b** has a square-planar geometry since styrene occupies two coordination sites. The distances are 2.203 \AA and 2.143 \AA for Rh-C_t (terminal carbon atom) and Rh-C_i (internal carbon atom) of the double bond, and 2.328 \AA and 2.557 \AA for Rh-C_{ipso} and Rh-C_{orto} of the phenyl ring, respectively. The coordination of another styrene molecule to the metal center as well as the occupation of the formal empty site by a solvent molecule (toluene) did not result in stable structures in the potential energy surface. The possibility of coordination of the oxygen atom from the DPEphos ligand was also evaluated (intermediate **4.1bO**), but such intermediate is 5.3 kcal/mol higher in energy than intermediate **4.1b** and was not further considered.

From this initial study, we decided to consider all the three structures as starting points for the different hydroamination mechanisms that we describe in the next section.

4.3.1.1 Amine vs alkene activation mechanism

a) Amine activation mechanism

This subsection describes the amine activation mechanism for the formation of the hydroamination product (see **Section 1.2.1.2** for more details about this mechanism).

According to literature, the reaction mechanism through an amine activation pathway can be divided into four steps: oxidative addition of the amine, coordination of the alkene to the metal center, migratory insertion and reductive elimination step. The calculated reaction profile following this sequence of steps is depicted in **Figure 4.2**.

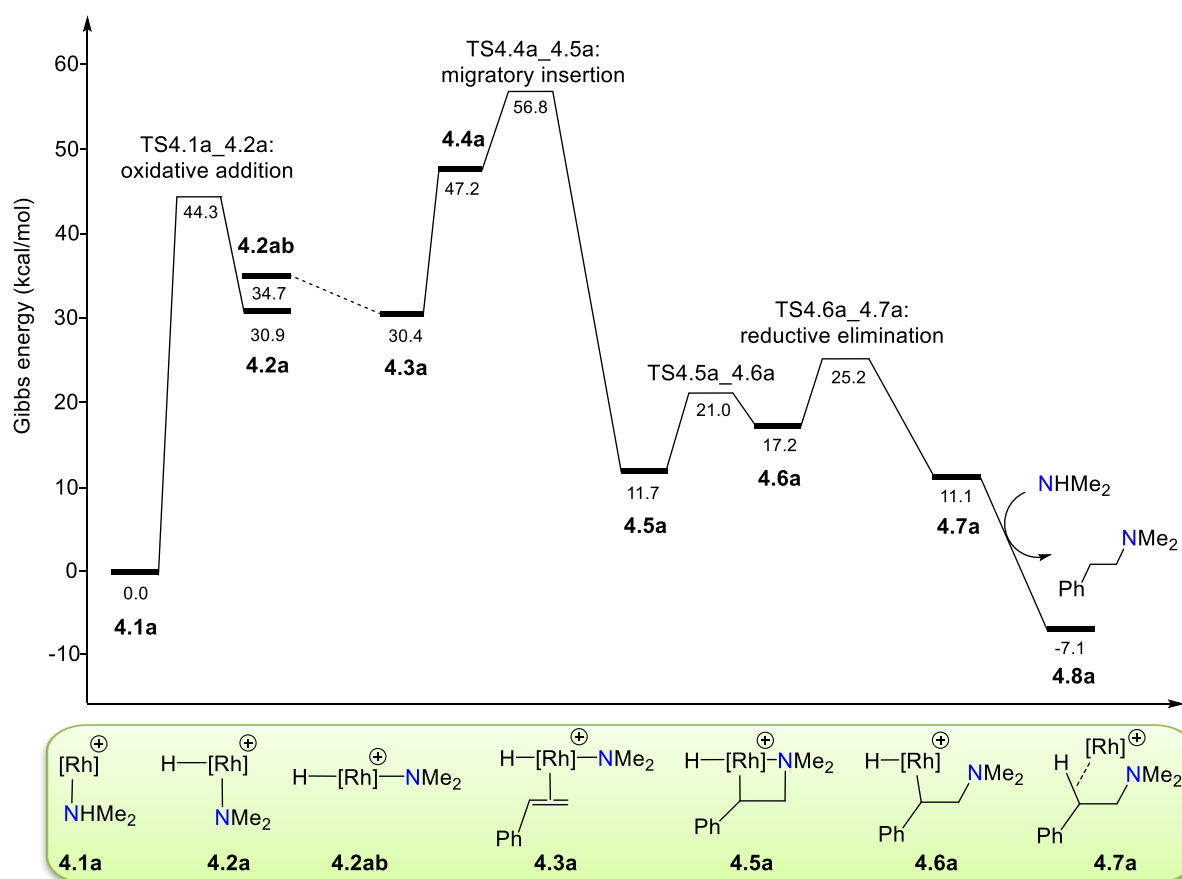
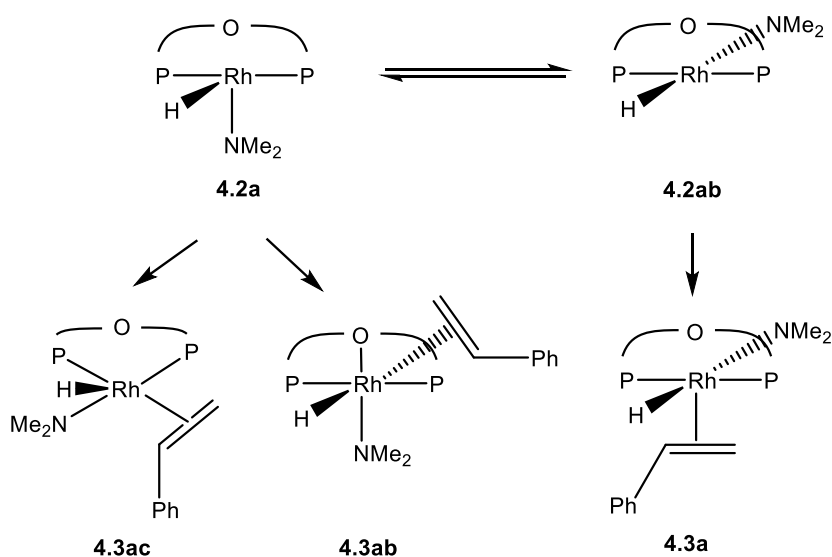


Figure 4.2: Gibbs energy profile in toluene of the Rh-catalyzed hydroamination of styrene through an amine activation pathway.

From intermediate **4.1a**, the first step involves the oxidative addition of the N-H bond of the amine to the Rh(I) center. The corresponding transition state, **TS4.1a_4.2a**, has a relative energy of 44.3 kcal/mol. The breaking N-H bond distance is 1.645 Å, whereas the forming Rh-N and Rh-H bond distances are 1.996 Å and 1.571 Å, respectively. The intermediate formed, which has the amine and the hydride *cis* to each other (**4.2a**), is located at 30.9 kcal/mol. Another isomer of this intermediate (structure **4.2ab**) with the amine and hydride ligands *trans* to each other, lies at 34.7 kcal/mol.

The subsequent coordination of the alkene can take place at several positions. Among the three isomers found, the most stable one, (**4.3a** which is formed from the coordination of the amine into intermediate **4.2ab** with the NMe₂ and the H ligands *trans* to each other) has a relative Gibbs energy of 30.4 kcal/mol. The other two isomers (structures **4.3ab** and **4.3ac**, resulting from the coordination of the amine into structure **4.2a** in which the NMe₂ and the H ligands *cis* to each other) are 4.1 and 6.7 kcal/mol higher in energy, respectively. The different structures involved in this step are summarized in **Scheme 4.2**.



Scheme 4.2: Schematic representation of different structures obtained for the coordination of the alkene after the oxidative addition of the amine.

From intermediate **4.3a**, a conformational change (rotation of both amine and alkene ligands) is required in order to take place the migratory insertion of the alkene into the Rh-N bond. Such conformational arrangement gives intermediate **4.4a** with a relative Gibbs energy of 47.2 kcal/mol. The transition state for the migratory insertion, **TS4.4a_4.5a** has a Gibbs energy barrier of 56.8 kcal/mol. The distance of the forming N-C bond at the transition state is 2.335 Å and is shortened to 1.494 Å in the intermediate **4.5a**, which has an octahedral geometry. The structures of oxidative addition and migratory insertion steps are drawn in **Figure 4.3**. The high barriers involved make the amine activation pathway completely unfeasible.

From intermediate **4.5a**, the mechanism ends with an elimination process. This process that gives the aminoalkyl product takes place in two steps: decoordination of the amine first and then a reductive elimination yielding the final reaction product. The transition state for the first step, **TS4.5a_4.6a** lies at 21.0 kcal/mol (with a relative energy barrier of 8.3 kcal/mol) and yields intermediate **4.6a** (at 17.2 kcal/mol). The reductive elimination step takes place from this intermediate. The corresponding transition state (**TS4.6a_4.7a**) has a Gibbs energy of 25.2 kcal/mol with a C-H forming bond and Rh-H breaking bond distance of the is 1.812 and 1.560 Å, respectively. In the subsequent intermediate (**4.7a**) the formed aminoalkyl

product is bonded to the catalyst through an agostic interaction. Replacement of the reaction product by a new amine molecule closes the catalytic cycle.

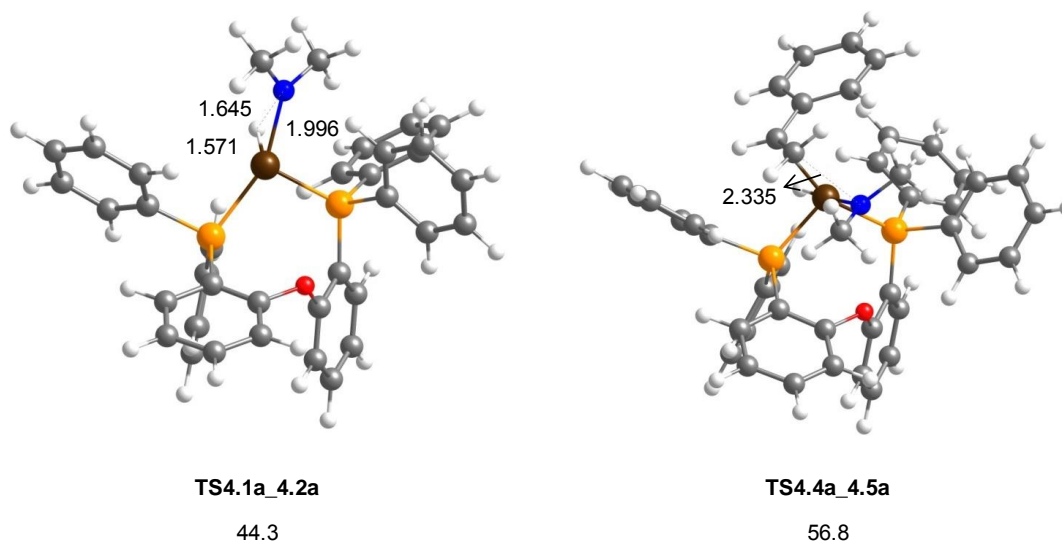


Figure 4.3: Optimized structures of transition states for the oxidative addition and migratory insertion steps in the amine activation pathway. Relative Gibbs energy values are given under each structure in kcal/mol.

b) Alkene activation mechanism

This subsection outlines the alkene activation mechanism for the formation of the hydroamination product (see **Section 1.2.1.1** for more details about this mechanism).

In this pathway a styrene molecule needs to be initially coordinated to the catalyst. As commented at the beginning of **Section 4.1.3**, there are two structures with a coordinated styrene ligand (**4.1b** and **4.1c**) that differ only by 0.3 kcal/mol. Thus, this process may take place starting from any of the two intermediates. Both possibilities were evaluated and are presented in this subsection. In addition, the reaction pathway analyzed from each intermediate may proceed through a *syn* or an *anti* addition of the amine to the double bond. If the reaction starts with a *syn* addition of the amine, the reaction ends up with the protonation of the metal center followed by a reductive elimination step. When the reaction starts with an *anti* addition of the amine, the reaction can end with the direct protonolysis or assisted by a second amine. All the possibilities were evaluated and are described in this subsection. An additional pathway where the reaction starts with the *anti* addition and ends with the protonation of the metal center followed by a reductive elimination step was also evaluated.

For the pathway starting from intermediate **4.1b**, a transition state for the *anti* nucleophilic addition of the amine to the coordinated alkene (**TS4.1b_4.2b**; giving rise to the addition to the terminal carbon atom to form the *anti*-Markovnikov product), was located with a relative Gibbs energy of 16.5 kcal/mol. Such transition state displays a forming N-C bond

distance of 2.074 Å. This distance is shortened to 1.554 Å upon the formation of intermediate **4.2b** whose relative Gibbs energy is 9.5 kcal/mol.

Next step in the process should be the proton migration from the amine group to the contiguous carbon atom. The transition state for the direct proton transfer in a single step, **TS4.2b_4.9b**, was located at 54.0 kcal/mol. The energy required for this pathway is too high to be considered a feasible process; the possibility of a second amine molecule assisting the proton transfer was also evaluated. The process was found to take place in two steps since the protonated amine, **4.11b** $[\text{H}_2\text{NMe}_2]^+ \cdots [(\text{Me}_2\text{N}-\text{CH}_2\text{CHPh})\text{Rh}(\text{DPEphos})]$ was found as a stable intermediate in the PES but the formation of such intermediate is a barrierless process in the Gibbs energy profile (**TS4.10b_4.11b** is slightly lower than intermediate **4.11b**). The Gibbs energies for such intermediate is 6.5 kcal/mol and the transition state for the protonation of the alkyl group (**TS4.11b_4.12b**) was found at 29.6 kcal/mol. The complete energy profile for the hydroamination reaction of styrene through an *anti* addition pathway is represented in **Figure 4.4**.

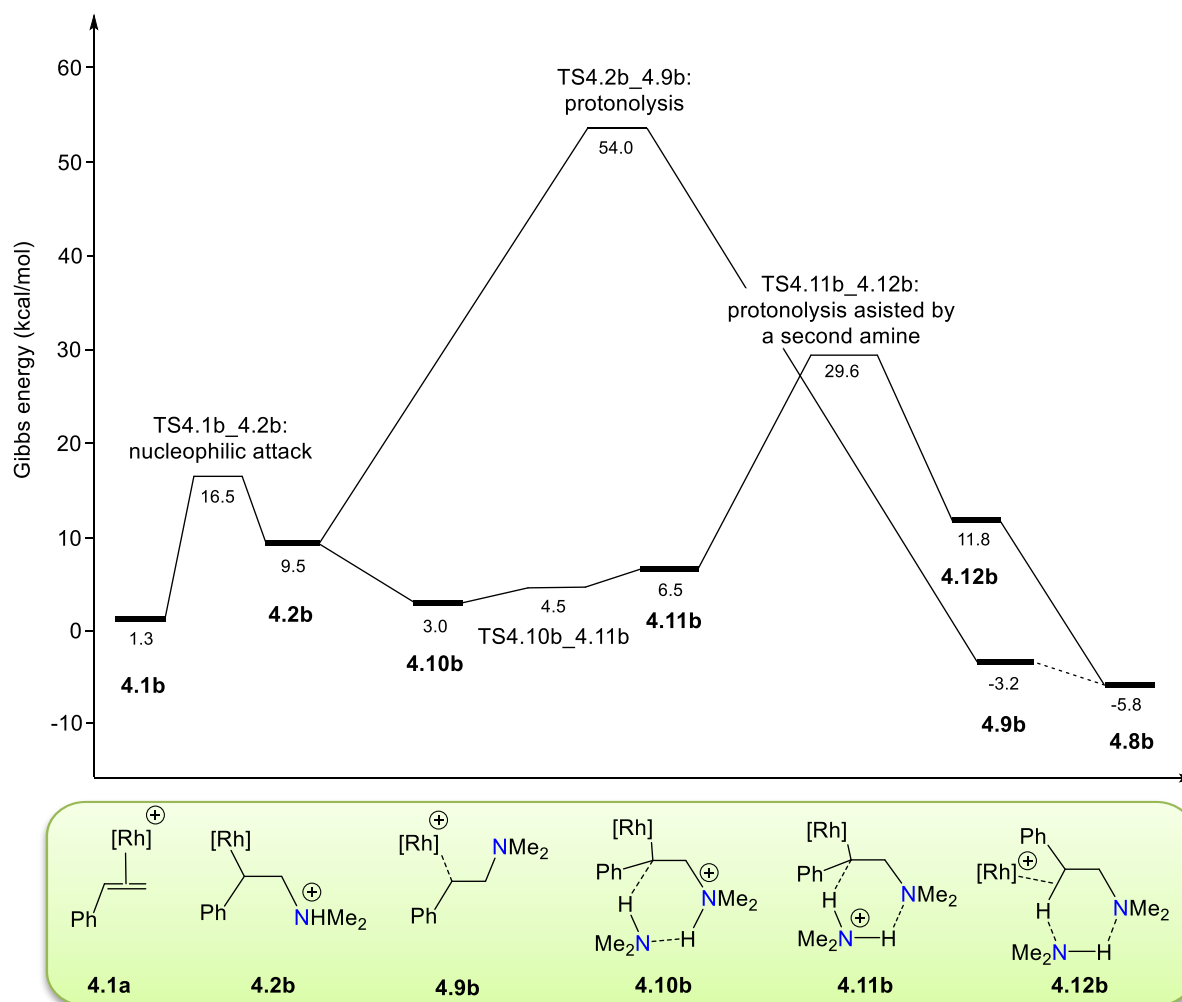


Figure 4.4: Gibbs energy profile in toluene of the Rh-catalyzed hydroamination of styrene through an *anti* addition of the amine (alkene activation pathway).

Starting from intermediate **4.1b**, the *syn* nucleophilic addition of the amine was also evaluated. The transition state for the *syn* addition (**TS4.1b_4.5b**) was located at 22.7 kcal/mol (6.2 kcal/mol higher in energy than the *anti* nucleophilic addition of the amine). The distance for the forming C-N bond is 2.198 Å, a little longer than the same distance for the *anti* addition of the amine. This step gives rise to intermediate **4.5b** whose relative Gibbs energy is 7.7 kcal/mol. From this intermediate the reaction continues by a metal center protonation step followed by a reductive elimination step. The transition state for the proton transfer process **TS4.5b_4.6b** is located at 22.5 kcal/mol yielding intermediate **4.6b** located at 18.3 kcal/mol. The N-H breaking and the Rh-H forming bond distances at the transition state are 2.276 and 1.518 Å, respectively. Such a process produces the formal oxidation of the metal center from Rh(I) to Rh(III). Finally, a reductive elimination takes place through transition state **TS4.6b_4.7b** (located at 21.3 kcal/mol) with forming C-H bond and a breaking Rh-H bond distances of 1.841 and 1.568 Å, respectively. The subsequent intermediate (**4.7b**) is located at 8.0 kcal/mol and has the aminoalkyl product formed attached to the Rh center by means of an agostic interaction. Finally, the substitution of the aminoalkyl product by a styrene molecule closes the catalytic cycle.

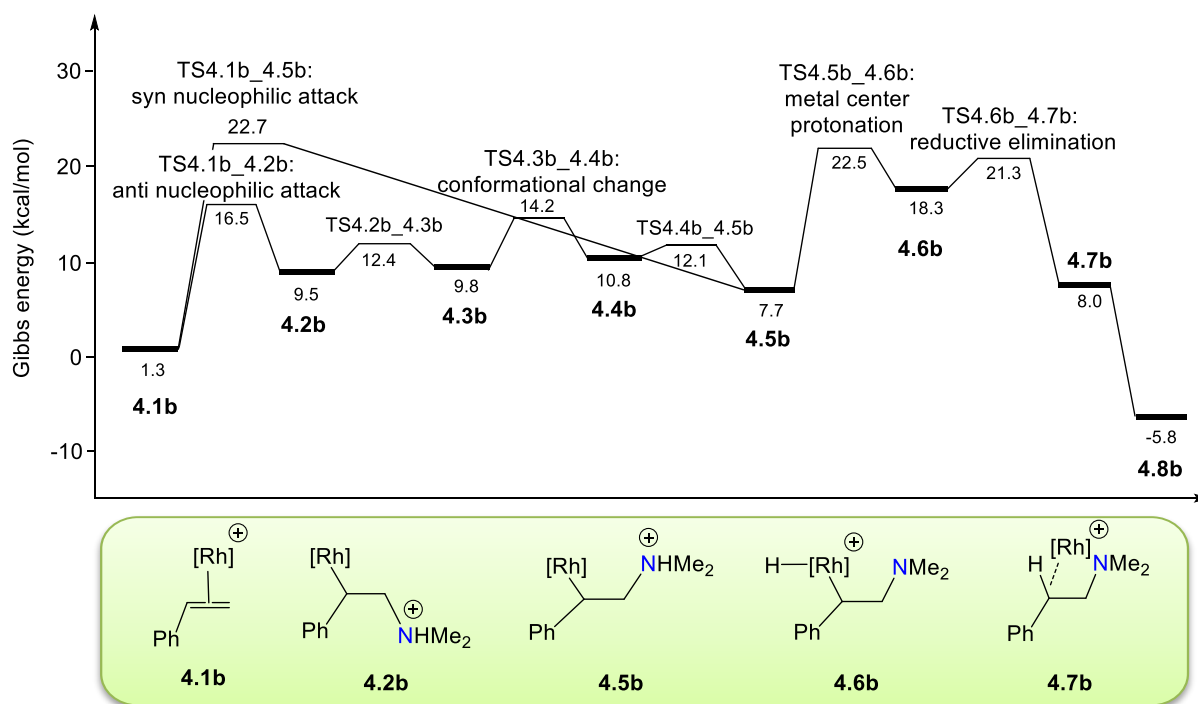


Figure 4.5: Gibbs energy profile in toluene of the Rh-catalyzed hydroamination of styrene through an alkene activation pathway.

Alternatively, a complete different pathway starting with an *anti* addition was found involving a conformational change on the aminoalkene ligand that allows the migration of the proton from the amine to the metal center. This conformational change involves the rotation of the amine modifying the \widehat{RhCCN} dihedral angle and was characterized to take place in three steps, whose transition states are identified as **TS4.2b_4.3b**, **TS4.3b_4.4b** and

TS4.4b_4.5b. The relative position of the N-H and the Rh in the formed intermediate **4.5b** (**Figure 4.7**) is the same formed with the *syn* addition and is the appropriate for the protonation of the metal center.

The reaction through this pathway arrives to intermediate **4.5b**, as for the *syn* addition pathway explained above. Therefore in the overall pathway the highest point in the Gibbs energy profile corresponds to the metal center protonation step (**TS4.5b_4.6b**). The energy profile for this mechanism as well as the energy profile for the *syn* addition pathway is represented in **Figure 4.5**. The main transition states involved in the alkene activation mechanism are represented in **Figure 4.6**.

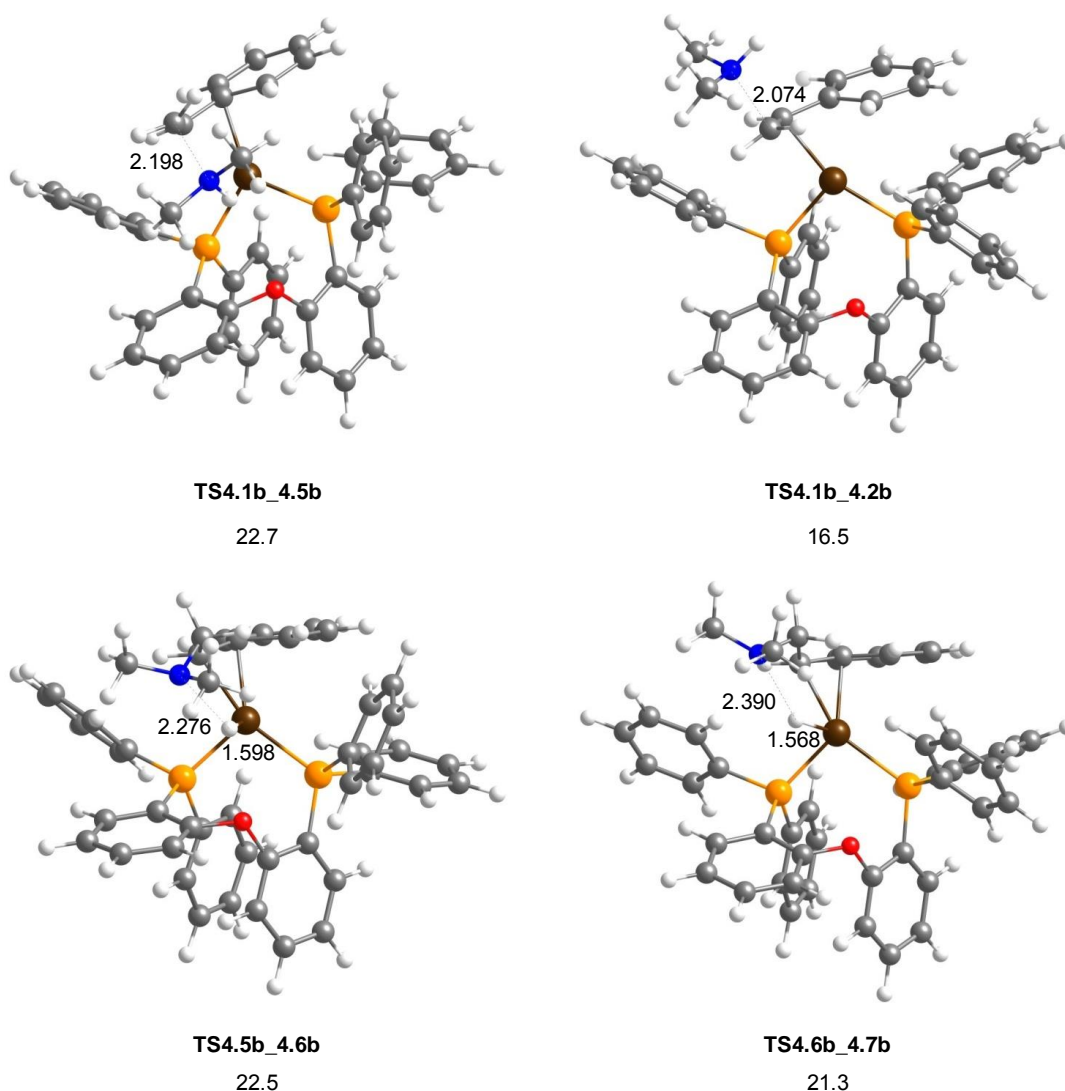


Figure 4.6: Optimized structures of main transition states involved in the alkene activation mechanism: nucleophilic attack (*syn* and *anti*), metal center protonation and reductive elimination. Relative Gibbs energy values are given under each structure in kcal/mol.

The reaction starting from intermediate **4.1c** with both, amine and styrene coordinated, was also evaluated. Despite of the computational efforts devoted, no transition state could be located for the internal nucleophilic attack form the coordinated amine ligand.

From intermediate **4.1c**, the nucleophilic addition of the amine can proceed through an *anti* or a *syn* addition of the external amine (not coordinated) to the double bond. The transition state for the *anti* nucleophilic attack (**TS4.1c_4.2c**) was located with a relative Gibbs energy of 23.7 kcal/mol. The N-C distance in this step is shortened from 1.973 Å in the transition state to 1.573 Å in intermediate **4.2c**.

Regarding to the *syn* nucleophilic addition, the energy barrier of the transition state is 32.4 kcal/mol and the distance for the forming N-C bond in this transition state (**TS4.1c_4.3c**) is 2.051 Å. This distance is shortened to 1.513 Å in the formed complex **4.3c** which is located at 15.2 kcal/mol. The next step of this pathway is the metal center protonation whose transition state (**TS4.3c_4.4c**) was located at 26.1 kcal/mol, whereas its subsequent intermediate (intermediate **4.4c**) is located at 25.9 kcal/mol.

The reaction starting from intermediate **4.1b** requires less energy than starting from intermediate **4.1c**. For this reason the reaction from intermediate **4.1c** was not further considered.

From intermediate **4.1b**, the overall energy barriers for the *syn* and *anti* pathways are rather similar (only differ in 0.2 kcal/mol). As consequence, in principle both pathways should be possible. The energy barrier for the *syn* addition has the highest energy transition state in the first step, the nucleophilic addition (**TS4.1b_4.5b**; 22.7 kcal/mol), whereas the *anti* addition is significantly lower (**TS4.1b_4.2b**; 16.5 kcal/mol). Thus, the *anti* addition can take place more easily.

The magnitude of the KIE should be able in principle to distinguish whether the rate determining step is prior or after the proton transfer. Following this idea, we have calculated the kinetic isotope effects (KIEs) using a N-deuterated amine (NDMe₂). The calculated KIEs for each pathway are very different. Hence, for the *syn* pathway, where the nucleophilic addition has the highest Gibbs energy barrier, the calculated KIE is rather low (1.05 at 100 °C). Nevertheless, for the case of the *anti* pathway, the highest Gibbs energy transition state corresponds to the proton transfer to form the Rh-H intermediate; accordingly, the calculated KIE is higher (2.69 at 100 °C). Experimental data is not available for direct comparison.

In related experiments performed in a different system, Hartwig measured the KIEs for intramolecular hydroamination reactions catalyzed by rhodium. For the case of an intramolecular hydroamination using a primary amine and a Rh catalyst with a Xantphos derivative ligand, the observed KIE was 1.16 ± 0.10 .²⁵⁴ This was an indication that proton transfer takes place after the turnover-limiting step. For another intramolecular hydroamination using a secondary amine and a Rh catalyst with a phosphane-arene ligand instead, the observed KIE was 2.5 ± 0.6 .²⁵⁵ This data was consistent with a mechanism where the protonation of the Rh-C bond is the turnover-limiting step. Our calculations are in good agreement with these experiments, showing that *anti* and *syn* pathways are very close

in energy, so subtle changes in the catalyst may affect their relative energy barriers, thus favoring one over the other.

4.3.1.2 Mechanism of the competing side reaction

The main competing side reaction for the hydroamination process gives rise to the oxidative amination product.^{104,114} In the previous section, it has been shown that the most feasible reaction mechanism goes through an alkene activation pathway which involves an initial *anti* nucleophilic addition of the amine to the coordinated alkene, followed by a conformational change of the amine to favor the protonation of the metal center, giving rise to intermediate **4.6b**. A subsequent reductive elimination (**TS4.6b_4.7b**; 21.3 kcal/mol) yields the hydroamination product. From such intermediate (**4.6b**) the formation of the enamine product can be explained by a β -hydride elimination of the aminoalkyl ligand. The transition state for this process (**TS4.6b_4.7ba**) is located at 28.0 kcal/mol, with a Gibbs energy barrier of 9.7 kcal/mol. The breaking C-H and forming Rh-H bond distances are 2.297 and 1.693 Å, respectively. This step generates a Rh-dihydride intermediate which has the aminoalkene product coordinated (intermediate **4.7ba** which lies at 11.7 kcal/mol). The energy profile for the oxidative amination reaction is depicted in **Figure 4.7**.

We also evaluated an alternative mechanism, proposed by Togni and coworkers,⁷² to account the oxidative amination product. In this mechanism, once the nucleophilic addition to the alkene has happened (intermediate **4.5b**), the generation of the Rh-(H)₂ intermediate **4.7ba** takes place by means a β -hydride elimination and a subsequent proton transfer from the amine to the metal center (**TS4.5b_4.6ba** and **TS4.6ba_4.7ba** respectively). The relative Gibbs energy of the transition states for these two steps are 27.6 and 37.9 kcal/mol, respectively, clearly higher than the barrier of the pathway commented above (28 kcal/mol).

Experimentally, it is also observed the formation of some quantity of ethylbenzene. The formation of that product can be explained by hydrogenation of styrene by means of the Rh-dihydride intermediate formed after the β -elimination step (**4.7ba**). From this intermediate, it can take place the replacement of the enamine product by an styrene molecule, giving rise to intermediate **4.8ba**, which is located at 18.7 kcal/mol. The hydrogenation process occurs in two steps that can be described as two insertions of the organic ligand into the Rh-H bonds. The transition state for the first insertion (**TS4.8ba_4.9ba**) has a relative Gibbs energy of 20.7 kcal/mol. The forming C-H and breaking Rh-H bond distances are 1.747 and 1.608 Å respectively. In this step the Rh alkyl monohydride intermediate is formed, which lies at 12.1 kcal/mol. The transition state for the second insertion into the Rh-H bond (**TS4.9ba_4.10ba**) is located at 18.3 kcal/mol. In this transition state the forming C-H bond distance is 1.681 Å meanwhile the breaking Rh-H bond distance is 1.584 Å.

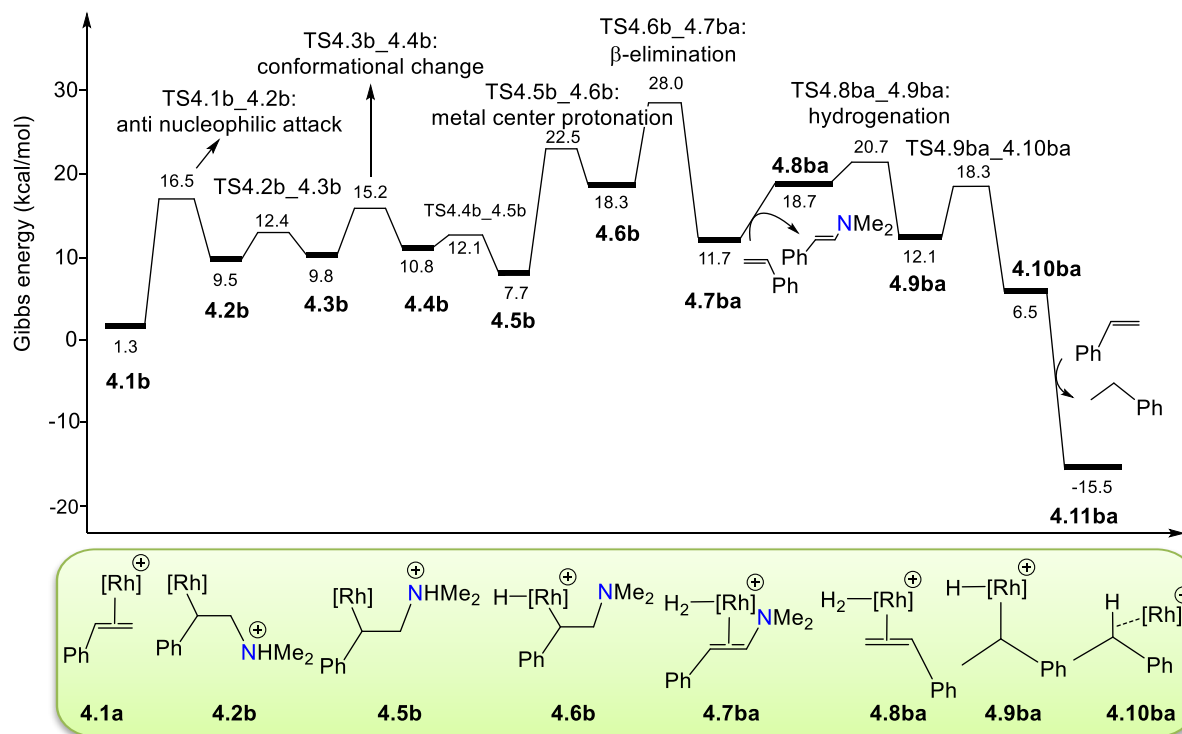


Figure 4.7: Gibbs energy profile in toluene of the Rh-catalyzed oxidative amination of styrene (the competing side reaction).

Structure **4.6b** has two empty sites at the coordination sphere. Coordination of a second styrene molecule in the ligand sphere was also considered, as proposed by Hartwig.¹¹⁴ Surprisingly, the coordination of the second styrene is endergonic by 7.5 kcal/mol. Moreover, the transition state for the styrene coordination (**TS4.6b_4.6bb**) is located at 25.0 kcal/mol. From this intermediate the reaction can evolve through a reductive elimination step to yield the hydroamination product (**TS4.6bb_4.7bb**) or it can take place a insertion of this second alkene into the metal-hydride bond (**TS4.6bb_4.8bb**), followed by a β -elimination step to yield the enamine product; a second insertion into the other Rh-H bond yields the hydrogenated styrene. The transition state of the elimination step to yield the hydroamination product is located at 30.7 kcal/mol, much higher than the transition state for this same step without having coordinated a second styrene molecule (21.3 kcal/mol). Regarding to the formation of the enamine product from intermediate **4.6bb**, the transition state for the first step; which is the insertion of the alkene into the metal-hydride bond, requires an energy of 28.7 kcal/mol, also higher than the β -elimination step in the pathway without the coordination of the second styrene, whose energy is 28.0 kcal/mol. Therefore the latter steps for this pathway were not calculated and the coordination of the second styrene was not further considered.

4.3.2 Analysis of the selectivity (amine vs enamine)

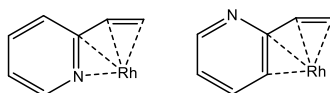
The previous section was devoted to study the operative mechanism for the hydroamination reaction as well as the mechanism for the competing side oxidative amination reaction. The proposed mechanism starts with one alkene molecule coordinated to the metal center (intermediate **4.1b**). From this intermediate the reaction continues with the *anti* nucleophilic attack of the amine followed by a conformational change of the molecule to place the amine close to the metal center, allowing a metal center protonation step which gives intermediate **4.6b**. The reaction finishes with a reductive elimination step to yield the hydroamination product or with a β -elimination step to yield the enamine product. In the competing side reaction the formation of the hydrogenated styrene product is explained through the exchange of the enamine product by a second alkene molecule and two consecutive insertion steps of this alkene molecule into two rhodium-hydride bonds.

In this section is explored the effect of the substituent as well as the catalyst into the selectivity observed along with a comparison of our theoretical results with the experimental studies carried out by Hartwig¹¹⁴ and Beller.¹¹¹

According to the mechanism above described, the hydroamination/oxidative amination products ratio is governed by the energy difference between the rate determining steps for the hydroamination and the oxidative amination reactions, which are the metal center protonation transition state (**TS4.5b_4.6b** which Gibbs energy is 22.5 kcal/mol) and β -elimination transition state (**TS4.6b_4.7ba** which Gibbs energy is 28.0 kcal/mol), respectively.

Experimentally, the reaction using $[\text{Rh}(\text{DPEphos})]^+$ as catalyst and HNMe_2 as amine was carried out using three different vinylarenes: 3,4-dimethoxy-1-vinylbenzene, 4-methyl-1-vinylbenzene and 2-vinylpyridine obtaining in the three cases the hydroamination product as the major one.¹¹⁴ The hydroamination/oxidative amination products ratios were 82:19, 54:46 and 90:10 respectively. The reaction of several substituted styrenes catalyzed by $[\text{Rh}(\text{PPh}_3)_2]^+$ was studied experimentally by Beller¹¹¹ demonstrating the oxidative amination product is the major one in all cases. Unfortunately, there are no experimental data using $[\text{Rh}(\text{PPh}_3)_2]^+$ as catalyst and HNMe_2 as amine for direct comparison. The complete profile for the hydroamination reaction as well as for the oxidative addition reaction was calculated using the three vinylarenes employed experimentally (**Table 4.1**).

For 2-vinylpyridine two structures differing in the coordination mode of the substrate to metal center were considered. In one structure the pyridine nitrogen atom is coordinated to the rhodium atom whereas in the second it is not (see **Scheme 4.3**).



Scheme 4.3: Initial structures considered for reaction of 2-vinylpyridine.

All the intermediates and transition states along the reaction are lower in energy when the nitrogen pyridine atom is not coordinated to the rhodium center. The values in **Table 4.1** correspond to the reaction starting from the structure where the nitrogen pyridine atom is not coordinated to rhodium atom.

Table 4.1: Gibbs energies obtained for the reaction of 4-dimethoxy-1-vinylbenzene, 4-methyl-1-vinylbenzene and 2-vinylpyridine catalyzed by $[\text{Rh}(\text{DPEphos})]^+$ and for styrene catalyzed by $[\text{Rh}(\text{PPh}_3)_2]^+$.

Column	1	2	3	4
System				
Amine:enamine ratio ^a	54:46	90:10	82:19	17:78 ^b
4.1b	0.0	0.0	0.0	0.0
TS4.1b_4.2b	13.7	16.2	16.7	15.3
4.2b	6.4	10.2	10.6	9.0
4.5b	4.0	7.6	8.1	10.4
TS4.5b_4.6b	23.6	22.6	21.3	23.5
4.6b	17.4	18.9	17.4	17.2
TS4.6b_4.7b	20.8	20.4	21.3	27.6
4.7b	6.1	8.4	7.0	19.5
TS4.6b_4.7ba	27.7	29.5	30.1	18.9
4.7ba	9.5	13.3	13.2	13.1
Overall barrier for hydroamination (TS4.5b_4.6b)	23.6	22.6	21.3	23.5
Overall barrier for oxidative amination (TS4.6b_4.7ba)	27.7	29.5	30.1	18.9
$\Delta\Delta G^\ddagger$	4.1	6.9	8.8	-4.1

^a Experimental values (reference 114). ^b Experiments were carried out using a different amine (morpholine).

The energy difference between the metal center protonation transition state (higher point in hydroamination reaction) and the β -elimination transition state (higher point in oxidative

amination reaction) for 3,4-dimethoxy-1-vinylbenzene (column 3), 4-methyl-1-vinylbenzene (column 2) and 2-vinylpyridine (column 1) are 8.8, 6.9 and 4.1 kcal/mol respectively in favor of hydroamination reaction. In the Beller's system ($[\text{Rh}(\text{PPh}_3)_2]^+$; column 4) our calculations give an energy barrier of the oxidative amination reaction 4.1 kcal/mol lower than the barrier for hydroamination reaction.

From our calculations can be concluded that in all cases the major product predicted is the one experimentally obtained, but the Gibbs energy differences between both pathways are always too big compared with the product ratios obtained experimentally. According to the values obtained an alternative pathway, with lower barrier, for the oxidative amination reaction cannot be fully discarded.

4.3.3 Analysis of the regioselectivity

In **section 4.3.1**, was studied the mechanism of the formation of the *anti*-Markovnikov product and was found that the most plausible mechanism is the alkene activation mechanism.

In order to discuss the regioselectivity, the energy profile for the Markovnikov isomer starting from intermediate **4.1b** was computed. Both *anti* and *syn* additions of the amine were considered. The transition state for the Markovnikov *anti* addition was found to be located at 22.4 kcal/mol, which is 5.9 kcal/mol higher in energy than the *anti*-Markovnikov addition. The next step in the process should be the proton migration from the amine group to the contiguous carbon atom. The transition state for the direct proton transfer, **TS4.2bm_4.7bm**, was located at 53.5 kcal/mol. The alternative reaction assisted by a second amine molecule from intermediate **4.2bm** was also evaluated. This process was found to take place in two steps in the PES since the intermediate where the second amine is protonated was found as a stable intermediate. However, the formation of such intermediate appears as a barrierless process in the Gibbs energy profile (similarly as for the formation of the *anti*-Markovnikov isomer). The relative Gibbs energies for such intermediate (**4.3bm**) and for the transition state of the protonation of the alkyl group (**TS4.3bm_4.4bm**) are 18.6 kcal/mol and 35.1 kcal/mol. The *syn* addition of the amine into the alkene (**TS4.2bm_4.8bm**) has a Gibbs activation barrier of 34.0 kcal/mol.

As far as the comparison between the Markovnikov and *anti*-Markovnikov hydroamination processes is concerned, the Markovnikov hydroamination is, as expected, thermodynamically favorable because it yields the most stable product. Using styrene as substrate the Markovnikov hydroamination product is 0.8 kcal/mol more stable than the product obtained in the *anti*-Markovnikov hydroamination. However, the *anti*-Markovnikov nucleophilic addition has a lower Gibbs energy barrier for both *syn* and *anti* pathways of the styrene activation mechanism. For the *anti* pathway the *anti*-Markovnikov nucleophilic addition for the reaction of styrene catalyzed by $[\text{Rh}(\text{DPEphos})]^+$ is preferred by 5.9 kcal/mol

(16.5 kcal/mol for the *anti*-Markovnikov addition; **TS4.1b_4.2b** and 22.4 for the Markovnikov version; **TS4.1b_4.2bm**).

In order to prove if our calculations are able to reproduce the regioselectivity obtained during the hydroamination reaction, some calculations of the reaction using other rhodium-phosphine complexes as catalyst were carried out. Beller et al. reported the reaction of styrene catalyzed by $[\text{Rh}(\text{PPh}_3)_2]^+$ showing that the *anti*-Markovnikov regioselectivity is obtained.¹¹¹ Conversely in another experimentally study performed by Philippot et al. it was found that the hydroamination of styrene, using $[\text{Rh}(\text{PEt}_3)_2\text{Cl}]_2$ as catalyst, the Markovnikov isomer was as the major product.¹¹⁰

Our calculations pointed out that, using $[\text{Rh}(\text{PPh}_3)_2]^+$ as catalyst, the *anti*-Markovnikov nucleophilic attack is preferred by 5.8 kcal/mol (barriers are 15.3 kcal/mol for the *anti*-Markovnikov addition and 21.1 kcal/mol for the Markovnikov addition). For the reaction catalyzed by $[\text{Rh}(\text{PMe}_3)_2\text{Cl}]$, taken as model of $[\text{Rh}(\text{PEt}_3)_2\text{Cl}]_2$ to avoid conformational issues, the Markovnikov nucleophilic attack is preferred by 0.6 kcal/mol (barriers are 27.9 kcal/mol for the *anti*-Markovnikov addition and 27.3 kcal/mol for the Markovnikov addition, respectively). The values obtained in our calculations are in fair agreement with the experimental trends observed. The next subsections are devoted to further study the origin of the *anti*-Markovnikov regioselectivity observed during this reaction.

4.3.3.1 Energy decomposition analysis

The regioselectivity was analyzed in terms of an energy decomposition analysis (EDA), also called activation strain model.²⁵⁶ The bond energy between two interacting fragments (ΔE) is divided into two major components: the preparation energy (ΔE_{prep}) and the interaction energy (ΔE_{int}) that in this case was obtained as follows:

$$\Delta E = \Delta E_{\text{prep}} + \Delta E_{\text{int}} = (\Delta E_{\text{prep cat-alkene}} + \Delta E_{\text{prep amine}}) + \Delta E_{\text{int}} \quad [4.1]$$

The preparation as well as interaction energies were calculated for the step where the regioselectivity is defined (the nucleophilic addition step). The preparation energy (ΔE_{prep}) is the energy required to distort the fragments from the stable structure they have initially to those in the transition state. This energy can be divided into the preparation energy for the alkene coordinated to metal center fragment ($\Delta E_{\text{prep cat-alkene}}$) and the preparation energy of the amine fragment ($\Delta E_{\text{prep amine}}$). This energy is calculated as the difference energy between a single point calculation of the structure they have at the reagent and in the transition state. The interaction energy (ΔE_{int}) account for the interaction between the distorted fragments at their transition state geometries.

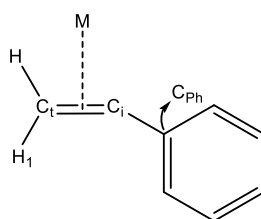
This analysis was performed in five points along the reaction pathway close to the transition state (two points before the transition state, the transition state and two points after the transition state) in order to check if the variation in energies are continuous. The energies obtained for the transition state structure are collected in **Table 4.2**. The results obtained

showed that whereas the interaction energy is quite similar for both the Markovnikov and *anti*-Markovnikov additions ($\Delta\Delta E_{int} = 1.4$ kcal/mol), the preparation energy term is quite different ($\Delta\Delta E_{prep} = 6.3$ kcal/mol). Further analysis display that the alkene coordinated to the metal center fragment is mostly responsible of the preparation energy (96%), so the alkene-rhodium moiety is the one mainly distorted. Therefore the regioselectivity can be in some way related with the structure of the alkene-metal moiety.

Table 4.2: Energy decomposition analysis for the nucleophilic addition step giving rise to Markovnikov and *anti*-Markovnikov products for the *anti* addition of HNMe₂ to coordinated styrene. Energies in kcal/mol.

	<i>anti</i> -Markovnikov	Markovnikov	Difference ($\Delta\Delta E$)
$\Delta E_{interaction}$	-7.3	-8.7	-1,4
$\Delta E_{prep [Rh]-alkene}$	14.7	20.7	6.0
$\Delta E_{prep amine}$	0.5	0.8	0.3
$\Delta E_{preparation}$	15.2	21.5	6.3
ΔE	7.9	12.8	4.9

This fact is reflected in the structural analysis by analyzing the C_t-C_i-C_{Ph} angle and the H₁-C_t-C_i-C_{Ph} dihedral angle for the transition state of the nucleophilic addition in both pathways (C_t and C_i are the terminal and internal carbon atoms of the alkene respectively, C_{Ph} is the ipso carbon of the phenyl ring and H₁ is the hydrogen placed in cis respect to the phenyl ring; **Scheme 4.4**).



Scheme 4.4: Schematic representation of structural parameters calculated for alkenes.

C_t-C_i-C_{Ph} angle has a value of 123.6° in **TS4.1b_4.2b** (*anti*-Markovnikov addition) and 113.5° in **TS4.1b_4.2bm** (Markovnikov one), showing that the sp³ character of C₂ carbon atom is higher in the Markovnikov addition than in the *anti*-Markovnikov addition. In other words, these facts reflects that the structure of the alkene-metal moiety is more distorted in the Markovnikov version. Dihedral angles also show the same trend. Values of the dihedral angle H₁-C_t-C_i-C_{Ph} are -9.7° in the *anti*-Markovnikov addition (**TS4.1b_4.2b**) and 58.7° in the

Markovnikov addition (**TS4.1b_4.2bm**). In all cases, preparation energy is larger for internal than for terminal C atom.

4.3.3.2 The effect of modifying the alkene's substituent properties

In order to check whether regioselectivity depends on the nature of the substrate, in addition to styrene, the nucleophilic attack of dimethylamine to several terminal alkenes with different aliphatic and aromatic groups bearing a series of electron-donor and electron-acceptor substituents was also evaluated.

The relative Gibbs energy for transition states of Markovnikov and *anti*-Markovnikov nucleophilic attack (ΔG_M^\ddagger and ΔG_{aM}^\ddagger respectively) as well as the difference between both energies ($\Delta\Delta G^\ddagger$) are collected in **Table 4.3**. For the case of aromatic substituents seven different substrates were analyzed, including an electron-withdrawing group and/or an electrodonating group in different positions. In all cases the *anti*-Markovnikov addition is preferred but with different barrier differences ($\Delta\Delta G^\ddagger$). Styrene (entry 3) displays a $\Delta\Delta G^\ddagger$ of 5.9 kcal/mol. Including an electron-withdrawing substituent in *para* position (-NO₂, entry 1) slightly increases the $\Delta\Delta G^\ddagger$ to 6.1 kcal/mol, whereas an electrodonating group (-OMe) also in *para* position (entry 7) decreases such difference to 2.9 kcal/mol. The addition of electrodonating MeO⁻ groups in *meta* position increases the barrier differences up to 6.0 kcal/mol and 5.5 kcal/mol (entries 2 and 4), as compared to those with H in such position (entries 3 and 7, with energy barriers of 5.9 and 2.9 kcal/mol respectively). When a methyl group is added the $\Delta\Delta G^\ddagger$ difference is 5.1 kcal/mol and for the case of 2-vinylpyridine as substrate the barrier difference is 4.4 kcal/mol (entries 5 and 6).

Terminal alkenes with aliphatic groups (which are in principle better electrodonors than aromatic groups) were also investigated, despite of very few cases have been experimentally reported.^{110,257} The results show that the $\Delta\Delta G^\ddagger$ is decreased when the electrodonor character of the substituent is increased. The values obtained for *tert*-butyl, ethyl and methyl groups, were 3.9, 1.3 and 0.8 kcal/mol respectively (entries 8, 9 and 10). The 1,2-dimethylethene substrate (entry 11), with two groups at the internal carbon atom, shows a smaller preference for the *anti*-Markovnikov addition with a barrier difference of 0.4 kcal/mol. For analytical purposes, terminal alkenes with much better electrodonating groups (MeO⁻, PhO⁻ and AcO⁻) were also investigated. In this case the regioselectivity was reversed, in favor of the Markovnikov addition. The $\Delta\Delta G^\ddagger$ obtained for these cases were -5.1, -3.6 and -0.8 kcal/mol, respectively (entries 12, 13 and 15).

According to results showed in **Table 4.3**, the difference in energy between Markovnikov and *anti*-Markovnikov addition is higher using substrate with electron-withdrawing groups, like aromatics substituents, and this difference is reduced when the electrodonating character of the group increases. The results obtained revealed that the *anti*-Markovnikov addition is the most favored process for the most of terminal alkenes, (independently of the aromatic or aliphatic character of the organic substituent) and only for particular cases with

highly electrodonor substituents (entries 12, 13 and 15) the regioselectivity was reversed to favor the Markovnikov addition.

Eisenstein and Hoffmann studied in the eighties, by means of external Hückel calculations and fragment molecular orbital analysis, the activation toward nucleophilic attack of olefins coordinated to transition metal complexes.^{75,76} They demonstrated that symmetric η^2 -olefins are not directly activated on coordination, but the activation occurs on going from η^2 to η^1 coordination. **Figure 4.8** displays the main geometrical parameters associated with the η^2 to η^1 slippage of a π -coordinated unsaturated carbon-carbon bond. This slippage of the coordinated olefin localizes the LUMO of the $L_nM(\text{alkene})$ complex on the further carbon atom from the metal center, enhancing the interaction with the incoming nucleophile. Later on, Tamasi et. al. experimentally and with DFT calculations studied the regiochemistry of nucleophilic additions to Pt-coordinated styrene.²⁵⁸ They showed that the regioselectivity can be understood on the basis of the interaction between the olefin and the metal center, concluding that the carbon which is closer to the metal center is less susceptible of nucleophilic attack.

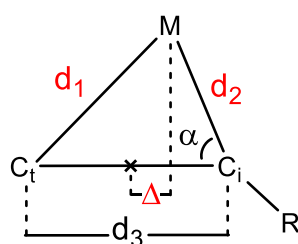
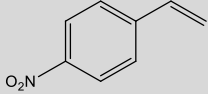
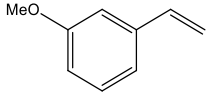
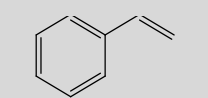
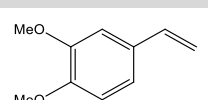
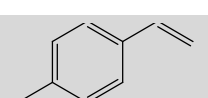
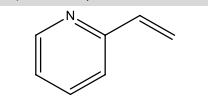
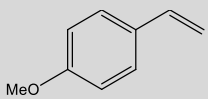
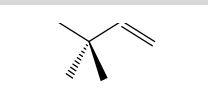
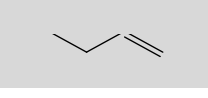
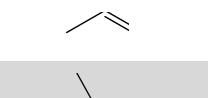
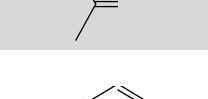
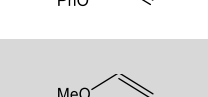
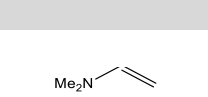
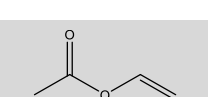
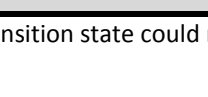


Figure 4.8: Schematic representation of structural parameters associated with the η^2 to η^1 slippage.

Following these ideas, the complexes where the alkene is coordinated to the metal center were analyzed. For the case of styrene coordinated to $[\text{Rh}(\text{DPEphos})]^+$, three different structures with different ligands coordinated to metal center were analyzed: structure **4.1b** (styrene), structure **4.1c** (alkene and amine) and structure **4.1bO** (alkene and the oxygen of the DPEphos ligand). In structure **4.1b** the distances between metal and both carbons of alkene are 2.203 and 2.143 Å for the terminal and internal carbon atoms, respectively, so the internal carbon atom is closer to the metal center than the terminal carbon. For structures **4.1c** and **4.1bO** the internal carbon is further away from metal center than terminal carbon. The difference can be attributed to the fact that the alkene is occupying two coordination sites in structure **4.1b**, thus forcing the internal carbon to be closer to the metal center than the terminal carbon.

Table 4.3: Gibbs energy barriers (Markovnikov, ΔG_M^\ddagger and *anti*-Markovnikov, ΔG_{aM}^\ddagger) for the *anti* nucleophilic attack, along with the corresponding geometrical parameters for their initial intermediates calculated for each alkene (see **Figure 4.8**). Gibbs energies in kcal/mol and distances in Å

Entry	Substrate	ΔG_{aM}^\ddagger	ΔG_M^\ddagger	$\Delta\Delta G^\ddagger^a$	d_1 (Rh-C _t)	d_2 (Rh-C _i)	d_3 (C _t -C _i)	Δ	d_1-d_2
1		13.6	19.6	6.1	2.199	2.150	1.393	0.077	0.049
2		15.5	21.5	6.0	2.207	2.148	1.392	0.093	0.059
3		15.2	21.1	5.9	2.203	2.143	1.392	0.094	0.060
4		16.7	22.2	5.5	2.198	2.137	1.392	0.095	0.061
5		16.2	21.3	5.1	2.201	2.139	1.392	0.096	0.062
6		13.7	18.1	4.4	2.208	2.147	1.391	0.095	0.061
7		16.9	19.8	2.9	2.204	2.133	1.392	0.111	0.071
8		21.8	25.6	3.9	2.185	2.209	1.385	-0.039	-0.024
9		17.5	18.7	1.3	2.204	2.127	1.387	0.121	0.077
10		17.9	18.7	0.8	2.199	2.132	1.388	0.104	0.067
11		22.3	22.7	0.4	2.213	2.141	1.391	0.113	0.072
12		22.2	18.6	-3.6	2.159	2.174	1.386	-0.024	-0.015
13		20.6	15.5	-5.1	2.205	2.106	1.382	0.154	0.099
14		22.0	*	-	2.218	2.094	1.387	0.193	0.124
15		18.0	17.2	-0.8	2.206	2.097	1.382	0.170	0.109

* This transition state could not be found. ^a $\Delta\Delta G^\ddagger = \Delta G_M^\ddagger - \Delta G_{aM}^\ddagger$

The distances between rhodium atom and terminal (d_1) and internal (d_2) carbon atoms were analyzed for all the complexes with the alkene coordinated to metal center for the substrates here studied (**Table 4.3**). According with Tamasi results, the carbon which is closer to the metal center is less susceptible of nucleophilic attack.²⁵⁸ Therefore, the internal carbon atom is expected to be closer to the rhodium center when the *anti*-Markovnikov addition is preferred (entries 1-11), whereas the terminal carbon atom should be closer to the rhodium center when the Markovnikov addition is preferred (entries 12-15).

Surprisingly for 3,3-dimethyl-1-butene, methyl-vinyl ether and N,N-dimethylamineethene (entries 8, 13 and 14) the carbon atom closer to the metal center is most susceptible of nucleophilic attack. For 3,3-dimethyl-1-butene (entry 8) the *anti*-Markovnikov regioselectivity is obtained (the nucleophilic attack occurs in the terminal carbon atom) but terminal carbon is closer to the metal center (distances of terminal and internal carbon atoms are 2.185 and 2.209 Å, respectively). For methyl-vinyl ether and N,N-dimethylamineethene (entries 13 and 14), the internal carbon is closer to the metal center and a Markovnikov regioselectivity is expected.

In general, in most of cases the internal carbon atom is closer to the metal center independently of *anti*-Markovnikov or Markovnikov regioselectivity is observed. Only for 3,3-dimethyl-1-butene and phenyl-vinyl ether (entries 8 and 12) the terminal carbon atom is closer to rhodium center.

The shape of the LUMO of the coordinated alkenes can be thought as a mixture of four orbitals (the filled b_2 and π_{CC} and the empty a_1 and π_{CC}^*) and depends on their relative contributions. When the complex is symmetrical ($\Delta=0$), the ML_n fragment has a high-lying filled orbital of b_2 symmetry to interact with ethylene π^* and a more or less low-lying vacant a_1 orbital to mix with π . Olefin slipping results in a lowering of symmetry, which allows orbitals to mix which could not mix in the most symmetrical complex geometry. This mixture of orbitals is depicted in **Figure 4.9**.

According to the proposal of Eisenstein and Hoffmann, the displacement in the alkene coordination defines what carbon of the olefin has a major contribution into the LUMO of the $L_nM(\text{alkene})$ complex.^{75,76} Two different parameters which can measure the degree of the η^2 to η^1 slippage were analyzed. These parameters are the difference of two rhodium-C alkene distances (d_1-d_2) and the displacement of the $[\text{Rh}(\text{DPEphos})]^+$ fragment respect to the center of the double bond of the olefin (Δ). A graphical representation of both parameters is drawn in **Figure 4.8**.

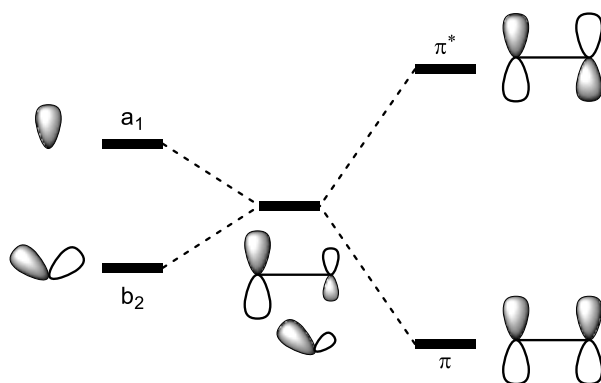


Figure 4.9: Representation of LUMO of the coordinated alkenes as a mixture of four orbitals. Figure adapted from reference 76.

To study the relationship between alkene coordination and regioselectivity, we have plotted in **Figure 4.10** the difference between the Markovnikov and *anti*-Markovnikov barriers against the d_1 - d_2 parameter. This representation displays a very good correlation between both parameters. If the values using 3,3-dimethyl-1-butene and phenyl vinyl ether as substrates are omitted (entries 8 and 12), a correlation coefficient of 0.74 is obtained (12 alkenes are included in the correlation). A similar correlation is found using the Δ parameter.

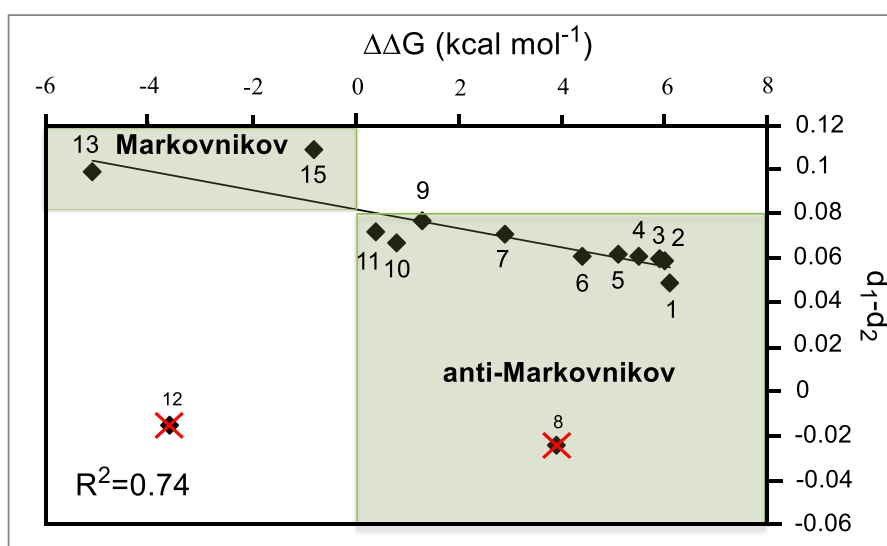


Figure 4.10: Plot of the energy difference between Markovnikov and *anti*-Markovnikov barriers ($\Delta\Delta G^\ddagger$) against difference in Rh-C distances of both carbon atoms of alkene (d_1 - d_2 parameter). Numbers corresponds with entries in **Table 4.3**.

The anomalous behavior of 3,3-dimethyl-1-butene and phenyl vinyl ether (entries 8 and 12, respectively) can be explained from the Rh-C distances collected in **Table 4.3**. The presence of three methyl groups (in case of 3,3-dimethyl-1-butene) or a phenoxide group (in case of phenyl vinyl ether) avoid the alkene from approaching the metal as much as the other alkenes. Therefore, in these cases steric factors override electronic effects.

4.3.3.3 Orbital and NBO analysis

To further analyze the origin of the regioselectivity, we calculated NBO charges in three representative terminal alkenes ($\text{CH}_2=\text{CH-R}$): styrene ($\text{R}=\text{Ph}$) and propene ($\text{R}=\text{Mw}$) where the *anti*-Markovnikov regioselectivity is observed and methoxyethene ($\text{R}=\text{OMe}$) which presents Markovnikov regioselectivity. The charges for the hydroamination reaction catalyzed by $[\text{Rh}(\text{DPEphos})]^+$ complex were studied at different points along the nucleophilic attack pathway: the free alkene, the initial intermediate (alkene π -coordinated to metal center, **4.1b**), and the intermediate formed after the nucleophilic attack with an *anti*-Markovnikov as well as with a Markovnikov regioselectivity (**4.2b** and **4.2bm** respectively). The NBO charges were also studied in the initial intermediate (**4.1b**) for the reaction catalyzed by $[\text{Rh}(\text{PPh}_3)_2]^+$ and $[\text{Rh}(\text{PMe}_3)_2\text{Cl}]$ complexes where *anti*-Markovnikov and Markovnikov regioselectivity is obtained, respectively. Results are shown in **Table 4.4**.

Table 4.4: Evolution of NBO charges along the addition of NHMe_2 to terminal alkenes ($\text{C}_t\text{H}_2=\text{C}_i\text{H-R}$) in presence of different catalyst.

Catalyst	R group	Structure	C_tH_2	C_t	C_iH	C_i	R^a	Rh
$[\text{Rh}(\text{DPEphos})]^+$	Ph	Free	0.02	-0.43	0.00	-0.24	-0.02	-
		4.1b	0.05	-0.46	0.04	-0.24	0.08	-0.01
		4.2b	-0.26	-0.72	0.19	-0.08	0.04	-0.16
		4.2bm	0.26	-0.26	-0.20	-0.45	-0.08	-0.18
	CH_3	Free	-0.02	-0.47	0.01	-0.22	0.01	-
		4.1b	0.03	-0.48	0.03	-0.25	0.08	-0.07
		4.2b	-0.33	-0.76	0.20	-0.06	0.04	-0.12
		4.2bm	0.25	-0.27	-0.21	-0.46	0.07	-0.27
	OMe	Free	-0.11	-0.58	0.35	0.14	-0.23	-
		4.1b	-0.04	-0.58	0.37	0.12	-0.16	-0.05
		4.2b	-0.32	-0.80	0.48	0.27	-0.22	-0.21
		4.2bm	0.23	-0.31	0.08	-0.13	-0.24	-0.20
$[\text{Rh}(\text{PPh}_3)_2]^+$	Ph	4.1b	0.05	-0.47	0.04	-0.24	0.08	-
$[\text{Rh}(\text{PMe}_3)_2\text{Cl}]$	Ph	4.1b	-0.03	-0.53	0.04	-0.23	-0.02	-

^a Correspond to the sum of charges of all atoms of the R group.

The NBO charges in the π -coordinated intermediate (**4.1b**) reveals that the most negatively charged carbon atom is always the terminal atom (C_t). For substrate with phenyl as well as methyl substituents, the *anti*-Markovnikov selectivity is preferred. The nucleophilic attack takes place over the most negatively charged atom, thus the charges cannot be the driving force of the *anti*-Markovnikov regioselectivity.

Trying to get more information about the origin of the *anti*-Markovnikov selectivity, other NBO parameters were analyzed. In particular, the atomic contribution to the π_{CC} orbital for

the alkene coordinated to the metal center (intermediate **4.1b**) was studied. Second order perturbation analysis was also performed to analyze the donation from the alkene to the metal center and back-donation from metal to double bond. The Markovnikov and *anti*-Markovnikov transition states of the nucleophilic attack were also studied by means of second order perturbation analysis, analyzing the donation from the lone pair of the nitrogen to the antibonding orbital of the double bond. Unfortunately, a clear conclusion on the origin of regioselectivity cannot be inferred from results obtained in the NBO analysis.

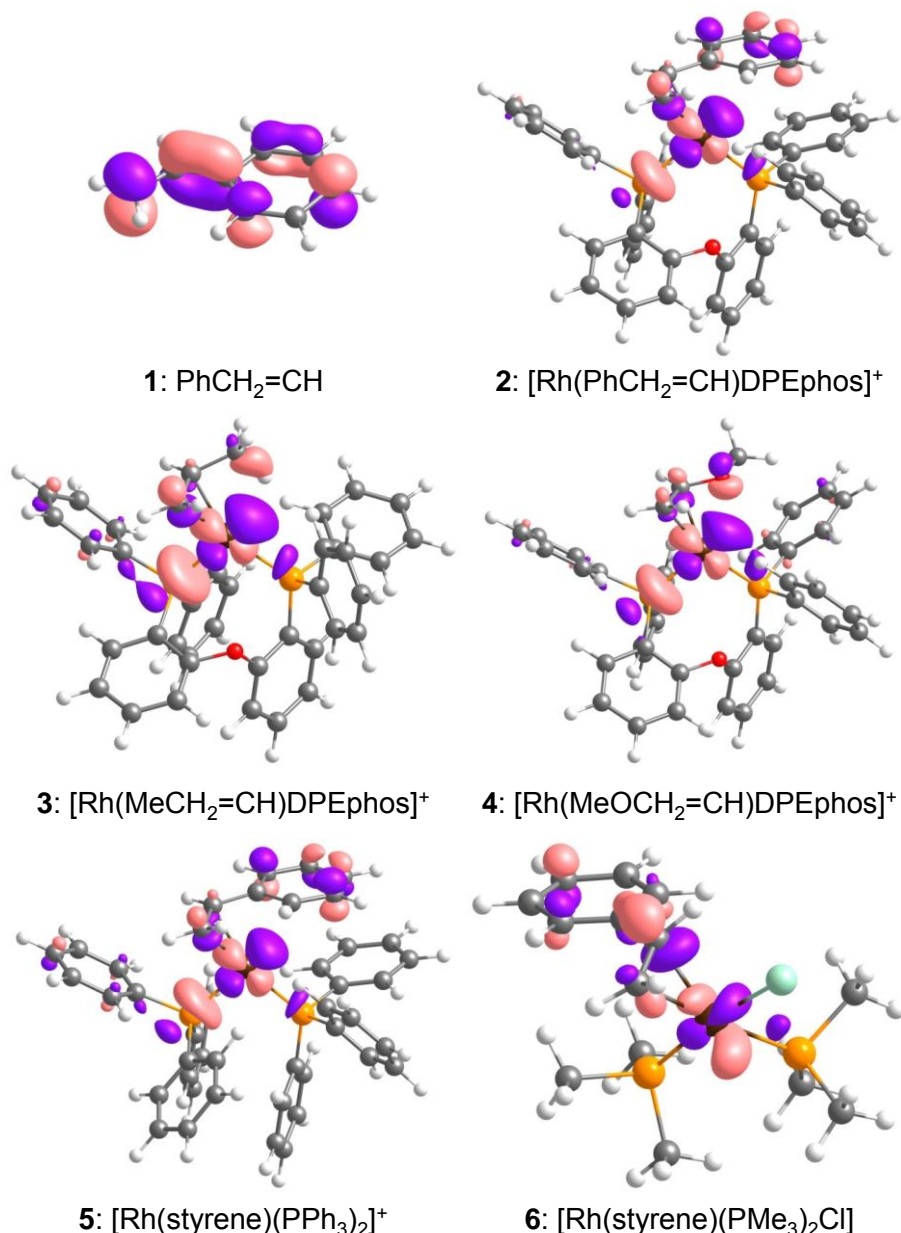


Figure 4.11: Representation of LUMO for (1) free styrene and alkenes coordinated to the rhodium catalysts: (2) styrene, (3) propene and (4) methyl-vinyl-ether coordinated to [Rh(DPEphos)]⁺, (5) styrene coordinated to [Rh(PPh₃)₂]⁺, and (6) styrene coordinated to [Rh(PMe₃)₂Cl].

The molecular orbitals involved in the nucleophilic attack were analyzed in order to study whether regioselectivity may be orbitally driven. The LUMO orbitals were calculated for free styrene and for the CH₂-CH-R terminal alkenes coordinated to [Rh(DPEphos)]⁺ (for all alkenes which appear in **Table 4.3**). The LUMO orbital of styrene coordinated to [Rh(PPh₃)₂]⁺ and [Rh(PMe₃)₂Cl] was also studied. The LUMO orbitals for the most representative terminal alkenes are depicted in **Figure 4.11**.

The LUMO of styrene coordinated to [Rh(DPEphos)]⁺ has a significant contribution from the d orbital of rhodium and a p orbital of terminal carbon atom. The same trend is found for all the alkenes in **Table 4.3**, except for those with the double bond directly bonded to a heteroatom where the Markovnikov regioselectivity is observed (entries 12-15). This fact suggests that nucleophilic addition should take place over the terminal carbon atom for most of the alkenes of **Table 4.3**, since the terminal carbon has a larger contribution into the LUMO orbital. On the contrary, performing this analysis on entries 12-15 suggests that the addition should be into the internal carbon atom. When the catalyst is [Rh(PPh₃)₂]⁺, the LUMO orbital of π-coordinated styrene is also mostly located on the terminal carbon atom, making it suitable for the *anti*-Markovnikov addition as indeed it was found experimentally. For the case of styrene coordinated to [Rh(PMe₃)₂Cl], the contribution of the internal carbon atom in the LUMO is major than that of the terminal carbon atom, thus, this complex is suitable for Markovnikov addition, also in agreement with experimental observation.

4.4 Conclusions

The mechanism as well as the regioselectivity of the *anti*-Markovnikov hydroamination of styrene with dimethylamine catalyzed by a cationic rhodium (I) complex with a DPEphos ligand has been studied by means of DFT calculations.

Two main mechanisms were evaluated, the alkene activation and the amine activation mechanism. Calculations presented here indicate that the most feasible mechanism for the reaction analyzed, using NHMe₂ and styrene as reactants and [Rh(DPEphos)]⁺ as catalyst, is the alkene activation mechanism involving an *anti* nucleophilic attack of the amine into the coordinated alkene. This step is followed by conformational change of the amine, metal center protonation and reductive elimination steps.

The mechanism for the formation of enamine as a competing side reaction has been also evaluated. The side product is formed through a β-hydride elimination on the Rh-hydride intermediate obtained after metal center protonation. This β-hydride elimination produces a Rh-dihydride intermediate. The reaction of a second styrene molecule with the Rh-dihydride intermediate explains the formation of ethylbenzene as side product which takes place by two consecutive insertion steps of the styrene into the two Rh-H bonds.

To understand the factors that govern the regioselectivity, the Markovnikov addition was also computed. For both Markovnikov and *anti*-Markovnikov pathways, nucleophilic

addition was investigated by means of analyzing molecular orbitals, atomic charges and by energy decomposition analysis.

The energy decomposition analysis reveals that the main difference is obtained in the preparation energy term (the energy necessary to distort reactants from their original geometry to that in the transition state). The NBO charges show that the terminal carbon atom is always the most negatively charged atom of the substrate, thus reaction is not charge governed. Orbital analysis displays that the LUMO of alkene coordinated to $[\text{Rh}(\text{DPEphos})]^+$ have a significant higher contribution of the orbital from the terminal carbon atom for the systems where the *anti*-Markovnikov regioselectivity is favored. However, the contribution of p orbital of internal carbon atom is higher for those cases where Markovnikov regioselectivity is obtained. This behavior can be related with the η^2 to η^1 slippage of the coordinated alkene. In fact, as proposed by Eisenstein and Hoffman, this slippage can be responsible of the LUMO shape. Indeed, the difference of the Markovnikov and *anti*-Markovnikov barriers was plotted versus such geometrical parameters (measuring the degree of slippage). A good correlation between both parameters was found. The analysis here presented opens the door to anticipate the regioselectivity of nucleophilic additions from structural information of metal-alkene complexes. The reliability of the proposed mechanism to other chemo- and regioselective was also evaluated for related systems. Such studies are presented in the followed chapters.

*Science never solves a problem
without creating ten more.*

George Bernard Shaw

~Chapter 5~

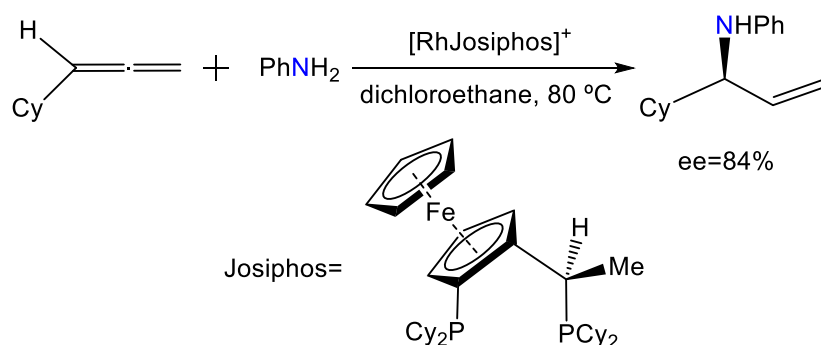
ENANTIOSELECTIVE HYDROAMINATION OF ALLENES

This chapter collects the computational study of the enantioselective hydroamination of allenes catalyzed by rhodium complexes reported by Breit et al.¹²² A manuscript summarizing these results is under preparation.

5.1 Introduction

As discussed in **Chapter 1**, hydroamination reaction has been extensively studied.^{34–38} Regarding the mechanism, two different main possibilities have been proposed: amine activation mechanism or carbon-carbon unsaturated activation mechanism. All the proposed mechanisms for the hydroamination reaction are collected in **Section 1.21**.

In the previous chapter it was presented a theoretical study of the mechanism of the hydroamination reaction of alkenes catalyzed by rhodium complexes. It was found that the reaction starts with the coordination of the alkene to the metal center followed by the *anti* nucleophilic attack of the amine into the coordinated alkene. Subsequently it takes place a metal center protonation and the reaction ends up with a reductive elimination step. It was also found that the amine activation mechanism requires too high activation energy, thus in this chapter the amine activation energy has not been considered as a feasible pathway.²⁵² In this chapter we theoretically study another example of hydroamination reaction catalyzed by rhodium complexes which has a prominent feature, the enantioselectivity of the reaction. In particular, a system developed by Breit et al. that yields a high enantiopure hydroamination product was selected to carry out mechanistic studies.¹²² They studied the process using different reaction conditions and they found that changing the catalyst as well as the solvent substantially modifies the reaction yield as well as the enantioselectivity obtained.¹²² Among all the catalyst studied by Breit we selected for the computational analysis the one that gave the best results. The system selected for our calculations is shown in **Scheme 5.1**.



Scheme 5.1: Enantioselective system selected used for the mechanistic study of hydroamination of allenes.

5.2 Computational methods and models

All calculations were carried out using Gaussian 09 program. Calculations were performed at DFT level by means of the M06 functional with and ultrafine grid option. The basis sets used were the 6-31G(d,p) for all the atoms, except for Rh where the SDD (with an additional f orbital) along with the associated pseudopotential was employed. The structures were fully optimized in solution using CPCM model with standard parameters and dichloroethane

(DCE) as solvent ($\epsilon=10.125$). The nature of stationary points (minima and TS) was confirmed by frequency calculations. A correction was applied to all Gibbs energies to change the standard state from gas phase (1 atm) to solvent state (1M). This correction increase the free energy on each species by 1.90 kcal/mol.^{259,260} Connections between the transition states and the minima were checked by following the IRC and subsequent geometry optimization till the minima. Energy values given in the text correspond to Gibbs energies at 298K calculated including solvent effects.

The energy decomposition analysis was performed using ADF program by means of the hybrid PBE0 functional. Those calculations were carried out in gas phase using ZORA/TZP basis set for all atoms. Preparation energies of EDA were computed with Gaussian 09 software in solution (dichloroethane) using M06 functional. The basis sets used were 6-31G(d,p) for all the atoms, except for Rh where the SDD (with an additional f orbital) along with the associated pseudopotential was employed.

The initial structure of catalyst was adapted from an X-ray crystallographic study of Josiphos ligand coordinated to Pd, Pt and Au.²⁶¹ The cationic rhodium complex was considered for all the calculations (**Scheme 5.1**) instead of the $[\{\text{Rh}(\text{COD})\text{Cl}\}_2]$ dimeric rhodium complex used experimentally. In all cases 3-cyclohexyl-1-allene was used as substrate and aniline as amine. The structures are named according the following procedure: **5x.y** where x correspond to the point in the energy profile and y correspond to the initial isomer (for example, **5.1a** correspond to the first point for the reaction starting with isomer **a**).

The theoretical enantiomeric excess was calculated according to the following scheme. The enantiomeric excess is defined by equation [5.1]:^{262,263}

$$ee = \frac{[S] - [R]}{[S] + [R]} \cdot 100 \quad [5.1]$$

Since enantioselective reactions are, in most cases, under kinetic control, the enantiomeric excess can be computed by assuming that the [S]/[R] ratio is given by equation [5.2], at a certain temperature, by the Boltzmann distribution of the transition states leading to each enantiomer:

$$\frac{[S]}{[R]} = e^{-\Delta\Delta G^\ddagger/RT} \quad [5.2]$$

Combining equations [5.1] and equation [5.2] is obtained the next equation for the enantiomeric excess:

$$ee = \frac{1 - e^{-\Delta\Delta G^\ddagger/RT}}{1 + e^{-\Delta\Delta G^\ddagger/RT}} \cdot 100 \quad [5.3]$$

This same equation can be obtained in terms of kinetic constants. The enantiomeric excess is given by next equation:²⁶⁴

$$ee = \frac{k_{favored} - k_{disfavored}}{k_{favored} + k_{disfavored}} \quad [5.4]$$

In the present case, as showed later, two isomers yield the major product and also two isomers yield the minor product. The favored product is obtained when isomers **b** and **d** are considered whereas the disfavored product is obtained for the reaction starting with isomers **a** and **c**, so the previous equation is transformed into the next equation:

$$ee = \frac{(k_b + k_d) - (k_a + k_c)}{(k_b + k_d) + (k_a + k_c)} \quad [5.5]$$

The previous equation can be also written in terms of ΔG^\ddagger using the Eyring equation obtaining the following equation:

$$ee = \frac{\left(e^{-\Delta G_b^\ddagger/RT} + e^{-\Delta G_d^\ddagger/RT} \right) - \left(e^{-\Delta G_a^\ddagger/RT} + e^{-\Delta G_c^\ddagger/RT} \right)}{\left(e^{-\Delta G_b^\ddagger/RT} + e^{-\Delta G_d^\ddagger/RT} \right) + \left(e^{-\Delta G_a^\ddagger/RT} + e^{-\Delta G_c^\ddagger/RT} \right)} \quad [5.6]$$

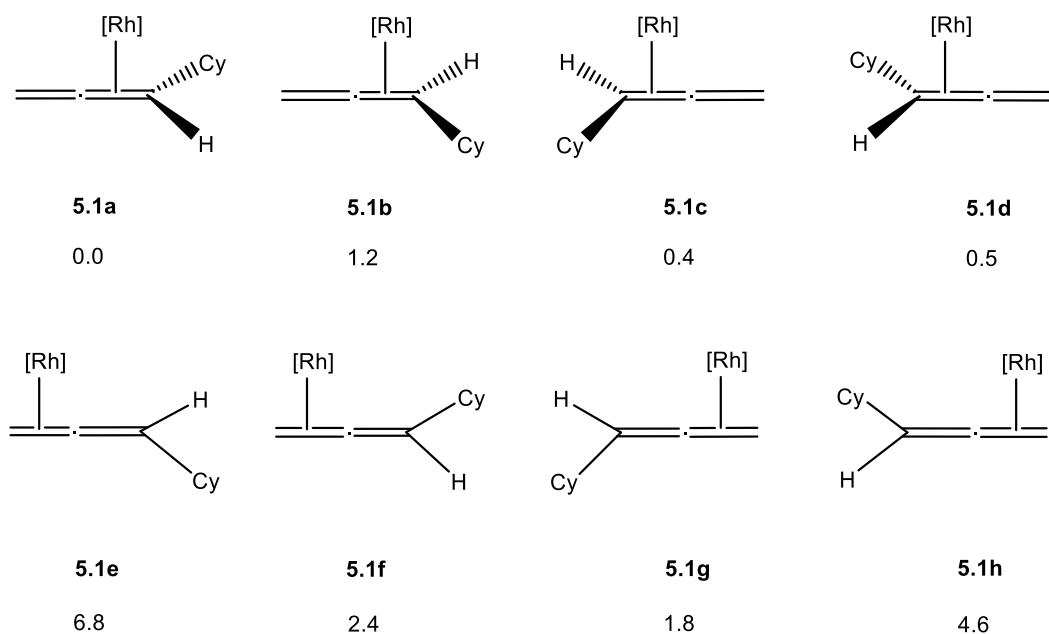
5.3 Results and Discussion

The results obtained are presented in six subsections. The first one describes the coordination of the allene to the catalyst, which is the initial step in the electrophile activation mechanism that we assume (**Section 1.2.1.2**). The second one is devoted to discuss the mechanistic aspects of the reaction, where three different options for the alkene activation mechanism were considered. The third section contains an explanation of the results obtained during isotopic labeling experiments carried out by Breit et al.¹²² The fourth is devoted to study the regioselectivity at the nucleophilic addition step. The fifth section presents an analysis of the enantioselectivity obtained using the most favorable mechanism obtained in the previous section and in the last one is analyzed the effect of changing the substituents in the Josiphos ligand.

5.3.1 Coordination of allene to the $[\text{Rh}(\text{Josiphos})]^+$ catalyst

The first step in an electrophile activation mechanism is the π -coordination of the electrophile molecule to the metal center. In this case the electrophile is an allene so different isomers can be obtained when the allene is coordinated to metal center. As the allene is monosubstituted and the two sides of the catalyst are not equivalent, 8 different isomers can be generated depending to the relative position of the allene to the catalyst. These structures are depicted in **Scheme 5.2** including values of the relative Gibbs energy obtained for each isomer.

In the first four isomers (**5.1a-d**), the rhodium is bonded to the internal double bond of the allene, however, in the other four isomers (**5.1e-h**) it is bonded to the external double bond. It is well known that the double bond that is coordinated to the metal center is activated and is going to be prone towards the nucleophilic addition; so the reaction product will be different depending on the initial isomer. The experimental product is observed only for the addition to the internal carbon atom. Thus we will focus on those isomers that has this carbon coordinated (**5.1a-d**).



Scheme 5.2: Possible allene-catalyst π -complexes and their relative Gibbs energies (kcal/mol). [Rh] = [Rh(Josiphos)]⁺

Calculations show that the isomers where the allene is bonded to the external double bond (the less substituted double bond, isomers **5.1e-h**) are higher in energy than the isomers where allene is bonded to the internal double bond (isomers **5.1a-d**) but not high enough as to count them out. It was also found that the allene-[Rh(Josiphos)]⁺ π -complex has a square-planar geometry with one empty position and in all cases this complex is only stable when the cyclohexyl group is placed over this empty position. This can be explained because one hydrogen of the cyclohexyl group of allene is occupying this empty position interacting with the rhodium center through an agostic interaction. The optimized structures of allenes bonded to rhodium by the internal double bond (**5.1a-d**) are depicted in **Figure 5.1**. The formation of the agostic bond is evident in all the structures.

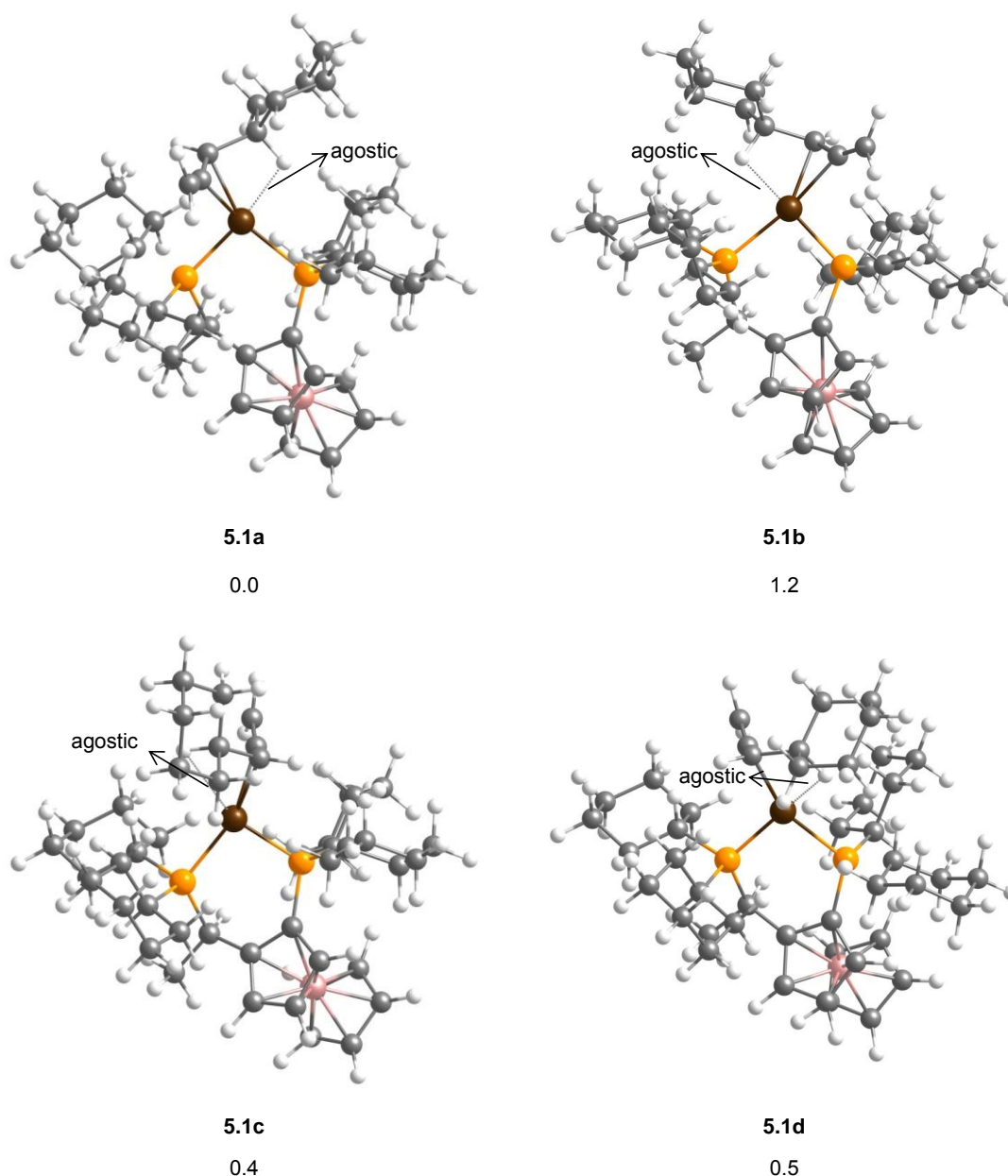


Figure 5.1: Lowest-energy structures for the coordination of the allene to metal center. Relative Gibbs energy values are given under each structure in kcal/mol.

We also explored the possibility to fulfill the empty coordination site by coordinating a solvent molecule (dichloroethane, DCE). We tried to optimize isomers **5.1a-d** including a coordinated dichloroethane molecule. We were not able to find any stable structure in the potential energy surface when we tried to optimize isomers **5.1a_DCE** and **5.1c_DCE**. In case of isomers **5.1b_DCE** and **5.1d_DCE** the structures including a dichloroethane molecule have been located with relative Gibbs energies of 8.1 and 7.4 kcal/mol, respectively.

5.3.2 Mechanistic analysis of the feasible pathways.

In this section is presented the mechanistic study of different plausible mechanisms starting with the alkene activation. Three different pathways were studied for the hydroamination reaction of allenes catalyzed by $[\text{Rh}(\text{Josiphos})]^+$ complex. The pathways studied can be described as:

- a) *Syn* nucleophilic attack of amine into the coordinated alkene followed by a metal center protonation and a reductive elimination steps.
- b) *Anti* nucleophilic attack of amine into the coordinated alkene followed by a conformational change to allow metal center protonation and reductive elimination steps. This mechanism was found the most feasible one for hydroamination of alkenes catalyzed by rhodium complexes (**Section 4.3.1**).
- c) *Anti* nucleophilic attack of amine into the coordinated allene followed by a proton transfer step supported by a second amine.

The mechanistic comparison among these a priori feasible mechanistic pathways was performed on the most stable isomer after coordination of allene to $[\text{Rh}(\text{Josiphos})]^+$, **5.1a**. From this intermediate (**5.1a**) the *syn* addition is going to yield the S enantiomer (**5.14a**) and the *anti* addition the R enantiomer (**5.8a**).

Additionally, some other pathways were considered to be able to explain the isotopic labeling experiments carried out by Breit et al.¹²² Such experiments as well as the pathways analyzed are summarized in **Section 5.3.3**.

a) *Syn* nucleophilic attack

This pathway can be described as an initial *syn* nucleophilic attack of the amine into the coordinated allene followed by metal center protonation and reductive elimination steps.

The *syn* nucleophilic attack of amine into the coordinated double bond of the allene was located at 34.4 kcal/mol (**TS5.1a_5.11a**). The intermediate formed (**5.11a**) has a relative Gibbs energy of 18.3 kcal/mol (**Figure 5.2**, red line). In the next step a proton is transferred from the protonated amine to the rhodium center, giving rise to the hydride-complex **5.12a**. The barrier of such transition state (**TS5.11a_5.12a**) was located at 26.8 kcal/mol. This step is a formal oxidation of the metal center from Rh(I) to Rh(III). From the hydride complex (**5.12a**), a reductive elimination takes place involving transition state **TS5.12a_5.13a** with a Gibbs energy of 23.8 kcal/mol. After this step, complex **5.13a** is formed with a relative Gibbs energy of 0.4 kcal/mol. Finally an exchange of the reaction product by an allene molecule closes the catalytic cycle. In case of *syn* attack, isomer **5.1a** yields the S enantiomer (**5.14a**, major product).

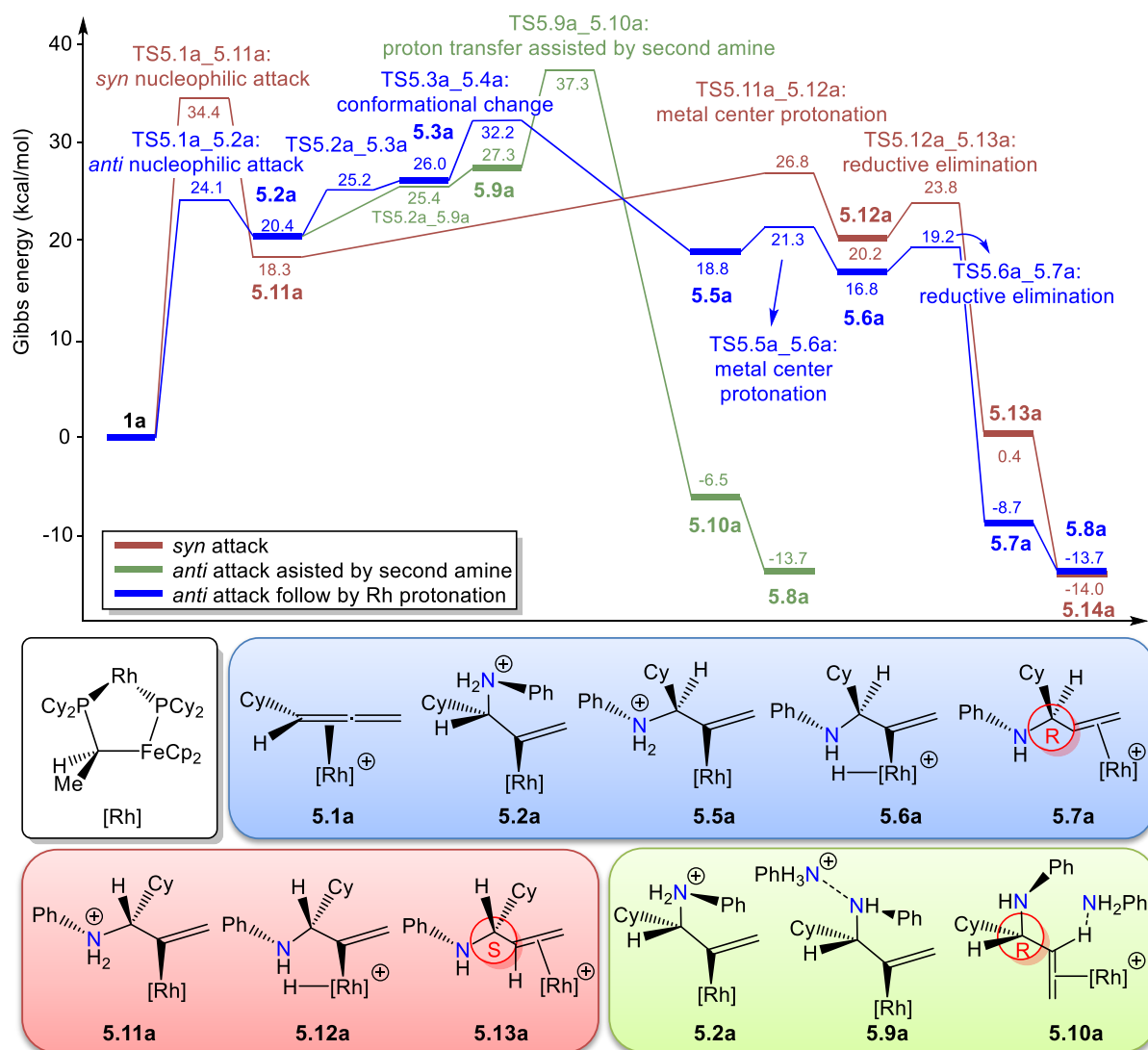


Figure 5.2: Mechanistic study of hydroamination of allenes catalyzed by rhodium complexes.

b) *Anti* nucleophilic attack followed by conformational change and metal center protonation

This pathway is analogous to the one presented in **Section 4.3.1** and can be described as an initial *anti* nucleophilic addition of the amine followed by a conformational change to place the amine close to the metal center. This conformational change yields an intermediate similar to the one obtained with a *syn* nucleophilic addition and allows the reaction to ending by a metal center protonation and a reductive elimination steps. The optimized structures of the main transition states along this pathway (nucleophilic addition, conformational change, metal center protonation and reductive elimination) are depicted in **Figure 5.3**.

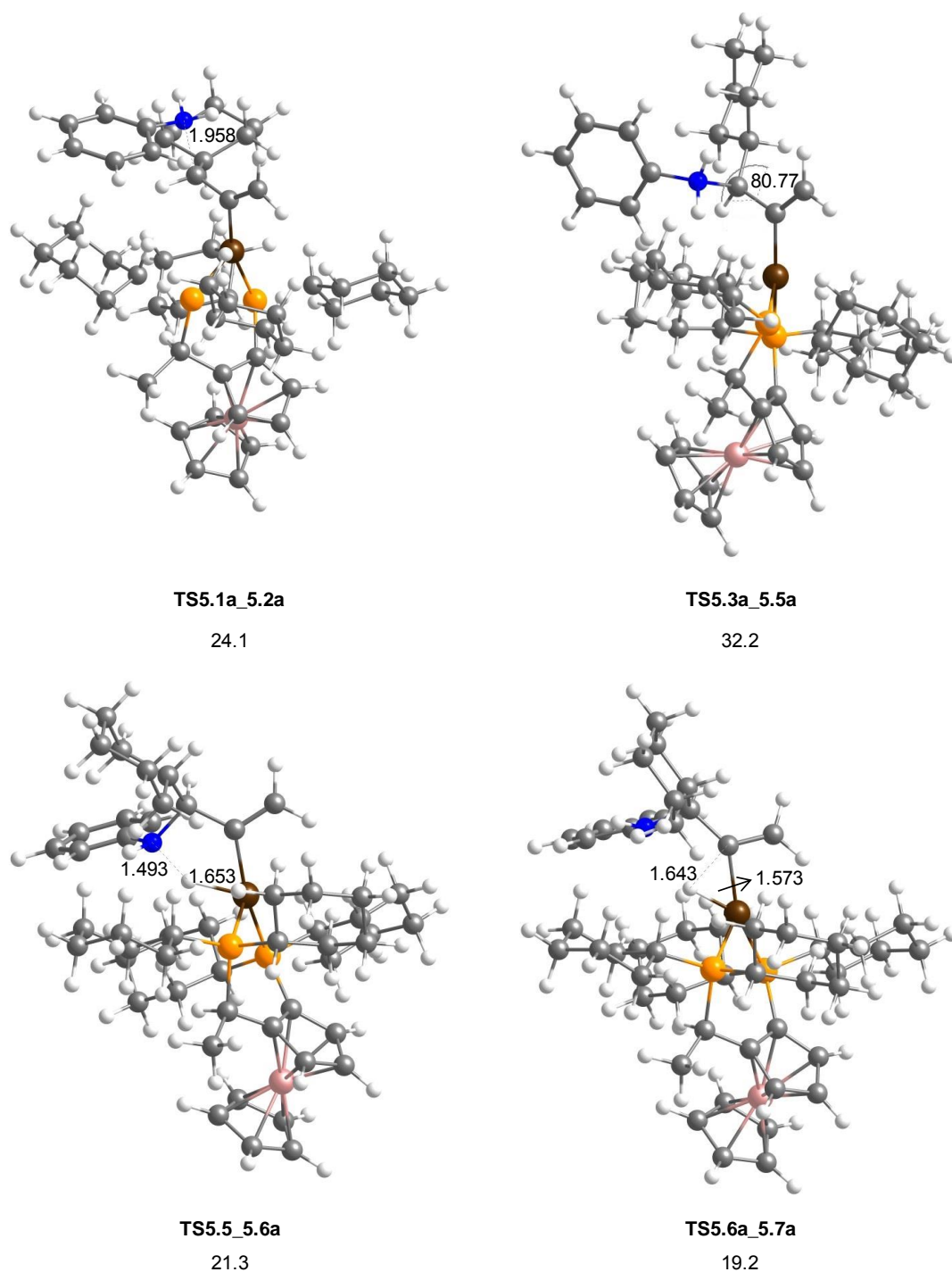


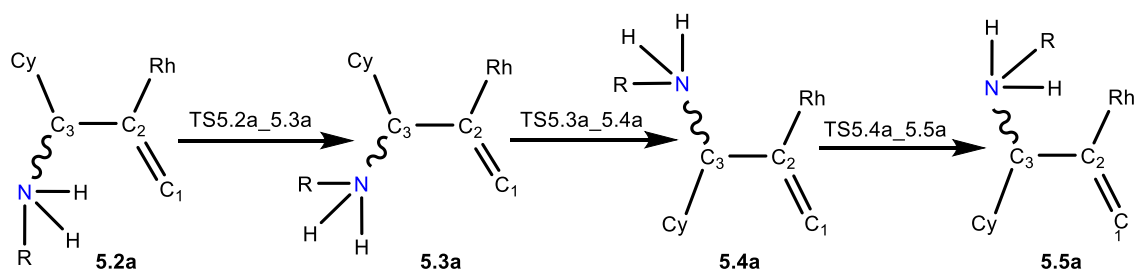
Figure 5.3: Optimized structure of transition states of alkene activation through a conformational change pathway starting with isomer **5.1a**. Relative Gibbs energy values are given under each structure in kcal/mol.

The *anti* nucleophilic attack of amine into the coordinated allene (**TS5.1a_5.2a**) has a Gibbs energy barrier of 24.1 kcal/mol (**Figure 5.2**, blue line), 10.9 kcal/mol lower in energy than the *syn* nucleophilic attack starting from the same intermediate (**5.1a**).

After the nucleophilic attack, a conformational change of the protonated amine is needed to place the amine close to rhodium in an appropriate manner to facilitate the subsequent

proton transfer to the metal center. This conformational change was found to take place in three steps. The first step is necessary in order to have the R group of the amine further away from the metal center to avoid steric hindrance during the conformational change of the amine, the second step is the conformational change of the amine and the third and last step is required to put back the R group of the amine to the initial relative position.

As it is shown in **Scheme 5.3**, the first step involves a change in the dihedral angle C₂-C₃-N-H (**TS5.2a_5.3a**) to yield complex **5.3a**, in the second step (**TS5.3a_5.4a**) the dihedral angle C₁-C₂-C₃-N changes, giving rise to complex **5.4a**, and the last step is again a change in the dihedral angle C₂-C₃-N-H (**TS5.4a_5.5a**) to yield complex **5.5a**. As explained in the following section, this final step is only needed when reaction starts from isomers **5.1b** and **5.1d**. In case of isomers **5.1a** and **5.1c**, the structure obtained from de IRC calculation of the transition state of the conformational change (**5.4**) and the initial intermediate of the metal center protonation step (**5.5**) are the same. Therefore, in the case of these two last isomers the conformational change only needs two steps (**TS5.2_5.3** and **TS5.3_5.4**).



Scheme 5.3: Conformational change of the protonated amine to allow proton transfer to the metal center.

The transition state of the second conformational change (**TS5.3a_5.4a**) has a relative Gibbs energy of 32.2 kcal/mol being the rate determining step for this pathway. From here the reaction evolves analogously to the *syn* nucleophilic addition pathway.

Once the N-H proton to be transferred has reached the right position, the next step is the metal center protonation that corresponds to a formal oxidation of rhodium from Rh(I) to Rh(III) to yield complex **5.6a**. The relative Gibbs energies of such transition state (**TS5.5a_5.6a**) and the complex formed (**5.6a**) are 21.3 kcal/mol and 16.8 kcal/mol respectively. Then, the reductive elimination takes place through **TS5.6a_5.7a** (19.2 kcal/mol) on this hydride complex giving rise to complex **5.7a** (-8.7 kcal/mol). Finally, in the last step the aminoalkene product is substituted by a new allene molecule to recover the catalyst and close the catalytic cycle. In case of *anti* attack, isomer **5.1a** yields the minor product (R enantiomer, **5.8a**).

c) *Anti* nucleophilic attack followed by protonation assisted by a second amine

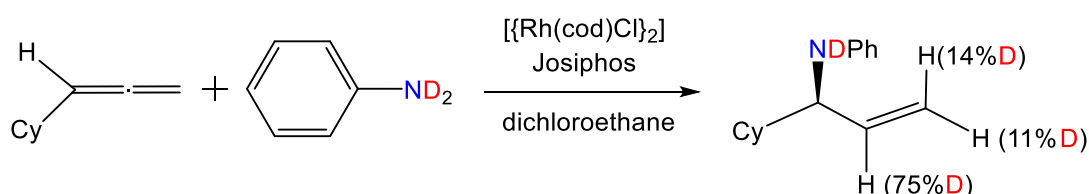
This mechanism starts with the same step as the previous one: the *anti* nucleophilic attack of amine into the coordinated double bond of the allene but it is finished by a proton transfer step assisted by a second amine molecule without participation of the metal center. It has already been demonstrated that a second amine molecule can assist the N-H to C proton transfer in the protonated amine intermediate.^{73,234}

The transition step of the *anti* nucleophilic attack step (**TS5.1a_5.2a**) has a relative Gibbs energy of 24.1 kcal/mol (**Figure 5.2**, green line). For the proton transfer step, two consecutive proton transfers were found: the first from the bonded amine to a second amine (**TS5.2a_5.9a**) to yield complex **5.9a** and the second one from the second amine to the carbon of the aminoalkyl (**TS5.9a_5.10a**) giving rise to complex **5.10a**. The Gibbs energies of the transition states and intermediates involved in this proton transfer step (**TS5.2a_5.9a**, **5.9a** and **TS5.9a_5.10a**) are 25.4, 27.3 and 37.3 kcal/mol respectively. Finally, like in the other evaluated mechanism, an exchange of aminoalkene compound by an allene molecule is required to recover the catalyst and close the catalytic cycle obtaining the R enantiomer (**5.8a**).

Comparing the three proposed pathways evaluated, the lowest energy pathway is the *anti* nucleophilic attack followed by a conformational change of the amine to allow metal center protonation and a reductive elimination steps (**Figure 5.2**, blue line). The highest barrier in this pathway corresponds to the conformational change (**TS5.3a_5.4a**, 32.2 kcal/mol).

5.3.3 Isotopic labeling experiments

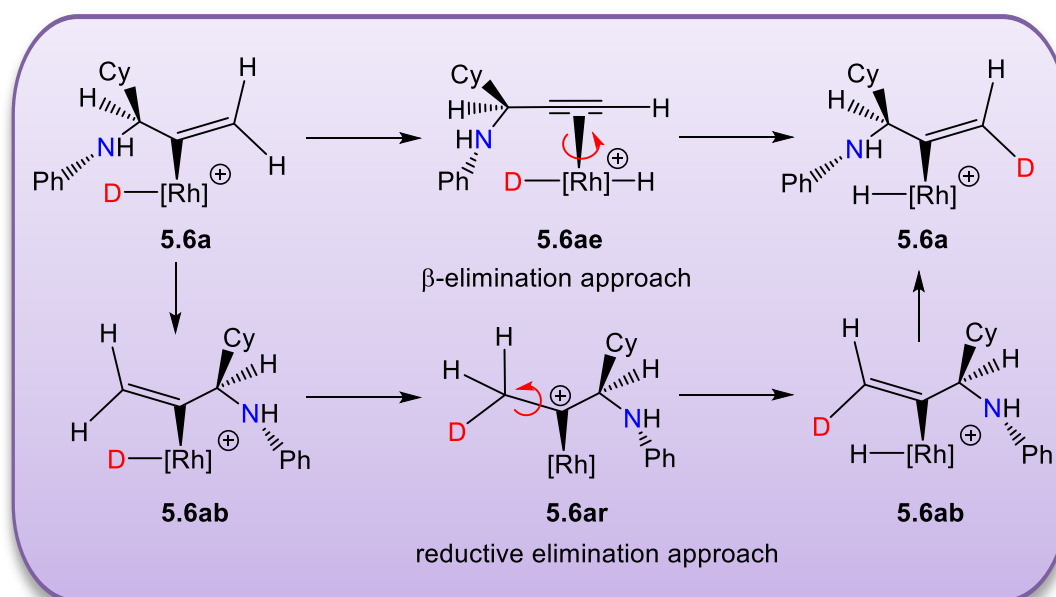
Isotopic labeling experiments were carried out for the hydroamination reaction of allenes using [D₇]-aniline as amine by Breit et al.¹²² Deuterium incorporation is observed not only in the central carbon but also in the terminal carbon of the allene. About 75% of deuterium incorporation is observed in the central carbon of the allene and about 15% of deuterium incorporation is observed over both positions of the terminal carbon of the allene (the one that is not involved in the nucleophilic addition step). The percentage of deuterium incorporation varies depending on the solvent used. The isotopic labeling experiments using dichloroethane as solvent are summarized in **Scheme 5.4**.



Scheme 5.4: Results obtained in the isotopic labeling experiments carried out by Breit et al. (reference 122).

The most plausible hydroamination mechanism obtained in the previous section consists in an *anti* nucleophilic attack followed by a conformational change of the amine to allow a metal center protonation and a reductive elimination step. Such proposed mechanism does not explain the abovementioned deuterium experiments; according to the proposed mechanism a 100 % of deuterium incorporation over the central carbon of the allene should be observed (the deuterium atom of the amine is transferred to the metal center and from here to the carbon atom by a reductive elimination step).

To explore competing side reactions which should take place during the catalytic cycle to explain the isotopic labeling experiments, two different alternatives were evaluated (**Scheme 5.5** and **Scheme 5.6**, respectively). The first alternative consists in an intramolecular pathway right after the formation of the Rh-D intermediate (**5.6a**). The other alternative is an intermolecular pathway involving a deuterated amine (ND_3Ph^+). This second pathway can take place at two different stages of the reaction: at the beginning of the reaction (**5.1a**), or just before proton transfer to Rh center (**5.5a**). All of them are side reactions out of the catalytic cycle. The energy profiles obtained are summarized in **Figure 5.4**.

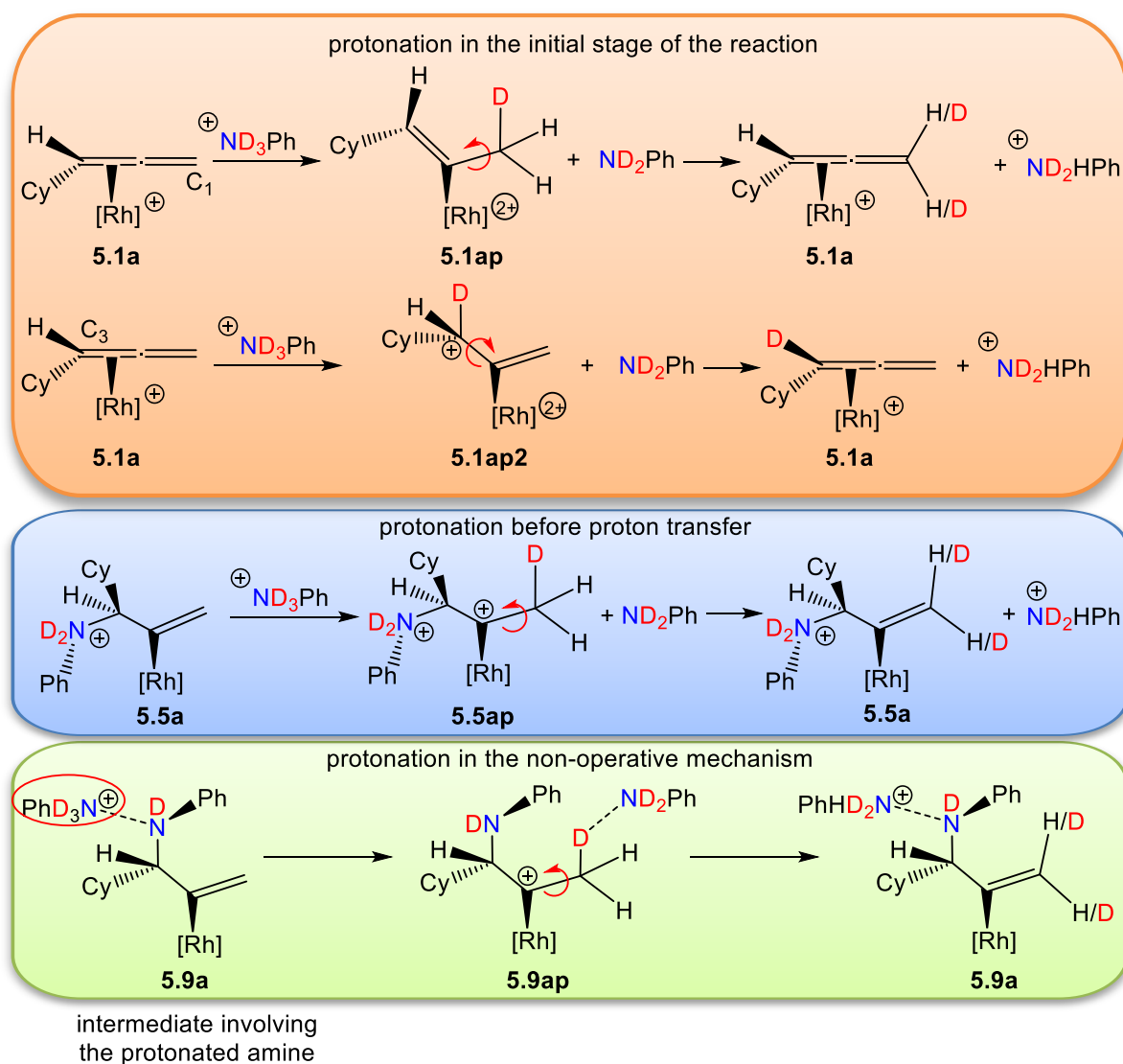


Scheme 5.5: β -elimination and reductive elimination reactions analyzed to explain the isotopic labeling experiments (intramolecular pathway).

Two different intramolecular pathways from intermediate **5.6a** were evaluated. The first approach consists in a β -elimination from the hydride intermediate formed after the metal center protonation step (**5.6a**), generating intermediate **5.6ae** (**Scheme 5.5**). To regenerate intermediate **5.6a** the insertion of the alkyne ligand into the Rh-D is needed. In such a way a deuterium could be incorporated at the terminal carbon atom of allene (C_1).

The second intramolecular approach consists in performing first a reductive elimination step from intermediate **5.6a**. A rotation of the alkenyl moiety places the alkene and the deuterium in the same side of the molecule (intermediate **5.6ab**, **Scheme 5.5**). Then it takes place the reductive elimination step to yield an alkenyl moiety where the sp^3 carbon formed can rotate. The reverse reaction, a β -hydrogen elimination, forms the hydride intermediate and the deuterium remains in the terminal carbon of the allene. Finally a rotation is necessary again to obtain structure **5.6a** in order to proceed with the catalytic cycle of hydroamination reaction.

The intermolecular approach consists in protonating the terminal carbon of the allene by a protonated amine (ND_3Ph^+). Such species is accessible as previously showed in **Section 5.3.2**. It is generated in the proton transfer step involving a second amine (intermediate **5.9a**, 27.3 kcal/mol). This intermediate is depicted in **Scheme 5.6**.



Scheme 5.6: Competing side reactions analyzed to explain the isotopic labeling experiments (intermolecular pathway).

The protonation was studied at two different stages of the reaction: in the initial point of the reaction (intermediate **5.1a**), and at the intermediate formed after the nucleophilic addition and the conformational change (intermediate **5.5a**). In both cases a two positively charged species can be formed (intermediates **5.1ap** and **5.5ap**, respectively). A sp^3 carbon is formed by deuterium addition. The reverse reaction regenerates the initial structure but with a deuterium incorporated at the terminal carbon of the allene.

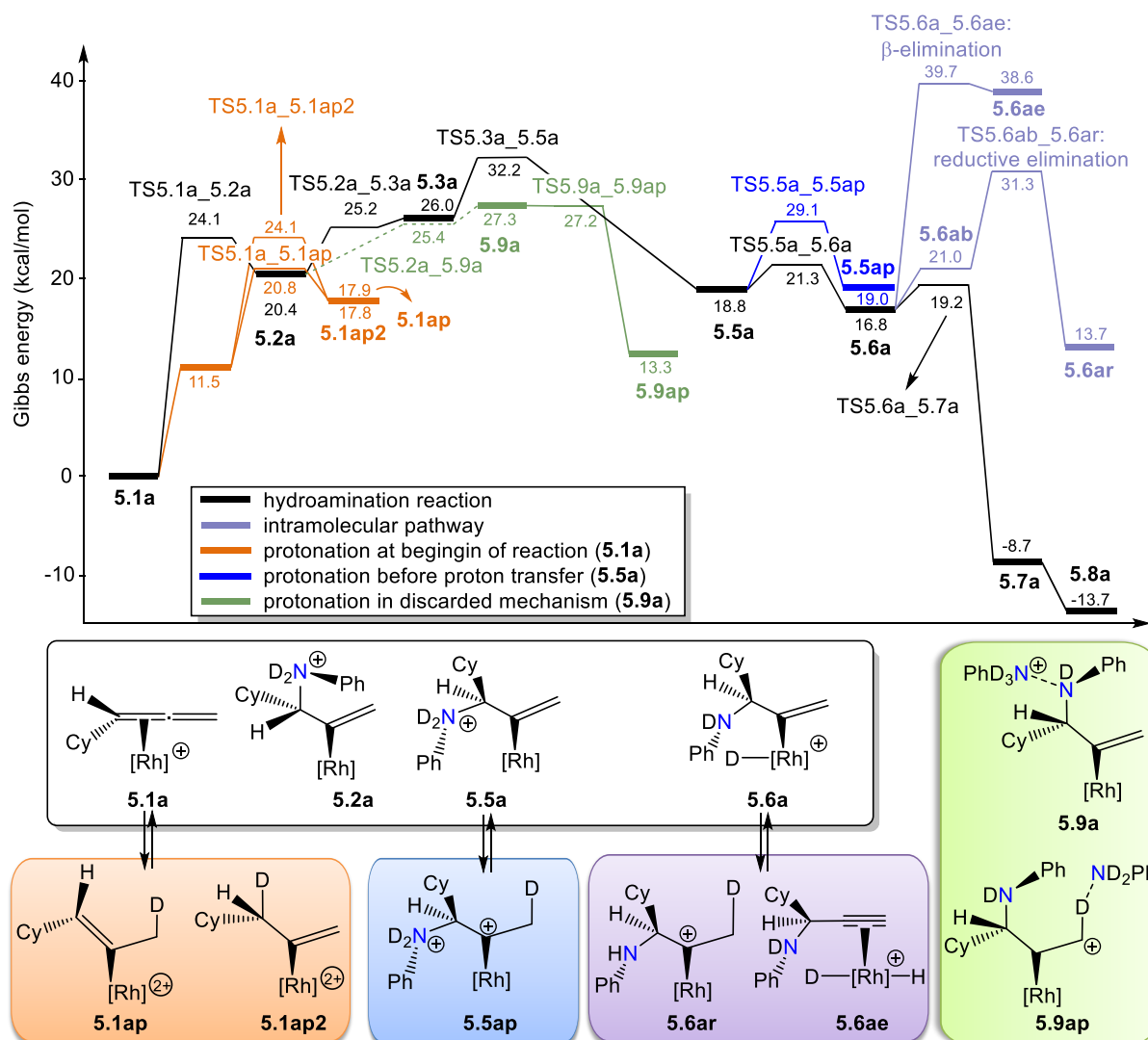


Figure 5.4: Complete Gibbs energy profiles for the competing side reactions studied to explain the isotopic labeling experiments carried out by Breit et al.¹²²

The protonation of the allene was also studied with a mechanism previously discarded for hydroamination process. This pathway has been discarded regarding the obtaining of hydroamination product due to the protonation of the carbon atom requires 37.3 kcal/mol. However the previous deprotonation of amine yielding intermediate **5.9a** is feasible and could be account in the deuterium exchange process. All this reactions are collected in **Scheme 5.6** and the profiles obtained depicted in **Figure 5.4**.

In the intramolecular approach (**Figure 5.4**, purple line), the β -elimination from intermediate **5.6a** giving rise to a dihydride complex and an alkyne (**5.6ae**), requires a relative Gibbs energy of 39.7 kcal/mol (20.5 kcal/mol higher than the reductive elimination step which yields the reaction product). The reductive elimination step over the terminal carbon atom of the allene (**TS5.6a_5.6ar**) has a Gibbs energy of 31.3 kcal/mol (12.1 kcal/mol higher in energy than the reductive elimination step over the central carbon of the allene). The energy required in both pathways are too high to be a feasible competing side reaction, mainly because the pathway from intermediate **5.6a** evolving to the formation of the hydroamination product has a relative Gibbs energy barrier of 2.4 kcal/mol (**Figure 5.4**, black line).

Regarding to the protonation approaches (intermolecular pathway), in all cases it is necessary a protonated amine. The formation of such species was previously calculated in **Section 5.3.2** with a relative Gibbs energy of 27.3 kcal/mol. Thus, the presence of such species is feasible if one looks at the overall reaction profile (RDS is 32.2 kcal/mol, see **Figure 5.4**, black line).

From the initial stage of the reaction (**5.1a**; **Figure 5.4**, orange line), the protonation of the terminal carbon atom of allene (C_1 , the one not involved in the nucleophilic addition step carbon) has a Gibbs barrier energy of 20.8 kcal/mol. This step gives rise to intermediate **5.1ap**, located at 17.9 kcal/mol being a reversible step. The protonation of the other carbon atom of the allene (internal carbon $-C_3-$; the one involved in the nucleophilic attack step) has a Gibbs barrier of 24.1 kcal/mol, significantly higher. After this step intermediate **5.1ap2** is formed. This reaction can explain the deuterium incorporation at all position of the alkene coordinated to metal center. This is a side reaction out of the catalytic cycle. The protonation of the intermediate **5.5a** (formed after the nucleophilic addition and consecutive conformational change) requires a Gibbs energy of 29.1 kcal/mol (**Figure 5.4**, blue line).

Regarding the mechanism consisted in the proton transfer assisted by a second amine (**Figure 5.4**, green line), the protonation of the terminal carbon atom in the intermediate **5.9a** is practically a barrierless process, since the transition state has almost the same energy than the intermediate, so this competing side pathway could also explain the deuterium incorporation observed in the isotopic labeling experiments.

5.3.4 Study of the regioselectivity in the nucleophilic addition.

The coordination of allene to the catalyst generates 8 different isomers (**5.1a-h**) and in each isomer the nucleophilic attack of amine can occur in both carbons of the coordinated alkene (the central carbon, C_2 , and the internal carbon, C_3), so there are 16 possibilities for the nucleophilic attack of amine into the allene. This section is devoted to study the regioselectivity observed during this reaction. Only the *anti* nucleophilic attack was considered since it is the one that requires less energy.

The experimentally observed reaction product is obtained when the nucleophilic attack occurs over the internal carbon (C_3). When the reaction starts with the first four isomers (isomers **5.1a-d**) this carbon atom is activated by the coordination to the metal center, but when the reaction starts with the isomers **5.1e-h** this carbon is the non-coordinated carbon atom.

The transition states of the nucleophilic attack step of the amine over both carbon atoms of the coordinated double bond of the allene were calculated for the 8 isomers (**5.1a-h**). The addition of the amine to the non-coordinated carbon atom (C_3) was analyzed in isomers **5.1e-h**. The relative Gibbs energies obtained are summarized in **Table 5.1**. The results obtained show that the nucleophilic attack has lower energy when it happens over the internal carbon atom (C_3) in isomers where the allene is bonded to its internal double bond (**5.1a-d**).

Table 5.1: Gibbs energies of transition state of nucleophilic attack over different carbon atoms in each isomer (in kcal/mol). $[Rh]^* = [RhJosiphos]^+$

Isomer		Isomer			
		5.1a	5.1b	5.1c	5.1d
Central: C_2 (sp)		27.6	25.8	27.8	25.4
Internal: C_3 (sp^2)		24.1	25.6	24.3	22.7
Isomer		Isomer			
		5.1e	5.1f	5.1g	5.1h
Central: C_2 (sp)		-	29.6	32.4	-
Terminal: C_1 (sp^2)		31.1	30.0	32.1	27.9
Internal (Non-coordinated): C_3		34.8	38.7		35.5

When the transition state of the nucleophilic addition of dimethylamine to the non-coordinated carbon of the allene was analyzed, we found that the energy is always much

higher than in the case of the nucleophilic attack over the coordinated carbon. The nucleophilic attack over the internal carbon (C_3) of the coordinated double bond in isomers **5.1a-d** were considered for the study of enantioselectivity in this reaction.

As pointed out in **Chapter 4, (Section 4.3.3.3)**, devoted to the hydroamination of alkenes catalyzed by rhodium complexes, the regioselectivity can be related with some structural parameters and with the LUMO's shape of the coordinated alkene: the carbon which is prone towards the nucleophilic addition has a major contribution on the LUMO of the complex. In order to show if the hydroamination of allenes also follows this approach, we computed the LUMO and LUMO +1 orbitals for the four isomers of the coordinated allene (compounds **5.1a-d**). We tried to relate the shape of the LUMO orbital with the regioselectivity observed. In **Figure 5.5** are plotted the LUMO and LUMO +1 orbitals of the most stable isomer of coordinated allene (compound **5.1a**).

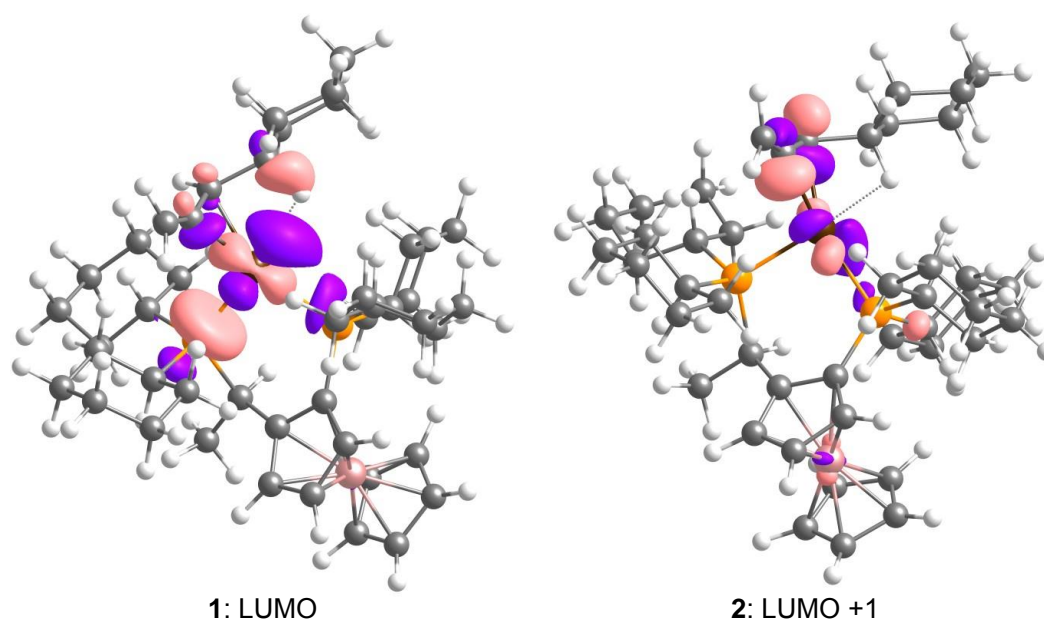


Figure 5.5: Representation of (1) LUMO and (2) LUMO +1 of most stable isomer of the coordinated allene (compound **5.1a**).

The LUMO of compound **5.1a** has a very small contribution from both carbons of the coordinated double bond of the allene (it is mainly a d orbital from rhodium), whereas the LUMO +1 orbital has a significant contribution from those carbons, being higher the contribution of the internal carbon (C_3) than the contribution of the central carbon of the allene (C_2). The LUMO and LUMO+1 orbitals for the other three isomers of coordinated allene were also analyzed (compounds **5.1b-d**). In all cases, the shapes of the orbitals were similar to those observed for compound **5.1a**.

According with the idea that the carbon which has a major contribution on the LUMO orbital is going to be prone towards the nucleophilic addition, in this case, the nucleophilic addition should take place over the internal carbon (C_3). This fact is in agreement with the calculated

Gibbs energies of the transition state of the nucleophilic addition, which are summarized in **Table 5.1**.

5.3.5 Study of the origin of the enantioselectivity

According to the aforementioned study over isomer **5.1a**, the most plausible mechanism goes through the *anti* nucleophilic attack of amine into the internal carbon atom (C₃) of the coordinated allene followed by the conformational change of amine that allow a metal center protonation step. In this section we extend the study of this mechanism to all initial isomers that that may be relevant to the process (isomers **5.1a-d**).

Nucleophilic addition of amine to isomers **5.1a** and **5.1c** gives rise to the R enantiomer (**Figure 5.6**, dashed line), whereas the addition to isomers **5.1b** and **5.1d** produces the S enantiomer (**Figure 5.6**, continuous line). When this reaction was carried out experimentally, the S enantiomer was obtained with an 84% enantiomeric excess. In this section the reaction starting with the four isomers is studied, with the aim to explain the enantioselectivity obtained experimentally.

5.3.5.1 Computational study of the reaction pathway for all the isomers

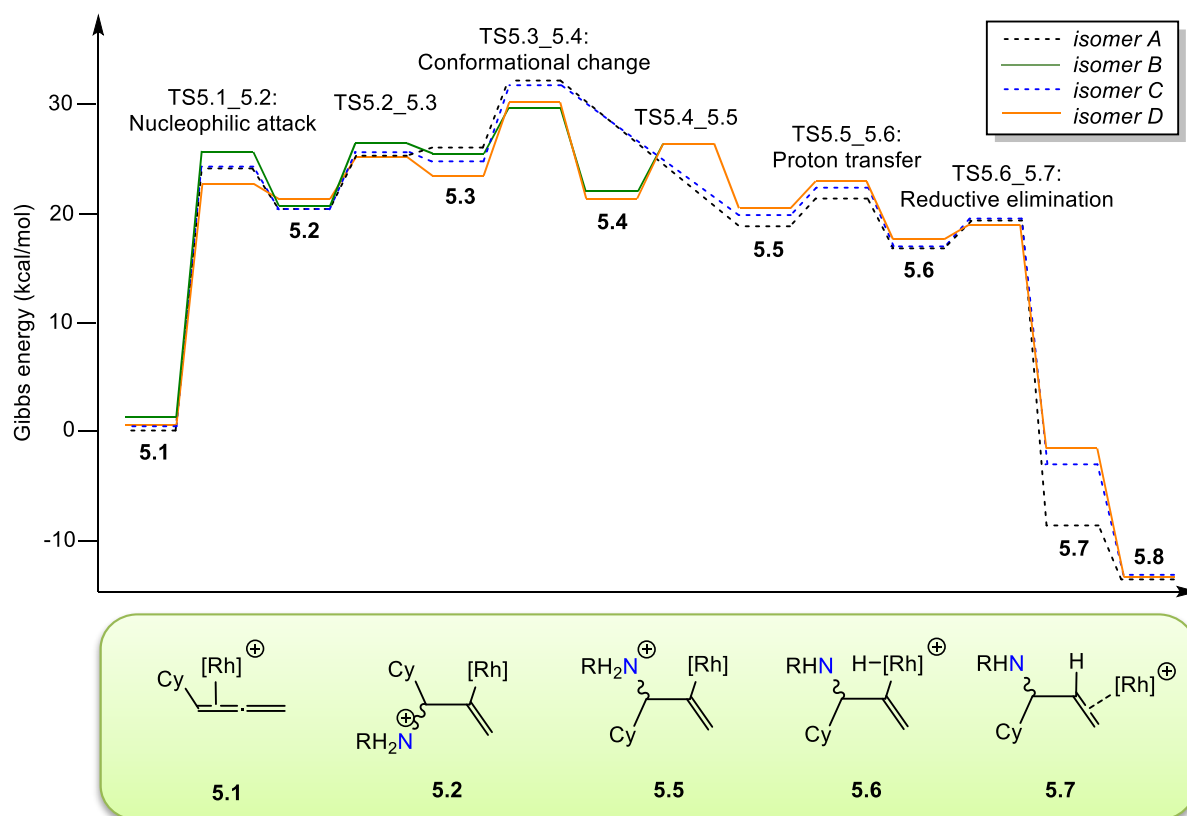
The most stable isomer results from the coordination of allene (isomer **5.1a**) has been chosen as the zero energy point. All energies presented in this section are referenced to this compound. The first step is the nucleophilic attack of amine into the coordinated double bond of the allene to yield complexes **5.2a-d**. The relative Gibbs energies of the transition states for this step are 24.1, 25.6, 24.3 and 22.7 kcal/mol in case of isomers **a-d**, respectively. The nucleophilic addition starting with isomer **5.1d** is the one that requires less energy whereas the highest energy corresponds to addition to isomer **5.1b**. In both cases the S enantiomer is going to be obtained, which is the enantiomer obtained as the major product when the reaction is carried out experimentally.

For the nucleophilic addition step, the distance of the forming C-N bond varies from 1.90 Å to 1.99 Å depending on the isomer. In this step square-planar intermediates with an empty site around the metal are formed (**5.2a-d**). In all cases, the phenyl ring of amine is placed at the opposite side of the cyclohexyl group of the allene. The energies of intermediates **5.2a-d** are 20.4, 20.6, 20.4 and 21.3 kcal/mol respectively. The reaction profile of the enantioselective hydroamination of allenes catalyzed by a cationic rhodium complex is shown in **Figure 5.6** and the values of Gibbs energy of the full catalytic cycle for each structure are collected in **Table 5.2**.

Table 5.2: Relative Gibbs energies of the hydroamination of allenes through an alkene activation mechanism. All values are in kcal/mol at 298 K.

Isomer	a	b	c	d
5.1	0.0	1.2	0.4	0.5
TS5.1_5.2	24.1	25.6	24.3	22.7
5.2	20.4	20.6	20.4	21.3
TS5.2_5.3	25.2	26.4 ¹	25.6	25.1
5.3	26.0	25.4	24.7	23.4
TS5.3_5.4	32.2	29.7	31.8	30.2
5.4	*	22.0	*	21.4
TS5.4_5.5	*	26.3 ²	*	26.3
5.5	18.8		19.8	20.5
TS5.5_5.6	21.3		22.3	22.9
5.6	16.8		16.9	17.6
TS5.6_5.7	19.2		19.5	18.9
5.7	-8.7		-3.1	-1.6
5.8	-13.7		-13.3	-13.5

* Intermediate **5.5** is directly obtained from **TS5.3_5.4**/ ¹ two negative frequencies (-46.16 and -26.54)/ ² from this TS the reaction finish as isomer **d**

**Figure 5.6:** Complete energy profile for hydroamination of allenes.

Regarding the last part of the reaction, in the previous section it was concluded that the most plausible mechanism for the hydroamination reaction consists of a nucleophilic attack step followed by a proton transfer step through the metal center. For this reason, to enable the proton transfer through the metal center, the hydrogen of the amine group has to be properly located to migrate to the metal center. This step (conformational change of amine) is the step that requires the highest Gibbs energy (rate determining step). Relative Gibbs energies of the species involved in this step are collected in **Table 5.2**.

The energy for this transition state was calculated as 32.2, 29.7, 31.8 and 30.2 kcal/mol for isomers **a-d**, respectively. The values of the dihedral angle C₁-C₂-C₃-N in this transition state are different depending on the isomer, being positive in case of reaction starting with isomers **5.1b** and **5.1d** and negative in case the reaction starts with isomers **5.1a** and **5.1c**. In **Table 5.3** are collected the dihedral angles C₁-C₂-C₃-N in transition states for each isomer.

Trying to understand the origin of the enantioselectivity we will study in more detail in the next subsection the transition state of the conformational change of amine, which is the rate determining step of this reaction.

Table 5.3: Value of dihedral angles C₁-C₂-C₃-N for conformational change of amine

Isomer	5.2	TS5.3_5.4	5.5	ΔG^\ddagger (kcal/mol)
a	-19.1	-80.76	163.0	32.2 (R)
b	16.7	92.30	-158.0	29.7 (S)
c	-21.1	-85.96	153.2	31.8 (R)
d	17.3	106.29	-162.6	30.2 (S)

The transition state for the conformational change of the amine requires the lowest energy when reaction starts from intermediate **5.1b**, which yields the experimentally observed major enantiomer (S). The ordering for the transition states involving the other isomers is **5.1b** > **5.1d** > **5.1c** > **5.1a**.

After the conformational change, a proton is transferred from the protonated amine to the metal center. The forming Rh-H bond distances in the proton transfer transition states vary from 1.64 Å to 1.66 Å and the N-H breaking bond distances vary from 1.49 to 1.51 Å, depending on the isomer. This step is a formal oxidation of rhodium from Rh(I) to Rh(III). In intermediates **5.6a-d** the metal has a T-shape geometry and the Rh-H bond is shortened to about 1.52 Å, due its does not have a trans ligand.

Then, the C-H reductive elimination takes place (**TS5.6_5.7**). In **Table 5.2** are collected the relative Gibbs energies for all isomers. The breaking Rh-H bond distances in this transition state is 1.57 Å and the Rh-C bond distance is 2.02 Å in all isomers whereas the forming C-H bond distances vary from 1.64 Å to 1.71 Å depending on the isomer. These transition states yields complexes **5.7a-d** with a C-H bond distance about 2.1 Å. In this intermediate the

organic amine product is bonded to rhodium by the coordination of the double carbon-carbon bond. Finally, the last step is the exchange of the alkylamine product for an allene molecule to recover the catalyst.

5.3.5.2 Structural analysis of RDS transition states

The rate determining step (RDS) of this reaction is the conformational change of the amine. This section is devoted to further analyze this step in order to get insight on the origin of the enantioselectivity. This conformational change is depicted in **Scheme 5.3** and the optimized structures of **TS5.3_5.4** for the different isomers (**a-d**) are represented in **Figure 5.7**.

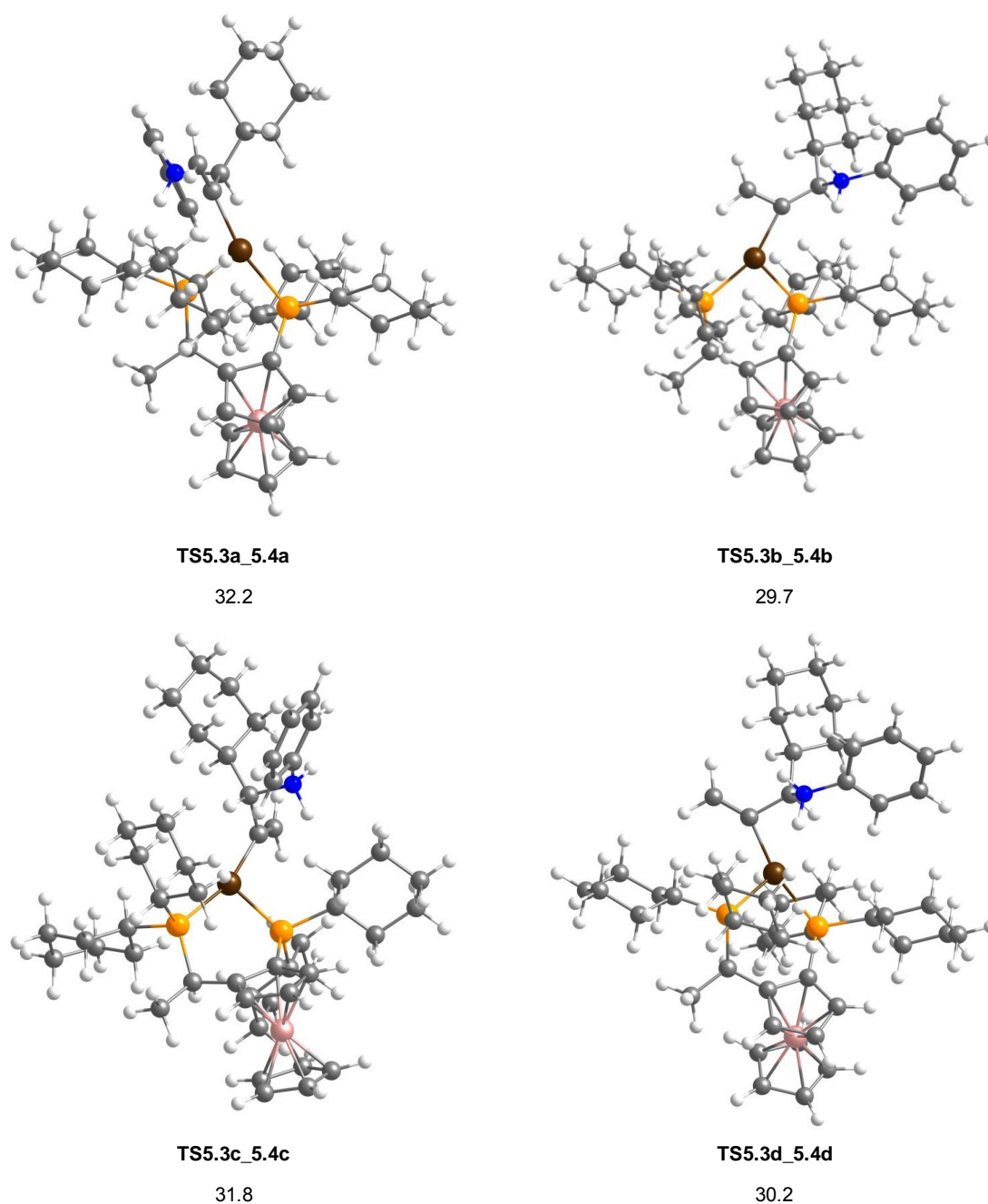
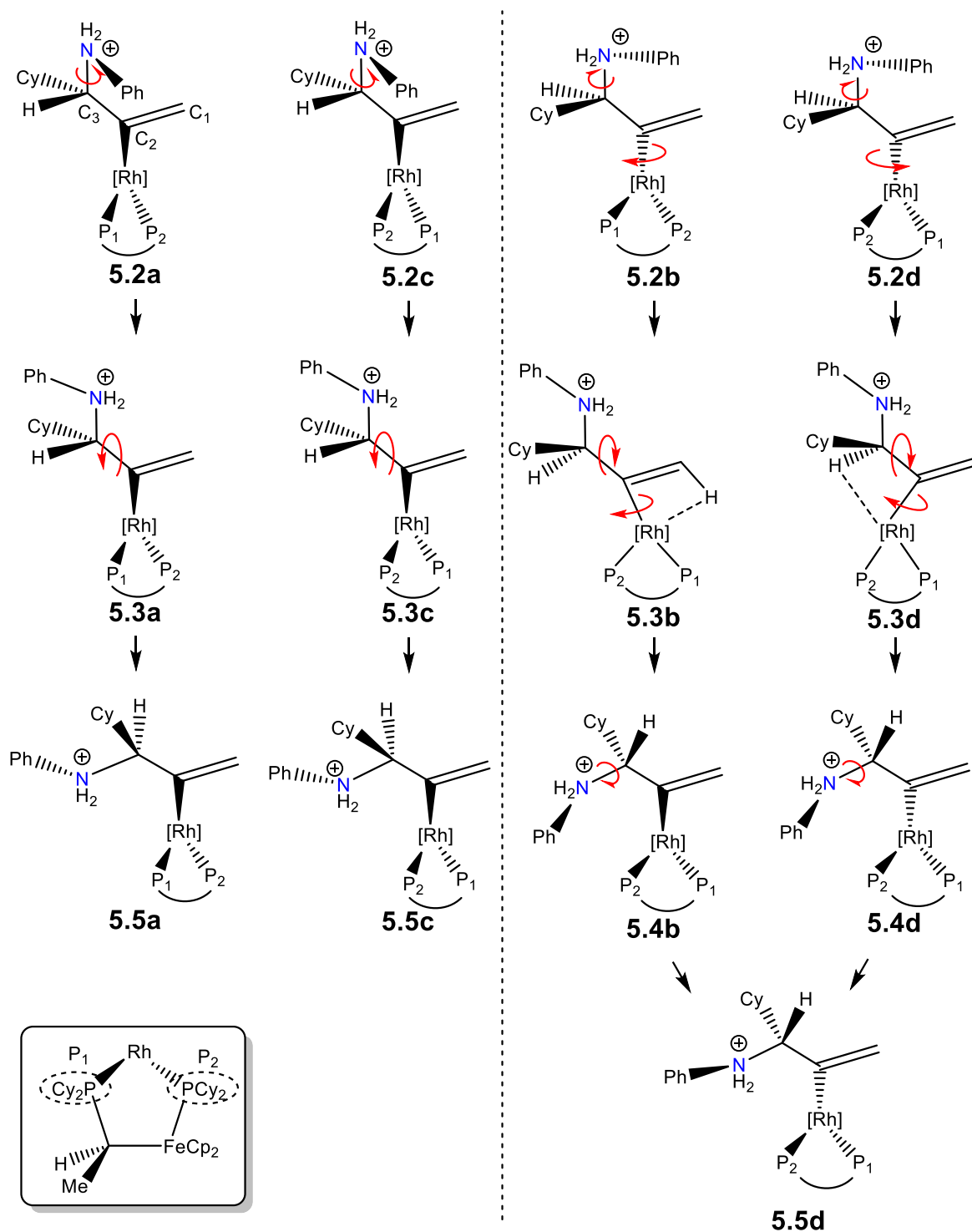


Figure 5.7: Optimized structure of transition states **TS5.3_5.4** in the different isomers. Relative Gibbs energy values are given under each structure in kcal/mol.

During the structural analysis of intermediates and transition states of the conformational change of the amine (**TS5.3_5.4**) some differences between isomers **a** and **c** (yielding R enantiomer) and isomers **b** and **d** (yielding S enantiomer) were found. Most of them are summarized in **Scheme 5.7**. Relative Gibbs energy values are given under each structure in kcal/mol.



Scheme 5.7: Structural analysis of conformational change of amine. Isomers **a** and **c** (enantiomer R) are depicted in left and **b** and **d** (enantiomer S) in right.

In all cases conformational changes of amine take place by the rotation of the internal carbon (C_3) of allene (through C_2-C_3) by the side where the phenyl group of the amine is placed. The phenyl group of amine is always placed in the opposite side of the cyclohexyl group of allene. As a consequence, in case of isomers **a** and **c** such rotation takes place in the opposite direction than for isomers **b** and **d**. This fact can be observed by analyzing the sign of the dihedral angles presented in the transition state of such rotation (see **Table 5.3**) and is depicted in **Scheme 5.7**.

We also found that only for isomers **b** and **d** the “allene” ligand is rotated and in both cases the internal carbon of allene (C_3) is placed over the phosphine which contains the ferrocene group (represented as P_2 in **Scheme 5.7**). It means that it is necessary to rotate the allene as well as the amine in the transition state which takes place just before this one (**TS5.2_5.3**). In case of isomers **a** and **c**, in this transition state only occurs the rotation of the amine. This can be seen in **Scheme 5.7** where both phosphines are in the same plane than the allene for isomers **b** and **d** but it is not for isomers **a** and **c**.

The last difference we found related with transition states of the conformational change, is that in case of isomers **b** and **d** a third transition state it is necessary to complete the conformational change whereas for isomers **a** and **c** after the transition state **TS5.3_5.4** the compound **5.5** is directly obtained.

During the study of this transition state we also found that for isomer **b** the compound obtained after conformational change (intermediate **5.5b**) is the same that the intermediate obtained when the reaction starts with isomer **d** (**5.5d**), due to the allene has rotated in the opposite direction that in case of isomer **d**. The transition states to obtain the structure expected starting from the compound **5.1b** cannot be optimized despite of computational efforts, all the attempts ended up obtaining the same intermediate than in the reaction starting from isomer **5.1d**; from this point on both pathways converge.

In order to get more information about the origin of the enantioselectivity, the transition state for the conformational change of the amine was studied in more detail, using the nciplot software. The nciplot software qualitatively describes the attractive and repulsive non-covalent forces present in the structure, based on the analysis of the electron density.^{265,266} The plots obtained with nciplot software for the transition state of the conformational change of the amine (**TS5.3_5.4**) for the four isomers considered are depicted in **Figure 5.8**.

In nciplot, the surfaces are colored on a blue-green-red scale according to values of $(\lambda_2)\rho$, ranging from -0.04 to 0.02 au. Bonding interactions can be identified by sign of the λ_2 eigenvalue of the electron-density Hessian. This eigenvalue is negative when there is a bonding interaction and is positive if atoms are non-bonded. Accordingly, blue indicates strong attractive interactions, and red indicates strong non-bonded overlap.

Analyzing the plots obtained, some differences were found between isomers **a** and **c** (where the R enantiomer is obtained) and isomers **b** and **d** (where the S enantiomer is obtained).

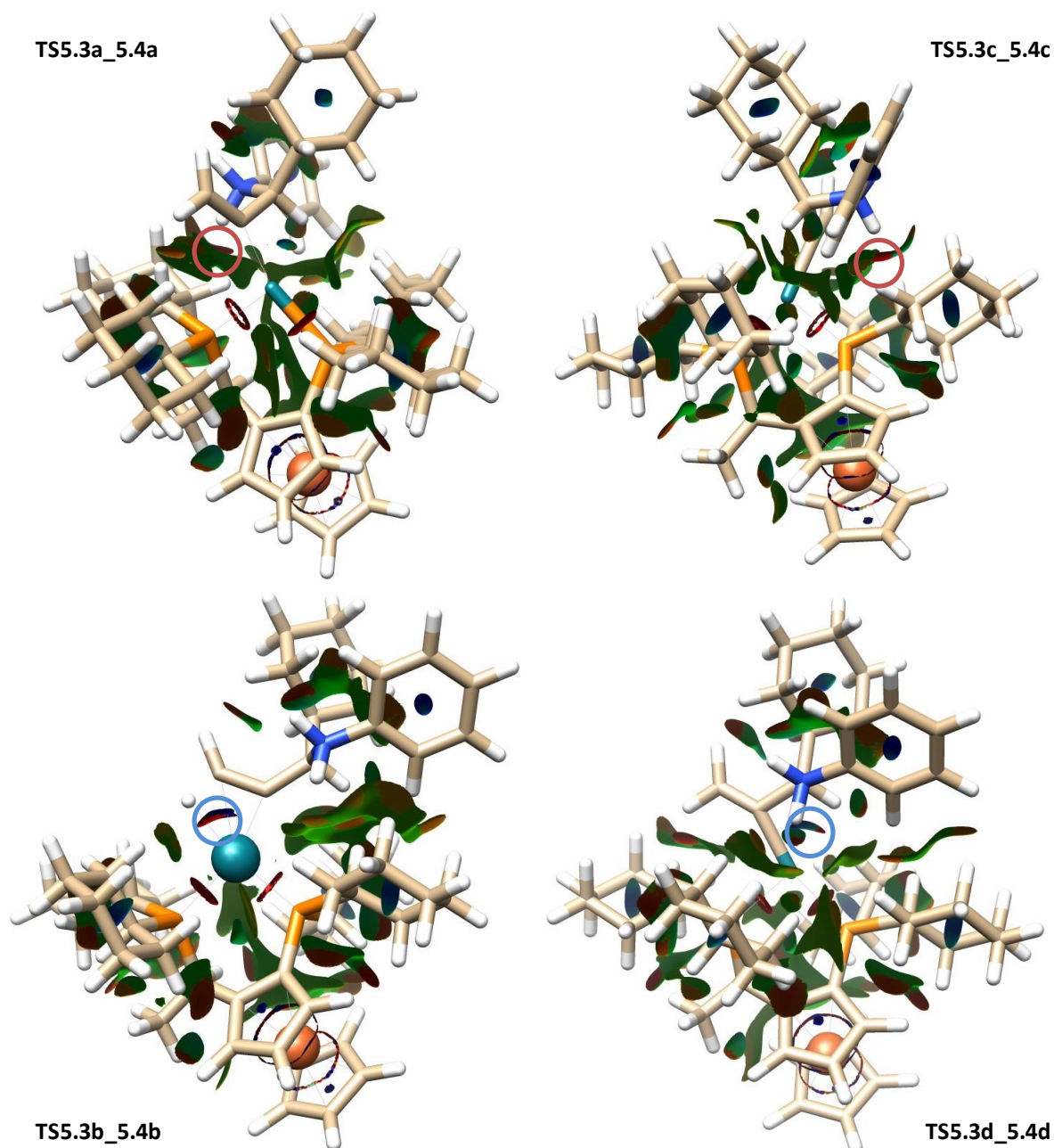


Figure 5.8: Non-covalent interactions presented in the different transition states for the conformational change of the amine (**TS5.3_5.4**) obtained with nciplot software.

The first difference is that in isomers **a** and **c** there is a repulsive interaction between one of the hydrogens of the amine and a hydrogen of one cyclohexyl group of the phosphine of the Josiphos ligand, whereas this repulsive interaction is not present in isomers **b** and **d** (**Figure 5.8**, red circles). The second difference is that in isomer **b** and **d** there is a blue plotted interaction between one hydrogen of the allene (from terminal carbon -C₁- in case of isomer

b and from the central carbon -C₂- in case of isomer **d**, but this blue-plotted interaction is almost inappreciable) and the metal center (**Figure 5.8**, blue circles). In case of isomers **a** and **c** this kind of attractive interactions which correspond with agostic interactions can not be found. The Rh-H distances in such transition state are 2.539 and 2.544 Å for isomers **a** and **c** respectively and 2.028 and 2.332 Å for isomers **b** and **d**, respectively, confirming this agostic interaction in the last two isomers, stronger for isomer **b**. This agostic interaction is also reflected in the C-H bond distances which are 1.105 and 1.106 Å for isomers **a** and **c** and 1.135 and 1.118 Å for isomers **b** and **d** respectively. However, this agostic interaction is also present for both isomers in the intermediate before the conformational change step, therefore it can not be the responsible the difference in energy between transition states of isomers **b** and **d** and isomers **a** and **c**.

In order to get a deeper insight about the origin of the enantioselectivity, the structures of transition states of conformational change of the amine were studied by means of an energy decomposition analysis (EDA) trying to relate the structural differences between such transition states for different isomers with their energy components. As mentioned in **Chapter 4**, the bond energy between two interacting fragments (ΔE) is divided into two components: the preparation energy (ΔE_{prep}) and the interaction energy (ΔE_{int}).

$$\Delta E = \Delta E_{prep} + \Delta E_{int} = (\Delta E_{prep f1} + \Delta E_{prep f2}) + \Delta E_{int} \quad [5.7]$$

The interaction energy between the two fragments is divided into three different contributions: the Pauli energy, the electrostatic interaction and the orbital interaction.^{256,267} The sum of the two first contributions results in the steric interaction.

$$E_{int} = \Delta E_{Pauli} + \text{Electrostatic} + \text{Orbital} = \text{Steric} + \text{Orbital} \quad [5.8]$$

This energies are calculated by means of energy decomposition analysis, (EDA), also called activation strain model.²⁵⁶ The structure of the transition state was decomposed in two fragments considering the allene bonded to the amine as one fragment (fragment 1) and the catalyst with Josiphos ligand as another fragment (fragment 2). For analyzing the transition state of this step (conformational change), the interaction energies are evaluated in comparison between the transition state and the precedent intermediate. The intermediate selected was the formed just after the nucleophilic addition (**5.2**); the interaction energies (Pauli, electrostatic, orbital and steric interactions) were calculated comparing to this intermediate. The interaction energies in the transition state **TS5.3_5.4** and their differences between the transition state and the corresponding intermediate **5.2** are collected in **Table 5.4**. The preparation energies (ΔE_{prep} , $\Delta E_{prep f1}$ and $\Delta E_{prep f2}$) required to distort the fragments from the stable structure they have in intermediate **5.2** to those in the transition state were also calculated. According with equation [5.7], the sum of total preparation energy and total interaction energy gives the total bond interaction energy. The preparation energies and the total bond energies in the process from intermediate **5.2** to the corresponding transition state are collected in **Table 5.5**.

Table 5.4: Interaction energies obtained for **TS5.3_5.4** and differences of interaction energies in such transition state and those in intermediate **5.2**. Fragments are shown in **Figure 5.9**.

TS5.3_5.4	ΔE_{Pauli}	Electrostatic interaction	Steric interaction	Orbital interaction	Total interaction energy (E_{int})	Relative Gibbs energy
Isomer a	197.92	-194.14	3.78	-84.35	-80.57	32.2
Isomer b	185.50	-170.95	14.55	-98.73	-84.18	29.7
Isomer c	193.31	-190.64	2.67	-83.46	-80.79	31.8
Isomer d	213.66	-205.83	7.83	-90.53	-82.70	30.2
Difference TS5.3_5.4 and 5.2	Difference in ΔE_{Pauli}	Difference in Electrostatic interaction	Difference in Steric interaction	Difference in Orbital interaction	Difference in Total interaction energy (ΔE_{int})	Gibbs energy barrier (from 5.2)
Isomer a	13.3	-10.2	3.1	-6.7	-3.6	11.8
Isomer b	3.6	11.7	15.3	-22.3	-7.0	9.1
Isomer c	12.9	-9.0	3.9	-7.3	-3.4	11.4
Isomer d	26.2	-22.0	7.2	-12.2	-5.0	8.9

Table 5.5: Preparation energy from intermediate after nucleophilic attack (**5.2**) to transition state of conformational change (**TS5.3_5.4**) and total bonding energy.

	Preparation energy fragment 1 ($\Delta E_{\text{prep f1}}$)	Preparation energy fragment 2 ($\Delta E_{\text{prep f2}}$)	Total preparation energy (ΔE_{prep})	Total bonding energy (ΔE)	Gibbs energy barrier (from 5.2)
Isomer a	9.0	1.5	10.5	6.9	11.8
Isomer b	10.5	-0.6	9.9	2.9	9.1
Isomer c	8.6	1.6	10.2	6.8	11.4
Isomer d	7.3	-0.2	7.2	2.1	8.9

As we can see in **Table 5.5**, the total preparation energies are very similar to the Gibbs energy barrier of transition state for conformational change. In addition, the deformation energy of fragment 2 for isomers **b** and **d** yielding enantiomer S have a negative preparation energy for fragment 2 whereas such energy is positive for isomers **a** and **c** yielding enantiomer R.

We try to correlate the different interactions obtained for the transition state of conformational change with the Gibbs energy of such transition state. A correlation between the Gibbs energy of the total interaction energies of the transition state was found. This correlation is also observed for the steric and orbital interactions. The Gibbs

energy of the transition state increases when the steric interaction decreases and the orbital interaction increases. This correlation is shown in **Figure 5.9**.

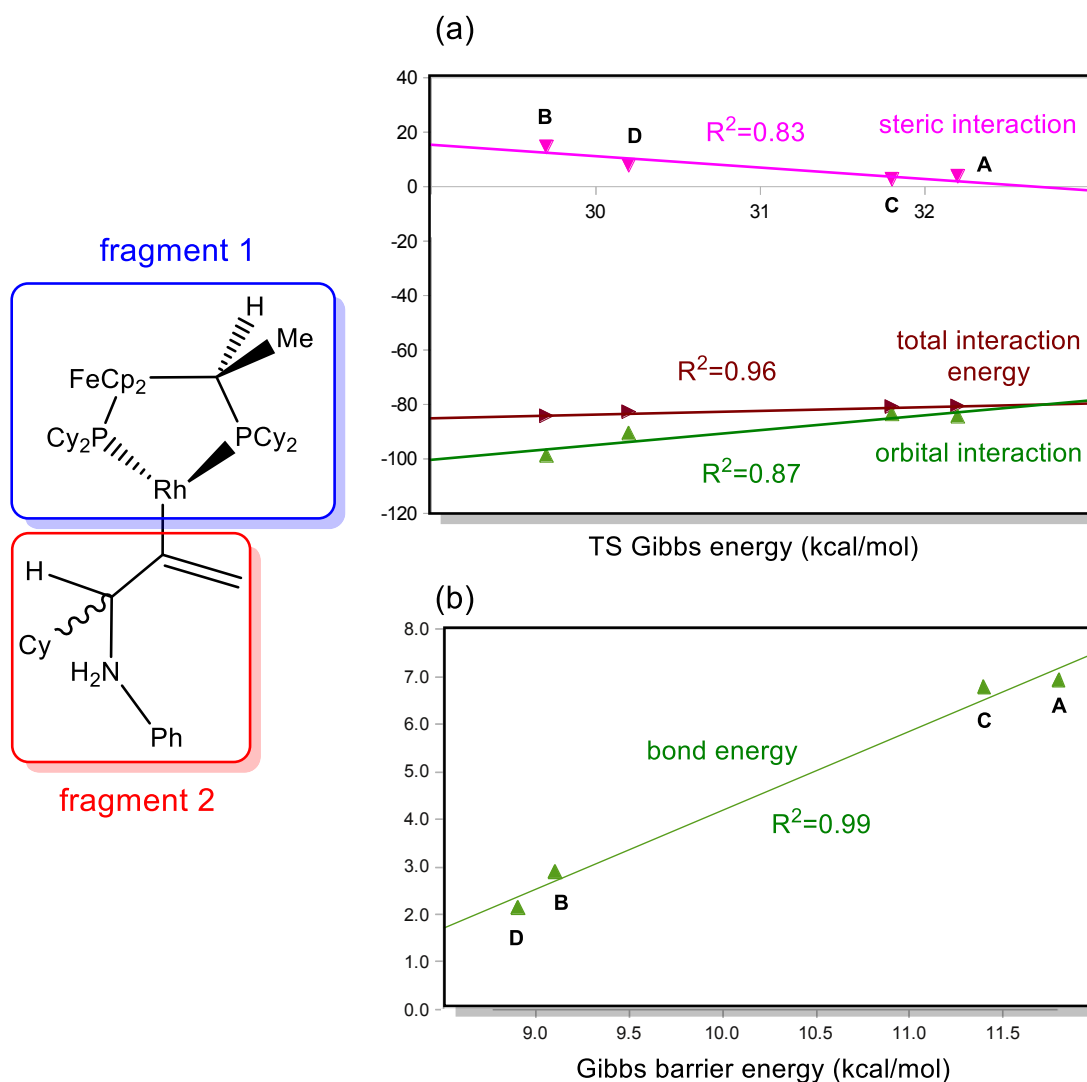
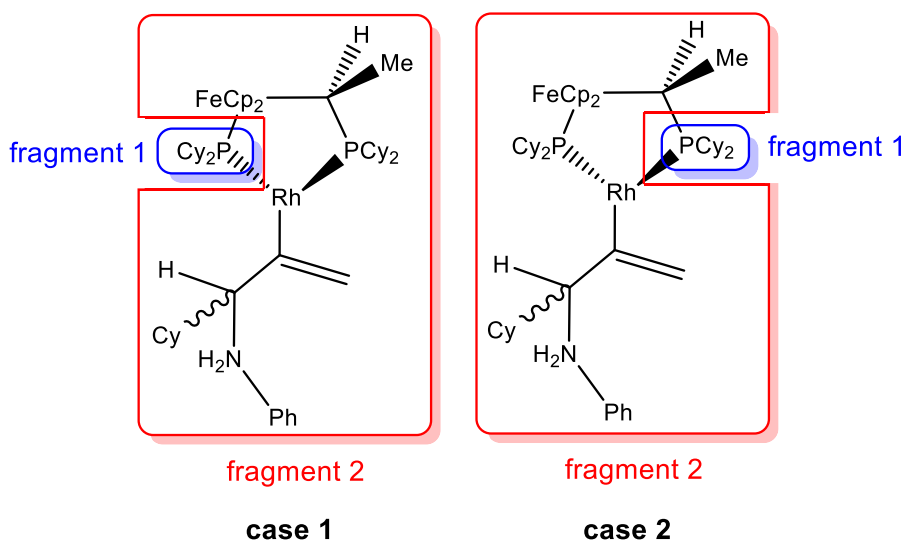


Figure 5.9: Correlation between (a) relative Gibbs energy of transition state **TS5.3_5.4** and interactions energies and (b) Gibbs energy barrier of transitions state **TS5.3_5.4** (from 5.2) and total bond energy (ΔE) obtained in the energy decomposition analysis.

In order to study the interaction between both phosphines of Josiphos ligands (because they are not equivalent) and the rest of the structure, the interactions energies were computed decomposing the structure of the transition state in two different ways: one of the phosphines of Josiphos with both cyclohexyl groups as a fragment and the rest of the structure as another fragment and the same but with the other phosphine of the Josiphos ligand. The different fragments analyzed are depicted in **Scheme 5.8**. The interaction energies are collected in **Table 5.6**.



Scheme 5.8: Different fragments analyzed by means of an energy decomposition analysis.

Table 5.6: Different energy terms (in kcal/mol) obtained in the different energy decomposition analysis carried out for both phosphines.

Case 1	ΔE_{Pauli}	Electrostatic interaction	Steric interaction	Orbital interaction	Total interaction energy (E_{int})	Relative Gibbs energy
Isomer a	668.48	-317.20	351.28	-516.49	-165.21	32.2
Isomer b	717.00	-356.88	360.12	-542.94	-182.82	29.7
Isomer c	720.29	-361.23	359.06	-541.01	-181.95	31.8
Isomer d	652.88	-308.60	344.28	-508.45	-164.17	30.2
Case 2	ΔE_{Pauli}	Electrostatic interaction	Steric interaction	Orbital interaction	Total interaction energy (E_{int})	Relative Gibbs energy
Isomer a	638.30	-330.84	307.46	-474.87	-167.41	32.2
Isomer b	578.50	-282.28	296.22	-449.94	-153.72	29.7
Isomer c	587.56	-284.43	303.13	-452.86	-149.73	31.8
Isomer d	626.37	-321.62	304.75	-475.72	-170.97	30.2

It is observed that all the interaction energies are always stronger for the phosphine in the side of ferrocene group (case 1) than for the other phosphine (case 2). Regarding the total interaction energy, for isomers **b** and **c** the phosphine in the side of ferrocene group (case 1) is higher than for the other phosphine (case 2) whereas in isomers **a** and **d** the opposite trend is found. This can be related with the fact that in isomers **b** and **c** the “allene” is coordinated *cis* to the phosphine in the side of ferrocene group while for in isomers **a** and **d** the “allene” is coordinated *cis* to the other phosphine (see **Scheme 5.7**). In summary, the interaction energy is higher with the phosphine coordinated *cis* with the “allene”.

5.3.6 Effect of temperature

In this section the effect of changing temperature is evaluated. In **Table 5.7** are summarized the Gibbs energies at 298 and 353 K (experimental conditions). Comparing the values of Gibbs energies at 298 K and 353 K, we can observe that the values obtained at 353 K are higher than those obtained at 298 K, but the trend observed is the same at both temperatures.

We can see that in both cases, the isomer **5.1a** is the most stable one. For this reason was taken as zero point energy at both temperatures.

Table 5.7: Comparison of Gibbs energies at 298 K and 353 K.

Isomer	298 K				353 K			
	a	b	c	d	a	b	c	d
5.1	0.0	1.2	0.4	0.5	0.0	1.3	0.3	0.7
TS5.1_5.2	24.1	25.6	24.3	22.7	26.8	28.2	26.8	25.3
5.2	20.4	20.6	20.4	21.3	23.0	23.1	23.0	24.0
TS5.3_5.4	32.2	29.7	31.8	30.2	35.0	32.6	34.5	33.1
5.5	18.8	20.4 ²	19.8	20.5	21.2	23.0 ²	22.3	23.0
TS5.5_5.6	21.3		22.3	22.9	24.1		25.1	25.7
5.6	16.8		16.9	17.6	19.6		19.7	20.5
TS5.6_5.7	19.2		19.5	18.9	22.0		22.2	21.7
5.7	-8.7		-3.1	-1.6	-6.0		-0.7	0.9

² from this intermediate the reaction finish as isomer **d**

The rate determining step is the conformational change of the amine (**TS5.3_5.4**) at both temperatures and the energy of the rate determining step is lower for the reaction starting with isomers **5.1b** and **5.1d** than for the reaction starting from isomers **5.1a** and **5.1c**.

5.3.6 Theoretical enantiomeric excess

The rate determining step of this reaction is the conformational change of amine. Accordingly, when applying the equation [5.3] (explained in the computational details section) to calculate the enantiomeric excess, ΔG^\ddagger will be the activation energy of the transition state of the conformational change of amine step. There are 4 different ΔG^\ddagger values in this equation depending on the isomer that we are using: ΔG^\ddagger_b , ΔG^\ddagger_d , ΔG^\ddagger_a and ΔG^\ddagger_c . The first two (ΔG^\ddagger_b and ΔG^\ddagger_d) refer to the previously mentioned activation energy in the cases where the major product is obtained (isomers **b** and **d**) and the other two (ΔG^\ddagger_a and ΔG^\ddagger_c) refer to the cases in which the minor product is obtained (isomers **a** and **c**).

The enantiomeric excess obtained using the aforementioned equation is 94% at 298 K, and decreases to 88% at 353 K. This value is in accordance with experimental results where the

enantiomeric excess obtained is 84 % when dichloroethane is used as solvent (the enantiomeric excess obtained experimentally varies between 84% and 89% depending of the solvent).¹²²

5.4 Conclusions

The reaction of enantioselective hydroamination was computationally studied. It is worth mentioning that eight isomers of the π -coordinated allene complex were considered. The four where the allene coordinates by the internal double bond are more stable and will leads to the reaction products observed experimentally.

From the results obtained in the **Chapter 4 (Section 4.3.1)**, the amine activation mechanism was discarded, thus meaning that only the alkene activation mechanism was computed. Three different possibilities were studied and it was identified that the most plausible pathway is the *anti* nucleophilic attack of the amine followed by a conformational change of the amine to allow the proton transfer through metal center protonation step. During the study of the aforementioned reaction pathway it has been identified that the rate determining step is the conformational change. The reaction was studied at two different temperatures and the enantiomeric excess was calculated.

Depending on the initial coordination mode of the allene to the catalyst there are four pathways (a-d) that can give the final enantiomers. Pathways **a** and **c** give the R enantiomers, whereas pathways **b** and **d** yields the S enantiomer. Theoretical calculations give enantiomeric excesses of 94 % and 88 % at 353 and 298 K, respectively. They are in very good agreement with experiment, where enantiomeric excess is 84 % at room temperature. The rate determining step is associated to a conformational change of the complex once the amine is added to the allene. Such conformational change is more favored for those pathways giving rise to the S enantiomer. We can conclude that our calculations are capable of reproduce the enantiomeric excess experimentally observed.

*Chemistry is necessarily an
experimental science:
its conclusions are drawn from data,
and its principles supported by evidence from facts.*

Michael Faraday

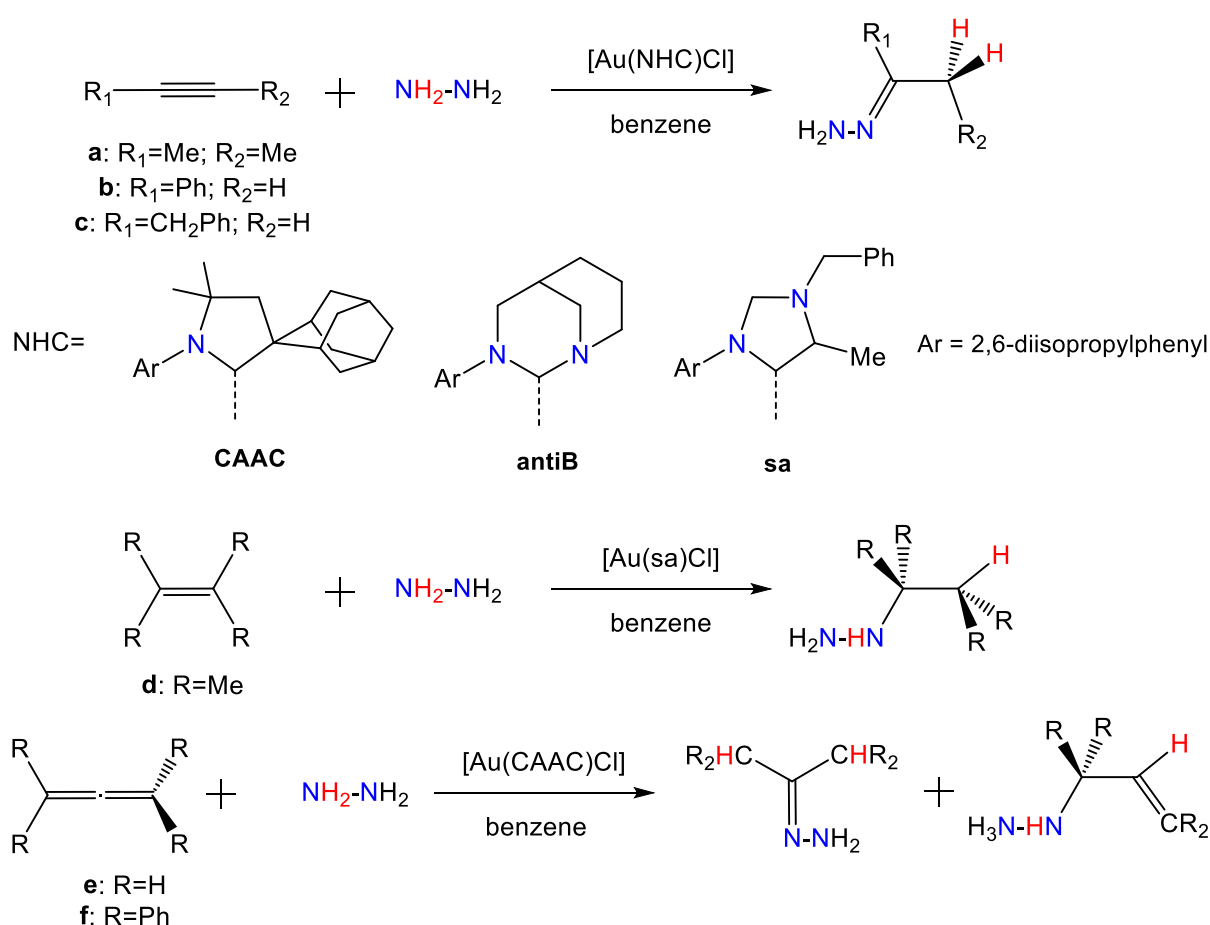
~Chapter 6~

GOLD-CATALYZED HYDROAMINATION REACTION USING HYDRAZINE AS N-NUCLEOPHILE

This chapter is devoted to extend the previous studies on hydroamination reaction catalyzed by gold complexes. The hydroamination of alkynes, alkenes and allenes with hydrazine as N-nucleophile are analyzed. These results have been published in *ACS Catal.* **2015**, 5 (2), 815–829: Hydroamination of C–C Multiple Bonds with Hydrazine Catalyzed by N-Heterocyclic Carbene–Gold(I) Complexes: Substrate and Ligand Effects (reference 234).

6.1 Introduction

Gold complexes have shown very high turnover numbers (TON) catalyzing the hydroamination reaction of alkynes and allenes.^{47,49} The mechanism of hydroamination reactions catalyzed by gold complexes has been intensively studied.^{124–127} The general mechanism has been proposed by our group for the hydroamination of alkynes with ammonia catalyzed by gold(I) complexes with cyclic(alkyl)(amino)carbene (CAAC) ligand. This reaction takes place by ammonia coordination followed by its exchange by an electrophilic CC bond substrate molecule.⁷⁴ The mechanism continues with the nucleophilic attack of the ammonia to the coordinated carbon-carbon bond and a protodeauration step (see **Section 1.2.1.1** for more details about this mechanism).



Scheme 6.1: Hydroamination reactions studied in this chapter.

As mentioned in **Chapter 1**, the reaction with a small molecule as hydrazine is a challenging task. One of the main difficulties of using small nucleophiles (like hydrazine or ammonia) is the formation of stable Werner complexes, deactivating the catalyst.^{53–57} However, Bertrand et al. demonstrated that cationic gold (I) complexes bearing a CAAC ligand is able to promote the reaction of alkynes and allenes with hydrazine.¹³⁷ Later the same group improved this reaction by using a different NHC ligand where one of the nitrogen atoms of the classical NHC ligand is placed in a strained bridgehead position. This ligand is named as

anti-Bredt NHC ligand.¹⁴⁰ Later Hashmi's group, reported the reaction of alkynes with hydrazine at room temperature by using a gold(I) complex with an abnormal NHC ligand.¹⁴¹ (see **Section 1.2.3** for more information about gold-catalyzed hydroamination reactions reported in literature).

This chapter is devoted to the computational study of hydrohydrazination reaction of alkynes and allenes. The study is addressed catalyzed by the three gold(I) complexes reported experimentally. In addition, the hydrohydrazination reaction of alkenes is study since there are no experimental examples of this reaction. All the reactions studied are depicted in **Scheme 6.1**.

Some aspects, such as the associative or dissociative nature of the exchange of the amine for the electrophile substrate and the inner- or outer-sphere mechanism for the nucleophilic attack of the amine are also analyzed in this chapter.

6.2 Computational methods and models

All calculations were carried out using Gaussian 09 program. Calculations were performed at DFT level by means of the M06 functional with and ultrafine grid option. The basis sets used were the 6-31G(d,p) for all the atoms, except for Au where the SDD (with an additional f orbital) along with the associated pseudopotential was employed. The structures were fully optimized in solution using SMD model with standard parameters and benzene as solvent ($\epsilon=2.2706$). Atomic charges were calculated using the Charge Model 5 (CM5). This population analysis approach gives charges essentially independent of the basis set. The nature of stationary points (minima and TS) was confirmed by frequency calculations. Connections between the transition states and the minima were checked by following the IRC and subsequent geometry optimization till the minima. Energy values given in the text correspond to Gibbs energies at 298K calculated including solvent effects.

Calculations have been performed with the gold(I)-NHC complexes (**CAAC**, **antiB** and **sa**; **Scheme 6.1**) without simplifications in the ligands. Three alkynes (2-butyne: **a**, phenylacetylene: **b** and benzylacetylene: **c**), as well as one alkene (2,3-dimethyl-2-butene: **d**) and two allenes (1,2-propadiene: **e** and tetraphenyl-1,2-propadiene: **f**) have been employed as substrates. Hydrazine has been selected as N-nucleophile in all cases. All the reactions studied in this chapter are depicted in **Scheme 6.1**. The structures are named according the following procedure: **6x.y** where x corresponds to the point in the energy profile and y corresponds to the substrate (for example, **6.1a** correspond to the first point of reaction of substrate **a**: 2-butyne).

6.3 Results and Discussion

This section is divided in four subsections. The first one is devoted to analyze the catalyst's active specie. In the other three sections the hydroamination reactions of alkynes, alkenes and allenes are sequentially analyzed.

6.3.1 Generation of the active species

According to the previous results obtained by our group with NH_3 and a Au(I) catalyst,⁷⁴ is expected that hydrazine initially coordinates to the metal center. However, nucleophilic attack takes place in the coordinated carbon-carbon bond. Therefore the exchange of hydrazine by the C-C substrate must happens. This section is devoted to analyze the ligand substitution since in this step is formed the catalytic active species.

The catalyst used is a (carbene)gold chloride species, so the first step is the chloride abstraction. This step requires the use of a halide abstractor as tetrakis(3,5-bis(trifluoromethyl)phenyl)borate potassium. The calculated ΔG of the chloride abstraction ($[\text{Au}(\text{NHC})\text{Cl}] \rightarrow [\text{Au}(\text{NHC})]^+ + \text{Cl}^-$) are 78.4, 78.1 and 82.0 kcal/mol for $[\text{Au}(\text{CAAC})\text{Cl}]$, $[\text{Au}(\text{antiB})\text{Cl}]$ and $[\text{Au}(\text{sa})\text{Cl}]$ respectively. The high energy demand for removing the halide points out the compulsory use of a chloride abstractor.

To estimate the electrophilicity of the gold center in the carbene gold cations we performed a charge analysis. The charges over the gold center are as +0.16, +0.13 and +0.20 when the carbene is CAAC, antiB and sa, respectively. For comparative purposes, the charge was calculated for the gold center in $[\text{Au}(\text{PPh}_3)]^+$ fragment. The value obtained was lower (+0.11), in agreement with more acidic $[(\text{NHC})\text{Au}]^+$ fragments.

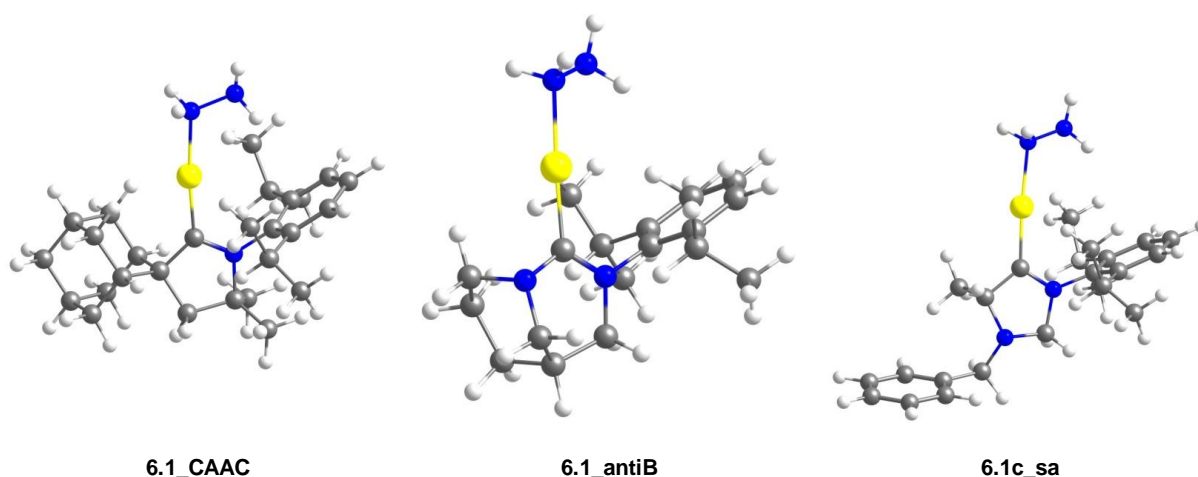


Figure 6.1: Optimized structures of the hydrazine-gold Werner complexes formed with $[\text{Au}(\text{CAAC})]^+$, $[\text{Au}(\text{antiB})]^+$ and $[\text{Au}(\text{sa})]^+$ metal fragments. Relative Gibbs energy values are given under each structure in kcal/mol.

Hydrazine coordinates to the cationic metal center forming the so-called Werner complex (intermediate **6.1**). These complexes are very stable, having $\Delta G_{\text{binding}}$ of 45.6, 45.4 and 48.0 kcal/mol for the CAAC, antiB and sa carbenes, respectively. Therefore, the hydrazine Werner complexes can be considered the resting state of the catalyst. These structures have been considered as zero-point energy in the Gibbs energy profiles. The optimized structures of the three intermediates **6.1** are depicted in **Figure 6.1**.

To yield the catalytic active species it is necessary to exchange hydrazine by the substrate containing the carbon-carbon multiple bond. The transition state for this exchange has been calculated for all the reactions studied over this chapter. The results agree with an associative exchange mechanism, through a tricoordinated species. The Gibbs energy profiles for the exchange step are depicted in **Figure 6.2**.

Regarding the exchange of hydrazine for an alkyne molecule, the barriers range from 10.0 to 14.4 kcal/mol. For the three alkynes studied, the benzylacetylene (substrate **c**) is the one that requires the lowest energy and the phenylacetylene (substrate **b**) the one that requires the highest energy. Comparing the energies for the same substrate but changing the carbene ligand, the barriers are quite similar, being the sa carbene complex (**Scheme 6.1**) the one that requires the lowest energies. The coordination of the alkyne to the metal center is not symmetrical; in all cases studied, the terminal carbon atom is around 0.15 Å closer to the metal center than the internal carbon atom.

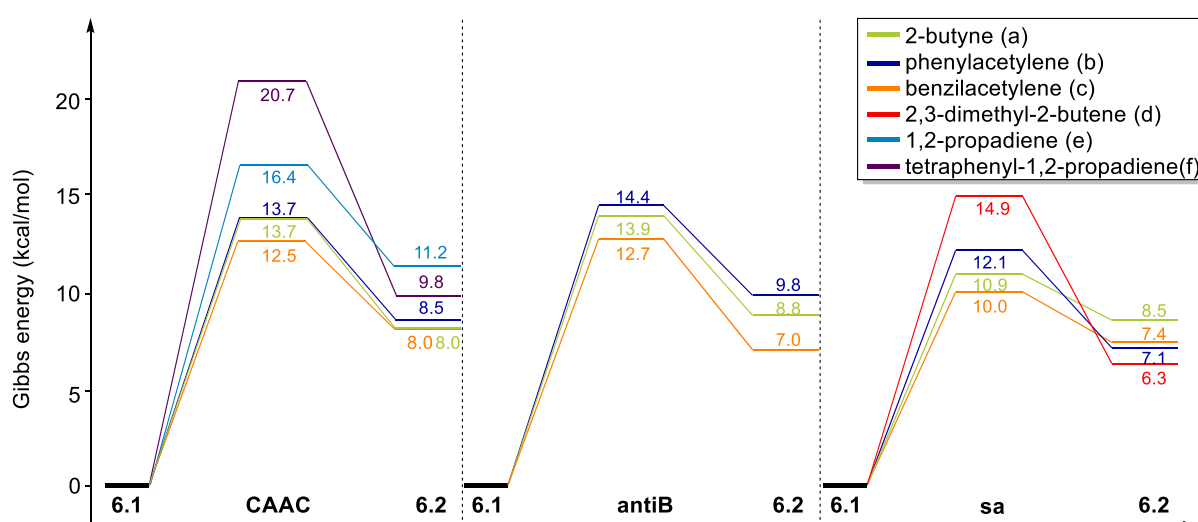


Figure 6.2: Gibbs energy profiles in benzene for the hydrazine by substrate exchange (TS6.1_6.2).

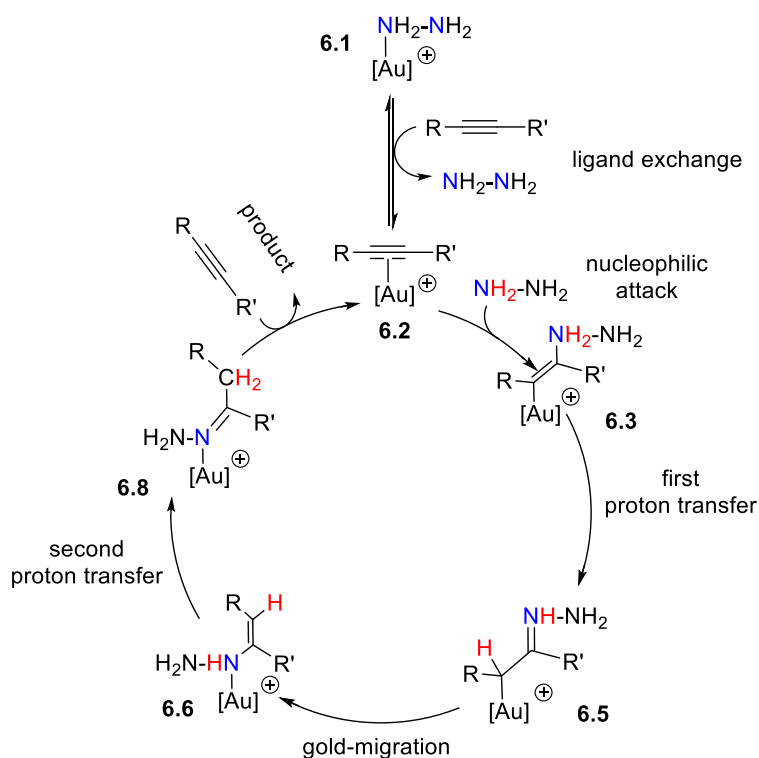
The exchange of hydrazine for an alkene molecule was only studied for 2,3-dimethyl-2-butene (substrate **d**) using the sa carbene. The energy barrier for the substitution of hydrazine by the alkene is somewhat higher (14.9 kcal/mol) than for the substitution by an alkyne molecule (from 10.0 to 12.1 kcal/mol).

The ligand substitution step when the substrate is an allene (1,2-propadiene; substrate **e** and tetraphenyl-1,2-propadiene; substrate **f**) was only studied for the CAAC carbene. The exchange of hydrazine for an allene requires much more energy than substitution by an alkyne. Coordination of the allene gives rise to a η^2 complex which coordination is not totally symmetrical. For the case of tetraphenyl-1,2-propadiene (**f**), the π -allene complex formed is not favorable (20.7 kcal/mol) due to the presence of four bulky phenyl groups.

Regarding the stability of the π -complexes formed, these intermediates are about 10 kcal/mol less stable than their corresponding complexes with hydrazine bonded to the gold center. Comparing the stability of the different intermediates formed in this step (intermediate **6.2**), the alkene π -complex is the most stable one and the allene π -complexes are the less stable structures. Overall, the study of the generation of the active species reveal that despite cationic gold-NHC complexes form strong Werner complexes with hydrazine, they also form strong complexes with unsaturated hydrocarbons, thus facilitating its replacement and the subsequent nucleophilic attack.

6.3.2 Hydroamination of alkynes

As earlier mentioned, the mechanism of the hydroamination of alkynes with NH_3 using the $[(\text{CAAC})\text{Au}]^+$ catalyst provides the basis for our analysis.⁷⁴ The operative mechanism for the hydroamination reaction of alkynes catalyzed by $[\text{Au}(\text{NHC})]^+$ complexes is depicted in **Scheme 6.2**.



Scheme 6.2: Proposed catalytic cycle for the hydrohydrazination of alkynes catalyzed by NHC-Au(I) complexes.

The general mechanism for the hydroamination of alkynes catalyzed by gold complexes was described as an electrophile activation mechanism followed by a nucleophilic addition of the amine and a protodeauration step. In this case, the reaction product is not a hydrazone, so two consecutive proton transfer steps are required. Therefore, after the hydrazine by alkyne ligand exchange, the reaction mechanism explored consists of four main steps: nucleophilic addition of hydrazine, first proton transfer (assisted by a second hydrazine molecule), gold migration (first tautomerization) and second proton transfer (also assisted by a second hydrazine molecule) which can be also described as a second tautomerization.

The hydrohydrazination reaction of three different alkynes (2-butyne: **a**, phenylacetylene: **b** and benzylacetylene: **c**) has been analyzed. This section is divided in two subsections, in the first one the reaction of an internal alkyne is described and the second subsection is devoted to analyze the reaction of terminal alkynes.

6.3.2.1 Internal alkynes

2-butyne was chosen as an example of symmetrically substituted internal alkyne. Hydroamination with hydrazine of internal alkynes has been only reported for diphenylacetylene. It takes place at 90°C when is catalyzed by $[\text{Au}(\text{CAAC})]^+$ complex with a 91% yield in 14 hours at 110 °C. The reaction with $[\text{Au}(\text{antiB})]^+$ complex yields the corresponding hydrazone in 6 hours with a 82% yield.^{137,140} No data is available for the hydroamination reaction of internal alkynes catalyzed by $[\text{Au}(\text{sa})]^+$ complex.

The Gibbs energy profiles for the hydroamination of 2-butyne (substrate **a**) catalyzed by $[\text{Au}(\text{CAAC})]^+$, $[\text{Au}(\text{antiB})]^+$ and $[\text{Au}(\text{sa})]^+$ complexes are depicted in **Figure 6.3**. The initial step is the exchange of the hydrazine for an alkyne molecule which have been already discussed in **Section 6.3.1**. This step is followed by the nucleophilic addition of hydrazine to the coordinated alkyne, which occurs through an outer sphere mechanism. Then a proton transfer step assisted by a second hydrazine molecule takes place through two consecutive transition states connected by intermediate **6.4a** involving a $[\text{NH}_2\text{-NH}_3]^+$ moiety. Nevertheless, although two transition states and one intermediate was found in the potential energy surface, the three structures are very close in energy and only one transition state remains when thermal and entropic corrections are added. This step yields intermediate **6.5a** which can be described as protonated hydrazone, with planar N atom and a simple carbon-carbon bond.

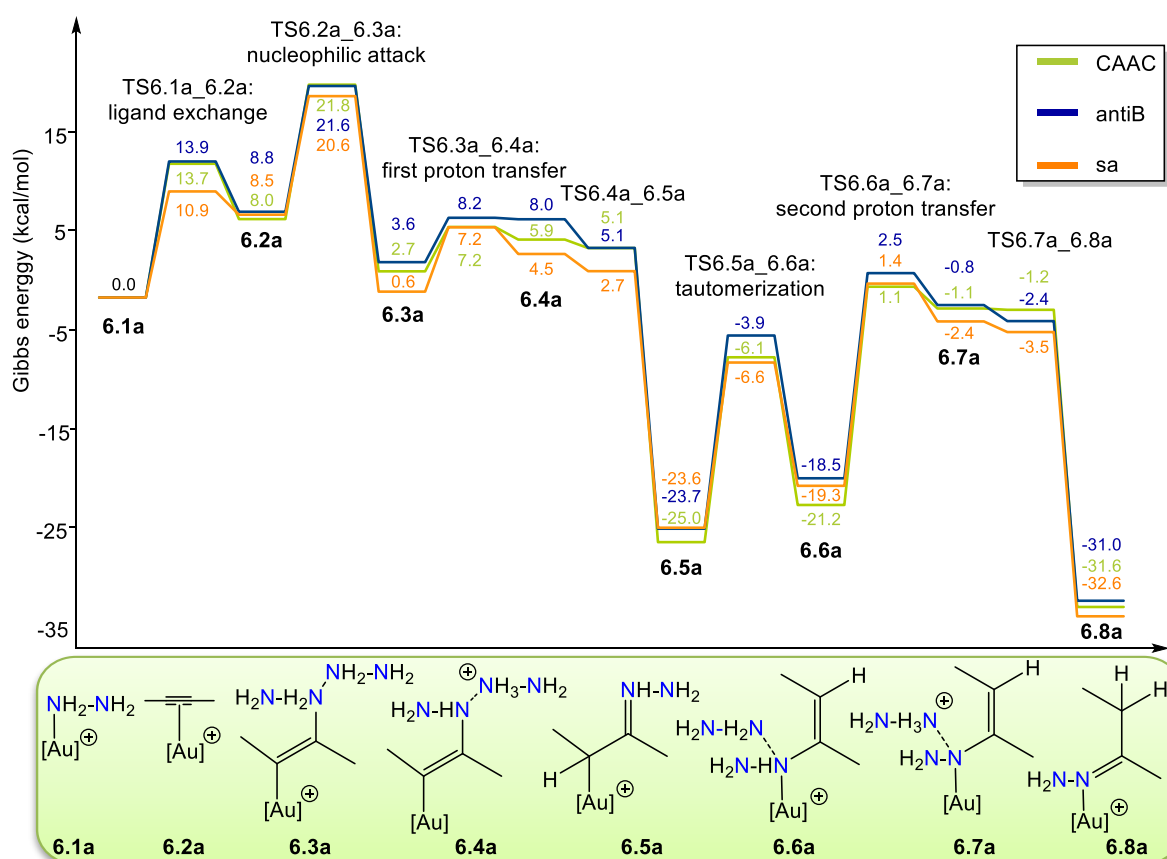


Figure 6.3: Gibbs energy profiles in benzene for the hydrohydrazination of 2-butyne (substrate **a**) catalyzed by [Au(CAAC)]⁺ (green), [Au(antiB)]⁺ (blue) and [Au(sa)]⁺ complexes (orange).

From intermediate (**6.5a**), two consecutive tautomerization steps are required to obtain the final product. The first tautomerization (**TS6.5a_6.6a**) is a gold-center migration where the gold-moiety migrates from the carbon to the nitrogen atom leading to the intermediate **6.6a** which can be described as an enamine-tautomer. This step is followed by a second proton transfer step from nitrogen to carbon yielding the final hydrazone product (**6.8a**), Analogously to the first proton transfer, this second proton transfer happens in two steps (**TS6.6a_TS6.7a** and **TS6.7a_6.8a**) through an intermediate involving a [NH₂-NH₃]⁺ moiety, although the Gibbs energy profile presents a single step for the second proton transfer step. The optimized structures of the most relevant transition states involved in this reaction are depicted in **Figure 6.4**.

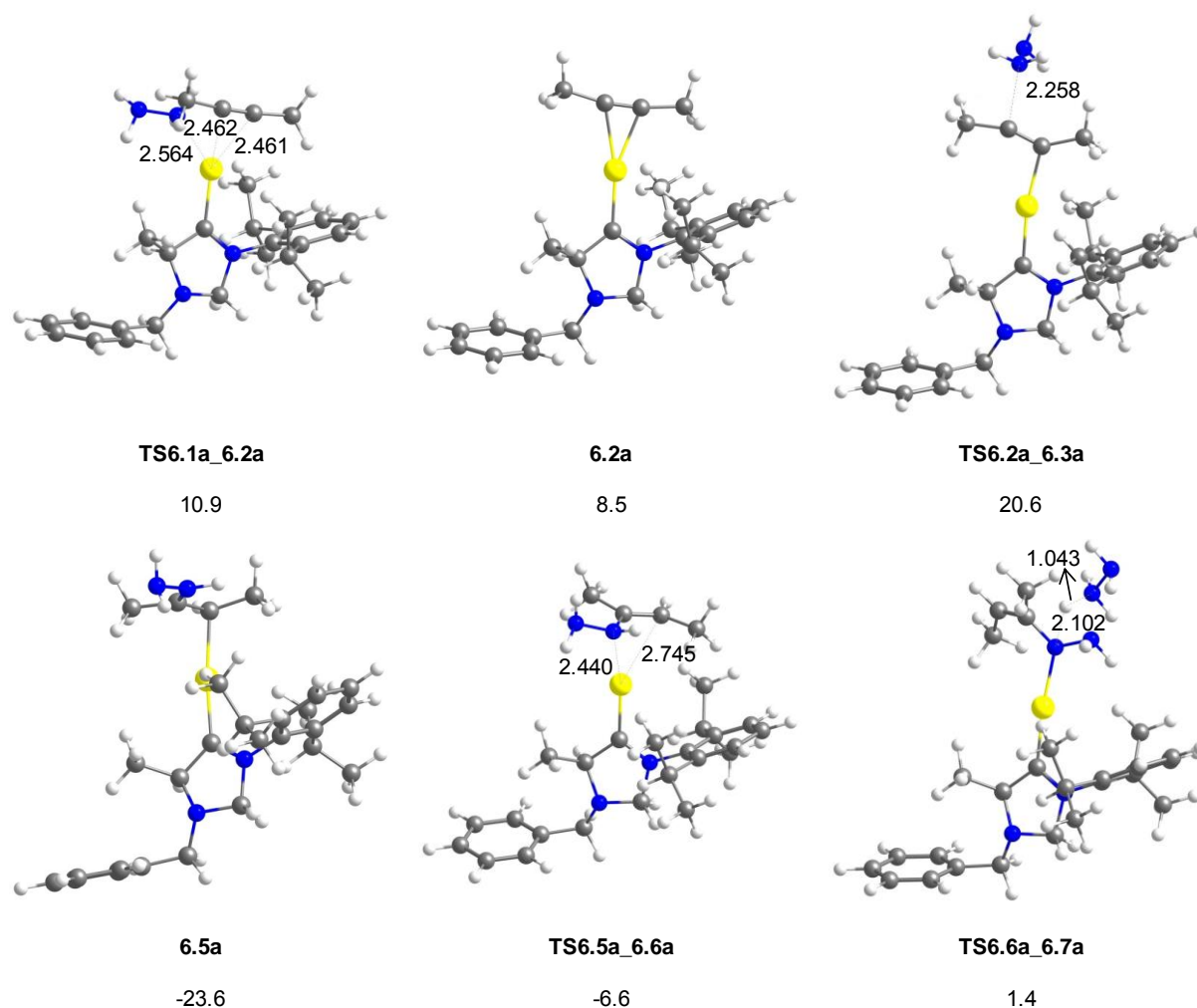


Figure 6.4: Optimized structures of the most important transition states and intermediates for the hydrohydrazination of 2-butyne (substrate **a**) catalyzed by $[\text{Au}(\text{sa})]^+$ complex. Relative Gibbs energy values are given under each structure in kcal/mol.

Regarding the thermodynamics of this reaction, there is a strong driving force due to the hydrazone product (**6.8a**) is about 30 kcal/mol more stable than the reactants (Werner complex: **6.1** plus the alkyne). According to the energy span model, the activation energy of the full catalytic cycle (ΔG^\ddagger) is determined by the difference between intermediate **6.5a** (protonated hydrazone) and the transition state of the second proton transfer (**TS6.6a_6.7a**). The activation energies obtained are practically equal for $[(\text{CAAC})\text{Au}]^+$ and $[(\text{antiB})\text{Au}]^+$ catalyst (26.1 and 26.2 kcal/mol, respectively), and slightly lower for $[(\text{sa})\text{Au}]^+$ catalyst (25.0 kcal/mol). Calculations predict a good efficiency of the $[(\text{sa})\text{Au}]^+$ catalyst for the hydrohydrazination of internal alkynes, although no experimental results of this reaction have been reported.

6.3.2.2 Terminal alkynes

The hydrohydrazination reaction of phenylacetylene with hydrazine has been reported by Bertrand using $[(\text{CAAC})\text{AuCl}]^{137}$ (at 100 °C, 0.5h, 95% yield) and $[(\text{antiB})\text{AuCl}]$ (at 90 °C, 3h, 87% yield)¹⁴⁰ and by Hashmi using $[(\text{sa})\text{AuCl}]$ (at 20 °C, 4h, 90% yield).¹⁴¹ When benzylacetylene was used as substrate, the reaction was catalyzed with $[(\text{CAAC})\text{AuCl}]$ (at 100 °C, 3h, 95% yield),¹³⁷ $[(\text{antiB})\text{AuCl}]$ (room temperature, 4h, 83% yield)¹⁴⁰ and $[(\text{sa})\text{AuCl}]$ (20 °C, 4h, 73% yield).¹⁴¹

The whole hydrohydrazination Gibbs energy profiles for phenylacetylene (substrate **b**) and benzylacetylene (substrate **c**) were calculated using the three catalysts commented above (Figures 6.5 and 6.6, respectively).

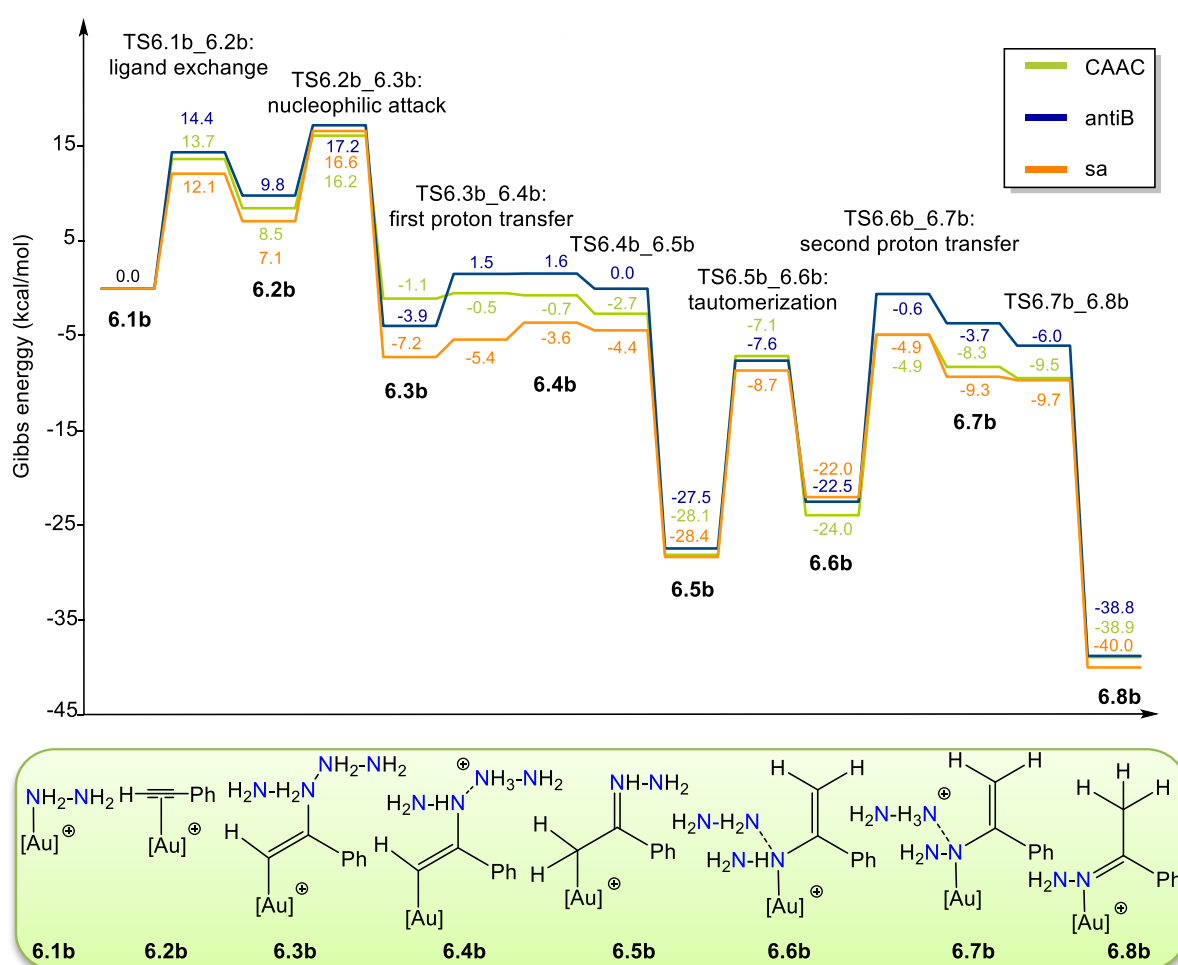


Figure 6.5: Gibbs energy profiles in benzene for the hydrohydrazination of 2-phenylacetylene (substrate **b**) catalyzed by $[\text{Au}(\text{CAAC})]^+$ (green), $[\text{Au}(\text{antiB})]^+$ (blue) and $[\text{Au}(\text{sa})]^+$ complexes (orange).

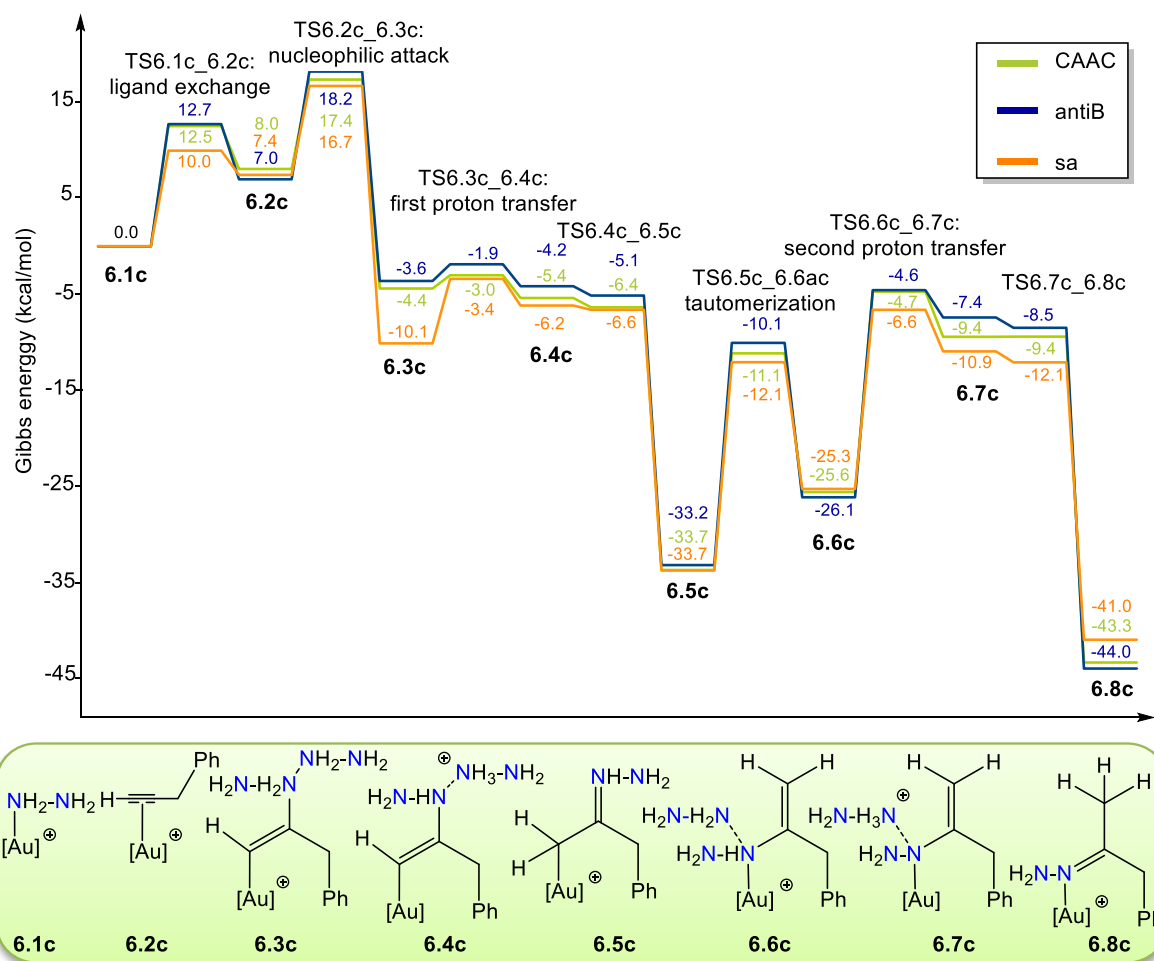


Figure 6.6: Gibbs energy profiles in benzene for the hydrohydrazination of 2-benzylacetylene (substrate **c**) catalyzed by $[\text{Au}(\text{CAAC})]^+$ (green), $[\text{Au}(\text{antiB})]^+$ (blue) and $[\text{Au}(\text{sa})]^+$ complexes (orange).

The general appearance of the energy profiles for the hydrohydrazination reaction of phenylacetylene (substrate **b**, **Figure 6.5**) and benzylacetylene (substrate **c**, **Figure 6.6**) is similar to that of 2-butyne (substrate **a**, **Figure 6.3**), although a deeper analysis reveals some differences. The relative Gibbs energies of the most important transition states, the Gibbs reaction energy as well as the global energy barriers for the three alkynes analyzed are collected in **Table 6.1**.

Table 6.1: Relative Gibbs energies of activation for the different steps and overall Gibbs energy of reaction (ΔG_r) and Gibbs energy barrier (ΔG^\ddagger) of the hydrohydrazination of alkynes, in kcal/mol.

		Ligand exchange: TS6.1_6.2	Nucleophilic attack: TS6.2_6.3	6.5	Tautomerization: TS6.5_6.6	2 nd proton transfer: TS6.6_6.7	ΔG^\ddagger	ΔG_r
2-butyne	CAAC	13.7	21.8	-25.0	-6.1	1.1	26.1	-31.6
	antiB	13.9	21.6	-23.7	-3.9	2.5	26.2	-31.0
	sa	10.9	20.6	-23.6	-6.6	1.4	25.0	-32.6
Phenylacetylene	CAAC	13.7	16.2	-28.1	-7.1	-4.9	23.2	-38.9
	antiB	14.4	17.2	-27.5	-7.6	-0.6	26.9	-38.8
	sa	12.1	16.6	-28.4	-8.7	-4.9	23.5	-40.0
Benzylacetylene	CAAC	12.5	17.4	-33.7	-11.1	-4.7	29.0	-43.3
	antiB	12.7	18.2	-33.2	-10.1	-4.6	28.6	-44.0
	sa	10.0	16.7	-33.7	-12.1	-6.6	27.1	-41.0

In agreement with the substituent effect expected for alkyl and aryl groups, the nucleophilic addition barriers for phenylacetylene (around 16 kcal/mol) are lower than those for 2-butyne (around 21 kcal/mol). Barriers for benzylacetylene are only around 1 kcal/mol higher than those for phenylacetylene. Overall, the nucleophilic addition step is easier with terminal alkynes than with internal alkynes. As mentioned before, the activation Gibbs energy of the hydrohydrazination reaction is not governed by the nucleophilic addition step but by the energy difference between intermediates **6.5** (the protonated hydrazone) and the transition states of the second proton transfer (**TS6.6_6.7**); so both reaction structures need to be analyzed in more detail. The comparison between the internal and the terminal alkynes evinces that the presence of benzyl or phenyl substituents substantially stabilizes intermediates **6.5** (around 3 and 10 kcal/mol respectively) and also lowers the energy of the transition step for the second proton transfer step (**TS6.6_6.7**, around 7 kcal/mol in both cases). Thus, the Gibbs barriers (ΔG^\ddagger) for the hydrohydrazination of benzylacetylene are about 2.5 kcal/mol higher whereas the barriers for phenylacetylene are about 2 kcal/mol lower than for 2-butyne with the same catalyst. Overall, the Gibbs energy barriers (ΔG^\ddagger) calculated for phenylacetylene are the lowest ones.

The relative stability of the intermediate formed after the first proton transfer step (**6.5**) appears as an important factor in the overall Gibbs energy barrier of the catalytic cycle. The other factor is the relative energy of the transition state corresponding to the deprotonation of the enamine (intermediate **6.6**) in the second transfer step. Removal of the proton is

more difficult for the 2-butyne intermediate than for the phenyl and benzyl alkynes, which exhibit similar ΔG values.

Regarding the thermodynamic of the reaction, the hydroamination of the terminal alkynes is even more exergonic (around 40 kcal/mol) than that of 2-butyne (around 30 kcal/mol). Comparing the three catalysts studied, $[(sa)Au]^+$ gives lower barriers than $[(antiB)Au]^+$ for both phenylacetylene and benzylacetylene substrates. This result agrees with the experimental milder conditions (20 °C) used to perform the hydrohydrazination of terminal alkynes catalyzed by $[(sa)Au]^+$. However the calculations do not reproduce the experimental trend found with the $[(antiB)Au]^+$ catalyst: hydrohydrazination of benzylacetylene takes place at room temperature while 90 °C are required for the hydrohydrazination of phenylacetylene. Conversely, the calculated barriers are 28.6 and 26.9 kcal/mol, respectively. Our calculated Gibbs barrier values for the hydroamination of benzylacetylene are always higher than those for phenylacetylene using the same catalyst. In addition to the accuracy of the computational methods for describing slight differences between overall energy barriers, factors not considered in the calculations, as the instability of the $[(NHC)Au]^+$ complex, its deactivation by formation of catalytically inactive species²⁶⁸ or the intervention of adventitious water molecules in the proton transfer step^{129,269,270} may be at work.

6.3.3 Hydroamination of alkenes

The intermolecular hydroamination of alkenes remains one of the most significant challenges in homogenous catalysis. There are no examples of hydroamination reaction of alkenes catalyzed by $[(NHC)Au]^+$ complexes. For comparative purposes and also to identify the bottlenecked of the reaction, the hydrohydrazination of 2,3-dimethyl-2-butene (substrate **d**), using $[(sa)Au]^+$ as catalyst, has been computationally studied. The obtained Gibbs energy profile is compared in **Figure 6.7** with the Gibbs energy profile obtained for 2-butyne (substrate **a**).

Analogously to the hydrohydrazination of alkynes catalyzed by gold complexes, the reaction of alkenes starts with the coordination of hydrazine to the metal center. Thus, the initial step is a ligand exchange where hydrazine is substituted by an alkene molecule in the coordination sphere of the metal and is followed by the nucleophilic attack of the hydrazine into the coordinated alkene. The reaction ends up with the proton transfer step to yield the alkylamine product. This proton transfer step takes place involving two transition states. In the first step, which involves less barrier, the proton is transferred from the hydrazine bonded to the carbon to the external hydrazine yielding an intermediate with a $NH_2-NH_3^+$ moiety. Protodeauration is the second step.

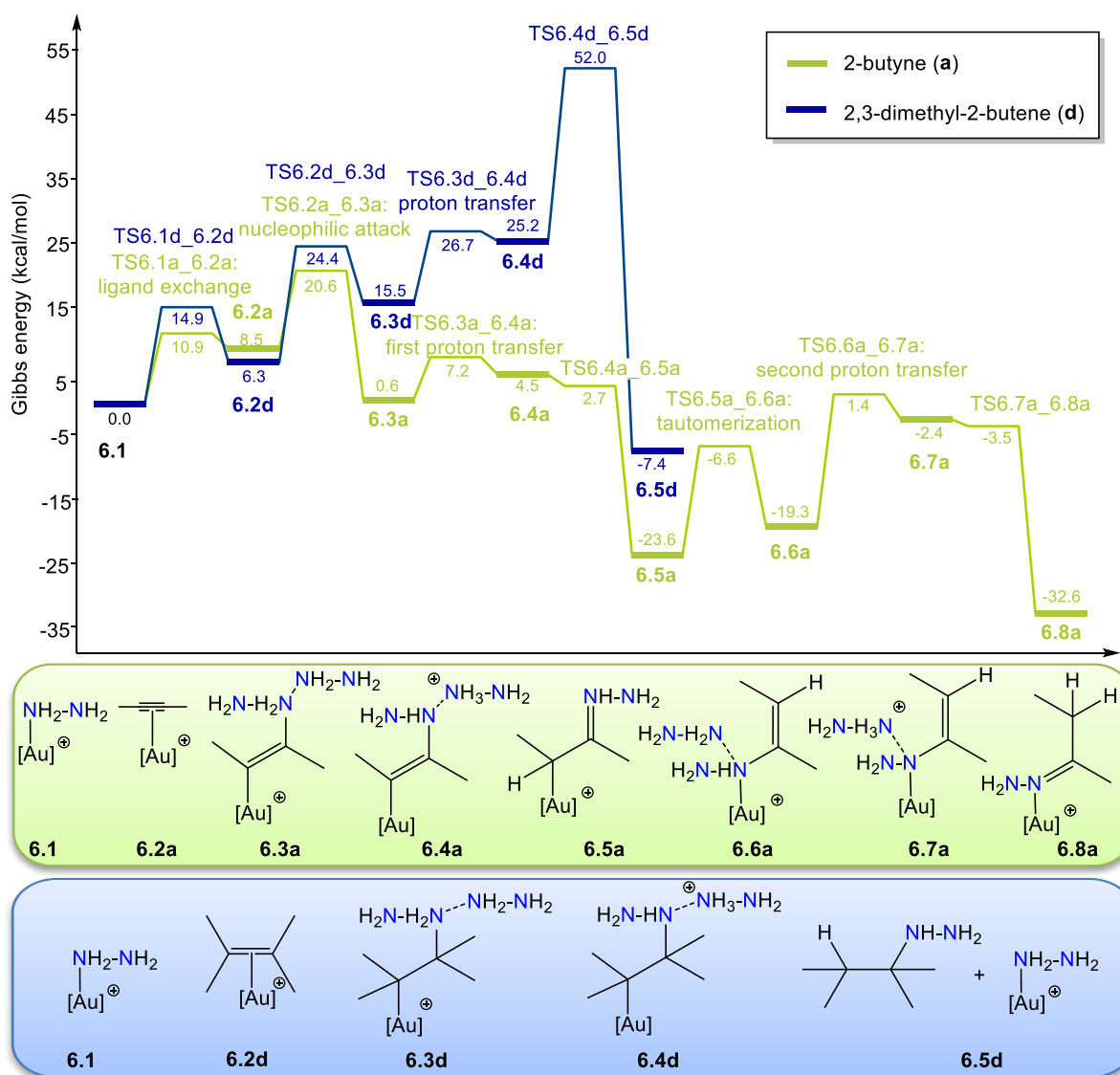


Figure 6.7: Gibbs energy profiles in benzene for the hydroamination of 2-butyne (substrate **a**, green) and 2,3-dimethyl-2-butene (substrate **d**, blue) catalyzed by $[\text{Au}(\text{sa})]^+$.

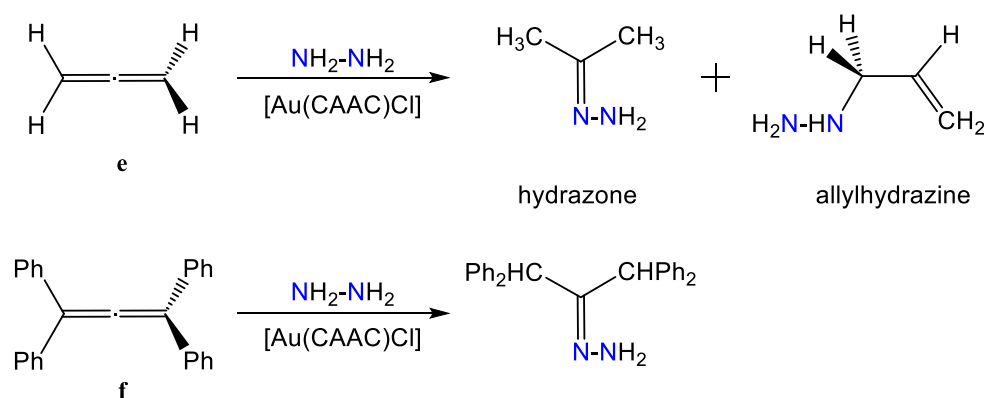
The barriers for the first two steps (ligand exchange and nucleophilic attack) are about 4 kcal/mol higher for the alkene than for the alkyne, but are still reachable. Both energy profiles markedly differ in the stability of the intermediate formed after the nucleophilic attack. When the nucleophilic attack takes place over the alkyne, it is located at 0.6 kcal/mol whereas when occurs over the alkene it lies at 15.5 kcal/mol. However, the main discrepancy between both energy profiles is found in the proton transfer step, specifically in the second part of this proton transfer step which is the protonation of the carbon atom of the alkylamine. For the alkyne this step leads, after crossing a low barrier, to a very stable protonated hydrazone intermediates (**6.5a**). For the alkene, this protonation step corresponds to the protodeauration step and already provides the final product (2-hydrazido-2,3-dimethylbutane) and regenerates the catalyst (**6.1**). The transition state for this reaction is found at 52.0 kcal/mol, making the hydroamination reaction of alkenes

completely unfeasible. Our calculation showed that the main difficulty for the hydroamination reaction of alkenes is not the reactivity of the η^2 -alkene gold(I) complex towards the nucleophilic attack but the protodeauration step.²⁷¹

6.3.4 Hydroamination of allenes

The hydroamination reaction of two different allenes with hydrazine has also been computationally studied. For the analysis we selected two allenes studied by Bertrand et al. 1,2-propadiene (substrate **e**) and tetraphenyl-1,2-propadiene (substrate **f**).¹³⁷

Experimental results show that the hydrohydrazination reaction of 1,2-propadiene catalyzed by the gold-CAAC complex yields a 2:1 mixture of hydrazone and allylhydrazine products, whereas in the case of tetraphenyl-1,2-propadiene only the hydrazone derivative was observed (**Scheme 6.3**). The reaction takes place at higher temperatures than for alkynes (130 °C for 1,2-propadiene and 150 °C for tetraphenyl-1,2-propadiene).¹³⁷



Scheme 6.3: Catalytic hydrohydrazination reactions of allenes using $[\text{Au}(\text{CAAC})]^+$ complex.¹³⁷

As reported for alkynes and alkenes, an outer-sphere attack of hydrazine into the π -coordinated allene active species was also characterized. However, when the substrate is an allene, the nucleophilic attack of hydrazine can take place over two different carbon atoms (the terminal or the central), giving rise to two different intermediates.

It is noteworthy that, usually, in the intermolecular hydroamination of allenes, the nucleophilic attack only occurs over the terminal carbon atom of the allene, like it happens and is discussed in the previous chapter in the hydroamination reaction of allenes catalyzed by $[\text{Rh}(\text{Josiphos})]^+$ complex.¹²² However, the nucleophilic addition of hydrazine to 1,2-propadiene (substrate **e**) catalyzed by $[\text{Au}(\text{CAAC})]^+$ takes place over both terminal and central carbon atoms being the latter the major reaction product (hydrazone product).¹³⁷ For the tetraphenyl-1,2-propadiene (substrate **f**) addition of ammonia¹³³ and hydrazine¹³⁷ only occurs over the central carbon atom.

The calculated Gibbs energy profiles for 1,2-propadiene (substrate **e**) and tetraphenyl-1,2-propadiene (substrate **f**) are displayed in **Figures 6.8** and **6.10**, respectively.

The Gibbs energy profile obtained for the hydrohydrazination reaction of 1,2-propadiene (**Figure 6.8**) reveals very similar barriers for the nucleophilic attacks over both carbon atoms of allene, with the formed intermediates (**6.3e** and **6.7e**) having also similar stability. The optimized structures of the transition states of the nucleophilic addition step into both carbon atoms of allene are depicted in **Figure 6.9**.

The nucleophilic addition is followed in both pathways by a proton transfer step which generates for both pathways much more stable intermediates (**6.4e** and **6.8e**). The proton transfers involved in the reaction of allenes take place in a single step, unlike hydroamination reaction of alkynes and alkenes where the proton transfers takes place through two transition states connected by an intermediate involving a $\text{NH}_2\text{-NH}_3^+$ moiety.

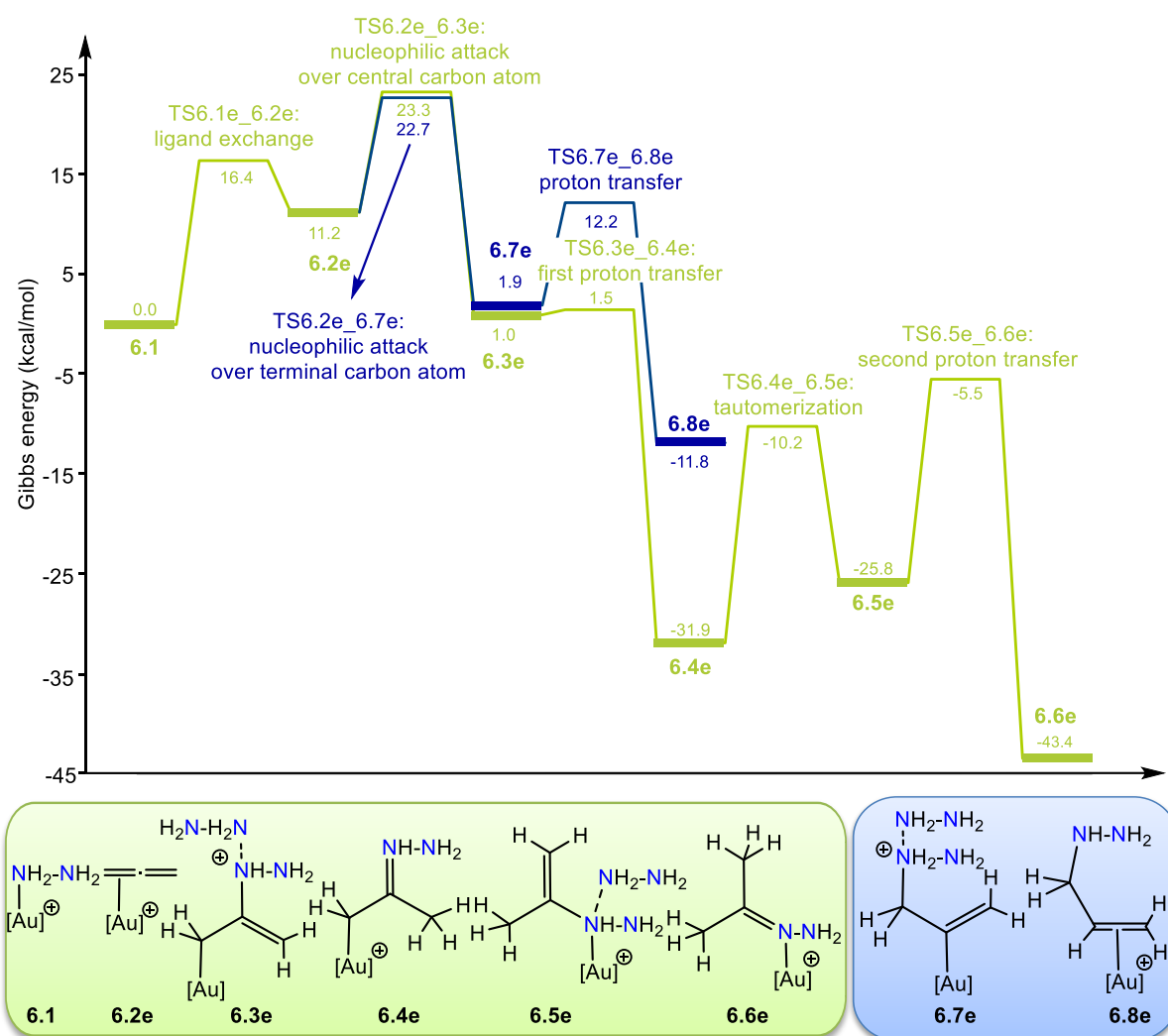


Figure 6.8: Gibbs energy profile in benzene for the hydrohydrazination of 1,2-propadiene (substrate **e**) catalyzed by $[\text{Au}(\text{CAAC})]^+$ complex. Green color: energy profile for the central nucleophilic addition leading to the major product (hydrazone); blue color: energy profile for the terminal nucleophilic addition leading to the minor product (allylhydrazine).

When the nucleophilic attack takes place over the terminal carbon atom, the reaction ends up after this first proton transfer and the subsequent decoordination to generate the allylhydrazine product. The global barrier (ΔG^\ddagger) obtained for this pathway is 22.7 kcal/mol. For the pathway involving the addition of hydrazine over the central carbon atom the process takes place similarly to that for alkynes, leading to the hydrazone. Thus, it is necessary to carry out a gold migration from carbon to nitrogen and a second proton transfer from nitrogen to carbon to yield this product. In this pathway the Gibbs barrier of the full catalytic cycle is given by the energy difference between intermediate **6.4e** and the transition state of the second proton transfer (**TS6.5e_6.6e**). The global barrier obtained ($\Delta G^\ddagger = 26.4$ kcal/mol) is very close to that for the 2-butyne hydroamination using the same catalyst (**Table 6.1**).

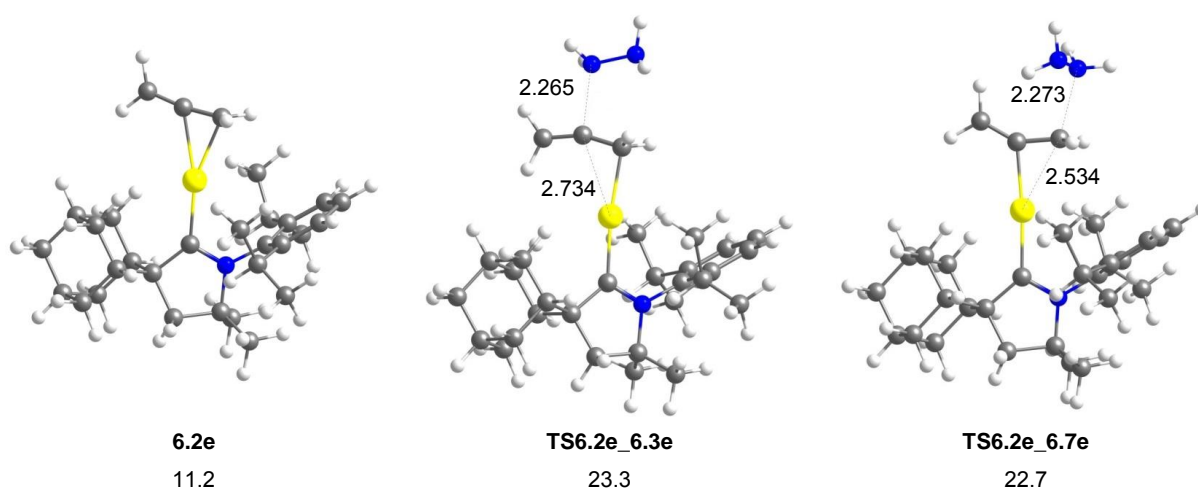


Figure 6.9: Optimized structures of intermediate involving the coordinated allene and transition states of the nucleophilic attack for the hydroamination reaction of 1,2-propadiene (substrate **e**) catalyzed by $[\text{Au}(\text{CAAC})]^+$ complex. Relative Gibbs energy values are given under each structure in kcal/mol.

The selectivity for the hydroamination reaction of allenes is governed by the nucleophilic addition step. The experimentally observed regioselectivity for hydroamination of 1,2-propadiene (2:1 for hydrazone:allylhydrazine products) would imply an energy difference between transition states of 0.4 kcal/mol favoring the addition over the central carbon atom. The results obtained showed the external addition pathway is favored by 0.6 kcal/mol. This energy difference lies within the error bars of the computational method used; showing that both pathways are quite close in energy and the regioselectivity is thus quite subtle.

Regarding the hydroamination reaction of tetraphenyl-1,2-propadiene, the transition state of the nucleophilic addition over the terminal carbon atom of the allene is placed at a very similar energy than that for 1,2-propadiene (**TS6.2f_6.7f**; 21.3 and **TS6.2e_6.7e**; 22.7 kcal/mol, respectively). However, the transition state for the nucleophilic attack over the central carbon atom is located considerably higher than that for 1,2-propadiene (30.3 and

23.3 kcal/mol, respectively). Both adducts formed by hydrazine addition to the central and terminal carbons of tetraphenyl-1,2-propadiene (**6.3f** and **6.7f** located at 13.6 and 19.5 kcal/mol respectively) are significantly destabilized compared with those for the reaction of 1,2-propadiene (**6.3e** and **6.7e** located at 1.0 and 1.9 kcal/mol respectively).

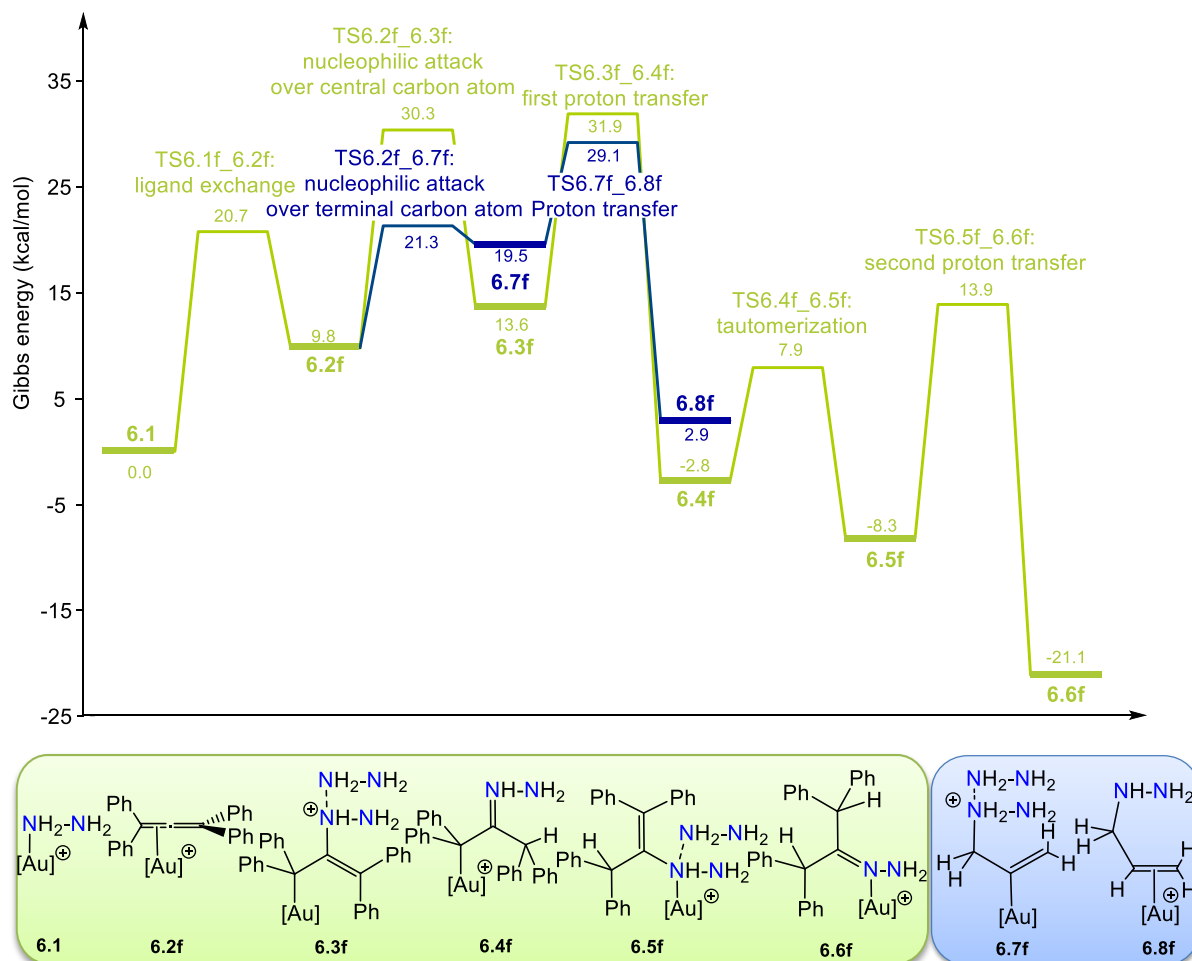


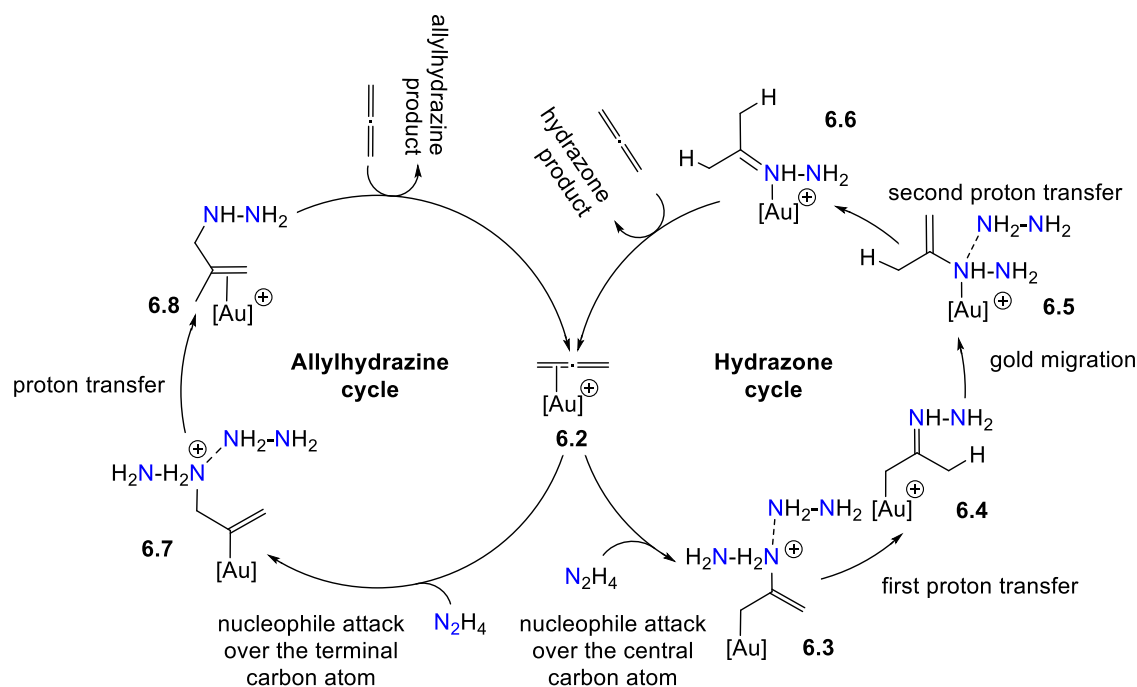
Figure 6.10: Gibbs energy profile in benzene for the hydrohydrazination of tetraphenyl-1,2-propadiene (substrate **f**) catalyzed by $[\text{Au}(\text{CAAC})]^+$ complex. Green color: energy profile for the central nucleophilic addition leading to the reaction product (hydrazone); blue color: energy profile for the terminal nucleophilic addition leading to the side reaction product (allylhydrazine).

The largest difference appears when comparing the first proton transfer step in the reaction over the central carbon atom. This step involves a low barrier with 1,2-propadiene (**TS6.3e_6.4e** is located at 1.5 kcal/mol), whereas for the tetraphenyl-1,2-propadiene is the transition state which requires the highest energy in the overall process (such transition state **TS6.3f_6.4f** is located at 31.9 kcal/mol). The global activation energy of the hydroamination process (ΔG^\ddagger) is given by the energy difference between the initial hydrazine coordinated to metal center (**6.1f**) and the transition state of the first proton transfer step (**TS6.3f_6.4f**). The ΔG^\ddagger values for tetraphenyl-1,2-propadiene (31.9 and 29.1 kcal/mol for central and terminal carbon respectively) agree with the harsh conditions at

which this reaction takes place (150 °C). The species formed by protonation at the carbon atom after this first proton transfer step in the reaction over the central carbon atom (intermediate **6.4f** located at -2.8 kcal/mol) is less stable than that for the 1,2-propadiene (intermediate **6.4e** located at -31.9 kcal/mol). The same behaviour is obtained when comparing the final hydrazone product bonded to metal center for the reaction which energies are -21.1 and -43.4 kcal/mol for the reaction starting with tetraphenyl-1,2-propadiene and 1,2-propadiene, respectively.

The energy profile obtained show the hydrohydrazination of tetraphenyl-1,2-propadiene starts with the nucleophilic addition to the terminal carbon atom which is faster but reversible being the energy barrier for the reverse reaction from the allylhydrazone complex (**6.8f**) 26.2 kcal/mol, whereas the nucleophilic addition over the central carbon atom is slower but irreversible (the reverse reaction from intermediate **6.4f** requires 34.7 kcal/mol). Overall, despite addition on both the terminal and the central carbon atoms may take place the addition over central carbon yields the experimentally observed product (the hydrazone product).

The mechanistic study with the two different substrates shows that for allenes the hydroamination reaction may take place through two different pathways. The operative mechanism obtained for the hydroamination reaction of allenes catalyzed by hydrazine is summarized in **Scheme 6.4**. They differ in the first step, the nucleophilic addition, which can take place at the central or at the terminal allene carbon atom. This step governs the regioselectivity of the process and, for the hydrazination, depending on the degree of substitution of the allene one or both pathways are taking place.



Scheme 6.4: Proposed catalytic cycle for the hydroamination of allenes.

For the pathway where the addition takes place at the terminal carbon the reaction ends with a proton transfer step which gives rise to the allylhydrazine product, whereas for the pathway where the addition takes place over the central carbon atom the reaction ends with two proton transfer steps connected by a gold migration step yielding the hydrazone product, analogously to the reaction of alkynes.

6.4 Conclusions

The mechanism of the hydroamination reaction of alkynes, alkenes and allenes with hydrazine catalyzed by the (carbene)gold(I) complexes experimentally reported by Bertrand^{137,140} and Hashmi¹⁴¹ ($[\text{Au}(\text{CAAC})]^+$, $[\text{Au}(\text{antiB})]^+$ and $[\text{Au}(\text{sa})]^+$ complexes) has been studied by means of DFT calculations. The general mechanism reported by our group for the reaction of alkynes with ammonia⁷⁴ is also operating in the case of the hydrohydrazination reaction of alkynes with hydrazine. This mechanism starts with the coordination of the hydrazine to the metal center forming the Werner complex and it is followed by a ligand exchange step where the hydrazine is substituted by the unsaturated hydrocarbon, leading to the gold π -complex which is the catalytically active species. The $[(\text{NHC})\text{Au}]^+$ species form strong Werner complexes with hydrazine, but they also form strong complexes with the unsaturated hydrocarbons. Then, it takes place a nucleophilic attack of hydrazine into the activated π -carbon-carbon bond and a proton transfer assisted by a second hydrazine molecule. The subsequent carbon to nitrogen gold migration yields the enamine intermediate. From the enamine, a second proton transfer step assisted again by hydrazine leads to the more stable imine tautomer. The energy barriers for the ligand substitution step with all the substrates analyzed are low, making this step feasible. It is associative, taking place through a tricoordinated transition state. The subsequent nucleophilic addition of hydrazine to the unsaturated hydrocarbon, happens by an outer sphere mechanism. For alkynes, the activation barrier of the full catalytic cycle is determined by the energy difference between the protonated hydrazone and the transition state of the second proton transfer. This energy barrier follows the order benzylacetylene > 2-butyne > phenylacetylene. Comparing the different carbene ligands used, the activation barriers are similar for the three gold-carbene complexes but slightly lower for $[(\text{sa})\text{Au}]^+$, in agreement with the milder reaction conditions used experimentally for this catalyst.

Regarding the hydrohydrazination of alkenes, our study shows that the main difficulty for this reaction is not the reactivity of the η^2 -alkene gold(I) complex towards the nucleophilic attack, but the protodeauration step. The high energy of the transition state of this step makes completely unfeasible this reaction.

For the hydroamination of allenes with hydrazine, it has been found that the operative mechanism is similar to that for the alkynes. The nucleophile attack on both the terminal and the central carbon atom of the η^2 -allene complexes was analyzed. The nucleophilic attack into the central carbon and two consecutive proton transfer steps connected by a

gold migration step yields the hydrazone product which is the major product for reaction of 1,2-propadiene and the only product in the reaction of tetraphenyl-1,2-propadiene. Instead, the nucleophilic attack into the terminal carbon atom and one proton transfer step gives rise to the allylhydrazine product which is the minor product in the reaction of 1,2-propadiene, and is not observed in the reaction of tetraphenyl-1,2-propadiene. For 1,2-propadiene, the nucleophilic addition has very similar barriers for the attacks into both carbon atoms, allowing the formation of a hydrazone and allylhydrazine mixture. For the tetraphenyl-1,2-propadiene, the energy barrier is defined by the energy difference between the initial Werner complex and the transition state of the first proton transfer step. The reaction initiated by the nucleophilic addition to the terminal carbon atom is faster but reversible, whereas the nucleophilic addition to the central carbon atom is slower but irreversible (from intermediate **6.4f**). Thus, only the latter product (hydrazone) is formed. This result contrasts with the usual regioselectivity in the intermolecular hydroamination of allenes, in which the nucleophile only adds to the terminal carbon atom of the allene, like in **Chapter 5** for the hydroamination reaction of allenes catalyzed by rhodium(I) complexes.

*Nothing can be more certain than this:
that we are just beginning to learn something
of the wonders of the world on which
we live and move and have our being.*

William Ramsay

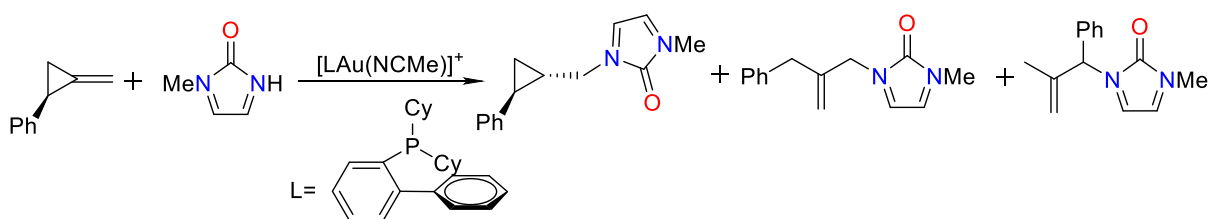
~ Chapter 7 ~

GOLD-CATALYZED ANTI-MARKOVNIKOV HYDROAMINATION OF ALKENES

This chapter collects the study of the *anti*-Markovnikov hydroamination of alkenes catalyzed by the gold(I) $[\text{Au}(\text{P}2)]^+$ complex ($\text{P}2 = \text{PCy}_2(\text{o-biphenyl})$; $\text{Cy} = \text{cyclohexyl}$) recently reported by Widenhoefer.¹⁶² The reaction mechanism and the effect of modifying the alkene and the ligand were evaluated. A manuscript summarizing these results is under preparation.

7.1 Introduction

The hydroamination reaction of alkenes catalyzed by gold(I) complexes employing NHC ligands was analyzed in **Chapter 6**. However, no experimental reports of alkene hydroamination of alkenes catalyzed by NHC complexes have been reported yet. In contrast with the cases showed in previous chapter, Widenhoefer et al. showed that gold(I)-phosphine complexes can catalyze hydroamination of ethylene and terminal alkenes.¹⁶¹ Remarkably, the same authors have published that these gold(I)-phosphine complex can also catalyze the *anti*-Markovnikov hydroamination of alkylidenecyclopropanes with an urea-based N-nucleophile.¹⁶² This is the first example of gold-catalyzed *anti*-Markovnikov hydroamination. This reaction is summarized in **Scheme 7.1**.



Scheme 7.1: Hydroamination reactions of ACP developed by Widenhoefer.

This chapter is devoted to the computational study of the Au(I) catalyzed *anti*-Markovnikov hydroamination of alkenes developed by Widenhoefer. The effect in the regioselectivity of modifying the alkene and the ligand of the catalyst is also addressed.

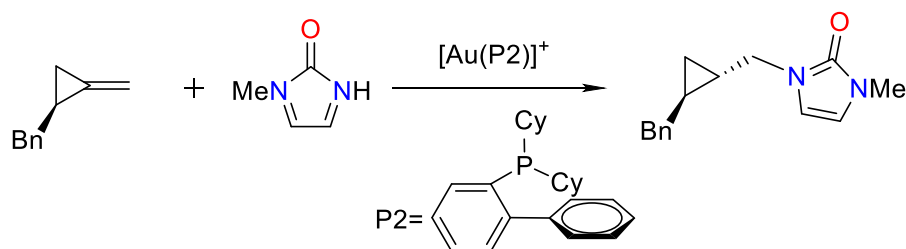
7.2 Computational methods and models

All calculations were carried out using Gaussian 09 program. Calculations were performed at DFT level by means of the M06 functional with and ultrafine grid option. The basis sets used were the 6-31G(d,p) for all the atoms, except for Au where the SDD (with an additional f orbital) along with the associated pseudopotential was employed. The structures were fully optimized in solution using SMD model with standard parameters and 1,4-dioxane as solvent ($\epsilon=2.2706$). The nature of stationary points (minima and TS) was confirmed by frequency calculations. Connections between the transition states and the minima were checked by following the IRC and subsequent geometry optimization till the minima. Energy values given in the text correspond to Gibbs energies at 298K calculated including solvent effects.

The energy decomposition analysis was performed using ADF program by means of the hybrid BP86-D3 functional. Those calculations were carried out in gas phase using TZ2P+ basis set for all atoms.

Calculations have been performed taking the $[Au(P2)]^+$ gold(I) complex without simplifications in the ligand (P2= $PCy_2(o\text{-biphenyl})$; Cy=cyclohexyl). 1-benzyl-2-

methylenecyclopropane has been employed as alkylidenecyclopropane (ACP) substrate in the analysis of the reaction mechanism. The reaction studied is depicted in **Scheme 7.2**.



Scheme 7.2: Hydroamination reactions of ACP catalyzed by $[\text{Au}(\text{P}2)]^+$ complex.

Other different alkenes and gold(I) complexes ($[\text{Au}(\text{PMe}_3)]^+$ and $[\text{Au}(\text{sa})]^+$; **Scheme 7.4**) were also employed to study the nature of the substrate and the gold ligand. 1-methylimidazolidin-2-one has been selected as N-nucleophile in all cases. The structures are named according to the following procedure: **7x.y** where x correspond to the point in the energy profile and y correspond to the Markovnikov (m) or *anti*-Markovnikov (a) isomer obtained (for example, **7.2a** correspond to the second point for the reaction yielding the *anti*-Markovnikov isomer).

7.3 Results and Discussion

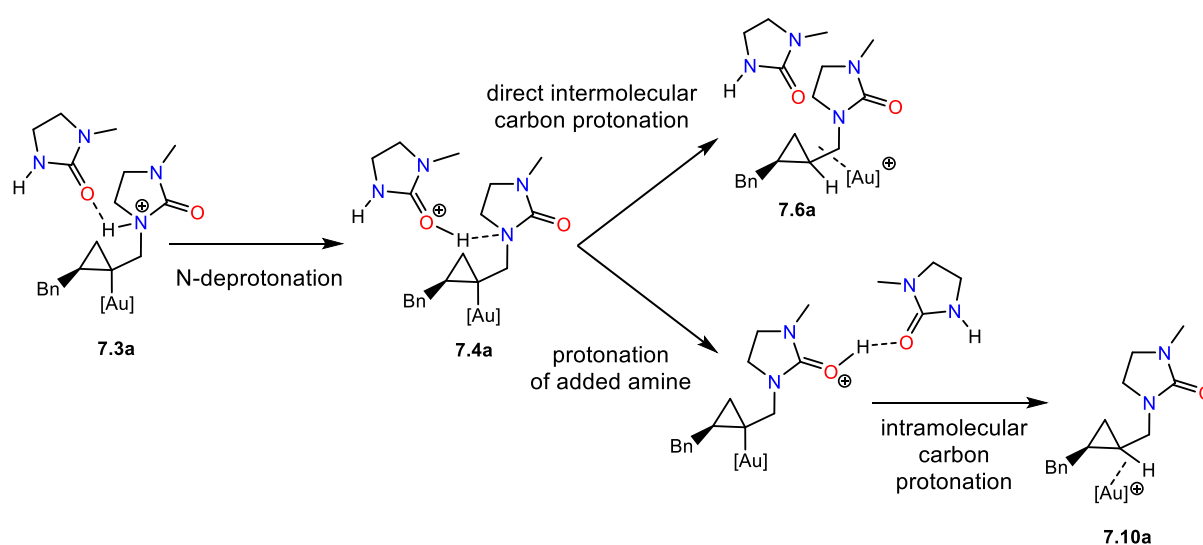
This chapter is divided in three main sections. The first one analyzes the operative mechanism for the hydroamination reaction of alkylidenecyclopropanes catalyzed by a gold(I) complex with a phosphine ligand using 1-methylimidazolidin-2-one as nucleophile. In the next sections the influence of nature of the substrate and the gold ligand are evaluated by analyzing the hydroamination reactions of eight different alkenes catalyzed by three different gold(I) catalysts including different ligands (P2, PMe_3 and sa ligands, **Schemes 7.2** and **7.4**).

7.3.1 Analysis of the reaction mechanism

As discussed in the precedent chapter, the mechanism for the gold(I) catalyzed hydroamination of alkenes is generally described as an initial generation of a catalytically active gold- π complex from a gold-chloride precursor followed by the nucleophilic addition of the nucleophile into the carbon-carbon double bond activated by coordination to the gold center. Then takes place the proton migration from nitrogen to carbon atoms and finally a protodeauration of the alkenyl gold(I) intermediate to generate the final reaction product.²³⁴

The complete energy profile for the hydroamination of an alkylidenecyclopropane (ACP) with a benzyl substituent (1-benzyl-2-methylenecyclopropane) with a urea-base N-nucleophile (1-methylimidazolidin-2-one) has been computed. For the mechanistic evaluation, the nucleophilic addition over both terminal and internal carbon atoms of the

ACP was analyzed. As we will see later, the regioselectivity of the reaction is defined in the nucleophilic addition step. The proton migration has been already shown to be significantly favored by the presence of the counterion or the nucleophile itself.⁷³ For the proton migration assisted by the nucleophile, the first step is the deprotonation of the nucleophile by protonating a second amine molecule. From the protonated amine, two different possibilities were evaluated (**Scheme 7.3**): the direct protonation of the carbon atom of the alkenyl moiety (intermolecular pathway, **Figure 7.1** colors orange and green) or the protonation of the oxygen of the added urea-based nucleophile (intramolecular pathway **Figure 7.1** colors blue and purple) before the protonation of the carbon atom of the alkenyl moiety. Both possibilities were evaluated for both Markovnikov and *anti*-Markovnikov processes. The Gibbs energy profiles of the four pathways analyzed are depicted in **Figure 7.1**.



Scheme 7.3: Pathways analyzed for the protodeauration process.

The first step of the hydroamination reaction of alkylidenecyclopropanes is the nucleophilic addition of the amine into the coordinated alkene. The Gibbs energy barriers for the nucleophilic addition step into terminal and internal carbon atoms of alkene (**TS7.1_7.2a** and **TS7.1_7.2m**) are 21.0 and 21.7 kcal/mol, respectively. The adducts formed after the Markovnikov and *anti*-Markovnikov nucleophilic addition (**7.2m** and **7.2a**) were located at 13.5 and 20.2 kcal/mol, respectively. As it can be appreciated in **Figure 7.1**, the nucleophilic addition is the rate determining step of the process. The energy difference ($\Delta\Delta G^\ddagger$) between *anti*-Markovnikov and Markovnikov pathways is 0.7 kcal/mol in favor of the *anti*-Markovnikov isomer, agreement with the experimental observation. However, our calculations predict a 1:3 Markovnikov/*anti*-Markovnikov product ratio but the Markovnikov isomer is not observed experimentally.

The deprotonation of the amine by protonating the oxygen of a second amine molecule takes place from the adduct product formed in the nucleophilic addition. Thus, it is necessary to bring together the adduct product and the second amine forming intermediate

7.3 which in an exergonic process (6.9 kcal/mol for the *anti*-Markovnikov version; **7.3a** and 9 kcal/mol for Markovnikov one; **7.3m**). The subsequent deprotonation transition state for the *anti*-Markovnikov pathway (**TS7.3a_7.4a**) is located at 18.5 kcal/mol whereas for the Markovnikov pathway (**TS7.3m_7.4m**) it could not be found due to the flatness of the transition state. The intermediate with the second amine protonated (**7.4**) is much more stable for the Markovnikov pathway than for the *anti*-Markovnikov one (3.6 and 18.2 kcal/mol respectively).

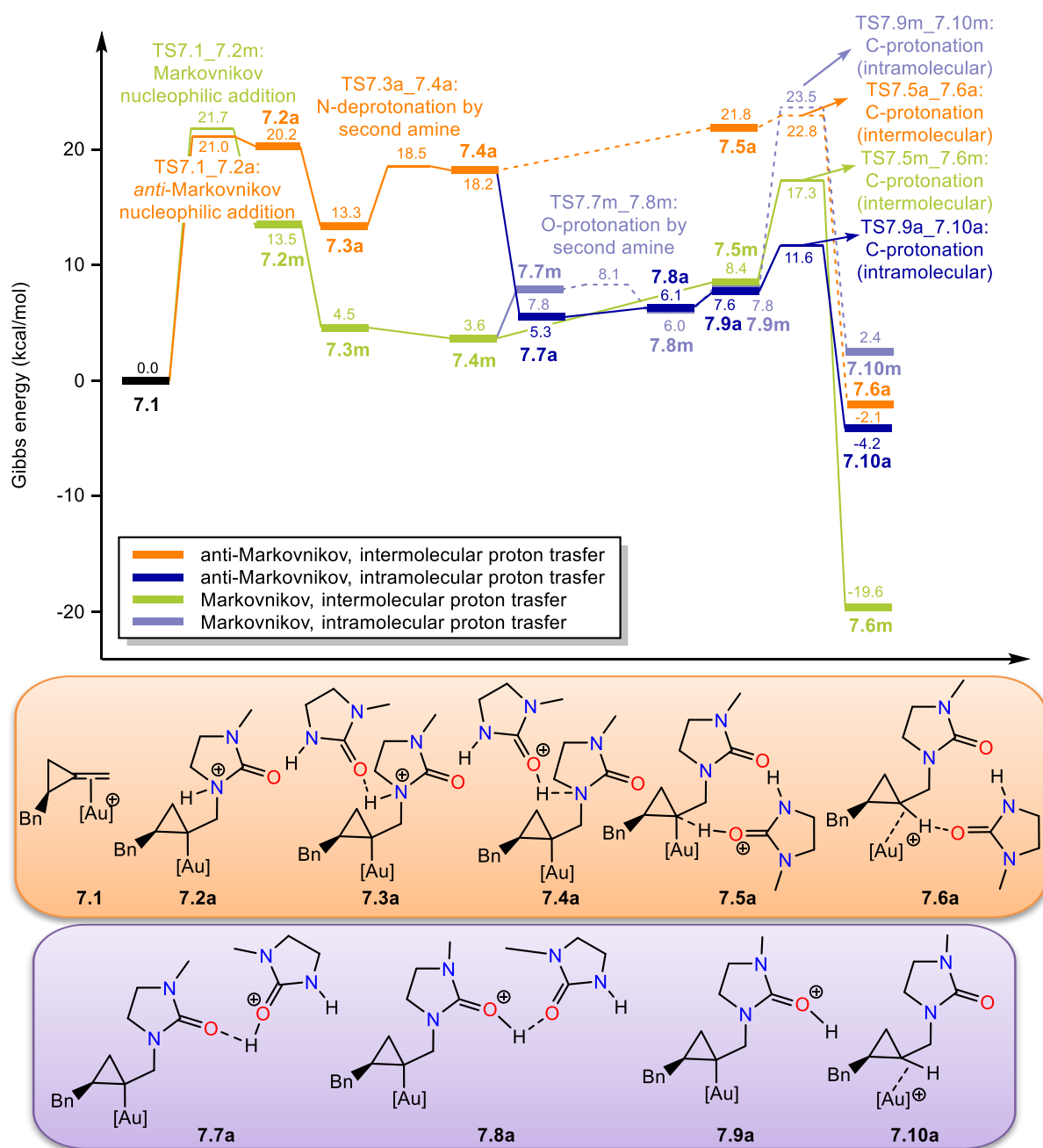


Figure 7.1: Mechanistic study of hydroamination of 1-benzyl-2-methylenecyclopropane with 1-methyl-imidazolidin-2-one catalyzed by a gold(I) complex with a phosphine ligand (P2).

From this intermediate (**7.4**) it happens the protonation of the carbon atom of the alkenyl moiety. As mentioned before, two different pathways were evaluated (**Scheme 7.3**): the direct protonation of the carbon atom of the alkenyl moiety (intermolecular pathway) and the protonation of the oxygen of the added urea-based nucleophile before the protonation of the carbon atom of the alkenyl moiety (intramolecular pathway).

For the direct protonation it is necessary to move the second amine close to the carbon atom yielding intermediate **7.5** whereas for the intramolecular pathway the second amine has to be placed close to the added amine giving rise to intermediate **7.7**. These three intermediates (**7.4**, **7.5** and **7.7**) have formally the same structure but exhibit different interaction energies due to the second amine is placed at different positions.

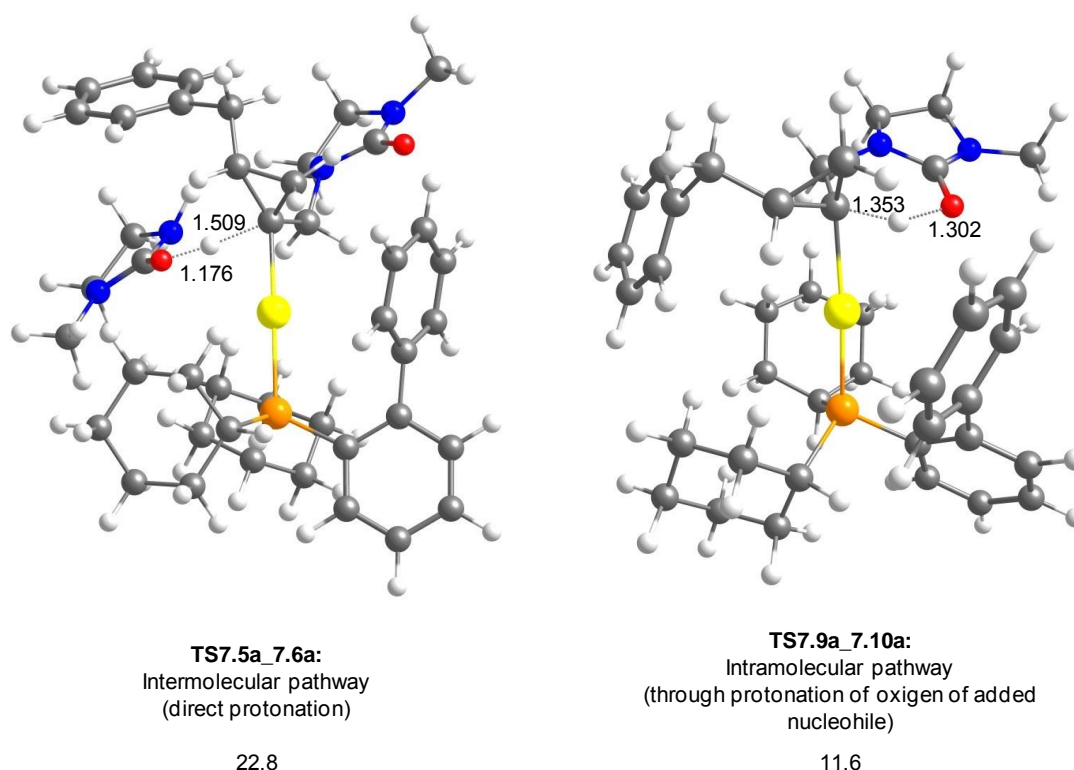


Figure 7.2: Optimized structures of transition states of direct protonation of carbon (**TS7.5a_7.6a**) and protonation of carbon through intramolecular pathway (**TS7.9a_7.10a**) for the *anti*-Markovnikov version. Relative Gibbs energy values are given under each structure in kcal/mol.

For the *anti*-Markovnikov addition, the transition state for the direct protonation of the carbon atom (**TS7.5a_7.6a**) lies at 22.8 kcal/mol whereas the transition state for the protonation of the carbon atom through the migration to the oxygen of the added nucleophile (**TS7.9a_7.10a**, intramolecular pathway) only requires 11.6 kcal/mol. The transition states for the direct protonation of carbon and the protonation of carbon through intramolecular pathway (from the protonated added amine) are depicted in **Figure 7.2**. For the Markovnikov addition, however, the results show the opposite tendency; the barrier for

the direct pathway is lower since the transition state of the direct carbon protonation (**TS7.5m_7.6m**) lies at 17.3 kcal/mol whereas that going through the added nucleophile (**TS7.9m_7.10m**) is found at 23.5 kcal/mol.

According with this results the protonation of the carbon atom in the *anti*-Markovnikov isomer requires 11.6 kcal/mol (intramolecular pathway, **TS7.9a_7.10a**) whereas the transition state for the protonation of the carbon atom for the Markovnikov isomer lies at 17.3 kcal/mol (intermolecular pathway, **TS7.5m_7.6m**). As it can be appreciated in **Figure 7.1**, for both the *anti*-Markovnikov and Markovnikov additions, the energy barriers for the protonation of the carbon atom are lower than those for the nucleophilic addition, so the highest point of the energy profiles correspond to the nucleophilic addition step (**TS7.1_7.2a**; 2.1.0 kcal/mol and **TS7.1_7.2m**; 21.7 kcal/mol, respectively).

The nucleophilic addition of the amine to the ring of the ACP substrate which also includes the ring-opening process was also analyzed. The transition states for the nucleophilic addition to the carbons of cyclopropane (the one containing the benzyl group and the contiguous) were located at 39.8 and 38.4 kcal/mol respectively, clearly higher than the addition over both carbons of the alkene. Our calculations do not explain the formation of the competing side reaction products involving the ring opening (**Scheme 7.1**). For the hydroamination of 1-benzyl-2-methylenecyclopropane a 25:1 product ratio is obtained experimentally.

During the course of this study, a manuscript studying the hydroamination of alkylidenecyclopropanes (ACP) was published.²⁷² In this manuscript, Wang et al. reported the mechanistic evaluation of Markovnikov and *anti*-Markovnikov hydroamination of 1-phenyl-2-methylenecyclopropane. They also included the study of the side-reaction products involving the opening of the cyclopropane ring obtained experimentally (**Scheme 7.1**). They demonstrate that the ring opening always takes place by the sp^3 C- sp^3 C bond and then takes place the nucleophilic attack of the urea-based N-nucleophile. The barrier energy for the formation of the ring-opening products is 0.3 kcal/mol higher in energy than the formation of the *anti*-Markovnikov product in very agreement with the 2.5:1 product ratio obtained experimentally for the hydroamination of 1-phenyl-2-methylenecyclopropane.

Overall, the most favored pathway gives the *anti*-Markovnikov addition, with the urea-based nucleophile playing a dual role in the proton migration step. This implies that the nucleophile, for its assisting role, has to be basic enough to take the proton from the added nucleophile, and acid enough to give it back to either the C atom (direct protonation) or the O of the added nucleophile (intramolecular pathway) to generate the final product. The participation of the nucleophile allowing the intramolecular pathway may be related to the fact that this type of nucleophiles is more active upon hydroamination than other secondary amines, such as the ones studied in previous chapters.

7.3.2 Effect of modifying the alkene

The nucleophilic addition is the rate determining step, thus, the difference in the energy barriers for both pathways should correspond with the regioselectivity. This section is devoted to analyze how nature of the alkene affects the regioselectivity. To this aim, the nucleophilic addition for both Markovnikov and *anti*-Markovnikov pathways was computed for a set of eight alkenes. Five different alkenes studied experimentally by Widenhoefer were analyzed: ethylene (entry 1), styrene (entry 5), isobutene (entry 7), 1-benzyl-2-methylenecyclopropane (entry 6), and methylenecyclobutene (MCB) (entry 8).^{161,162} For styrene (entry 5), isobutene (entry 7) and methylenecyclobutene (MCB) (entry 8) the Markovnikov isomer is the major one and only for 1-benzyl-2-methylenecyclopropane (entry 6) the *anti*-Markovnikov regioselectivity is preferred. Unfortunately, reaction of ethylene (entry 1), styrene (entry 5) and isobutene (entry 7) were carried out experimentally using a different catalyst, and no experiments with $[\text{Au}(\text{P}2)]^+$ catalyst are available for direct comparison.

Additionally, a series of alkenes including substituents that modify the backbonding capacity of the terminal alkene have been analyzed, CF_3 was used as electrowithdrawing group and Me as donating group. In this line three alkene were studied: the alkene including one CF_3 group (entry 3), two CF_3 groups (entry 2) and one CF_3 and one methyl group (entry 4). The energy barriers for Markovnikov and *anti*-Markovnikov addition as well as the energy differences for the series of alkenes considered are collected in **Table 7.1**.

As previously showed in **Section 7.3.1**, the energy difference between Markovnikov and *anti*-Markovnikov addition for ACP (entry 6) is 0.7 kcal/mol in favor of the *anti*-Markovnikov adduct. Following the available experimental data, the MCB was also evaluated. For the MCB reactant (entry 8) calculations give an energy difference of -7.3 kcal/mol in favor of the Markovnikov product, in agreement with experiments, where the *anti*-Markovnikov product is not observed.

As mentioned before, a series of alkenes including substituents that modify the backbonding capacity of the terminal alkene have been analyzed. When isobutene was used as reactant, where both substituents are donating groups (entry 7), the energy difference is 7.0 in favor of the Markovnikov product, in agreement with experimental data. When one substituent is CF_3 (entry 3) the difference of the energy barrier for the Markovnikov and *anti*-Markovnikov addition is 8.4 kcal/mol in favor of the *anti*-Markovnikov version. When both substituents are CF_3 (entry 2), the regioselectivity was even much more pronounced with an energy difference of 15.1 kcal/mol. For the case where one of the substituents is an electrowithdrawing group and the other a donating group (entry 4), regioselectivity decreases respect having only one electrowithdrawing group since the energy difference is 7.4 kcal/mol. Styrene was also analyzed (entry 5) and the difference energy obtained was 2.0 kcal/mol therefore according with our results, the *anti*-Markovnikov isomer should be

obtained. As mentioned before, styrene hydroamination have been experimentally performed with a slightly different gold(I) complex ((L)AuCl catalyst; L=2-di-tert-butylphosphino-1,1'-binaphthyl) obtaining the exclusively the Markovnikov isomer.¹⁶¹

Table 7.1: Gibbs energy barriers (Markovnikov, ΔG_M^\ddagger and *anti*-Markovnikov, ΔG_{aM}^\ddagger) for the *anti* nucleophilic attack catalyzed by $[\text{Au}(\text{P}2)]^+$ and geometrical parameters for their initial intermediates (π -coordinated alkenes).

Entry	Substrate	ΔG_M^\ddagger	ΔG_{aM}^\ddagger	$\Delta\Delta G^\ddagger$	d_1 (Rh-C _t)	d_2 (Rh-C _i)	d_3 (C _t -C _i)	Δ	d_1-d_2
1		15.4	-	-	2.306	2.308	1.364	0.004	-0.002
2		23.2	8.1	15.1	2.302	2.295	1.367	0.010	0.007
3		19.0	10.6	8.4	2.297	2.299	1.365	0.003	-0.002
4		23.5	16.1	7.4	2.272	2.377	1.369	0.178	-0.105
5		21.4	19.4	2.0	2.259	2.413	1.375	0.261	-0.154
6		21.7	21.0	0.7	2.276	2.395	1.358	0.205	-0.119
7		20.4	27.4	-7.0	2.249	2.506	1.376	0.444	-0.257
8		20.0	27.3	-7.3	2.246	2.502	1.366	0.445	-0.256

As discussed in **Chapter 4 (Section 4.3.3)**, the activation of an olefin ligand by a metal center toward the nucleophilic addition was qualitatively analyzed by Eisenstein and Hoffman in the 80s.^{75,76} They realized that the activation of an olefin takes place by an η^2 to η^1 slippage and is also related with the shape of the LUMO. Distortion of the ideal position (from symmetric olefin where the distance between metal and both carbons of the alkene is the same) drives the activation of the olefin. This idea was applied in **section 4.3.3** for rhodium complexes.

In **Figure 7.3** is represented the difference between ΔG^\ddagger for the Markovnikov and *anti*-Markovnikov addition against the difference between both carbons of the alkene and the

metal center (d_1-d_2). All the distances are collected in **Table 7.1**. There is a very good correlation between both parameters, similarly to what happens for hydroamination of alkenes catalyzed by [Rh(DPEphos)] complex (**Section 4.3.3**).

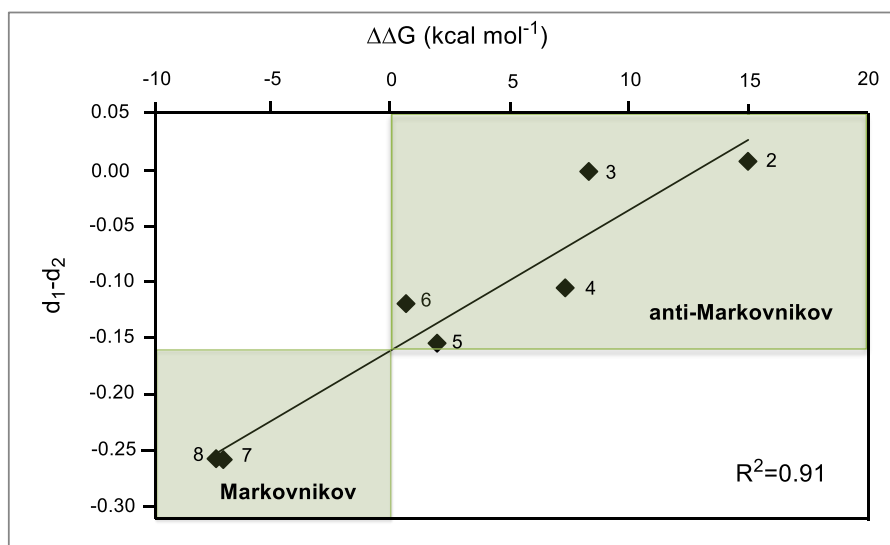


Figure 7.3: Representation of difference in Gibbs energy between Markovnikov and *anti*-Markovnikov addition barriers ($\Delta\Delta G^\ddagger$) against difference in distance of both carbon atoms of alkene and the metal center (d_1-d_2 parameter). Numbers corresponds with entries in **Table 7.1**.

Note that a kinetic parameter ($\Delta\Delta G^\ddagger$) can be correlated to a magnitude that can be obtained by knowing the coordination mode of the alkene to the catalyst (an intermediate, that corresponds to a minima of the potential energy surface). This opens the door to estimate regioselectivity by measuring geometrical parameters of reactants.

The results summarized in **Table 7.1** showed that modifying the alkene substituents of the alkene also modifies the Gibbs energy barriers for the Markovnikov and *anti*-Markovnikov additions and their energy difference ($\Delta\Delta G^\ddagger$). To further analyze the regioselectivity the backdonation for the gold to the antibonding orbital of the alkene was estimated from the orbital term of an EDA. **Figure 7.4** shows the representation of the backdonation versus the barrier Gibbs energy of the Markovnikov and *anti*-Markovnikov nucleophilic additions.

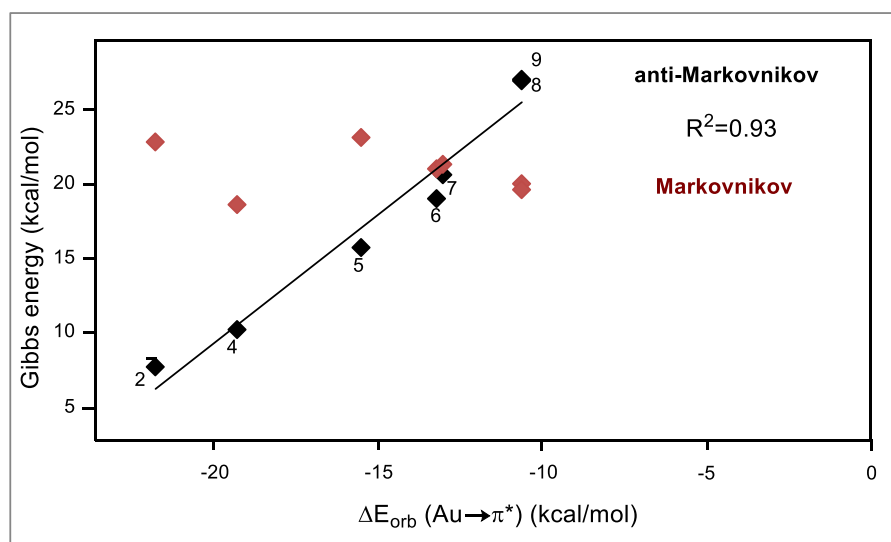
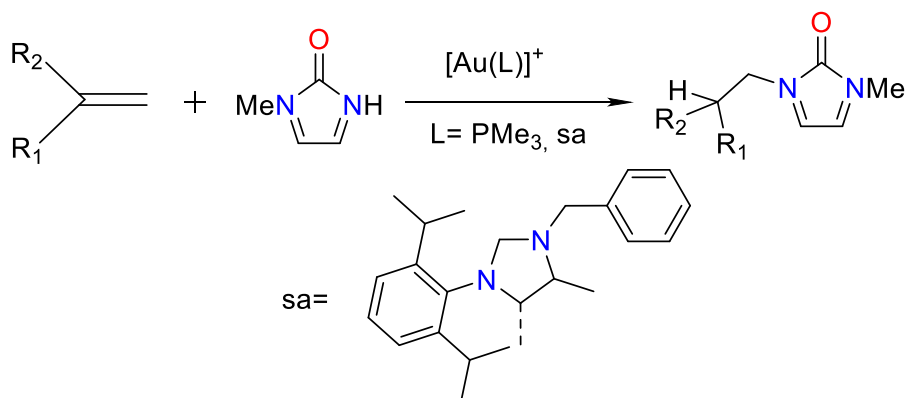


Figure 7.4: Representation of backdonation versus relative Gibbs energy of Markovnikov (red squares) and *anti*-Markovnikov (black line) addition. Numbers corresponds with entries in **Table 7.1**.

Our results indicate that the backdonation from the metal to the alkene increases (more negative values) by increasing the capacity of the alkene for accepting metal electron donation including electrowithdrawing substituents. In **Figure 7.4** can be appreciated that there is a linear relationship between the magnitude of the backdonation and the barrier for *anti*-Markovnikov addition: the higher the capacity of the alkene for accepting metal electron donation (including electrowithdrawing substituents), the higher backdonation from the metal (more negative values) and the lower the *anti*-Markovnikov energy barrier. Such relationship is not observed for the Markovnikov addition; in this case the energy barriers are kept in a much narrower range, between 19 and 24 kcal/mol with a non-clear trend. At a backdonation strength of about 13 kcal/mol regioselectivity is reversed.

7.3.3 Effect of modifying the ligand

The effect of modifying the ligand of the catalyst was also computationally evaluated. The nucleophilic addition of eight different alkenes was studied by using as catalyst a gold(I) complex with two additional ligands: the trimethylphosphine (PMe_3) which is a stronger electron-donor phosphine than P2-phosphine and an abnormal N-heterocyclic carbene (sa), which is also a more electron-donating ligand. Such reactions are summarized in **Scheme 7.4**.

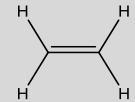
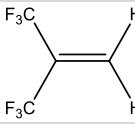
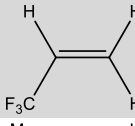
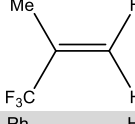
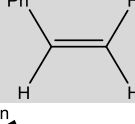
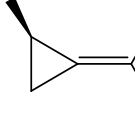
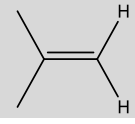
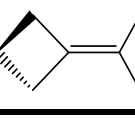


Scheme 7.4: Hydroamination reactions studied in this section.

The trimethylphosphine (PMe₃) was selected as ligand because it is one of the better electron-donating phosphine ligands. Following the tendency found in previous section (**Figure 7.4**, higher backdonation implies a lower *anti*-Markovnikov barrier), it was expected that the use of this ligand should improve the regioselectivity for the *anti*-Markovnikov product compared to the P2 ligand. The Gibbs energy barriers for both Markovnikov and *anti*-Markovnikov additions obtained as well as the difference energies are collected in **Table 7.2**. Comparing data in **Table 7.2** (PMe₃ ligand) with **Table 7.1** (P2 ligand), it can be observed that, the Gibbs energy barrier for both Markovnikov and *anti*-Markovnikov nucleophilic additions generally decreases when changing the P2 ligand for the trimethylphosphine ligand (PMe₃). Nevertheless, even though *anti*-Markovnikov barrier have been decreased with PMe₃ catalyst, in all cases the reduction of the Markovnikov barriers is higher than for the *anti*-Markovnikov addition. As consequence, *anti*-Markovnikov hydroamination is not enhanced with this ligand, in contrast the opposite tendency is found.

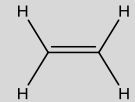
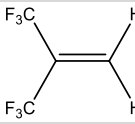
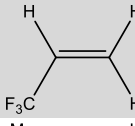
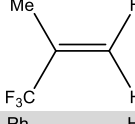
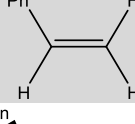
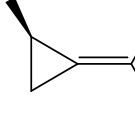
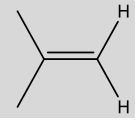
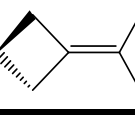
For the alkene including two electrowithdrawing groups (entry 2), the *anti*-Markovnikov addition is preferred by 12.4 kcal/mol using the PMe₃ ligand while such energy difference for P2 ligand is 15.1 kcal/mol. For the case where one of the substituents is an electrowithdrawing group and the other a donating group (entry 4), the energy difference is 2.9 kcal/mol (such difference when using the P2 ligand was 7.4 kcal/mol). For styrene as reactant (entry 5), the Markovnikov addition was preferred by 1.4 kcal/mol when using the trimethylphosphine, whereas for the P2 ligand the *anti*-Markovnikov addition was preferred by 2.0 kcal/mol. The same behavior was found for the reaction of ACP where the *anti*-Markovnikov regioselectivity is observed for P2 ligand whereas the other regioisomer is favored for the PMe₃ ligand (the energy difference is 0.7 and - 1.9 kcal/mol respectively). Isobutene and MCB (entries 7 and 8) show lower Gibbs barrier for the Markovnikov additions.

Table 7.2: Gibbs energy barriers (Markovnikov, ΔG_M^\ddagger and *anti*-Markovnikov, ΔG_{aM}^\ddagger) for the *anti* nucleophilic attack catalyzed by $[\text{Au}(\text{PMe}_3)]^+$, and the corresponding geometrical parameters for their initial intermediates calculated for each alkene.

Entry	Substrate	ΔG_M^\ddagger	ΔG_{aM}^\ddagger	$\Delta\Delta G^\ddagger$	d_1 (Rh-C _t)	d_2 (Rh-C _i)	d_3 (C _t -C _i)	Δ	d_1-d_2
1		14.4	-	-	2.318	2.317	1.363	- 0.0011	0.001
2		18.4	6	12.4	2.355	2.309	1.364	- 0.0794	0.046
3		16.3	8.7	7.6	2.337	2.315	1.361	- 0.0384	0.022
4		17.7	14.8	2.9	2.303	2.383	1.367	0.1370	-0.080
5		17.1	18.5	-1.4	2.272	2.424	1.375	0.2597	-0.152
6		19.9	21.8	-1.9	2.275	2.405	1.358	0.2245	-0.130
7		19.2	27.4	-8.2	2.253	2.483	1.376	0.3953	-0.230
8		16.9	24.8	-7.9	2.257	2.509	1.366	0.4407	-0.252

The hydroamination reaction of alkenes was also analyzed by using the catalyst with the best performance of the three studied in the previous chapter: the abnormal-NHC ligand (**Scheme 7.4**). The Gibbs energies for both Markovnikov and *anti*-Markovnikov nucleophilic additions for the hydroamination reaction of the same eight alkenes as well as the energy differences between both pathways are gathered in **Table 7.3**.

Table 7.3: Gibbs energy barriers (Markovnikov, ΔG_M^\ddagger and *anti*-Markovnikov, ΔG_{aM}^\ddagger) for the *anti* nucleophilic attack catalyzed by $[\text{Au}(\text{sa})]^+$, and the corresponding geometrical parameters for their initial intermediates calculated for each alkene.

Entry	Substrate	ΔG_M^\ddagger	ΔG_{aM}^\ddagger	$\Delta\Delta G^\ddagger$	d_1 (Rh-C _t)	d_2 (Rh-C _i)	d_3 (C _t -C _i)	Δ	d_1-d_2
1		16.9	-	-	2.282	2.288	1.365	0.009	-0.006
2		21	5.6	15.4	2.303	2.266	1.368	-0.063	0.037
3		18.4	11	7.4	2.296	2.276	1.364	-0.034	0.020
4		21.1	15.4	5.7	2.278	2.346	1.369	0.115	-0.068
5		19.9	21.7	-1.8	2.262	2.353	1.376	0.154	-0.091
6		19.4	20.8	-1.4	2.247	2.336	1.36	0.150	-0.089
7		20.5	27.7	-7.2	2.243	2.425	1.377	0.309	-0.182
8		19.4	27	-7.6	2.236	2.441	1.367	0.350	-0.205

The Gibbs energy differences obtained using the abnormal NHC ligand are quite similar of that obtained for the P2 ligand. However, the regioselectivity is reversed in favor of the Markovnikov isomer for entries 5 and 6. The *anti*-Markovnikov regioselectivity is observed for those reactants including an electrowithdrawing CF₃ group (entries 2, 3 and 4) with an energy difference of 15.4, 7.4 and 5.7 kcal/mol respectively. Such energy differences for the case of using the P2 ligand are 15.1, 8.4 and 7.4 kcal/mol, respectively. For the reaction of styrene and ACP the Markovnikov addition is preferred by 1.8 and 1.4 kcal/mol, respectively (entries 5 and 6); for the P2 ligand the *anti*-Markovnikov regioselectivity was preferred by 2.0 and 0.7 kcal/mol respectively. When the reactant is isobutene or MCB (entries 7 and 8) the Markovnikov addition is preferred using both sa and P2 ligands (energy differences are 7.2 and 7.6 for sa ligand and 7.0 and 7.3 for P2 ligand, respectively).

Overall, calculations indicate that the *anti*-Markovnikov regioselectivity is lower using the trimethylphosphine ligand (PMe₃) or the abnormal NHC ligand (sa) than for P2 ligand.

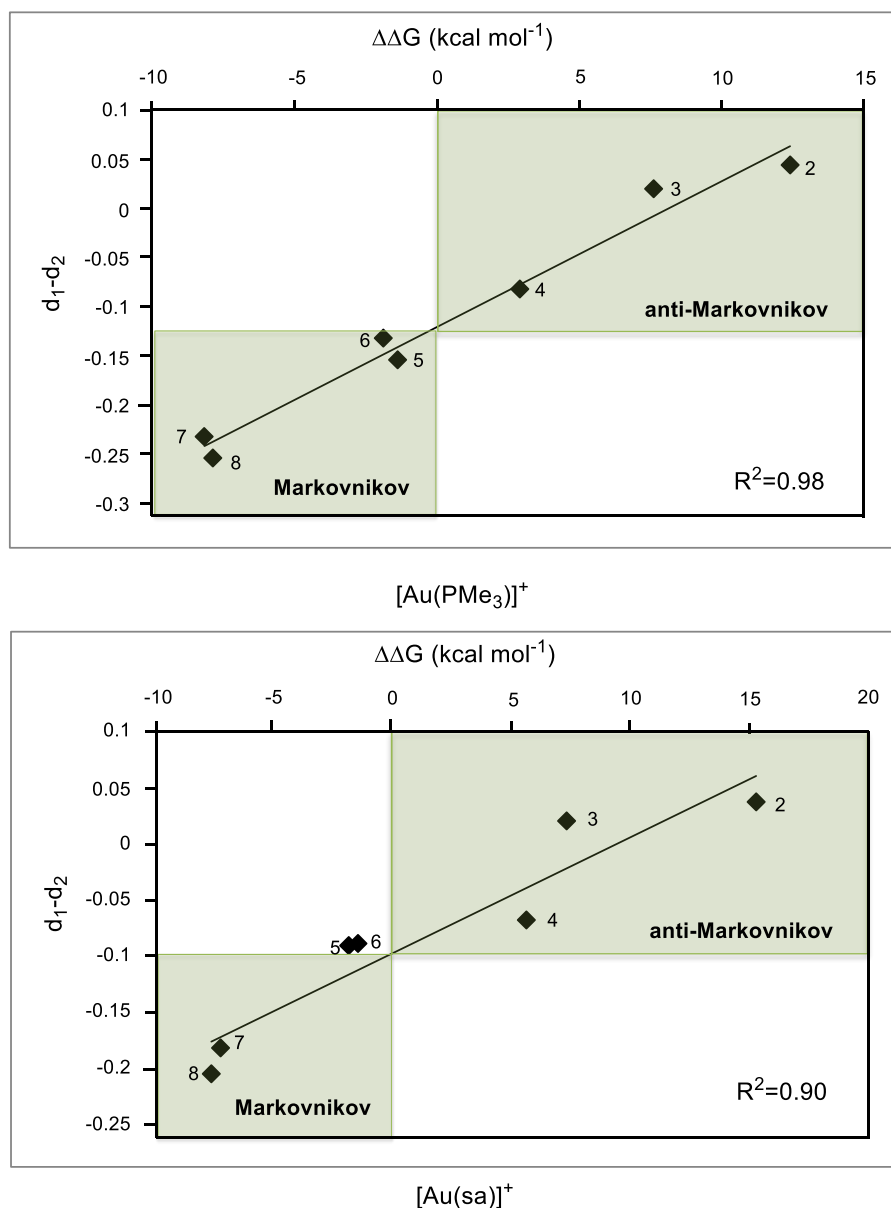


Figure 7.5: Representation of difference in energy between Markovnikov and *anti*-Markovnikov addition ($\Delta\Delta G^\ddagger$) against difference in distance of both carbon atoms of alkene and the metal center (d_1-d_2 parameter) for hydroamination of alkenes catalyzed by $[\text{Au}(\text{PMe}_3)]^+$ and $[\text{Au}(\text{sa})]^+$.

In order to prove that the regioselectivity can be also related with the coordination mode of the alkene when these two ligands was used (PMe₃ and sa), the difference of distances between both carbon atoms of alkene and the metal center (d_1-d_2) was plotted versus the energy difference of Markovnikov and *anti*-Markovnikov additions ($\Delta\Delta G^\ddagger$). Such representations are depicted in **Figure 7.5**. A very good correlations were found for the reactions catalyzed by the gold(I) complex with both PMe₃ and sa ligands.

7.3 Conclusions

The mechanism of the hydroamination reaction of ACP with a urea-based amine catalyzed by a gold(I) complex with a phosphine P2 ligand was analyzed by means of DFT calculations. The general mechanism is described as an alkene activation mechanism. The first step is the coordination of the alkene to the metal center with a subsequent nucleophilic addition of the amine into the activated alkene. This step is the rate determining step for both Markovnikov and *anti*-Markovnikov reactions. Then it takes place the metal center protonation assisted by a second amine molecule. The protonation can occur directly from the second amine or through the previous protonation of the added amine.

The reaction mechanism was studied with 1-benzyl-2-methylenecyclopropane for both Markovnikov and *anti*-Markovnikov additions being the *anti*-Markovnikov the one that requires less energy. The effect of modifying the backdonation character of the alkene was analyzed and it was found that the energy barrier for the *anti*-Markovnikov addition decreases when the capacity of the alkene for accepting metal electron donation increases. The difference of the Markovnikov and *anti*-Markovnikov barriers was plotted versus a geometrical parameter that measures the degree of slippage of the alkene in the π -coordinated intermediate and a good correlation between both parameters was found.

The effect of modifying the ligand of the catalyst was also analyzed. In this line, two different ligands were also analyzed: the trimethylphosphine (PMe₃) because it is one of the better electron-donating phosphine ligands and the so abnormal N-heterocyclic carbene since, of the three studied in the previous chapter, it is the one providing the better results. In both cases *anti*-Markovnikov regioselectivity was reduced with respect to the P2 ligand.

*Everything is theoretically
impossible, until it is done.*

Robert A. Heinlein

~ Chapter 8 ~

GENERAL CONCLUSIONS

This chapter is devoted to present a general overview of concluding remarks as well as a comparison between different studies included in this dissertation.

The main goal of this thesis is to acquire a deeper knowledge on the intermolecular hydroamination reaction by means of DFT calculations. As mentioned in the introduction, there are some challenges about the hydroamination reaction yet to be undertaken, such as the use of unactivated olefins and small N-nucleophile reagents, like hydrazine or ammonia, the control of the regioselectivity, especially the *anti*-Markovnikov addition, and the control of the enantioselectivity.

As is remarked in the objectives section (Chapter 3), all the particular reactions studied in this thesis are focused to analyze several of the abovementioned challenges of the hydroamination reactions. In this line the concrete selected reaction for the computational analysis of their reaction mechanisms are the following:

- In Chapter 4 the intermolecular *anti*-Markovnikov hydroamination reaction of styrene catalyzed by a cationic rhodium(I) complex has been studied, as an example of regioselectivity.
- Chapter 5 is devoted to analyze the enantioselective hydroamination reaction of allenes catalyzed by a cationic rhodium (I) complex.
- In Chapter 6 the hydroamination reaction of alkynes, alkenes and allenes catalyzed by a cationic gold(I) is studied. The importance of this chapter is the study of use hydrazine as amine, as an important case for the use of small N-nucleophile molecules.
- Chapter 7 is focused to analyze the hydroamination reaction of alkenes catalyzed by gold(I) complexes as another example of *anti*-Markovnikov regioselectivity of alkenes.

The specific conclusions of each study have been described in the corresponding section. Herein, a general overview of concluding remarks as well as a comparison between different studies is presented.

The general mechanism for hydroamination reaction catalyzed by rhodium and gold complexes is an electrophile activation mechanism which involves the initial coordination of the electrophile molecule as a π -complex and the nucleophilic attack of amine into the coordinated carbon-carbon multiple bond. The main difference between rhodium and gold catalyst remains in the subsequent proton transfer. For the rhodium-catalyzed hydroamination this proton transfer takes place by a protonation of the metal center and a reductive elimination steps. For the hydroamination reaction catalyzed by gold complexes, the proton transfer takes place assisted by a second nucleophile molecule through an intermediate which involves the protonated amine.

This nature of the operative mechanism can be the reason, or at least one of the main reasons why the hydroamination reaction of alkenes catalyzed by gold complexes does not work with secondary amines (reaction studied in Chapter 6). This reaction requires an amine basic enough to accept the proton of the added amine and acid enough to be able to

protonate the carbon of the aminoalkyl complex during the proton transfer step, such as the urea-based N-nucleophile used in Chapter 7. On the contrary, hydroamination of alkenes catalyzed by rhodium complexes can take place with secondary amines because the proton transfer step goes through protonation of the metal center (see Chapter 4).

Regarding the analysis of the anti-Markovnikov regioselectivity in the hydroamination of alkenes, for all the reactions studied in this thesis, catalyzed by both rhodium and gold complexes (studied in Chapter 4 and 7 respectively), the regioselectivity can be related with structural parameters related with the degree of slippage in the intermediate involving the electrophile molecule coordinated to the metal center. Our studies also showed that the presence of electrodonating or electronwithdrawing groups in the alkene molecule can modify the ratio of both regioisomers (they can even reverse the regioselectivity observed). The origin of the regioselectivity was found not to be driven by the charges but the shape of the LUMO orbital.

The regioselectivity in allenes has also been analyzed. It was found that the nucleophilic addition of the amine is also orbitally driven. They give that the nucleophilic attack over the internal carbon atom of allenes coordinated to rhodium complexes is the most stable one, as the most of cases found in literature. Instead the nucleophilic addition into allenes catalyzed by $[\text{Au}(\text{CAAC})]^+$ complex follows a different behavior, the addition over the central carbon is the most favorable one.

Regarding the study of the enantioselectivity, it was found that for the case studied in Chapter 5, the conformational change associated to locate the amine (after the *anti* nucleophilic addition) close to the metal center is the rate determining step for the process. Very subtle interactions between the catalyst and the allene are responsible for the enantio-differentiation.

Overall, we can conclude that the results presented in this thesis prove that use of computational methods, specifically the DFT calculations, is a very useful tool for the study of reaction mechanisms of homogeneous catalytic reactions, allowing us to find the most plausible mechanisms and to explore other aspect such as the origin of the regioselectivity or the enantioselectivity.

*Books are the carriers of civilization.
Without books, history is silent,
literature dumb, science crippled,
thought and speculation at a standstill.*

Barbara Tuchman

~ BIBLIOGRAPHY ~

- (1) Elschenbroich, C.; Salzer, A. *Organometallics: A Concise Introduction*, Edición: 2nd Revised edition.; Wiley-VCH Verlag GmbH: Weinheim; New York, 1992.
- (2) Crabtree, R. H. *The Organometallic Chemistry of the Transition Metals*, 5 edition.; Wiley: Hoboken, New Jersey, 2009.
- (3) Hartwig, J. F. *Organotransition Metal Chemistry: From Bonding to Catalysis*; University Science Books: Sausalito, California, 2010.
- (4) Tolman, C. A. The 16 and 18 Electron Rule in Organometallic Chemistry and Homogeneous Catalysis. *Chem. Soc. Rev.* **1972**, 1 (3), 337.
- (5) Van Vleck, J. H. Theory of the Variations in Paramagnetic Anisotropy Among Different Salts of the Iron Group. *Phys. Rev.* **1932**, 41 (2), 208–215.
- (6) Jean, Y. *Molecular Orbitals of Transition Metal Complexes*, 1 edition.; Marsden, C., Translator; Oxford University Press: Oxford; New York, 2005.
- (7) Laidler, K. J. *Chemical Kinetics*, 2nd edition.; McGraw-Hill, 1965.
- (8) Harris, G. M. *Chemical Kinetics*; Heath, 1966.
- (9) Avery, H. E. *Basic Reaction Kinetics and Mechanisms*; Palgrave: London, 1974.
- (10) Chorkendorff, I.; Niemantsverdriet, J. W. *Concepts of Modern Catalysis and Kinetics*, 2nd ed.; Wiley-VCH, 2007.
- (11) Houston, P. L. *Chemical Kinetics and Reaction Dynamics*; Dover Publications Inc.: Mineola, New York, 2006.
- (12) Marin, G.; Yablonsky, G. S. *Kinetics of Chemical Reactions*; Wiley, 2011.
- (13) Kozuch, S.; Shaik, S. How to Conceptualize Catalytic Cycles? The Energetic Span Model. *Acc. Chem. Res.* **2011**, 44 (2), 101–110.
- (14) Kozuch, S. A Refinement of Everyday Thinking: The Energetic Span Model for Kinetic Assessment of Catalytic Cycles. *Wiley Interdiscip. Rev. Comput. Mol. Sci.* **2012**, 2 (5), 795–815.
- (15) Kozuch, S. Steady State Kinetics of Any Catalytic Network: Graph Theory, the Energy Span Model, the Analogy between Catalysis and Electrical Circuits, and the Meaning of “Mechanism.” *ACS Catal.* **2015**, 5 (9), 5242–5255.
- (16) Eyring, H. The Activated Complex in Chemical Reactions. *J. Chem. Phys.* **1935**, 3 (2), 107.
- (17) Eldik, R. van; Harvey, J. *Theoretical and Computational Inorganic Chemistry, Volume 62*, 1 edition.; Academic Press: London; Burlington, MA, 2010.
- (18) Ostwald, W. *Zeitschrift für physikalische Chemie* **1894**, 15, 705–706.
- (19) Maseras, F.; Lledós, A. *Computational Modeling of Homogeneous Catalysis*; Springer: Dordrecht, 2010.
- (20) Rothenberg, G. *Catalysis: Concepts and Green Applications*, 1st edition.; Wiley-VCH: Weinheim, Germany, 2008.

-
- (21) Cornils, B.; Herrmann, W. A.; Beller, M.; Paciello, R. *Applied Homogeneous Catalysis with Organometallic Compounds: A Comprehensive Handbook in Four Volumes*, 3rd Edition.; Wiley, 2017.
- (22) Cornils, B.; Herrmann, W. A. *Aqueous-Phase Organometallic Catalysis: Concepts and Applications*, 2nd, Completely Revised and Enlarged Edition ed.; Wiley, 2006.
- (23) Cornils, B.; Herrmann, W. A.; Horvath, I. T.; Leitner, W.; Mecking, S.; Olivier-Bourbigou, H.; Vogt, D. *Multiphase Homogeneous Catalysis, 2 Volumes*; Wiley, 2005.
- (24) Kozuch, S.; Shaik, S. A Combined Kinetic–Quantum Mechanical Model for Assessment of Catalytic Cycles: Application to Cross-Coupling and Heck Reactions. *J. Am. Chem. Soc.* **2006**, *128* (10), 3355–3365.
- (25) Kozuch, S.; Martin, J. M. L. What Makes for a Bad Catalytic Cycle? A Theoretical Study on the Suzuki–Miyaura Reaction within the Energetic Span Model. *ACS Catal.* **2011**, *1* (4), 246–253.
- (26) Uhe, A.; Kozuch, S.; Shaik, S. Automatic Analysis of Computed Catalytic Cycles. *J. Comput. Chem.* **2011**, *32* (5), 978–985.
- (27) March, J. *Advanced Organic Chemistry: Reactions, Mechanisms, and Structure.*, 6th ed.; Chapter 15; John Wiley & Sons, Inc.: New Jersey, 2007.
- (28) Gibson, M. S. *The Chemistry of the Amino Group*, Edited by S. Patai.; Interscience: New York, 1968.
- (29) Ricci, A. *Amino Group Chemistry: From Synthesis to the Life Sciences*, 1 edition.; Wiley-VCH: Weinheim, 2008.
- (30) Seayad, J.; Tillack, A.; Hartung, C. G.; Beller, M. Base-Catalyzed Hydroamination of Olefins: An Environmentally Friendly Route to Amines. *Adv. Synth. Catal.* **2002**, *344* (8), 795–813.
- (31) Haggin, J. Chemists Seek Greater Recognition for Catalysis. *Chem. Eng. News Arch.* **1993**, *71* (22), 23–27.
- (32) Johns, A. M.; Sakai, N.; Ridder, A.; Hartwig, J. F. Direct Measurement of the Thermodynamics of Vinylarene Hydroamination. *J. Am. Chem. Soc.* **2006**, *128* (29), 9306–9307.
- (33) O’Hagan, D. Pyrrole, Pyrrolidine, Pyridine, Piperidine and Tropane Alkaloids. *Nat. Prod. Rep.* **2000**, *17* (5), 435–446.
- (34) Müller, T. E.; Beller, M. Metal-Initiated Amination of Alkenes and Alkynes. *Chem. Rev.* **1998**, *98* (2), 675–704.
- (35) Müller, T. E.; Hultsch, K. C.; Yus, M.; Foubelo, F.; Tada, M. Hydroamination: Direct Addition of Amines to Alkenes and Alkynes. *Chem. Rev.* **2008**, *108* (9), 3795–3892.
- (36) Hesp, K. D.; Stradiotto, M. Rhodium- and Iridium-Catalyzed Hydroamination of Alkenes. *ChemCatChem* **2010**, *2* (10), 1192–1207.
- (37) Patil, N. T.; Kavthe, R. D.; Shinde, V. S. Transition Metal-Catalyzed Addition of C-, N- and O-Nucleophiles to Unactivated C–C Multiple Bonds. *Tetrahedron* **2012**, *68* (39), 8079–8146.

- (38) Huang, L.; Arndt, M.; Gooßen, K.; Heydt, H.; Gooßen, L. J. Late Transition Metal-Catalyzed Hydroamination and Hydroamidation. *Chem. Rev.* **2015**, *115* (7), 2596–2697.
- (39) Li, Z.; Zhang, J.; Brouwer, C.; Yang, C.-G.; Reich, N. W.; He, C. Brønsted Acid Catalyzed Addition of Phenols, Carboxylic Acids, and Tosylamides to Simple Olefins. *Org. Lett.* **2006**, *8* (19), 4175–4178.
- (40) Rosenfeld, D. C.; Shekhar, S.; Takemiya, A.; Utsunomiya, M.; Hartwig, J. F. Hydroamination and Hydroalkoxylation Catalyzed by Triflic Acid. Parallels to Reactions Initiated with Metal Triflates. *Org. Lett.* **2006**, *8* (19), 4179–4182.
- (41) Beller, M.; Breindl, C. Base-Catalyzed Hydroamination of Aromatic Olefins—an Efficient Route to 1-Aryl-4-(Arylethyl)piperazines. *Tetrahedron* **1998**, *54* (23), 6359–6368.
- (42) J. D. Danforth. *French Patent*. 917060, 1946.
- (43) J. D. Danforth. *Canadian Patent*. 461783, 1949.
- (44) J. D. Danforth. *U.S. Patent*. 2,449,644, 1948.
- (45) A. W. Weston. *U.S. Patent*. 2,437,984, 1948.
- (46) Howk, B. W.; Little, E. L.; Scott, S. L.; Whitman, G. M. Alkali Metal-Catalyzed Amination of Olefins. *J. Am. Chem. Soc.* **1954**, *76* (7), 1899–1902.
- (47) Dorel, R.; Echavarren, A. M. Gold(I)-Catalyzed Activation of Alkynes for the Construction of Molecular Complexity. *Chem. Rev.* **2015**, *115* (17), 9028–9072.
- (48) Bandini, M. *Au-Catalyzed Synthesis and Functionalization of Heterocycles*; Springer, 2016.
- (49) Widenhoefer, R. A.; Han, X. Gold-Catalyzed Hydroamination of C–C Multiple Bonds. *Eur. J. Org. Chem.* **2006**, *2006* (20), 4555–4563.
- (50) Coulson, D. R. Catalytic Addition of Secondary Amines to Ethylene. *Tetrahedron Lett.* **1971**, *12* (5), 429–430.
- (51) Diamond, S. E.; Mares, F.; Szalkiewicz, A. Formation of Heterocycles from Aniline and Olefins Catalyzed by Group VIII Metal Complexes. In *Fundamental Research in Homogeneous Catalysis*; Tsutsui, M., Ed.; Springer US, 1979; pp 345–358.
- (52) Pez, G. P.; Galle, J. E. Metal Amide Catalyzed Amination of Olefins. *Pure Appl. Chem.* **1985**, *57* (12).
- (53) Klinkenberg, J. L.; Hartwig, J. F. Catalytic Organometallic Reactions of Ammonia. *Angew. Chem. Int. Ed.* **2011**, *50* (1), 86–95.
- (54) Heaton, B. T.; Jacob, C.; Page, P. Transition Metal Complexes Containing Hydrazine and Substituted Hydrazines. *Coord. Chem. Rev.* **1996**, *154*, 193–229.
- (55) Vlught, J. I. van der. Advances in Selective Activation and Application of Ammonia in Homogeneous Catalysis. *Chem. Soc. Rev.* **2010**, *39* (6), 2302–2322.
- (56) Young, P. C.; Green, S. L. J.; Rosair, G. M.; Lee, A.-L. Deactivation of gold(I) Catalysts in the Presence of Thiols and Amines – Characterisation and Catalysis. *Dalton Trans.* **2013**, *42* (26), 9645–9653.

-
- (57) Kim, J.; Kim, H. J.; Chang, S. Synthetic Uses of Ammonia in Transition-Metal Catalysis. *Eur. J. Org. Chem.* **2013**, *2013* (16), 3201–3213.
- (58) Seligson, A. L.; Trogler, W. C. Protonolysis Approach to the Catalytic Amination of Olefins with bis(phosphine)palladium(II) Dialkyls. *Organometallics* **1993**, *12* (3), 744–751.
- (59) Ambuehl, J.; Pregosin, P. S.; Venanzi, L. M.; Consiglio, G.; Bachechi, F.; Zambonelli, L. Platinum-Promoted Cyclization Reactions of Amino Olefins: II. Regio- and Stereoselectivity in the Cyclization Reactions of C-Methyl Substituted Pent-4-Enylamines. *J. Organomet. Chem.* **1979**, *181* (1), 255–269.
- (60) Müller, T. E.; Berger, M.; Grosche, M.; Herdtweck, E.; Schmidtchen, F. P. Palladium-Catalyzed Cyclization of 6-Aminohex-1-ene. *Organometallics* **2001**, *20* (21), 4384–4393.
- (61) Müller, T. E.; Grosche, M.; Herdtweck, E.; Pleier, A.-K.; Walter, E.; Yan, Y.-K. Developing Transition-Metal Catalysts for the Intramolecular Hydroamination of Alkynes. *Organometallics* **2000**, *19* (2), 170–183.
- (62) Hesp, K. D.; Tobisch, S.; Stradiotto, M. [Ir(COD)Cl]₂ as a Catalyst Precursor for the Intramolecular Hydroamination of Unactivated Alkenes with Primary Amines and Secondary Alkyl- or Arylamines: A Combined Catalytic, Mechanistic, and Computational Investigation. *J. Am. Chem. Soc.* **2010**, *132* (1), 413–426.
- (63) Li, X.; Chianese, A. R.; Vogel, T.; Crabtree, R. H. Intramolecular Alkyne Hydroalkoxylation and Hydroamination Catalyzed by Iridium Hydrides. *Org. Lett.* **2005**, *7* (24), 5437–5440.
- (64) Cochran, B. M.; Michael, F. E. Mechanistic Studies of a Palladium-Catalyzed Intramolecular Hydroamination of Unactivated Alkenes: Protonolysis of a Stable Palladium Alkyl Complex Is the Turnover-Limiting Step. *J. Am. Chem. Soc.* **2008**, *130* (9), 2786–2792.
- (65) Cochran, B. M.; Michael, F. E. Synthesis of 2,6-Disubstituted Piperazines by a Diastereoselective Palladium-Catalyzed Hydroamination Reaction. *Org. Lett.* **2008**, *10* (2), 329–332.
- (66) Karshtedt, D.; Bell, A. T.; Tilley, T. D. Platinum-Based Catalysts for the Hydroamination of Olefins with Sulfonamides and Weakly Basic Anilines. *J. Am. Chem. Soc.* **2005**, *127* (36), 12640–12646.
- (67) Brunet, J.-J.; Cadena, M.; Chu, N. C.; Diallo, O.; Jacob, K.; Mothes, E. The First Platinum-Catalyzed Hydroamination of Ethylene. *Organometallics* **2004**, *23* (6), 1264–1268.
- (68) Bender, C. F.; Hudson, W. B.; Widenhoefer, R. A. Sterically Hindered Mono(phosphines) as Supporting Ligands for the Platinum-Catalyzed Hydroamination of Amino Alkenes. *Organometallics* **2008**, *27* (10), 2356–2358.
- (69) Zhang, J.; Yang, C.-G.; He, C. Gold(I)-Catalyzed Intra- and Intermolecular Hydroamination of Unactivated Olefins. *J. Am. Chem. Soc.* **2006**, *128* (6), 1798–1799.

-
- (70) Löber, O.; Kawatsura, M.; Hartwig, J. F. Palladium-Catalyzed Hydroamination of 1,3-Dienes: A Colorimetric Assay and Enantioselective Additions. *J. Am. Chem. Soc.* **2001**, *123* (18), 4366–4367.
- (71) Akermark, B.; Almemark, M.; Almlof, J.; Backvall, J. E.; Roos, B.; Stoegard, A. Chemical Bonding and Reactivity in Nickel-Ethene Complexes. An Ab Initio MO-SCF Study. *J. Am. Chem. Soc.* **1977**, *99* (14), 4617–4624.
- (72) Senn, H. M.; Blöchl, P. E.; Togni, A. Toward an Alkene Hydroamination Catalyst: Static and Dynamic Ab Initio DFT Studies. *J. Am. Chem. Soc.* **2000**, *122* (17), 4098–4107.
- (73) Kovács, G.; Ujaque, G.; Lledós, A. The Reaction Mechanism of the Hydroamination of Alkenes Catalyzed by Gold(I)–Phosphine: The Role of the Counterion and the N-Nucleophile Substituents in the Proton-Transfer Step. *J. Am. Chem. Soc.* **2008**, *130* (3), 853–864.
- (74) Kovács, G.; Lledós, A.; Ujaque, G. Hydroamination of Alkynes with Ammonia: Unforeseen Role of the Gold(I) Catalyst. *Angew. Chem. Int. Ed.* **2011**, *50* (47), 11147–11151.
- (75) Eisenstein, O.; Hoffmann, R. Activation of a Coordinated Olefin toward Nucleophilic Attack. *J. Am. Chem. Soc.* **1980**, *102* (19), 6148–6149.
- (76) Eisenstein, O.; Hoffmann, R. Transition-Metal Complexed Olefins: How Their Reactivity toward a Nucleophile Relates to Their Electronic Structure. *J. Am. Chem. Soc.* **1981**, *103* (15), 4308–4320.
- (77) Meguro, M.; Yamamoto, Y. A New Method for the Synthesis of Nitrogen Heterocycles via Palladium Catalyzed Intramolecular Hydroamination of Allenes. *Tetrahedron Lett.* **1998**, *39* (30), 5421–5424.
- (78) Al-Masum, M.; Meguro, M.; Yamamoto, Y. The Two Component Palladium Catalyst System for Intermolecular Hydroamination of Allenes. *Tetrahedron Lett.* **1997**, *38* (34), 6071–6074.
- (79) Besson, L.; Goré, J.; Cazes, B. Synthesis of Allylic Amines through the Palladium-Catalyzed Hydroamination of Allenes. *Tetrahedron Lett.* **1995**, *36* (22), 3857–3860.
- (80) Zhu, S.; Buchwald, S. L. Enantioselective CuH-Catalyzed Anti-Markovnikov Hydroamination of 1,1-Disubstituted Alkenes. *J. Am. Chem. Soc.* **2014**, *136* (45), 15913–15916.
- (81) Pirnot, M. T.; Wang, Y.-M.; Buchwald, S. L. Copper Hydride Catalyzed Hydroamination of Alkenes and Alkynes. *Angew. Chem. Int. Ed.* **2016**, *55* (1), 48–57.
- (82) Pawlas, J.; Nakao, Y.; Kawatsura, M.; Hartwig, J. F. A General Nickel-Catalyzed Hydroamination of 1,3-Dienes by Alkylamines: Catalyst Selection, Scope, and Mechanism. *J. Am. Chem. Soc.* **2002**, *124* (14), 3669–3679.
- (83) Kawatsura, M.; Hartwig, J. F. Palladium-Catalyzed Intermolecular Hydroamination of Vinylarenes Using Arylamines. *J. Am. Chem. Soc.* **2000**, *122* (39), 9546–9547.
-

-
- (84) Sievers, C.; Jiménez, O.; Knapp, R.; Lin, X.; Müller, T. E.; Türlér, A.; Wierczinski, B.; Lercher, J. A. Palladium Catalysts Immobilized in Thin Films of Ionic Liquid for the Direct Addition of Aniline to Styrene. *J. Mol. Catal. Chem.* **2008**, *279* (2), 187–199.
- (85) Nettekoven, U.; Hartwig, J. F. A New Pathway for Hydroamination. Mechanism of Palladium-Catalyzed Addition of Anilines to Vinylarenes. *J. Am. Chem. Soc.* **2002**, *124* (7), 1166–1167.
- (86) Rigaut, S.; Touchard, D.; Dixneuf, P. H. Ruthenium-Allenylidene Complexes and Their Specific Behaviour. *Coord. Chem. Rev.* **2004**, *248* (15–16), 1585–1601.
- (87) Arndt, M.; Salih, K. S. M.; Fromm, A.; Goossen, L. J.; Menges, F.; Niedner-Schatteburg, G. Mechanistic Investigation of the Ru-Catalyzed Hydroamidation of Terminal Alkynes. *J. Am. Chem. Soc.* **2011**, *133* (19), 7428–7449.
- (88) Tokunaga, M.; Suzuki, T.; Koga, N.; Fukushima, T.; Horiuchi, A.; Eckert, M.; Ota, M.; Haga, M.; Honda, T.; Wakatsuki, Y. Hydration and Hydroamination of 1-Alkynes with Ruthenium Catalysts. *RIKEN Rev.* **2001**, *42*, 53–56.
- (89) Seul, J. M.; Park, S. Protonolysis of a Toluidinoalkyl Platinum(ii) Complex Derived from the Insertion of the C=C Bond into the Pt–NHR (Amido) Bond: The Role of Amine in Pt-Catalyzed Hydroamination of Acrylonitrile. *J. Chem. Soc. Dalton Trans.* **2002**, No. 6, 1153–1158.
- (90) Jiménez, M. V.; Bartolomé, M. I.; Pérez-Torrente, J. J.; Gómez, D.; Modrego, F. J.; Oro, L. A. Mechanistic Studies on the Catalytic Oxidative Amination of Alkenes by Rhodium(I) Complexes with Hemilabile Phosphines. *ChemCatChem* **2013**, *5* (1), 263–276.
- (91) Uhe, A.; Hölscher, M.; Leitner, W. A Computational Study of Rhodium Pincer Complexes with Classical and Nonclassical Hydride Centres as Catalysts for the Hydroamination of Ethylene with Ammonia. *Chem. - Eur. J.* **2010**, *16* (30), 9203–9214.
- (92) Casalnuovo, A. L.; Calabrese, J. C.; Milstein, D. Rational Design in Homogeneous Catalysis. Iridium (I)-Catalyzed Addition of Aniline to Norbornylene via Nitrogen-Hydrogen Activation. *J. Am. Chem. Soc.* **1988**, *110* (20), 6738–6744.
- (93) Sappa, E.; Milone, L. Reactions of $\text{Ru}_3(\text{CO})_{12}$ with Nitrobenzene and Aniline. *J. Organomet. Chem.* **1973**, *61*, 383–388.
- (94) Zhao, J. Oxidative Addition of Ammonia to Form a Stable Monomeric Amido Hydride Complex. *Science* **2005**, *307* (5712), 1080–1082.
- (95) Hanley, P. S.; Hartwig, J. F. Migratory Insertion of Alkenes into Metal-Oxygen and Metal-Nitrogen Bonds. *Angew. Chem. Int. Ed.* **2013**, *52* (33), 8510–8525.
- (96) Cowan, R. L.; Trogler, W. C. Regioselective Insertion of Acrylonitrile into the Platinum-Nitrogen Bond of hydrido(phenylamido)bis(triethylphosphine)platinum(II). A Model Step for Olefin Amination. *Organometallics* **1987**, *6* (11), 2451–2453.
- (97) Cowan, R. L.; Trogler, W. C. Syntheses, Reactions, and Molecular Structures of *Trans*-hydrido(phenylamido)bis(triethylphosphine)platinum(II) and *Trans*-hydridophenoxobis(triethylphosphine)platinum(II). *J. Am. Chem. Soc.* **1989**, *111* (13), 4750–4761.
-

- (98) Chemler, S. R.; Fuller, P. H. Heterocycle Synthesis by Copper Facilitated Addition of Heteroatoms to Alkenes, Alkynes and Arenes. *Chem. Soc. Rev.* **2007**, *36* (7), 1153.
- (99) Tsepis, C. A.; Kefalidis, C. E. How Efficient Are the Hydrido-Bridged Diplatinum Catalysts in the Hydrosilylation, Hydrocyanation, and Hydroamination of Alkynes: A Theoretical Analysis of the Catalytic Cycles Employing Electronic Structure Calculation Methods. *Organometallics* **2006**, *25* (7), 1696–1706.
- (100) Tye, J. W.; Hartwig, J. F. Computational Studies of the Relative Rates for Migratory Insertions of Alkenes into Square-Planar, Methyl-, Amido-, and Hydroxo Complexes of Rhodium. *J. Am. Chem. Soc.* **2009**, *131* (41), 14703–14712.
- (101) Walsh, P. J.; Baranger, A. M.; Bergman, R. G. Stoichiometric and Catalytic Hydroamination of Alkynes and Allene by Zirconium Bisamides $Cp_2Zr(NHR)_2$. *J. Am. Chem. Soc.* **1992**, *114* (5), 1708–1719.
- (102) Baranger, A. M.; Walsh, P. J.; Bergman, R. G. Variable Regiochemistry in the Stoichiometric and Catalytic Hydroamination of Alkynes by Imidozirconium Complexes Caused by an Unusual Dependence of the Rate Law on Alkyne Structure and Temperature. *J. Am. Chem. Soc.* **1993**, *115* (7), 2753–2763.
- (103) Straub, B. F.; Bergman, R. G. The Mechanism of Hydroamination of Allenes, Alkynes, and Alkenes Catalyzed by Cyclopentadienyltitanium-Imido Complexes: A Density Functional Study. *Angew. Chem. Int. Ed.* **2001**, *40* (24), 4632–4635.
- (104) Beller, M.; Trauthwein, H.; Eichberger, M.; Breindl, C.; Müller, T. E. Anti-Markovnikov Reactions, 6-Rhodium-Catalyzed Amination of Vinylpyridines: Hydroamination versus Oxidative Amination. *Eur. J. Inorg. Chem.* **1999**, 1121–1132.
- (105) Selent, D.; Scharfenberg-Pfeiffer, D.; Reck, G.; Taube, R. Molekül- Und Kristallstruktur Des Trans-Chloro-Ethen-Bis(Piperidin)-Rhodium(I), $Trans-[RhCl((C_2H_4)(C_5H_{10}NH)_2)]$, Eines Präkatalysators Für Die Hydroaminierung Des Ethens. *J. Organomet. Chem.* **1991**, *415* (3), 417–423.
- (106) Taube, R. Reaction with Nitrogen Compounds: Hydroamination. In *Applied Homogeneous Catalysis with Organometallic Compounds*; Cornils, B., Herrmann, W. A., Eds.; Wiley-VCH: Weinheim, 2002; pp 513–524.
- (107) Diamond, S. E.; Szalkiewicz, A.; Mares, F. Reactions of Aniline with Olefins Catalyzed by Group 8 Metal Complexes: N-Alkylation and Heterocycle Formation. *J. Am. Chem. Soc.* **1979**, *101* (2), 490–491.
- (108) Brunet, J.-J.; Neibecker, D.; Philippot, K. Unexpected Catalytic and Stereoselective Hydroarylation of Norbornene during the Attempted Rhodium-Catalysed Hydroamination of Norbornene with Aniline or Diphenylamine. *J. Chem. Soc., Chem. Commun.* **1992**, No. 17, 1215–1216.
- (109) Brunet, J.-J.; Commenges, G.; Neibecker, D.; Philippot, K. Rhodium-Catalysed Hydroamination-Hydroarylation of Norbornene with Aniline, Toluidines or Diphenylamine. *J. Organomet. Chem.* **1994**, *469* (2), 221–228.
- (110) Brunet, J.-J.; Neibecker, D.; Philippot, K. Rhodium-Mediated 100% Regioselective Oxidative Hydroamination of α -Olefins. *Tetrahedron Lett.* **1993**, *34* (24), 3877–3880.

-
- (111) Beller, M.; Trauthwein, H.; Eichberger, M.; Breindl, C.; Herwig, J.; Müller, T. E.; Thiel, O. R. The First Rhodium-Catalyzed Anti-Markovnikov Hydroamination: Studies on Hydroamination and Oxidative Amination of Aromatic Olefins. *Chem.-Weinh.-Eur. J.* **1999**, *5*, 1306–1319.
- (112) Beller, M.; Eichberger, M.; Trauthwein, H. Anti-Markovnikov Functionalization of Olefins: Rhodium-Catalyzed Oxidative Aminations of Styrenes. *Angew. Chem. Int. Ed. Engl.* **1997**, *36* (20), 2225–2227.
- (113) Jiménez, M. V.; Pérez-Torrente, J. J.; Bartolomé, M. I.; Lahoz, F. J.; Oro, L. A. Rational Design of Efficient Rhodium Catalysts for the Anti-Markovnikov Oxidative Amination of Styrene. *Chem. Commun.* **2010**, *46* (29), 5322.
- (114) Utsunomiya, M.; Kuwano, R.; Kawatsura, M.; Hartwig, J. F. Rhodium-Catalyzed Anti-Markovnikov Hydroamination of Vinylarenes. *J. Am. Chem. Soc.* **2003**, *125* (19), 5608–5609.
- (115) Fukumoto, Y.; Asai, H.; Shimizu, M.; Chatani, N. Anti-Markovnikov Addition of Both Primary and Secondary Amines to Terminal Alkynes Catalyzed by the $\text{TpRh}(\text{C}_2\text{H}_4)_2/\text{PPh}_3$ System. *J. Am. Chem. Soc.* **2007**, *129* (45), 13792–13793.
- (116) Baudequin, C.; Brunet, J.-J.; Rodriguez-Zubiri, M. Rhodium-Catalyzed Hydroamination of Ethylene. Highly Promoting Effect of Iodide Ions. *Organometallics* **2007**, *26* (22), 5264–5266.
- (117) Takemiya, A.; Hartwig, J. F. Rhodium-Catalyzed Intramolecular, Anti-Markovnikov Hydroamination. Synthesis of 3-Arylpiperidines. *J. Am. Chem. Soc.* **2006**, *128* (18), 6042–6043.
- (118) Liu, Z.; Hartwig, J. F. Mild, Rhodium-Catalyzed Intramolecular Hydroamination of Unactivated Terminal and Internal Alkenes with Primary and Secondary Amines. *J. Am. Chem. Soc.* **2008**, *130* (5), 1570–1571.
- (119) Shen, X.; Buchwald, S. L. Rhodium-Catalyzed Asymmetric Intramolecular Hydroamination of Unactivated Alkenes. *Angew. Chem. Int. Ed.* **2010**, *49* (3), 564–567.
- (120) Strom, A. E.; Balcells, D.; Hartwig, J. F. Synthetic and Computational Studies on the Rhodium-Catalyzed Hydroamination of Aminoalkenes. *ACS Catal.* **2016**, *6*, 5651–5665.
- (121) Dorta, R.; Egli, P.; Zürcher, F.; Togni, A. The $[\text{IrCl}(\text{Diphosphine})]_2/\text{Fluoride}$ System. Developing Catalytic Asymmetric Olefin Hydroamination. *J. Am. Chem. Soc.* **1997**, *119* (44), 10857–10858.
- (122) Cooke, M. L.; Xu, K.; Breit, B. Enantioselective Rhodium-Catalyzed Synthesis of Branched Allylic Amines by Intermolecular Hydroamination of Terminal Allenes. *Angew. Chem. Int. Ed.* **2012**, *51* (43), 10876–10879.
- (123) Li, C.; Kähny, M.; Breit, B. Rhodium-Catalyzed Chemo-, Regio-, and Enantioselective Addition of 2-Pyridones to Terminal Allenes. *Angew. Chem. Int. Ed.* **2014**, *53* (50), 13780–13784.
- (124) Hashmi, A. S. K. Homogeneous Gold Catalysis Beyond Assumptions and Proposals—Characterized Intermediates. *Angew. Chem. Int. Ed.* **2010**, *49* (31), 5232–5241.
-

- (125) Obradors, C.; Echavarren, A. M. Intriguing Mechanistic Labyrinths in gold(I) Catalysis. *Chem. Commun.* **2013**, 50 (1), 16–28.
- (126) Brooner, R. E. M.; Widenhoefer, R. A. Cationic, Two-Coordinate Gold π Complexes. *Angew. Chem. Int. Ed.* **2013**, 52 (45), 11714–11724.
- (127) Zuccaccia, D.; Belpassi, L.; Macchioni, A.; Tarantelli, F. Ligand Effects on Bonding and Ion Pairing in Cationic Gold(I) Catalysts Bearing Unsaturated Hydrocarbons. *Eur. J. Inorg. Chem.* **2013**, 2013 (24), 4121–4135.
- (128) Giner, X.; Nájera, C.; Kovács, G.; Lledós, A.; Ujaque, G. Gold versus Silver-Catalyzed Intermolecular Hydroaminations of Alkenes and Dienes. *Adv. Synth. Catal.* **2011**, 353 (18), 3451–3466.
- (129) Katari, M.; Rao, M. N.; Rajaraman, G.; Ghosh, P. Computational Insight into a Gold(I) N-Heterocyclic Carbene Mediated Alkyne Hydroamination Reaction. *Inorg. Chem.* **2012**, 51 (10), 5593–5604.
- (130) Wang, Z. J.; Benitez, D.; Tkatchouk, E.; Goddard III, W. A.; Toste, F. D. Mechanistic Study of Gold(I)-Catalyzed Intermolecular Hydroamination of Allenes. *J. Am. Chem. Soc.* **2010**, 132 (37), 13064–13071.
- (131) Kim, J. H.; Park, S.-W.; Park, S. R.; Lee, S.; Kang, E. J. Counterion-Mediated Hydrogen-Bonding Effects: Mechanistic Study of Gold(I)-Catalyzed Enantioselective Hydroamination of Allenes. *Chem. - Asian J.* **2011**, 6 (8), 1982–1986.
- (132) Mizushima, E.; Hayashi, T.; Tanaka, M. Au(I)-Catalyzed Highly Efficient Intermolecular Hydroamination of Alkynes. *Org. Lett.* **2003**, 5 (18), 3349–3352.
- (133) Lavallo, V.; Frey, G. D.; Donnadiou, B.; Soleilhavoup, M.; Bertrand, G. Homogeneous Catalytic Hydroamination of Alkynes and Allenes with Ammonia. *Angew. Chem. Int. Ed.* **2008**, 47 (28), 5224–5228.
- (134) Zeng, X.; Frey, G. D.; Kousar, S.; Bertrand, G. A Cationic Gold(I) Complex as a General Catalyst for the Intermolecular Hydroamination of Alkynes: Application to the One-Pot Synthesis of Allenes from Two Alkynes and a Sacrificial Amine. *Chem. - Eur. J.* **2009**, 15 (13), 3056–3060.
- (135) Zeng, X.; Frey, G. D.; Kinjo, R.; Donnadiou, B.; Bertrand, G. Synthesis of a Simplified Version of Stable Bulky and Rigid Cyclic (Alkyl)(amino)carbenes, and Catalytic Activity of the Ensuing Gold(I) Complex in the Three-Component Preparation of 1,2-Dihydroquinoline Derivatives. *J. Am. Chem. Soc.* **2009**, 131 (24), 8690–8696.
- (136) Zeng, X.; Kinjo, R.; Donnadiou, B.; Bertrand, G. Serendipitous Discovery of the Catalytic Hydroammoniation and Methylation of Alkynes. *Angew. Chem. Int. Ed.* **2010**, 49 (5), 942–945.
- (137) Kinjo, R.; Donnadiou, B.; Bertrand, G. Gold-Catalyzed Hydroamination of Alkynes and Allenes with Parent Hydrazine. *Angew. Chem. Int. Ed.* **2011**, 50 (24), 5560–5563.
- (138) Duan, H.; Sengupta, S.; Petersen, J. L.; Akhmedov, N. G.; Shi, X. Triazole–Au(I) Complexes: A New Class of Catalysts with Improved Thermal Stability and Reactivity for Intermolecular Alkyne Hydroamination. *J. Am. Chem. Soc.* **2009**, 131 (34), 12100–12102.

-
- (139) Hesp, K. D.; Stradiotto, M. Stereo- and Regioselective Gold-Catalyzed Hydroamination of Internal Alkynes with Dialkylamines. *J. Am. Chem. Soc.* **2010**, *132* (51), 18026–18029.
- (140) López-Gómez, M. J.; Martin, D.; Bertrand, G. Anti-Bredt N-Heterocyclic Carbene: An Efficient Ligand for the gold(I)-Catalyzed Hydroamination of Terminal Alkynes with Parent Hydrazine. *Chem. Commun.* **2013**, *49* (40), 4483.
- (141) Manzano, R.; Wurm, T.; Rominger, F.; Hashmi, A. S. K. Room-Temperature Hydrohydrazination of Terminal Alkynes Catalyzed by Saturated Abnormal N-Heterocyclic Carbene-Gold(I) Complexes. *Chem. - Eur. J.* **2014**, *20* (23), 6844–6848.
- (142) Kang, J.-E.; Kim, H.-B.; Lee, J.-W.; Shin, S. Gold(I)-Catalyzed Intramolecular Hydroamination of Alkyne with Trichloroacetimidates. *Org. Lett.* **2006**, *8* (16), 3537–3540.
- (143) Hashmi, A. S. K.; Rudolph, M.; Schymura, S.; Visus, J.; Frey, W. Gold Catalysis: Alkylideneoxazolines and -Oxazoles from Intramolecular Hydroamination of an Alkyne by a Trichloroacetimidate. *Eur. J. Org. Chem.* **2006**, *2006* (21), 4905–4909.
- (144) Ritter, S.; Horino, Y.; Lex, J.; Schmalz, H.-G. Gold-Catalyzed Cyclization of *O* - Propargyl Carbamates under Mild -Conditions: A Convenient Access to 4-Alkylidene-2-Oxazolidinones. *Synlett* **2006**, *2006* (19), 3309–3313.
- (145) Yu, Y.; Stephenson, G. A.; Mitchell, D. A Regioselective Synthesis of 3-Benzazepinones via Intramolecular Hydroamidation of Acetylenes. *Tetrahedron Lett.* **2006**, *47* (23), 3811–3814.
- (146) Monge, D.; Jensen, K. L.; Franke, P. T.; Lykke, L.; Jørgensen, K. A. Asymmetric One-Pot Sequential Organo- and Gold Catalysis for the Enantioselective Synthesis of Dihydropyrrole Derivatives. *Chem. - Eur. J.* **2010**, *16* (31), 9478–9484.
- (147) Kadzimirsz, D.; Hildebrandt, D.; Merz, K.; Dyker, G. Isoindoles and Dihydroisoquinolines by Gold-Catalyzed Intramolecular Hydroamination of Alkynes. *Chem. Commun.* **2006**, No. 6, 661.
- (148) Enomoto, T.; Obika, S.; Yasui, Y.; Takemoto, Y. Gold(I)-Catalyzed Hydroamination as a General Approach toward the Synthesis of Substituted Hydroisoquinolines: Remarkable Acceleration by Ethanol. *Synlett* **2008**, *2008* (11), 1647–1650.
- (149) Gimeno, A.; Medio-Simón, M.; de Arellano, C. R.; Asensio, G.; Cuenca, A. B. NHC-Stabilized Gold(I) Complexes: Suitable Catalysts for 6- *Exo* -Dig Heterocyclization of 1-(*O* -Ethynylaryl)ureas. *Org. Lett.* **2010**, *12* (9), 1900–1903.
- (150) Nishina, N.; Yamamoto, Y. Gold-Catalyzed Intermolecular Hydroamination of Allenes with Arylamines and Resulting High Chirality Transfer. *Angew. Chem. Int. Ed.* **2006**, *45* (20), 3314–3317.
- (151) Nishina, N.; Yamamoto, Y. Gold-Catalyzed Intermolecular Hydroamination of Allenes: First Example of the Use of an Aliphatic Amine in Hydroamination. *Synlett* **2007**, *2007* (11), 1767–1770.
- (152) Nishina, N.; Yamamoto, Y. Gold-Catalyzed Hydrofunctionalization of Allenes with Nitrogen and Oxygen Nucleophiles and Its Mechanistic Insight. *Tetrahedron* **2009**, *65* (9), 1799–1808.
-

-
- (153) Kinder, R. E.; Zhang, Z.; Widenhoefer, R. A. Intermolecular Hydroamination of Allenes with *N*-Unsubstituted Carbamates Catalyzed by a Gold(I) *N*-Heterocyclic Carbene Complex. *Org. Lett.* **2008**, *10* (14), 3157–3159.
- (154) Zeng, X.; Soleilhavoup, M.; Bertrand, G. Gold-Catalyzed Intermolecular Markovnikov Hydroamination of Allenes with Secondary Amines. *Org. Lett.* **2009**, *11* (15), 3166–3169.
- (155) Bartolomé, C.; García-Cuadrado, D.; Ramiro, Z.; Espinet, P. Exploring the Scope of Nitrogen Acyclic Carbenes (NACs) in Gold-Catalyzed Reactions. *Organometallics* **2010**, *29* (16), 3589–3592.
- (156) LaLonde, R. L.; Sherry, B. D.; Kang, E. J.; Toste, F. D. Gold(I)-Catalyzed Enantioselective Intramolecular Hydroamination of Allenes. *J. Am. Chem. Soc.* **2007**, *129* (9), 2452–2453.
- (157) Hamilton, G. L.; Kang, E. J.; Mba, M.; Toste, F. D. A Powerful Chiral Counterion Strategy for Asymmetric Transition Metal Catalysis. *Science* **2007**, *317* (5837), 496–499.
- (158) LaLonde, R. L.; Wang, Z. J.; Mba, M.; Lackner, A. D.; Toste, F. D. Gold(I)-Catalyzed Enantioselective Synthesis of Pyrazolidines, Isoxazolidines, and Tetrahydrooxazines. *Angew. Chem. Int. Ed.* **2010**, *49* (3), 598–601.
- (159) Han, X.; Widenhoefer, R. A. Gold(I)-Catalyzed Intramolecular Hydroamination of Alkenyl Carbamates. *Angew. Chem. Int. Ed.* **2006**, *45* (11), 1747–1749.
- (160) Bender, C. F.; Widenhoefer, R. A. Gold(I)-Catalyzed Intramolecular Hydroamination of Unactivated Alkenes with Carboxamides. *Chem. Commun.* **2006**, No. 39, 4143.
- (161) Zhang, Z.; Lee, S. D.; Widenhoefer, R. A. Intermolecular Hydroamination of Ethylene and 1-Alkenes with Cyclic Ureas Catalyzed by Achiral and Chiral Gold(I) Complexes. *J. Am. Chem. Soc.* **2009**, *131* (15), 5372–5373.
- (162) Timmerman, J. C.; Robertson, B. D.; Widenhoefer, R. A. Gold-Catalyzed Intermolecular Anti-Markovnikov Hydroamination of Alkylidenecyclopropanes. *Angew. Chem. Int. Ed.* **2015**, *54* (7), 2251–2254.
- (163) Heisenberg, W. Über den anschaulichen Inhalt der quantentheoretischen Kinematik und Mechanik. *Z. Für Phys.* **1927**, *43* (3–4), 172–198.
- (164) Szabo, A.; Ostlund, N. S. *Modern Quantum Chemistry: Introduction to Advanced Electronic Structure Theory*; Dover Publications: Mineola, New York, 1982.
- (165) Goodisman, J. *Diatomic Interaction Potential Theory: Fundamentals*; Academic Press, 1973.
- (166) Levine, I. N. *Quantum Chemistry*, 7 edition.; Pearson: Boston, 2013.
- (167) Jensen, F. *Introduction to Computational Chemistry*, 2 edition.; Wiley: Chichester, England; Hoboken, New York, 2007.
- (168) Noga, J.; Bartlett, R. J. The Full CCSDT Model for Molecular Electronic Structure. *J. Chem. Phys.* **1987**, *86* (12), 7041–7050.
- (169) Koch, W.; Holthausen, M. C. *A Chemist's Guide to Density Functional Theory*, 2nd edition.; Wiley-VCH: Weinheim; New York, 2001.
-

-
- (170) Burke, K. Perspective on Density Functional Theory. *J. Chem. Phys.* **2012**, *136* (15), 150901.
- (171) Becke, A. D. Perspective: Fifty Years of Density-Functional Theory in Chemical Physics. *J. Chem. Phys.* **2014**, *140* (18), 18A301.
- (172) Hohenberg, P.; Kohn, W. Inhomogeneous Electron Gas. *Phys. Rev.* **1964**, *136* (3B), B864–B871.
- (173) Kohn, W.; Sham, L. J. Self-Consistent Equations Including Exchange and Correlation Effects. *Phys. Rev.* **1965**, *140* (4A), A1133–A1138.
- (174) Thomas, L. H. The Calculation of Atomic Fields. *Math. Proc. Camb. Philos. Soc.* **1927**, *23* (5), 542–548.
- (175) Fermi, E. Un Metodo Statistico per La Determinazione Di Alcune Proprietà Dell'atomo. *Rendiconti Dell'Accademia Dei Lincei* **1927**, *6*, 602–607.
- (176) Dirac, P. a. M. Note on Exchange Phenomena in the Thomas Atom. *Math. Proc. Camb. Philos. Soc.* **1930**, *26* (3), 376–385.
- (177) Vosko, S. H.; Wilk, L.; Nusair, M. Accurate Spin-Dependent Electron Liquid Correlation Energies for Local Spin Density Calculations: A Critical Analysis. *Can. J. Phys.* **1980**, *58* (8), 1200–1211.
- (178) Perdew, J. P. Density-Functional Approximation for the Correlation Energy of the Inhomogeneous Electron Gas. *Phys. Rev. B* **1986**, *33* (12), 8822–8824.
- (179) Becke, A. D. Density Functional Calculations of Molecular Bond Energies. *J. Chem. Phys.* **1986**, *84*, 4524–4529.
- (180) Becke, A. D. Density-Functional Exchange-Energy Approximation with Correct Asymptotic Behavior. *Phys. Rev. A* **1988**, *38* (6), 3098–3100.
- (181) Perdew, J. P. In *Electronic Structure of Solids*; Ziesche, P., Eschrig, H., Eds.; Akademie Verlag, Berlin, 1991.
- (182) Perdew, J. P.; Chevary, J. A.; Vosko, S. H.; Jackson, K. A.; Pederson, M. R.; Singh, D. J.; Fiolhais, C. Atoms, Molecules, Solids, and Surfaces: Applications of the Generalized Gradient Approximation for Exchange and Correlation. *Phys. Rev. B* **1992**, *46* (11), 6671–6687.
- (183) Perdew, J. P.; Chevary, J. A.; Vosko, S. H.; Jackson, K. A.; Pederson, M. R.; Singh, D. J.; Fiolhais, C. Erratum: Atoms, Molecules, Solids, and Surfaces: Applications of the Generalized Gradient Approximation for Exchange and Correlation. *Phys. Rev. B* **1993**, *48* (7), 4978–4978.
- (184) Perdew, J. P.; Burke, K.; Wang, Y. Generalized Gradient Approximation for the Exchange-Correlation Hole of a Many-Electron System. *Phys. Rev. B* **1996**, *54* (23), 16533–16539.
- (185) Burke, K.; Perdew, J. P.; Wang, Y. In *Electronic Density Functional Theory: Recent Progress and New Directions*; Dobson, J. F., Vignale, G., Das, M. P., Eds.; Springer Science + Business Media: New York, 1998.
- (186) Handy, N. C.; Cohen, A. J. Left-Right Correlation Energy. *Mol. Phys.* **2001**, *99* (5), 403–412.

-
- (187) Hoe, W.-M.; Cohen, A. J.; Handy, N. C. Assessment of a New Local Exchange Functional OPTX. *Chem. Phys. Lett.* **2001**, *341* (3–4), 319–328.
- (188) Adamo, C.; Barone, V. Exchange Functionals with Improved Long-Range Behavior and Adiabatic Connection Methods without Adjustable Parameters: The mPW and mPW1PW Models. *J. Chem. Phys.* **1998**, *108* (2), 664–675.
- (189) Lee, C.; Yang, W.; Parr, R. G. Development of the Colle-Salvetti Correlation-Energy Formula into a Functional of the Electron Density. *Phys. Rev. B* **1988**, *37* (2), 785–789.
- (190) Becke, A. D. Density-functional Thermochemistry. IV. A New Dynamical Correlation Functional and Implications for Exact-exchange Mixing. *J. Chem. Phys.* **1996**, *104* (3), 1040–1046.
- (191) Perdew, J. P.; Burke, K.; Ernzerhof, M. Generalized Gradient Approximation Made Simple. *Phys. Rev. Lett.* **1996**, *77* (18), 3865–3868.
- (192) Perdew, J. P.; Burke, K.; Ernzerhof, M. Erratum: Generalized Gradient Approximation Made Simple. *Phys. Rev. Lett.* **1997**, *78* (7), 1396–1396.
- (193) Schmider, H. L.; Becke, A. D. Optimized Density Functionals from the Extended G2 Test Set. *J. Chem. Phys.* **1998**, *108* (23), 9624–9631.
- (194) Tao, J.; Perdew, J. P.; Staroverov, V. N.; Scuseria, G. E. Climbing the Density Functional Ladder: Nonempirical Meta-Generalized Gradient Approximation Designed for Molecules and Solids. *Phys. Rev. Lett.* **2003**, *91* (14), 146401.
- (195) Voorhis, T. V.; Scuseria, G. E. A Novel Form for the Exchange-Correlation Energy Functional. *J. Chem. Phys.* **1998**, *109* (2), 400–410.
- (196) Rey, J.; Savin, A. Virtual Space Level Shifting and Correlation Energies. *Int. J. Quantum Chem.* **1998**, *69* (4), 581–590.
- (197) B.Krieger, J.; Chen, J. Q.; Iafrate, G. J.; Savin, A. In *Electron Correlations and Materials Properties*; Gonis, A., Kioussis, N., Ciftan, M., Eds.; Springer US: Boston, MA, 1999.
- (198) Krieger, J. B.; Q.Chen, J.; Kurth, S. In *Density Functional Theory and its Application to Materials*; Doren, V. V., Alsenoy, C. V., Geerlings, P., Eds.; American Inst. of Physics: Melville, New York, 2001.
- (199) Toulouse, J.; Savin, A.; Adamo, C. Validation and Assessment of an Accurate Approach to the Correlation Problem in Density Functional Theory: The Kriger–Chen–Iafrate–Savin Model. *J. Chem. Phys.* **2002**, *117* (23), 10465–10473.
- (200) Becke, A. D. A New Mixing of Hartree–Fock and Local Density-functional Theories. *J. Chem. Phys.* **1993**, *98* (2), 1372–1377.
- (201) Stephens, P. J.; Devlin, F. J.; Chabalowski, C. F.; Frisch, M. J. Ab Initio Calculation of Vibrational Absorption and Circular Dichroism Spectra Using Density Functional Force Fields. *J. Phys. Chem.* **1994**, *98* (45), 11623–11627.
- (202) Becke, A. D. Density-functional Thermochemistry. III. The Role of Exact Exchange. *J. Chem. Phys.* **1993**, *98* (7), 5648–5652.
-

-
- (203) Klimeš, J.; Michaelides, A. Perspective: Advances and Challenges in Treating van Der Waals Dispersion Forces in Density Functional Theory. *J. Chem. Phys.* **2012**, *137* (12), 120901.
- (204) Grimme, S. Density Functional Theory with London Dispersion Corrections. *Wiley Interdiscip. Rev. Comput. Mol. Sci.* **2011**, *1* (2), 211–228.
- (205) Grimme, S.; Antony, J.; Ehrlich, S.; Krieg, H. A Consistent and Accurate Ab Initio Parametrization of Density Functional Dispersion Correction (DFT-D) for the 94 Elements H–Pu. *J. Chem. Phys.* **2010**, *132* (15), 154104.
- (206) Grimme, S. Accurate Description of van Der Waals Complexes by Density Functional Theory Including Empirical Corrections. *J. Comput. Chem.* **2004**, *25* (12), 1463–1473.
- (207) Zhao, Y.; Schultz, N. E.; Truhlar, D. G. Exchange–Correlation Functional with Broad Accuracy for Metallic and Nonmetallic Compounds, Kinetics, and Noncovalent Interactions. *J. Chem. Phys.* **2005**, *123* (16), 161103.
- (208) Zhao, Y.; Schultz, N. E.; Truhlar, D. G. Design of Density Functionals by Combining the Method of Constraint Satisfaction with Parametrization for Thermochemistry, Thermochemical Kinetics, and Noncovalent Interactions. *J. Chem. Theory Comput.* **2006**, *2* (2), 364–382.
- (209) Zhao, Y.; Truhlar, D. G. Density Functionals with Broad Applicability in Chemistry. *Acc. Chem. Res.* **2008**, *41* (2), 157–167.
- (210) Zhao, Y.; Truhlar, D. G. The M06 Suite of Density Functionals for Main Group Thermochemistry, Thermochemical Kinetics, Noncovalent Interactions, Excited States, and Transition Elements: Two New Functionals and Systematic Testing of Four M06-Class Functionals and 12 Other Functionals. *Theor. Chem. Acc.* **2008**, *120* (1–3), 215–241.
- (211) Zhao, Y.; Truhlar, D. G. A New Local Density Functional for Main-Group Thermochemistry, Transition Metal Bonding, Thermochemical Kinetics, and Noncovalent Interactions. *J. Chem. Phys.* **2006**, *125* (19), 194101.
- (212) Zhao, Y.; Truhlar, D. G. Density Functional for Spectroscopy: No Long-Range Self-Interaction Error, Good Performance for Rydberg and Charge-Transfer States, and Better Performance on Average than B3LYP for Ground States. *J. Phys. Chem. A* **2006**, *110* (49), 13126–13130.
- (213) Zhao, Y.; Truhlar, D. G. Comparative DFT Study of van Der Waals Complexes: Rare-Gas Dimers, Alkaline-Earth Dimers, Zinc Dimer, and Zinc-Rare-Gas Dimers. *J. Phys. Chem. A* **2006**, *110* (15), 5121–5129.
- (214) Zhao, Y.; Truhlar, D. G. Exploring the Limit of Accuracy of the Global Hybrid Meta Density Functional for Main-Group Thermochemistry, Kinetics, and Noncovalent Interactions. *J. Chem. Theory Comput.* **2008**, *4* (11), 1849–1868.
- (215) Peverati, R.; Truhlar, D. G. Improving the Accuracy of Hybrid Meta-GGA Density Functionals by Range Separation. *J. Phys. Chem. Lett.* **2011**, *2* (21), 2810–2817.
- (216) Yu, H. S.; He, X.; Li, S. L.; Truhlar, D. G. MN15: A Kohn–Sham Global-Hybrid Exchange–correlation Density Functional with Broad Accuracy for Multi-Reference

- and Single-Reference Systems and Noncovalent Interactions. *Chem. Sci.* **2016**, *7* (8), 5032–5051.
- (217) Medvedev, M. G.; Bushmarinov, I. S.; Sun, J.; Perdew, J. P.; Lyssenko, K. A. Density Functional Theory Is Straying from the Path toward the Exact Functional. *Science* **2017**, *355* (6320), 49–52.
- (218) Ernzerhof, M.; Scuseria, G. E. Assessment of the Perdew–Burke–Ernzerhof Exchange–Correlation Functional. *J. Chem. Phys.* **1999**, *110* (11), 5029–5036.
- (219) Perdew, J. P.; Ernzerhof, M.; Burke, K. Rationale for Mixing Exact Exchange with Density Functional Approximations. *J. Chem. Phys.* **1996**, *105* (22), 9982–9985.
- (220) Chai, J.-D.; Head-Gordon, M. Long-Range Corrected Hybrid Density Functionals with Damped Atom-Atom Dispersion Corrections. *Phys. Chem. Chem. Phys. PCCP* **2008**, *10* (44), 6615–6620.
- (221) Chai, J.-D.; Head-Gordon, M. Systematic Optimization of Long-Range Corrected Hybrid Density Functionals. *J. Chem. Phys.* **2008**, *128* (8), 84106.
- (222) Sun, J.; Remsing, R. C.; Zhang, Y.; Sun, Z.; Ruzsinszky, A.; Peng, H.; Yang, Z.; Paul, A.; Waghmare, U.; Wu, X.; Klein, M. L.; Perdew, J. P. Accurate First-Principles Structures and Energies of Diversely Bonded Systems from an Efficient Density Functional. *Nat. Chem.* **2016**, *8* (9), 831–836.
- (223) Curtiss, L. A.; Raghavachari, K.; Redfern, P. C.; Rassolov, V.; Pople, J. A. Gaussian-3 (G3) Theory for Molecules Containing First and Second-Row Atoms. *J. Chem. Phys.* **1998**, *109* (18), 7764–7776.
- (224) Nyden, M. R.; Petersson, G. A. Complete Basis Set Correlation Energies. I. The Asymptotic Convergence of Pair Natural Orbital Expansions. *J. Chem. Phys.* **1981**, *75* (4), 1843–1862.
- (225) Petersson, G. A.; Bennett, A.; Tensfeldt, T. G.; Al-Laham, M. A.; Shirley, W. A.; Mantzaris, J. A Complete Basis Set Model Chemistry. I. The Total Energies of Closed-shell Atoms and Hydrides of the First-row Elements. *J. Chem. Phys.* **1988**, *89* (4), 2193–2218.
- (226) Petersson, G. A.; Al-Laham, M. A. A Complete Basis Set Model Chemistry. II. Open-shell Systems and the Total Energies of the First-row Atoms. *J. Chem. Phys.* **1991**, *94* (9), 6081–6090.
- (227) Petersson, G. A.; Tensfeldt, T. G.; Jr, J. A. M. A Complete Basis Set Model Chemistry. III. The Complete Basis Set-quadratic Configuration Interaction Family of Methods. *J. Chem. Phys.* **1991**, *94* (9), 6091–6101.
- (228) Jr, J. A. M.; Ochterski, J. W.; Petersson, G. A. A Complete Basis Set Model Chemistry. IV. An Improved Atomic Pair Natural Orbital Method. *J. Chem. Phys.* **1994**, *101* (7), 5900–5909.
- (229) Ochterski, J. W.; Petersson, G. A.; Jr, J. A. M. A Complete Basis Set Model Chemistry. V. Extensions to Six or More Heavy Atoms. *J. Chem. Phys.* **1996**, *104* (7), 2598–2619.

-
- (230) Jr, J. A. M.; Frisch, M. J.; Ochterski, J. W.; Petersson, G. A. A Complete Basis Set Model Chemistry. VI. Use of Density Functional Geometries and Frequencies. *J. Chem. Phys.* **1999**, *110* (6), 2822–2827.
- (231) Jr, J. A. M.; Frisch, M. J.; Ochterski, J. W.; Petersson, G. A. A Complete Basis Set Model Chemistry. VII. Use of the Minimum Population Localization Method. *J. Chem. Phys.* **2000**, *112* (15), 6532–6542.
- (232) Eshuis, H.; Bates, J. E.; Furche, F. Electron Correlation Methods Based on the Random Phase Approximation. *Theor. Chem. Acc.* **2012**, *131* (1), 1084.
- (233) Ciancaleoni, G.; Rampino, S.; Zuccaccia, D.; Tarantelli, F.; Belanzoni, P.; Belpassi, L. An Ab Initio Benchmark and DFT Validation Study on Gold(I)-Catalyzed Hydroamination of Alkynes. *J. Chem. Theory Comput.* **2014**, *10* (3), 1021–1034.
- (234) Couce-Rios, A.; Kovács, G.; Ujaque, G.; Lledós, A. Hydroamination of C–C Multiple Bonds with Hydrazine Catalyzed by N-Heterocyclic Carbene–Gold(I) Complexes: Substrate and Ligand Effects. *ACS Catal.* **2015**, *5* (2), 815–829.
- (235) Hay, P. J.; Wadt, W. R. Ab Initio Effective Core Potentials for Molecular Calculations. Potentials for the Transition Metal Atoms Sc to Hg. *J. Chem. Phys.* **1985**, *82* (1), 270–283.
- (236) Andrae, D.; Häußermann, U.; Dolg, M.; Stoll, H.; Preuß, H. Energy-Adjusted ab Initio Pseudopotentials for the Second and Third Row Transition Elements. *Theor. Chim. Acta* **1990**, *77* (2), 123–141.
- (237) Bergner, A.; Dolg, M.; Küchle, W.; Stoll, H.; Preuß, H. Ab Initio Energy-Adjusted Pseudopotentials for Elements of Groups 13–17. *Mol. Phys.* **1993**, *80* (6), 1431–1441.
- (238) Tomasi, J.; Mennucci, B.; Cammi, R. Quantum Mechanical Continuum Solvation Models. *Chem. Rev.* **2005**, *105* (8), 2999–3094.
- (239) Vidossich, P.; Lledos, A.; Ujaque, G. First-Principles Molecular Dynamics Studies of Organometallic Complexes and Homogeneous Catalytic Processes. *Acc. Chem. Res.* **2016**, *49* (6), 1271–1278.
- (240) Vidossich, P.; Lledos, A.; Ujaque, G. Realistic Simulation of Organometallic Reactivity in Solution by Means of First-Principles Molecular Dynamics. In *Computational Studies in Organometallic Chemistry*; Macgregor, S. A., Eisenstein, O., Eds.; Springer Int Publishing Ag: Cham, 2016; Vol. 167, pp 81–106.
- (241) Woo, T. K.; Margl, P. M.; Deng, L.; Cavallo, L.; Ziegler, T. Towards More Realistic Computational Modeling of Homogenous Catalysis by Density Functional Theory: Combined QM/MM and Ab Initio Molecular Dynamics. *Catal. Today* **1999**, *50* (3–4), 479–500.
- (242) Marx, D.; Hutter, J. *Ab Initio Molecular Dynamics: Basic Theory and Advanced Methods*, 1 edition.; Cambridge University Press: Cambridge; New York, 2009.
- (243) Cramer, C. J.; Truhlar, D. G. Implicit Solvation Models: Equilibria, Structure, Spectra, and Dynamics. *Chem. Rev.* **1999**, *99* (8), 2161–2200.
- (244) Tomasi, J.; Cancès, E.; Pomelli, C. S.; Caricato, M.; Scalmani, G.; Frisch, M. J.; Cammi, R.; Basilevsky, M. V.; Chuev, G. N.; Mennucci, B. Modern Theories of Continuum

- Models. In *Continuum Solvation Models in Chemical Physics*; Mennucci, B., Cammi, R., Eds.; John Wiley & Sons, Ltd, 2007; pp 1–123.
- (245) Miertuš, S.; Scrocco, E.; Tomasi, J. Electrostatic Interaction of a Solute with a Continuum. A Direct Utilizaion of AB Initio Molecular Potentials for the Prevision of Solvent Effects. *Chem. Phys.* **1981**, *55* (1), 117–129.
- (246) Marenich, A. V.; Cramer, C. J.; Truhlar, D. G. Universal Solvation Model Based on Solute Electron Density and on a Continuum Model of the Solvent Defined by the Bulk Dielectric Constant and Atomic Surface Tensions. *J. Phys. Chem. B* **2009**, *113* (18), 6378–6396.
- (247) Sunoj, R. B.; Anand, M. Microsolvated Transition State Models for Improved Insight into Chemical Properties and Reaction Mechanisms. *Phys. Chem. Chem. Phys.* **2012**, *14* (37), 12715–12736.
- (248) Díez, J.; Gimeno, J.; Lledós, A.; Suárez, F. J.; Vicent, C. Imidazole Based Ruthenium(IV) Complexes as Highly Efficient Bifunctional Catalysts for the Redox Isomerization of Allylic Alcohols in Aqueous Medium: Water as Cooperating Ligand. *ACS Catal.* **2012**, *2* (10), 2087–2099.
- (249) Ortuño, M. A.; Lledós, A.; Maseras, F.; Ujaque, G. The Transmetalation Process in Suzuki–Miyaura Reactions: Calculations Indicate Lower Barrier via Boronate Intermediate. *ChemCatChem* **2014**, *6* (11), 3132–3138.
- (250) McQuarrie, D. A.; Simon, J. D. *Molecular Thermodynamics*; University Science Books: Sausalito, California, 1999.
- (251) Ochterski, J. W. Thermochemistry in Gaussian. *Gaussian Inc* **2000**.
- (252) Couce-Rios, A.; Lledós, A.; Ujaque, G. The Origin of Anti-Markovnikov Regioselectivity in Alkene Hydroamination Reactions Catalyzed by [Rh(DPEphos)]⁺. *Chem. – Eur. J.* **2016**, *22* (27), 9311–9320.
- (253) Dallanegra, R.; Chaplin, A. B.; Weller, A. S. Rhodium Cyclopentyl Phosphine Complexes of Wide-Bite-Angle Ligands DPEphos and Xantphos. *Organometallics* **2012**, *31* (7), 2720–2728.
- (254) Julian, L. D.; Hartwig, J. F. Intramolecular Hydroamination of Unbiased and Functionalized Primary Aminoalkenes Catalyzed by a Rhodium Aminophosphine Complex. *J. Am. Chem. Soc.* **2010**, *132* (39), 13813–13822.
- (255) Liu, Z.; Yamamichi, H.; Madrahimov, S. T.; Hartwig, J. F. Rhodium Phosphine– π -Arene Intermediates in the Hydroamination of Alkenes. *J. Am. Chem. Soc.* **2011**, *133* (8), 2772–2782.
- (256) Fernández, I.; Bickelhaupt, F. M. The Activation Strain Model and Molecular Orbital Theory: Understanding and Designing Chemical Reactions. *Chem. Soc. Rev.* **2014**, *43* (14), 4953–4967.
- (257) Rodríguez-Zubiri, M.; Baudequin, C.; Béthegnies, A.; Brunet, J.-J. Intermolecular Rhodium-Catalysed Hydroamination of Non-Activated Olefins: Effect of Olefin, Amine, Phosphine and Phosphonium Salt. *ChemPlusChem* **2012**, *77* (6), 445–454.

-
- (258) Barone, C. R.; Cini, R.; Clot, E.; Eisenstein, O.; Maresca, L.; Natile, G.; Tamasi, G. A NMR, X-Ray, and DFT Combined Study on the Regio-Chemistry of Nucleophilic Addition to platinum(II) Coordinated Terminal Olefins. *J. Organomet. Chem.* **2008**, *693* (17), 2819–2827.
- (259) Jensen, J. H. Predicting Accurate Absolute Binding Energies in Aqueous Solution: Thermodynamic Considerations for Electronic Structure Methods. *Phys. Chem. Chem. Phys.* **2015**, *17* (19), 12441–12451.
- (260) Bryantsev, V. S.; Diallo, M. S.; Goddard III, W. A. Calculation of Solvation Free Energies of Charged Solutes Using Mixed Cluster/Continuum Models. *J. Phys. Chem. B* **2008**, *112* (32), 9709–9719.
- (261) Segapelo, T. V.; Lillywhite, S.; Nordlander, E.; Haukka, M.; Darkwa, J. Palladium(II), platinum(II) and gold(I) Complexes Containing Chiral Diphosphines of the Josiphos and Walphos Families – Synthesis and Evaluation as Anticancer Agents. *Polyhedron* **2012**, *36* (1), 97–103.
- (262) Balcells, D.; Maseras, F. Computational Approaches to Asymmetric Synthesis. *New J. Chem.* **2007**, *31* (3), 333–343.
- (263) Peng, Q.; Duarte, F.; Paton, R. S. Computing Organic Stereoselectivity – from Concepts to Quantitative Calculations and Predictions. *Chem. Soc. Rev.* **2016**, *45* (22), 6093–6107.
- (264) Schneebeli, S. T.; Hall, M. L.; Breslow, R.; Friesner, R. Quantitative DFT Modeling of the Enantiomeric Excess for Dioxirane-Catalyzed Epoxidations. *J. Am. Chem. Soc.* **2009**, *131* (11), 3965–3973.
- (265) Johnson, E. R.; Keinan, S.; Mori-Sánchez, P.; Contreras-García, J.; Cohen, A. J.; Yang, W. Revealing Noncovalent Interactions. *J. Am. Chem. Soc.* **2010**, *132* (18), 6498–6506.
- (266) Contreras-García, J.; Johnson, E. R.; Keinan, S.; Chaudret, R.; Piquemal, J.-P.; Beratan, D. N.; Yang, W. NCIPLOT: A Program for Plotting Non-Covalent Interaction Regions. *J. Chem. Theory Comput.* **2011**, *7* (3), 625–632.
- (267) te Velde, G.; Bickelhaupt, F. M.; Baerends, E. J.; Fonseca Guerra, C.; van Gisbergen, S. J. A.; Snijders, J. G.; Ziegler, T. Chemistry with ADF. *J. Comput. Chem.* **2001**, *22* (9), 931–967.
- (268) Kumar, M.; Jasinski, J.; Hammond, G. B.; Xu, B. Alkyne/Alkene/Allene-Induced Disproportionation of Cationic Gold(I) Catalyst. *Chem. – Eur. J.* **2014**, *20* (11), 3113–3119.
- (269) Krauter, C. M.; Hashmi, A. S. K.; Pernpointner, M. A New Insight into Gold(I)-Catalyzed Hydration of Alkynes: Proton Transfer. *ChemCatChem* **2010**, *2* (10), 1226–1230.
- (270) Kovács, G.; Lledós, A.; Ujaque, G. Reaction Mechanism of the Gold(I)-Catalyzed Addition of Phenols to Olefins: A Concerted Process Accelerated by Phenol and Water. *Organometallics* **2010**, *29* (15), 3252–3260.

- (271) BabaAhmadi, R.; Ghanbari, P.; Rajabi, N. A.; Hashmi, A. S. K.; Yates, B. F.; Ariafard, A. A Theoretical Study on the Protodeauration Step of the Gold(I)-Catalyzed Organic Reactions. *Organometallics* **2015**, *34* (13), 3186–3195.
- (272) Wang, C.; Ren, X.-R.; Qi, C.-Z.; Yu, H.-Z. Mechanistic Study on Gold-Catalyzed Highly Selective Hydroamination of Alkylidenecyclopropanes. *J. Org. Chem.* **2016**, *81* (17), 7326–7335.

*Any theory is true,
until proven wrong.*

Anonymous

~ Annex A ~

**PUBLISH PAPERS RELATED
TO THE PH.D. THESIS**

A.1 Article I:

The Origin of Anti-Markovnikov Regioselectivity in Alkene Hydroamination Reactions Catalyzed by [Rh(DPEphos)]⁺ (reference 252).

Couce-Rios, A.; Lledós, A.; Ujaque, G. *Chem. – Eur. J.* **2016**, *22* (27), 9311–9320.

Computational Chemistry

The Origin of Anti-Markovnikov Regioselectivity in Alkene Hydroamination Reactions Catalyzed by $[\text{Rh}(\text{DPEphos})]^+$ Almudena Couce-Rios, Agustí Lledós,* and Gregori Ujaque*^[a]

Abstract: The development of regioselective anti-Markovnikov alkene's hydroamination is a long-standing goal in catalysis. The $[\text{Rh}(\text{COD})(\text{DPEphos})]^+$ complex is the most general and regioselective group 9 catalyst for such a process. The reaction mechanism for intermolecular hydroamination of alkenes catalyzed by $[\text{Rh}(\text{DPEphos})]^+$ complex is analyzed by means of DFT calculations. Hydroamination (alkene vs. amine activation routes) as well as oxidative amination pathways are analyzed. According to the computational results the operating mechanism can be generally described by alkene co-

ordination, amine nucleophilic addition, proton transfer through the metal center and reductive elimination steps. The mechanism for the formation of the oxidative amination side product goes via a β -elimination after the nucleophilic addition and metal center protonation steps. The origin of the regioselectivity for the addition process (Markovnikov vs. anti-Markovnikov additions) is shown to be not charge but orbitally driven. Remarkably, η^2 to η^1 slippage degree on the alkene coordination mode is directly related to the regioselective outcome.

Introduction

Hydroamination reactions of alkenes with amines represent one of the most economical pathways (in terms of both price and atom economy) for generating substituted amines.^[1–3] This process poses significant issues regarding regio- and chemoselectivity^[1b,4] and avoiding side reactions, such as oxidative amination,^[5] and remains one of the challenges for homogeneous catalysis.^[6] Some metal-catalyzed processes by means of non-direct routes have been developed; outstanding are those published by the Grubbs^[7] and Lalic^[8] groups. Nicewick has developed a process based on organic photoredox systems.^[9]

The metal catalysts developed for direct hydroamination include lanthanides,^[10] early and late transition metals.^[11] The most versatile catalysts for intermolecular alkene hydroamination are based on late transition metals,^[1c,12,13] mainly providing Markovnikov products.^[14] In recent years, the use of Ir- and Rh-based catalysts, and more recently Cu hydride catalysts,^[15,16] has enabled significant advances in controlling regioselectivity.^[17] Rhodium(I) complexes have proven to be particularly efficient for promoting selective anti-Markovnikov hydroamination of both terminal alkynes^[18] and vinylarenes.^[19,20] In 1999, Beller reported the first intermolecular anti-Markovnikov oxidative amination and hydroamination of styrenes catalyzed by the cationic $[\text{Rh}(\text{COD})_2]\text{BF}_4/\text{PPh}_3$ complex.^[19] In 2003, Hartwig disclosed the first example of selective hydroamination of ole-

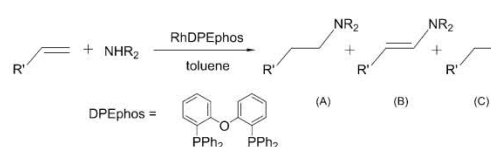


Figure 1. Hydroamination of vinylarenes with secondary amines catalyzed by $[\text{Rh}(\text{DPEphos})]^+$ developed by Hartwig.

fins to generate terminal amines as the major product.^[20] Using $[\text{Rh}(\text{COD})(\text{DPEphos})]^+$ as catalyst (DPEphos = bis[(2-diphenylphosphino)phenyl] ether), the intermolecular anti-Markovnikov hydroamination of unactivated vinylarenes with secondary amines, to yield hydroamination product (A) as the major product, was achieved. The enamine (B), from oxidative amination, and ethylbenzene (C) were formed as minor products (Figure 1).

This rhodium complex has been described as the most general and regioselective group 9 catalyst for the anti-Markovnikov hydroamination of olefins.^[17] An intramolecular version of this reaction was also described.^[21] In 2014, Hull et al. developed the hydroamination reaction of an allyl-imine and morpholine using this same catalyst but yielding the Markovnikov product.^[22] Other rhodium complexes have shown anti-Markovnikov directing capability, such as rhodium-porphyrin complexes for the hydrofunctionalization of olefins^[23] and $[\text{Rh}(\text{Ph}_2\text{P}(\text{CH}_2)_3\text{OEt})_2]$ for the oxidative amination of styrene.^[24] Rhodium-catalyzed chemo-, regio- and enantioselective additions of N-nucleophiles to terminal allenes have been recently described.^[25]

Computational methods have been widely applied to mechanistic studies of metal-catalyzed hydroamination reactions.

[a] A. Couce-Rios, Prof. Dr. A. Lledós, Dr. G. Ujaque
Departament de Química, Universitat Autònoma de Barcelona
08193 Cerdanyola del Vallès (Spain)
E-mail: agusti@klingon.uab.es
gregori.ujaque@uab.cat

Supporting information and ORCID from the author for this article are available on the WWW under <http://dx.doi.org/10.1002/chem.201504645>.

A.2 Article II:

Hydroamination of C–C Multiple Bonds with Hydrazine Catalyzed by N-Heterocyclic Carbene–Gold(I) Complexes: Substrate and Ligand Effects (reference 234).

Couce-Rios, A.; Kovács, G.; Ujaque, G.; Lledós, A. *ACS Catal.* **2015**, 5 (2), 815–829.

Hydroamination of C–C Multiple Bonds with Hydrazine Catalyzed by N-Heterocyclic Carbene–Gold(I) Complexes: Substrate and Ligand Effects

Almudena Couce-Rios, Gábor Kovács, Gregori Ujaque,* and Agustí Lledós*

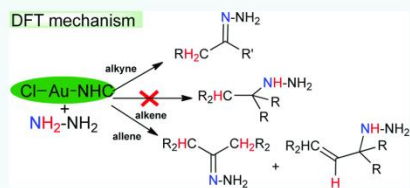
Departament de Química, Universitat Autònoma de Barcelona, 08193 Cerdanyola del Vallès, Spain

Supporting Information

ABSTRACT: In this work, we computationally address, from DFT calculations, mechanistic issues of the recently described hydroamination reactions catalyzed by (carbene) gold(I) complexes that use hydrazine as N-nucleophile. We have explored the hydroamination of alkynes, alkenes, and allenes using three gold–carbene catalysts reported by Bertrand's and Hashmi's groups. Aspects such as the associative or dissociative nature of the ligand exchange between hydrazine and the substrate, the generation of the catalytically active π -complex, the inner- or outer-sphere mechanism for the nucleophilic attack, the nitrogen to carbon proton transfer or the relative importance of the ligand substitution, the nucleophile addition, and the proton transfer barriers in the catalytic cycle are analyzed in light of the DFT results, taking into account the nature of the carbene ligand and the substrate. The study can provide background for the design of further hydroamination reactions using simple small N-nucleophiles.

KEYWORDS: DFT calculations, gold catalysis, hydrazine, hydroamination, N-heterocyclic carbene ligands

DFT mechanism

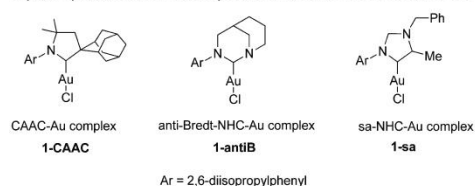


INTRODUCTION

Nitrogen-containing organic compounds (either acyclic or heterocyclic) are important chemical substances, ranging from agrochemicals to pharmaceuticals. Since traditional reactions for C–N bond formation face serious limitations, hydroamination catalyzed by different transition metal homogeneous complexes have been used as an effective synthetic method for such purpose.^{1–8} Several late transition metal complexes were found to be active catalysts of hydroamination reactions.⁹ Previously, these homogeneous catalysts had palladium,^{10–12} rhodium,^{13–15} ruthenium,^{16,17} and platinum^{18,19} centers. In recent years, gold(I) complexes have proven to be very efficient catalysts for activating C–C π bonds toward nucleophilic additions.^{20–33} Accordingly, gold has been identified as an efficient hydroamination catalyst,^{34–45} and a number of gold(I) complexes were found to work very efficiently with aryl and alkyl amines. However, hydroamination with small nucleophiles such as ammonia or hydrazine represents a much more challenging task.⁴⁶ In spite of the large interest for using these molecules in synthetic reactions, the examples available are yet rather scarce: Hartwig⁴⁷ and Buchwald⁴⁸ reported the palladium-catalyzed coupling of ammonia with aryl halides, whereas Stradiotto achieved the cross-coupling of aryl chlorides and tosylates with hydrazine.⁴⁹ One of the main difficulties that hamper the use of ammonia as N-nucleophile in transition-metal-catalyzed processes is the immediate formation of stable Werner ammine complexes, deactivating the catalyst.^{46,50–53} In addition, the moderate basicity and low acidity of ammonia disfavor proton exchanges, either to or from ammonia.

The versatility and robustness of N-heterocyclic carbene ligands (NHC) have found wide application in gold catalysis,^{54–56} and have allowed for the preparation of the first homogeneous catalyst active in the hydroamination with ammonia. Bertrand et al. reported gold(I) complexes with bulky cyclic (alkyl)(amino)carbene (CAAC) ligands^{57–59} (Scheme 1) as efficient catalysts for the hydroamination of nonactivated multiple bonds with a variety of amines.^{60–63} Moreover, they also discovered a CAAC–gold(I) complex as the first homogeneous catalyst active in the hydroamination of alkynes and allenes with ammonia.⁶⁴ Despite the fact that the gold(I)–CAAC species interacts with ammonia forming a Werner-type complex as the most stable initial intermediate, it

Scheme 1. Carbene–Gold(I) Catalysts for Hydroamination of Alkynes Studied in the Present Work



Received: October 31, 2014

Revised: December 17, 2014

Published: December 18, 2014